Plasmonic Material Induced and Quantum Dots Sensitised Nanomolecular Devices for Photocatalytic Water Splitting

A THESIS

Submitted for the

Award of Ph.D. Degree in Chemistry

(Faculty of Science)

To the

UNIVERSITY OF KOTA, KOTA

by

NIRANJAN KUMAR MANDAWAT

Under the Supervision of

Dr. Neelu Chouhan

Associate Professor

Department of Pure & Applied Chemistry
University of Kota, Kota (Rajasthan)

2019

CERTIFICATE

It is to certified that the:

Thesis entitled ***“Plasmonic Material Induced and Quantum Dots Sensitised Nanomolecular Devices for Photocatalytic Water Splitting”*** submitted by **Niranjan Kumar Mandawat (Registration No.RS/1765/13)** is an original piece of research work carried out by the candidate under my supervision. He has completed the following requirement as per Ph.D. regulation of the University:

a) Course work as per the University rules.
b) Residential requirement prescribed by the University. (200 days)
c) Regularly submitted annual progress report.
d) Presented his work in the department committee.
e) Published/accepted minimum of two research paper in a referred research journal and paper Presentation in seminar.

I recommend the submission of the thesis.

Dr. Neelu Chouhan
Associate Professor
(Research supervisor)
Department of Pure and Applied Chemistry,
University of Kota, Kota- (Raj.)-324005
Tel: 91-0744-2411742; Fax No. - 91-0744-2411742
Email: niloochauhan@hotmail.com & neeluchouhan@uok.ac.in

ANTIPLAGIARISM CERTIFICATE

It is certified that PhD Thesis Titled "**Plasmonic Material Induced and Quantum Dots Sensitised Nano molecular Devices for Photocatalytic Water Splitting"** by **Niranjan Kumar Mandawat** has been examined by us with the following anti-plagiarism tool. We undertake the follows:

a. Thesis has significant new work/knowledge as compared already published or are under consideration to be published elsewhere. No sentence, equation, diagram. Table. Paragraph or section has been copied verbatim from previous work unless it is placed under quotation marks and duly referenced.

b. The work presented is original and own work of the author (i.e. there is no plagiarism). No ideas, processes, results or work of others have been presented as author's own work.

c. There is no fabrication of data of or results which have been complied and analysed.

d. There is no falsification by manipulating research materials. Equipment or processes, or changing or omitting data or results such that the research is not accurately represented in the research record.

e. The thesis has been checked using urkund software found within limits as per HEC plagiarism Policy and instructions issued from time to time:

(Name & Signature of Research Scholar)	**(Name & Signature and seal of Research Supervisor)**
Place:	Place:
Date:	Date:

ABSTRACT

Energy plays a vital role in modernization of society and making life easy and healthy. Conventional fuels are most common source for exploiting energy, which contains higher carbon and these fossil fuels release green house gases in atmosphere on combustion. Moreover, these fuels are depleting day by day. Therefore, it became essential to replace the conventional fuel with the contemporary environmental friendly fuels. These eco-friendly fuels incude solar, wind, geothermal, hydrothermal tidal-energy. Although, all of these forms of energy are free but we need to be instrumental to harvest these energies. Out of above, we select solar energy to harvest the clean and green hydrogen energy by breaking of water (artificial photosynthesis) in presence of some plasmonic photocatalytic systems: Ag/AgCl@ZnO, Ag/AgCl($BaCl_2$)@ZnO, Ag/Ag_3PO_4@ZnO, Ag/Ag_2CO_3@ZnO, Ag/Ag_2SO_3@ZnO and Ag/$AgNO_3$@ZnO. Above samples were synthesized by using one pot conventional (all systems) and microwave methods (only Ag/AgCl@ZnO). As synthesized samples are well characterised at the beginning and end of the water splitting application by using different sophisticated analytical techniques such as: XRD, FTIR, FESEM, TEM, HRTEM, EDX, UV-Vis spectrophotometry, and spectrofluorimetry, etc. above samples are investigated for hydrogen generation through water splitting in 20% methanolic solution under 1Sun light irradiation. All samples show quite good water splitting efficiency. It was found that the sample prepared through microwave synthesis method show high activity towards hydrogen production in comparison to the samples prepared by conventional methods and plasmonic system Ag/AgCl@ZnO shows the maximum water splitting efficiency among all studied samples. Their efficiency exhibits good correlated with their observed properties. Moreover, on the basis of this correlation a mechanism for the water splitting process is proposed for the given series of the systems.

Key words: Plasmonic systems, nanocomposite, Ag/AgX@ZnO, water splitting, hydrogen generation, one pot convention method, microwave synthesizer, etc.

CANDIDATE’S DECLARATION

I hereby declare that the work, which is being presented in the thesis, entitled “**Plasmonic Material Induced and Quantum Dots Sensitised Nanomolecular Devices for Photocatalytic Water Splitting**” in partial fulfilment of the requirement for the award of the Degree of Doctor of Philosophy, carried under the supervision of **Dr. Neelu Chouhan**, Department of Pure and Applied Chemistry, University of Kota, Kota, (Rajasthan) and submitted to the Research Section, University of Kota, Kota represents my ideas in my own word and where others’ ideas or words have been included, I have adequately cited and referenced the original sources.

The work presented in this thesis as not been submitted elsewhere for the award of any other degree of diploma from any Institutions. I also declare that I have adhered to all principles of academic honesty and integrity and have not misrepresented or fabricated or falsified any idea/data/fact/source in my submission. I understand that any violation of the above will cause for disciplinary action by the University and can also evoke penal action from the sources which have not been property cited or from whom proper permission has not been taken when needed.

Date:

Niranjan Kumar Mandawat
(Research scholar)

This is to certify that the above statement made by **Niranjan Kumar Mandawat Registration No. RS/1765/13,** is correct to the best of my knowledge.

Date:
Place:

Dr. Neelu Chouhan
Associate Professor
(Research supervisor)
Department of Pure and Applied Chemistry
University of Kota, Kota- (Raj.)-324005

ACKNOWLEDGEMENT

One of the splendid moments of my life is completion of PhD thesis, it is a happy moment for me. When I look over the journey with different milestones found during the completion of this research work and thesis writing, I found almighty, my supervisor, all of my friends and family members at my side, who had helped at different fronts and gave me big hand whenever I need their support.

I take this opportunity to acknowledge their kind help with the deep sense of gratitude for helping me in the successful completion of the work. Firstly, I bow my head in front of God, who give me the strength and wisdom to lead me on the right path and enough courage to go through the toughest situations of the path.

Next to God I found my research supervisor **Dr. Neelu Chouhan,** whom I respect and appreciate from core of my heart for her constructive advice, precious knowledge and inspiring motivations. Her remarkable scientific aptitude, hard work and affectionate nature, always works as a catalyst for me towards achieving the short term and long term goals on time. Which, was impossible without her untiring tolerance, constant encouragement, kind concern and guidance offered to me. I found myself privileged enough to have her as my research supervisor.

I have no words to express my gratitude towards her indefatigable support with tireless enthusiasm to my efforts even in my critical condition. 1 am always grateful to her for sparing her valuable time on my research. Not only she direct my research as a mentor but she also played an important role of counsellor. With my heart and soul, I want to thank her for accepting me as her PhD scholar and guiding me through out. For all these, I sincerely thank her from bottom of my heart and will be truly indebted to her throughout my life time.

I gratefully acknowledge financial support received from UGC (JRF/SRF) that used for purchase of common chemicals and other supplies, along with the Junior / Senior Research Fellowship award, which strengthened me to perform my work comfortably.

I am also grateful to **Prof. Ashu Rani**, Dean, PG studies of the University along with all **faculty member of** the Department including **Dr. Bhawani Singh, Dr. Sushil Sharma, Dr. Shweta Vyas** and M**r. Ankit Sharma** as well as the official staff of Department, Research section and Accounts section of University, for their direct or indirect help and timely cooperation.

My special words of thanks should also go to **Prof. Suresh Chand Ameta,** Professor and Director, Department of Chemistry, Pacific University, Udaipur for his guidance and support throughout the research work. I am grateful to my ex-colleagues and seniors in the lab **Dr. Renu Hada, Dr. Sakshi Kabra, Dr. Khushboo Shirivastava, Dr. Stuti Katara, Dr. Niharika shringi, and Dr. Priynka rajoriya** for their guidance and moral support. In my daily work I have been blessed with a friendly and cheerful group of my lab mates' researchers, these are, **Rajesh Kumar Meeena, Kavita Nagar, Neeta Gurbani, Khaksaha Ansari, Tripti Berman, Naval Kishore Sahu, Hariom Gour, Deepak Karsoliya, Kiran Parashar, Niharika Shringi and Ashok Suman,** for their unconditional support and friendly atmosphere in the lab throughout my research career.

In the end, I am thankful to my family members for their unquestionable love. Words fail me in expressing my heartfelt thanks **to my parents Sh. Sohan Lal Mandawat and Smt. Kailash Devi** for their patience, understanding and belief in my effort. and for their constant support and prayers. and I extent my heartfelt thanks to my wife **Reena** for the support and care she had provided me during this work. I appreciate my baby, my little angel **Sanvi** for abiding my ignorance and patience she showed during my thesis writing. Words would never say how grateful I am to both of you. I am also thankful to my **brother Shashi Ranjan Mandawat** and my sister **Meenakshi and Urmila,** and my brother- in -law **Mr. Nandkishor Khinchi and Mr. Mukesh Kumar Chol, and my nephews** for their caring attitude. And my heartfelt thanks for the blessings of my father-in-law **Sh. Parmanand Verma** and mother-in-law **Smt. Mamata Verma** though they are not physically with me at this moment.

I would like to thanks my uncles Mr. **Kailash Paharia** and **Mr. Madan Lal Paharia** Lecturers, Govt. College, Bundi, who provides me the help and boost my moral time to time. My heartiest thank to my all friends including **Ashok, Dhanraj, Nemichand** and **Sandeep** for their constant encouragement.

At last but not least, I want to bestow my sincere thank the people who contributed directly and indirectly in making my dreams come true.

(Niranjan Kumar Mandawat)

TABLE OF CONTENTS

Introduction

CHAPTER-2 66-79

Instrumentation

LIST OF TABLES

LIST OF FIGURES

No. Figure	Title	Page No.

CHAPTER 1

CHAPTER 2

CHAPTER 3

LIST OF ABBREVIATIONS AND SYMBOLS

AP	Artificial Photosynthesis
AU	Arbitrary Unit
BE	Binding Energy
CB	Conduction Band
CIE	Commission Internationale de l'Eclairage
DIW	De-ionised Water
DRS	Diffuse Reflectance Spectroscopy
DSSC	Dye Sensitized Solar Cells
EC	Energy Carrier
EDS	Energy Dispersive X-ray Spectroscopy
E_g	Bond Gap
eV	Electron Volt
FC	Fuel Engine
FCC	Face Centred Cubic
FESEM	Field Emission Scanning Electron Microscopy
FTIR	Fourier Transform Infrared Spectroscopy
FWHW	Full Width Half Maxima
GHGs	Green House Gases
GHz	Gigahertz
h	Hour
HRSEM	High Resolution Scanning Electron Microscopy
HRTEM	High Resolution Transmission Electron Microscopy
ICE	International Combustion Engine
IEA	International Energy Agency
IR	Infrared

LSPR	Localized Surface Plasmonic Resonance
M/m	Molar
MEG	Multiple Excite Generation
MHz	Megahertz
Min	Minute
mL	Millilitre
mmol	Mill molar
MW	Microwave
NC	Nanocomposite
NG	Natural Gases
NIR	Near-Infrared Radiation
Nm	Nano meter
NP	Nanoparticle
NRs	Nano rods
PEC	Photo electrochemical
PED	Potential Energy Distribution
PL	Photoluminescence
PLE	Photoluminescence Emission
PV	Photo Voltaic
QDs	Quantum Dots
QSE	Quantum Size Effect
RES	Regenerative Energy Sources
RT	Room Temperature
SAED	Selected Area Electron Diffraction
Sec	Second
SPB	Surface Plasmon Band
SPR	Surface Plasmonic Resonance

STEM	Scanning Transmission Electron Microscopy
UV	Ultra Violet
VB	Valance Band
VW	Very Weak
W	Watt
WBG	Wide Bad Gap
XAS	X-ray Absorption Spectroscopy
XPS	X-ray Photoelectron Spectroscopy
XRD	X-ray Diffraction

Chapter- 1

Introduction

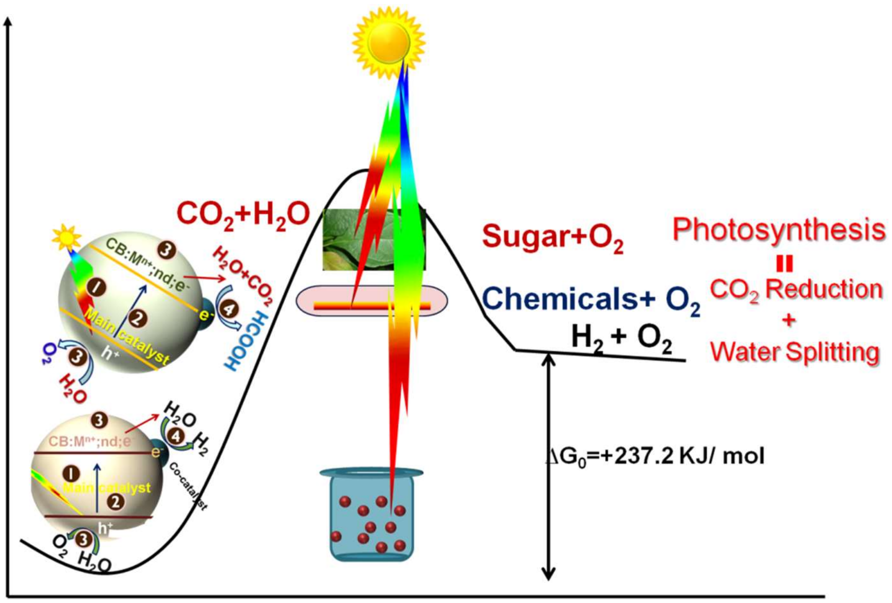

ABSTRACT

This chapter discussed the variety of materials in context of the energy and focused on efficient renewable energy sources that can replace current conventional source of the energy. Hydrogen is established as a good source and carrier of energy and can be easily produced by different sources (98% materials contain hydrogen). Water can be good eco-friendly source of hydrogen as it is not only abundantly available on earth but also combustion of hydrogen gives water without emission of green house gases. As water splitting can produce hydrogen and oxygen. Therefore, the water and solar energy is taken as a sustainable source of energy in presence of the photocatalyst. Nature abundantly blessed us with sunlight and water at almost no cost. Therefore, different class of photocalalysts was discussed in this chapter the light of their synthesis, efficiency of water splitting for hydrogen generation by using plasmonic material induced- and quantum dot sensitized- materials and other systems of similar category.

1.1 Introduction

Hydrogen can suppose to be treated as a future fuel and energy carrier because it can't librates the Greenhouse gases (GHGs) i.e. SO_x, NO_x, CH_4, CO, CO_2, etc on burning. Moreover it produces water on combustion and it as highest fuel efficiency (75%) among the presently available fuels. Therefore, it considered as a clean and efficient fuel and it also has good ability to replace the conventional fossil fuel. This replacement can significantly address the great problem of pollution. Hydrogen can be generated by the renewable (hydro, wind, wave, solar, biomass and geothermal) and non-renewable (coal, natural gas and nuclear) source of energy. Currently, it is produced mainly from steam reforming from hydrocarbon (obtained from conventional fuel or petroleum by product). And it can be generated by using carbon-free renewable/ sustainable energy sources through a energy-efficient route. Nature in form of plants motivate us to utilize water and carbon dioxide to produce H_2, O_2 or HCHO, CH_3OH, HCOOH, etc under the sunlight. Solar water splitting is a part of artificial photosynthesis (AP) and reduction of carbon dioxide is another part of it. artificial photosynthesis is a renewable and sustainable way to produce clean fuel (H_2 and O_2) by utilizing sunlight (which is the most abundant and free of cost available energy source on the Earth), photocatalyst (semiconductor) and water (which is also the most abundant (~75%) natural resource available on Earth). Few methods of hydrogen production and their application in livelihood are shown in Figure 1.1. We can produce hydrogen from breaking of water just like nature. Currently the most of the hydrogen is produced by electrolysis of water, which uses electricity that produced from conventional energy sources. So it is not an good choice. Another way used is a direct photoelectrochemical (PEC) method, which is more efficient and economic process than electrolysis because it is a combination of a solar cell and an electrolyzer. Furthermore, photocatalytic water splitting is also a way to split water by using water and photocatalyst material under sunlight irradiation over a reaction vessel.

Figure 1.1 explains the methods used for hydrogen production i.e. steam reforming, pyrolysis / plasma reforming of the natural gas, gasification/partial oxidation of coal or oil, by utilizing the solar energy for thermal, electrolysis, photocatalytical splitting of water, fission/fusion nuclear energy for thermal or electrical water splitting or biolysis.

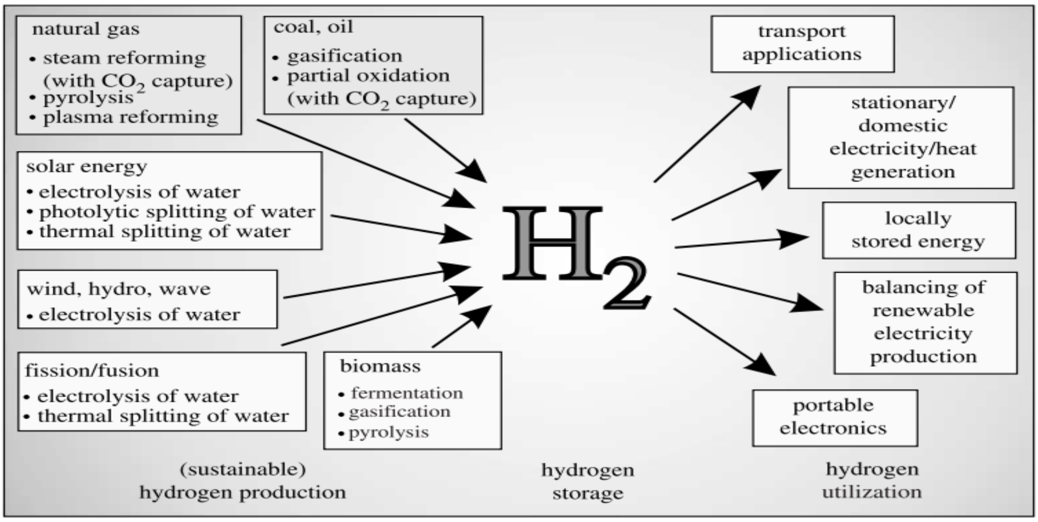

Figure 1.1 Hydrogen production, storage and application. (Edwards. et al., 2007) of water by fermentation, gasification and pyrolysis. After careful storage, it can be utilized in transport application electricity/heat generation, portable electronics or many more.

1.2 Current Energy Scenario

Behind the development/ urbanization (good living standard) in every facet of life (economical, social and political) there is a requirement of a safe, inexpensive, clean, uninterrupted, sufficient, and environment-friendly energy production. Which, is needed to maintain the global economic development and political stability. Worldwide our current energy (conventional energy) storage includes (Chouhan and Liu, 2017) coal (984 billion tons) oil (1047.7 billion barrels), nature gas (NG; 5501.5 trillion standard cubic foot (SCF)), which might be sustain our energy needs only for 205 40, and 54 years, respectively. (Chouhan and Liu, 2017) Furthermore, the available energy sources are not equally shared out in the world (25% of world coal reserves in United States, 60% of oil reserves in Middle East countries). (Chouhan and Liu, 2017) As generated energy resources-imbalance give rise to the energy insecurity among countries who has derisory energy supply/ assets will cause political turbulences. As per record, around one-fourth of the world's population (1.6 billion) still does not have electricity. Because the worldwide-energy consumption (~20 TW per year) rate is proportionally increases with the human population (~10 billion) and current electricity resources are limited. (Rogner, 2004) However, the continuous increase in energy requirements has been putting a lot of pressure on limited conventional energy sources. But the shortage of available fossil fuels and their over usages correspond to the environmental threat (due to the high excel of greenhouse gases) that compel us to explore an uninterrupted supply of environmentally benign energy by utilizing renewable energy sources. All conventional sources of energy are carbon rich and so their combustion leads to CO_2 or methane emission (main greenhouse gas) that adds to the extra burden on its naturally occurring amount. These greenhouse gases absorb the infrared part of the sun's radiation and radiates back to Earth's surface, which traps the heat and keeps Earth 30^0 C warmer than it would be otherwise – because without greenhouse gases Earth would be too cold to live. But the additional CO_2 leads to an extra rise in temperature (van Ruijven et al., 2011). As a consequence, Earth's average temperature increases, which will result in unpredictable changes in weather pattern of mother Earth in the form of natural disasters: inundates, famines, and go under water of low-lying areas due to melting of ice at the poles. The concentration of carbondioxide level in our atmosphere is found to be almost 408 ppm (Ruijven et al., 2011) besides the value suggested by scientists i.e. 400 ppm, which would result in to the irreversible disastrous outcome. Rate CO_2 emission in 2005 was found to be 27 Gigatons, which can be increased up to 42 Gigatons by 2030 and 62 Gigatons by 2050. (Mauna Loa Observatory in Hawaii, NOAA-ESRL, 2018) The country wise contribution to CO_2 emission is shown in Figure 1.2a (Mauna Loa Observatory in Hawaii, NOAA-ESRL, 2018) and it is found the most of this emission belongs to the power, transportation and industrial segments. Our historical energy utilization (1990-2011) value and advanced (2011-2035) energy projection are exhibited in Figure 1.2b, (Nezhad, 2009), which can be augmented by the rate of 1.4% per year till 2035.

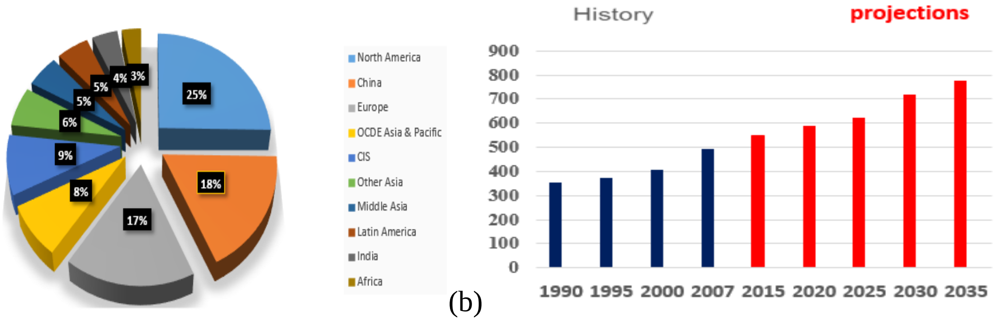

(a) (b)

Figure 1.2 (a) represents the country wise contribution in CO_2 emission and (b) our historical and futuristic energy profile 1990-2035. (Mauna Loa Observatory in Hawaii, NOAA-ESRL, 2018) and (Nezhad, 2009)

The worldwide energy consumption profile revealed the continuous increase in average capacity of energy exploitation rates with time from about 65% of the 1990 to 80% of 2009, will continue to be increase in the future (Nezhad, 2009). This increment in energy demand imposed great challenges before us in the form of upsetting climate and huge fund investments in energy segment. All are the problematic issues for the developing and developed countries. As per report of Nezhad, the increase in population and energy consumption rate was found among the both developed (20% and 60%) and developing countries (80% and 40%) (Nezhad, 2009). Now, to meet these requirements with no hurt to the environment is a big test for mankind.

The four major pillars of the energy scenarios are: (i) technological advancements rate, environmental-movement impact's, economic growth's status, and geopolitics conditions (including war, peace, and terrorism). To beat these energy problems, two main approaches are in practice to achieve the long-term energy situation: 1) the first scenario involves the advanced energy-producing technologies and/or hybrid fuel or engine implementation in place of the long-term development process to reduce the gasoline usages and to nullify the impact on environment or climate change effect by more fixations of the emitted gases in environment / discovery of new energy efficient gasoline product. The six prominently available renewable resources in nature are: solar, biomass, bio-fuels, wind, hydropower, and geothermal. These energy sources are economical, social, and environmental viable. Unfortunately till today, no single approach is capable enough to accomplish the goal. Therefore, a large number of energy scenarios are predicted by various energy agencies, including the International Energy Agency (IEA), Energy Information Administration (EIA), and many more, is dealing with the different proportions of all studied. The most authentic scenario on world energy scenario was predicted by IEA which was based on the world's energy facts and perceptions, which includes a committee of 5000 members (experts from 39 countries) working on Energy and Technology to development the best world energy scenario for 2050. They believe that the world energy requirement might be increased twice in 2050 and rate of carbon emission will be raised by 2.5 times. (Nezhad, 2007) Their recommendations focused on usages of alternative energy resources. IEA projected the plan for world energy scenario of 2050 to figure out the future world energy prospective, as represented by Figure 1.3 (Nezhad, 2009).

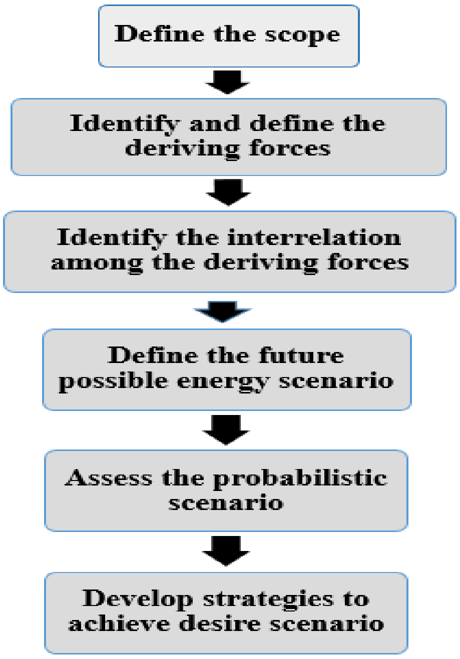

Figure 1.3. Stepwise planning to improve energy scenario. (Nezhad, 2009)

Figure 1.3 exhibits a flow chart for development of the energy scenario to attain the long lasting energy scenario. The scenario started with identification of the future scope of the given energy scenario model that followed by the assessment of the chief motive behind the dynamics of the expected energy bazaar, and analyzed by identification of the inter- and intra- relationship among the chief motives. The present state of energy is not sustain because of mismatch in energy demand *Vs* population ratio, based on supply of the fossil fuel that results in unacceptable high level of the CO_2 emission. Therefore, by defining and employing the technologies based on existing or under development sustainable energy solutions, lead to a path toward clean and competitive energy. Consequently, IEA suggested the possible models of future energy scenarios, which became the basis of futuristic energy blue map and their required technologies would be extended. By assuming that the future energy requirments and rate of CO_2 emissions under the above driving forces, IEA set the time based targets to achieve the most feasibly assessed energy at reduced rate of the CO_2 emission level for particular time period i.e. 2050, by utilizing decision supportive software. Finally, strategies will be developed to accomplish the goal. No single strategy is enough to reach the desired level of energy production, consumption and CO_2 reduction. Therefore, a fusion of the following step might be used for achieving the desired goal.

1. Research development, demonstration and deployment of new high technology
2. Environmental Repercussion and techniques to reduce CO_2 emission.
3. Investment strategies for Energy Business
4. Governmental involvement for effective development of clean energy reduce of CO_2 emission

1.3 Fuel: Past, Present and Future

Energy is the basis of all types of development of mankind that visualized in the form of living standard electricity production, mordenization, power, transport vehicles, industries, agriculture, commercial, public services, and, many more. Energy consumption is proportional to the living standard of the human being. Therefore, usages of energy is proportional to prosperity of the community/country in terms of the paying capacity, climate impact, income and urbanization level (Jiang and O' Neill, 2004). Fuel provides us energy, which is the basic grounds for all type of modernization. The major driving forces behind the world fuel supply and demand are: fuel growth rate, energy consumption rate, alternative energy sources, investment requirements, poltical/geographical changes, gasoline prices, global energy density, rate of CO_2 emission, and advancement in technology (Figure 1.4a). The renowned geophysicist H. K. Hubbert (1971) predicted that the fossil fuels era would be about to over shortly and the United States conventional fuel stock might be run out by 2050 and world's convention energy resources will be finished by 2100 (Hubbert, 1971). Soaring price of fuels Figure 1.4b, proving Hubbert's predictions correct. We cannot denied the present situation based on the current fuel status. Rather proactive action should be taken to avoid the futuristic repercussion of the energy crisis. The cost paid (by means of energy crisis, endangering rare species, climate change, ecological imbalance, pollution, human health, etc) for the economical prosperity and development of Human by environment is too high.

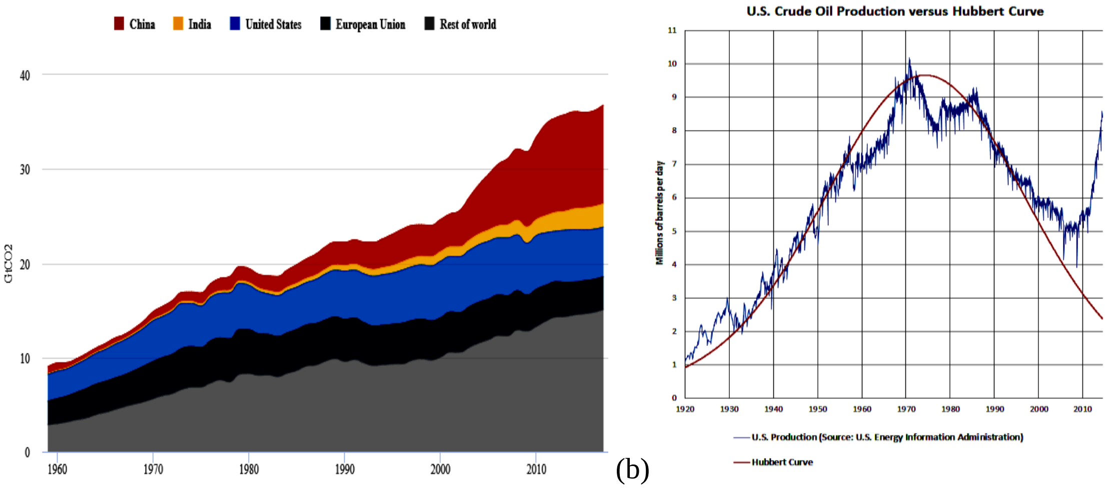

(a) (b)

Figure 1.4 (a) Annual CO_2 emissions from fossil fuels by major country and rest of world from 1959-2017, in gigatons CO_2 per year ($GtCO_2$). Note that 2017 numbers are preliminary estimates and (b) Hubbert bell plot predicting the Global oil asset. (Hubbert 1956,1971)

Approximately, three-quarter energy (86.4% share of fossil fuels) of world is obtained by combustion of nonrenewable fossil fuels (Yuksel, 2008) that includes: 36.0% petroleum, 27.4% coal and 23.0%, NG. The world mostly depends upon the fossil sources of energy, which are non-renewable because the millions of years required to creat fuel but its rate of consumption is quite fast than the formation of the new fuel reserves. On the other hand it creates a large amount of pollution. Therefore, for saving our earth from pollution and to give the solution to the scarcity of conventional oil, switching from fossil fuels to renewable/ sustainable/ nonconventional/ alternate energy sources of energy is the current need of a hour. That gives us freedom from day by day increasing price of fuel and pollution by creating a lot of new green jobs. And we are looking forward to offer the energy to the two billion no electricity access -population of earth (Hinrich-Rahlwes, 2013). The abundant availability and almost no or very small amount of generation of GHGs are the most common salient feature of the all type of renewable energy sources such as biomass/ biofuels, water, wind, Sun, geothermal and hydropower. Currently, we are tape this energy in form of the electrical energy. But we need to improve the technology to tape these unlimited “fuels”. In looking to the present energy scenario, the demands and interest of the political and industrial personals increases towards sustainable energy solution, which is now became an essential part of every country‘s energy policy. Some of the renewable technologies based on the solar and the wind energy, have already started maintaining their growth in double-digit since past decade at world level and leading to faster worldwide technological implement (Hairston, 1996). Therefore, RE technologies deployed in many area and it has been rapidly increasing to meet the growing energy demand. However, the main drawback associated with the technology is their unreliability because their encashment is seasonal/ time or nature -dependent which did not promise us for energy security but able to help environment to growth healthy and ability to face energy challenges to sustain the Universal commercial energy supply.

We had also take a step towards the above challenge for hydrogen production using water and sunlight in presence of photocatalyst. For this we had gone through the merits and demerits of the available technologies and ways out to make the technique more profitable. Therefore, we had selected the solar splitting of water for hydrogen production that can be used as a green and clean fuel. Because hydrogen is the lightest element among all available elements with highest energy density material (142kJ/kg) and its combustion gives water without GHGs emissions. Hence, in that way we can produce renewable power in terms of green fuel, a good and efficient energy carrier in an eco-benign way. Nature holds hydrogen in almost 98% of things found in nature in various chemical from with other elements. H_2 can be used as fuel but then it should be existed in free H_2 gas form. It had the highest energy-to-weight ratio among all of the available fuels. 1 Kg of hydrogen gas holds the equal amount of energy that belongs to 2.1 Kg of NG and 2.8 Kg of gasoline. possess the same amount of energy as 2.1 Kg of Natural Gas or 2.8 Kg of gasoline (Center for Strategic and International Studies, Global Strategy Institute, 2005). Hydrogen holds the great promise of providing most clean, renewable and abundant fuel when it extracted from its compound form furthermore even after burning it can make water, which can further delivered hydrogen on breaking down to its elements. In that way it can be recycled. Therefore we can say, hydrogen is the cleanest available fuel of the world. More to the point with grand approval and immense public concern towards the eco-health of the planet, only a few countries (e.g. Turkey, The Netherlands, etc.) contributing in countable amount of H_2 generation from regenerative resources of energy. Although, the benefits of hydrogen are great in number but with few demerits its storage /transportation and GHGs produced if hydrocarbon/hydrides used for preparation. Because hydrogen (in liquid form) storage requires four times larger space than conventional petroleum-base fuels needs. Currently, the hydrogen produced from the conventional fuel (petroleum) and used with archetype form such as: internal combustion engines [ICEs], fuel cells [FCs]) and engines of gas turbine that to be used for military purposes. Hence, the advancement in the technology to use hydrogen fuel, is desperately needed.

This can help us to conquer above troubles. By storing hydrogen in metal hydrides, metallic compounds or supramolecular entities that incorporate hydrogen atoms in them self where the metal binds to hydrogen as a solid metal hydride and store almost 1000 times or more amount of hydrogen than the H_2 gas cylinder storage ability. They gas can be released hydrogen by heating at given temperature or applying pressure. Section 1.6 answers the question how to produce hydrogen. As fast as the expansion of research and experiments on solar and geothermal heating systems grow, the potential of hydrogen as a renewable power resource get empowered. Presently, the hydrogen generated by electrolysis of water and decomposition of conventional fuel. Hydrogen can functioned as a chemical storage medium for electricity and good chemical in many chemical industries (a synthetic methane or liquid fuels) and can power the heat and electricity generation. Hydrogen generation from water/ hydride is a third renewable option after biofuels and electric battery due to the ease of the technology and market acceptability.

1.4 The Hydrogen: As Energy Source and Carrier

Hydrogen is a less dense- smallest element of the Universe and possesses the unique physicochemical properties that can persists the all benefits of a good fuel as well as the associated challenges. Besides from conventional fuels it falls into the category of alternative, non-conventional or advanced fuels. Moreover, the hydrogen is abundantly (almost 95%) available (as hydride /hydrocarbon) in the different form of the matter available on the Earth. It appears in very small amount in nature due to its tendency to tether with other elements such as carbon or metal and oxygen. The H_2 has exceptionally good properties such as highly diffusive, low viscous, unmatched chemical nature, high combustibility, and electrochemical properties are some unique properties that make hydrogen a different and better fuel than others, as shown in Table 1. Moreover, some other qualities such as odorless, invisibility, no toxicity, non carcinogenic, non-poisonous, smoke free and highly buoyant (lighter than air) gas that makes this gas easy to rises and diffuses to be leaked. Usually, IR device or thermal wave used to identify the H_2 gas presence (Table-1).

Table 1. Comparative specifications of hydrogen fuel with other gasoline are in-use.

Properties / Fuel	**Hydrogen**	**CH_4(CNG)**	**Gasoline**	**Diesel**
Molecular weight	2 (No-carbon)	16 (75% carbon)	100-105 (C_4-C_{12}, 88%)	200-300 (C_9-C_{25}, 87%)
Density (g/l)	0.0899(g) 70.990 (l)	1.8160 (g) 422.36 (l)	-	-
Auto ignition Temperature (^{o}C)	385	540-630	260-460	180-320
Air/ fuel ratio	34.3	17.2	14.6	14.5
Ignition energy (mJ)	0.002	0.28	0.24	-
Diffusion coefficient (cm^3/sec)	0.61	1.90	21.34	-
Energy Density KJ/Kg	142.00	45.30	48.6	33.8
Combustion temperature (^{o}C)	2318 (O_2)	1914 (O_2)	2307	2327
Combustion range in air (%)	4-75	5.3-15	1.4-7.6	0.6-5.5
Explosive range in air (%)	13-79	19	-	-
Octane number	130	87-93	91-99	
Fuel efficiency in internal combustion engine (%)	60	-	22	45

[Data source: Hydrogen Fuel cell Engines and Related Technologies, College of the Desert, Plam Desert CA, 2001.]

Furthermore, the high air-fuel ratio (34.3), low auto-ignition temperature (385^{o}C), high octane rating (130), 100 times low ignition energy (0.002 KJ), wide flammability ($H_2 \approx$ 4-75%) range and the highest heating value i.e. 52,000 Btu/lb (British thermal units per pound mass) are observed for hydrogen over the conventional available gasolines. (Coward and Jones, 1952) All of above properties rated the hydrogen fuel as a good fuel with better fuel economy, high fuel energy (142.00 KJ/Kg) and high efficiency (60%). Hence, the hydrogen engines are preferred over the gasoline engines. It also possesses the high compression ratio than the gasoline and lower than diesel, can be beneficial when lean fuel mixture can be used for the internal combustion engine(ICE) with high efficiency (diesel engines >hydrogen engines > gasoline (petrol) engines) and lower combustion temperatures especially at low power and engine at idle state. That can help to suppress the amount of nitrogen oxides (NOx) emissions, which can still occur in ICEs fueled by hydrogen. All parameters contributing in increasing efficiency of the hydrogen cleanest fuel as a result, the 57 million metric tons of hydrogen emulates 170 million tons of oil equivalent. (Coley and Field, 1973) It is not only important as a gasoline for transportation medium but also utilized as raw material in many chemical industries, as cooking gas, house warming, fuel cell, power production, high temperature welding. The molecular hydrogen has two spin isomers i.e. ortho (75%) and para (25%), which is discriminated by the spins alignment of two protons (same and different directions). The equilibrium mixture of ortho- and para-hydrogen at any temperature is referred to as equilibrium hydrogen that contains 75 percent ortho-hydrogen and 25 percent of para-hydrogen at room temperature is called normal hydrogen. The ortho to para-hydrogen conversion is accompanied by a release of 703 J/g (302.4 Btu/lb) heat at 20 K (-423 ^oF). Where, as 527 J/g (226.7 Btu/lb) heat required for normal to para-hydrogen conversion. (Jones, 1970) Catalysts can be used to accelerate this conversion, which produce almost pure para-hydrogen liquid ($\geq$95 percent).

1.5 The Hydrogen Economy

Presently, the gasoline (petrol, diesel, CNG, LPG, etc) powers our transportation business and coal rules to power our industries. The ignition of these carbon containing fuels in internal combustion engine of transport vehicle, releases the green house gases (GHGs) and other pollutants that directly or indirectly hazardous for our Nature. Furthermore, the conventional fuels resources are at the urge of the end and world population is growing. Therefore, to attain the growing energy demand of the world, particularly in Asian (China, India) countries and other developing countries, apt solution might be searched. The clean solution of energy problem attained if we shift our energy uses from the conventional energy sources to sustainable substitutes i.e. hydrogen economy, biofuel, biomass, hydrothermal, solar, wind, geothermal, and so on including hydrocarbon economy. Among above sources, the solar energy is the but-natural choice as clean energy because the sun is a free of cost available abundant source of energy forever. Our planet has plenty of renewable energy sources at almost free of cost (1 second, 100% sun exposure release almost 400 trillion watts energy that might satisfy the current needs for 500,000 years). This energy can be utilized to produce hydrogen gas fuel from the carbon-free chemicals (H_2O, H_2S etc.), which will be happy prospectus for energy generation and the environment. (McCarty et al., 1981) Because the hydrogen is considered as the most clean and benign fuel that can play a role of an energy carrier and a storage medium. Therefore, hydrogen can be acts as a good eco-friendly fuel especially for the transportation and process industries. For hydrogen fuel, Lawrece W. Jones of the University of Michigam had coined a new term hydrogen economy (Jones, 1970) in 1970. Later on, Sorensen (1975) first ever reveals the public interest in the hydrogen economy in his a technical report. He emphasized that the clean energy is the need of a society, which can be derived from renewable resources (Sorensen, 1975) that might constituted by the hydrogen fuel that contributed the first technical energy scenario. Industrial-scale production of hydrogen promotes the hydrogen economy as an environmental friendly solution of energy for end users (specially for transportation applications) without generating high pollutants (as particulate matter or GHGs). The technical obstacles faced by hydrogen economy are: hydrogen storage, vessel used for hydrogen storage and purity of hydrogen gas (99.999%) used in fuel combustion engine. Technological advancement in high purity hydrogen storage are in progress. Few of the notable systems: fullerenes (Chen and Wu, 2004), metal-organic frameworks (MOEs), organic chemical hydrides (can store 7.3% w/w hydrogen) (Newton, 1998), single-wall carbon nanotubes (2.5%-3.0% w/w hydrogen) (Dillon, 1997), activated carbon at low temperature (Hirano, 1993), silica microspheres (Schmitt et al., 2006), and metal hydrides (5.0%-7.0% w/w hydrogen) (Schlapbach and Zuttel, 2001) are usually used for energy storage. Metal hydrides used to capture s a huge amount of hydrogen at quite low pressure which is lower than the pressure in a car tire in a very small space. Beside above, Magnesium is also a good example that can store a maximum amount of hydrogen (around 8% w/w). Consequently, hydrogen emerged as a smart alternate to the conservative fossil fuel-based energy economy, until unless the bad global environmental impacts will be experienced either in production or usage of the hydrogen economy. A survey of 2004 confirmed that the pathway of the hydrogen production from clean sources emit considerable low CO_2 than the combustion of gasoline used in hybrid electric vehicles. More over the maximum efficiency of an auto-cycle is 38% (ICE running on hydrogen) higher than the vehicle running with gasoline (30% for ICE) (Schlapbach and Zuttel, 2001). Furthermore, the permutation of the ICE and electric motor will give almost two or three times more power than single ICE engine.

It was also observed that the impact of the uses of the hydrogen-based energy systems on our environment/ climate is much lower than those from fossil fuel-based conventional energy systems. Although, such impact might be rated on the basis of hydrogen leakage observed during the synthesis, storage and usages. The researchers estimated that the total 1% leakage rate of the produced hydrogen might produces 0.6% climate impact of the global hydrogen economy over the fossil fuel systems (Derwent, 2006). And if the hydrogen leakage rate increased up to the 10% than the climate impact would be enhanced by 6% over the fossil fuel system. The recent study advocated for the future hydrogen based economy, would not assured us that it is totally free from ecosystem damage but promise us that the impact of the damage will be less enunciated than the same caused by the current fossil fuel energy systems. The potential measure should be taken for reducing the hydrogen leakage up to the minimum level, which is potentially necessary for strengthening the future global hydrogen economy without realization of the adverse climate effects (Derwent et al., 2006). Currently, the hydrogen economy faces many technical challenges including the high costs that mainly focused on the infrastructural and storage problem (GM, 2007).

For the efficient and practical application of the hydrogen fuel in the vehicles for the road transportation, the Government has to seriously work out to establish the hydrogen gas-filling fuel-station in good numbers for the inside the towns/cities and along the roadsides. Almost, 11,700 fuelling station was proposed by GM for100 urban areas in the United States to cover the network of 130,000 miles' highway for connecting the most crowded transit zones, which would cost approximately US$10-15 billion. (GM, 2007). Shell estimated that the cost of the establishment of the hydrogen gas filling stations in the United States/ Europe and Japan will be US$20 billions and US$6 billions, respectively. (Shell, 2004). Despite the high estimated costs, Shell collaborates with General Motors, for futuristic development in technology based on hydrogen (Shell, 2004).

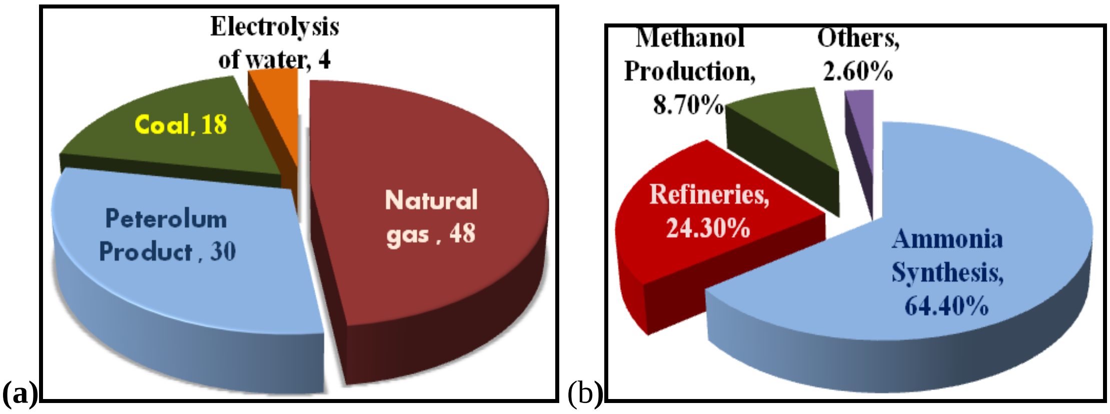

Figure 1.5 (a) Hydrogen production percentage from different sources: petroleum products, natural gases, coal and electrolysis of water and (b) worldwide percentage hydrogen consumption in various process industries**.** (Shell, 2004).

1.6 Hydrogen Production

In contrast to the can be mining or extraction of the conventional fossil fuels, the distinctiveness of the hydrogen gas lies on the methods of the hydrogen production from the variety of feed stocks, including the oil, natural gas, biomass, water, coal, and many more. Contemporary feedstock for large scale hydrogen production is NG because of the high efficiency and low production cost. In looking to the limited petroleum product supplies in near future, the hydrogen gas fuel has also been implied as the third sustainable fuel, which will act as a prime factor in transportation sector fuel that may play the most important role in transport sector by 2025. Recently, the majority of the hydrogen is extracted from the NG (48%), raw petroleum products (30%), coals (18%) and electrolysis of water (4%) for industrial uses as predicted by the Figure 1.5a. (Ruhl, 2012).

1.7 The Concept of Photochemical Water Splitting

In looking to the day by day growing need of the clean-energy and to save our earth from the environmental damage, Prof. James Barber state, "*Our sun is the champion of energy source and delivering more energy to Earth in an hour than we currently use in a year from fossil, nuclear, and all renewable source combined", which is contemporary*. The energy received from sun is inexhaustible causes no harm to our eco-system and atmosphere (Barber, 2009).

Hence, a huge number of scientific ventures are carried on worldwide by scientists to generate clean chemical fuels from sunlight. In this age of solar energy, carbon-neutral water can be considered as a potential future fuel. Because when the photocatalyst captured the sunlight in water , they produced clean fuel by cleavage of water in the form of hydrogen and oxygen. The by-products are carbon-neutral molecule combustion without exhaling the carbon-containing GHGs in atmosphere. Therefore, they can be treated as the green fuels. Furthermore, we had discussed the fundamental elements that necessary for the competent hydrogen generation through water splitting using photocatalyst under visible light exposure. Water splitting imitates the natural photosynthesis process, where water break into hydrogen and oxygen in presence of water and photocatalyst material. The basic standard consider behind the choice of photocatalytic material are: excitonic binding energy, carrier mobility, its over potential, diffusion length, band edge positions and band gap in solid state, the band edge bending of semiconductor in electrified environment and efficiency i.e. turn over number [TON], quantum yield, photo conversion efficiency, solar to H_2 (S-H) conversion efficiencies, incident photon-to-current efficiency {IPCE in %}, and absorbed photon- to-current efficiency [APCE] of photocatalyst. In the light of above criteria, we will discuss the merit of photocatalyst material that can rate the efficiency of the hydrogen production. It helps to develop the right material to make for water splitting. And researchers and scientist come forward with their knowledge and experience to win the nature by using the trick provided by the nature himself by using required parameter well, such as: light absorption, photovoltage, electrochemical transport, photo generated carrier collection, and catalytic behaviour of the photocatalytic material, so on.

1.8 Artificial Photosynthesis

Nature uses the photosynthesis process for making their food/fuel (i.e. carbohydrates) in a sustainable manner by consuming solar energy in plants. Even though, the total value of solar energy (43 x 10^{20}J per hour) approaching to the earth's surface is large, the energy incident on any give square meter of the planet's surface over time is diffuse and low due to dilution. The energy needs of the United States, required the average approximately 200 w/m^2 (Cogdell et al., 2010) energy. In this process plants, algae and some breads of bacteria usage solar energy to convert carbon dioxide and water into carbohydrates and oxygen. Artificial photosynthesis (Figure 1.6) is a photochemical process that mimics natural photosynthesis (Figure 1.6) for producing sustainable fuels by two process i.e. (i) reduction of carbon dioxide (carbon fixation) and water for production of hydrocarbons and oxygen and (ii) water splitting for production of H_2 and O_2. Usually, the term artificial photosynthesis refers to the two above path ways that used to arrest and accumulate the solar energy in the chemical bonds of a fuel. These procedures are capable enough to use solar energy for producing alternative clean fuels with elevated efficiency of hydrogen production by using water and photocatalyst under visible sunlight.

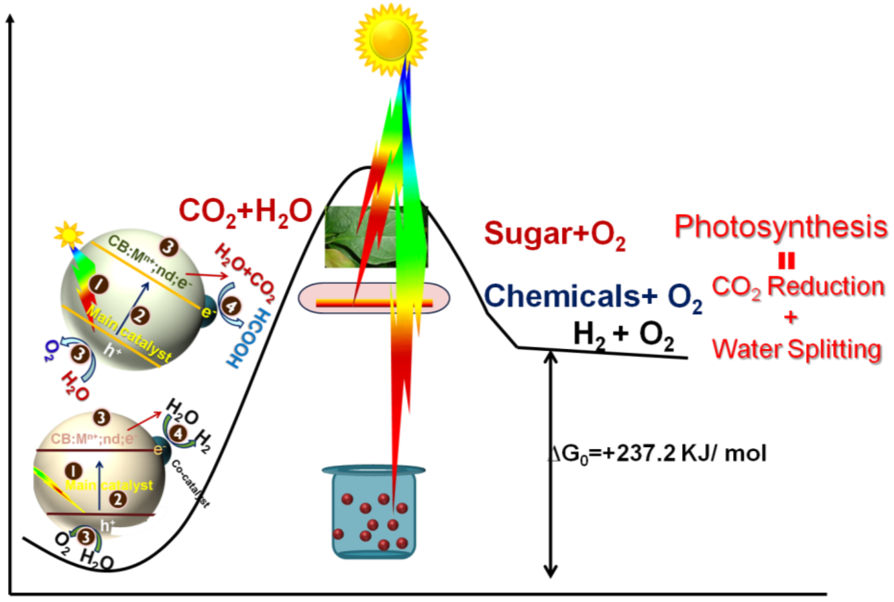

Figure 1.6 Scheme differentiating natural photosynthesis and artificial photosynthesis.

1.8.1 Reduction of Carbon dioxide and Water

Day by day depleting energy resources and estimated/observed risks behind the global climatic changes causes the big challenge. Carbon dioxide is identified as the biggest culprits behind the climate damage and the efforts are required for prevention of further increase in CO_2 concentrations in atmosphere. Several important majors are taken to fix CO_2 gas that includes carbon taxation, increase in plantation, sequential CO_2 deposition in the deep earth core, fruitful utilization of carbon dioxide in making of higher chemicals by using artificial photosynthesis, and so on.

Furthermore, the increasing world population and to meet their corresponding energy and electricity demands are the big challenges for leading the comfortable life style. It adds volumes to the emission levels of CO_2 in atmosphere and damage of our environment. Figures 1.7a and b exhibits the world wide trend of emission of carbon dioxide in atmospheric and anthropogenic contribution up 1725 to 2025 (Energy Information administration 2007).

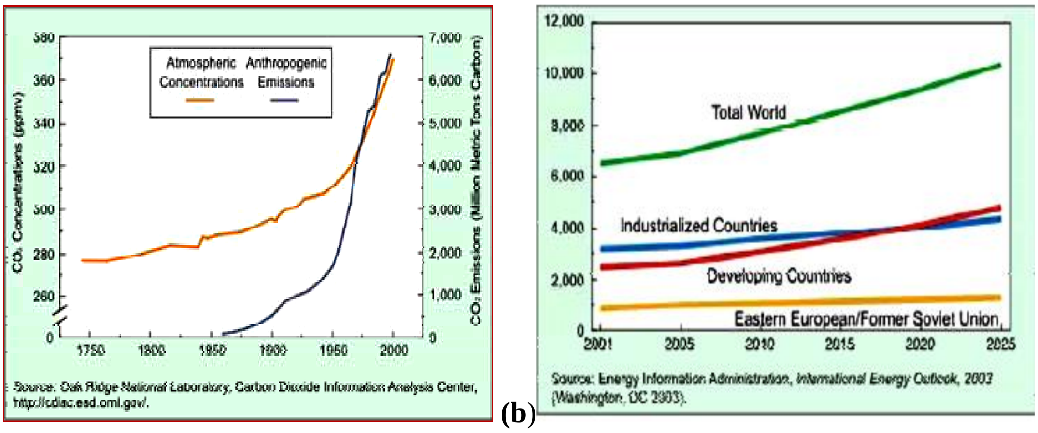

Source: Oak Ridge National Laboratory, Carbon Dioxide Information Analysis Center, http://cdiac.esd.ornl.gov/.

Source: Energy Information Administration, *International Energy Outlook, 2003* (Washington, DC 2003).

Figure. 1.7 (a) Carbon emission contribution by atmosphere (yellow) and anthropogenic (blue) emission from 1725 to 2025 and **(b)** worldwide zonal contribution in total anthropogenic emission from 2001 to 2025. (Source: (a) Oak Ridge National Laboratory, carbon dioxide information analysis centre and (b) Energy Information Administration, International Energy Outlook, Washington DC, 2003)

Extreme atmospheric carbon dioxide emissions along with other GHGs are main culprits that responsible for the drastic changes in global climate. To reduce this risk, we would carefully monitor the global climate change and systematic strategies/action plan are needed to suppress atmospheric CO_2 concentration. If we utilise this emitted CO_2 with a renewable energy, then it would be a win-win situation for our environment and economy. One of the best way to use CO_2 in an eco-friendly and sustainable manner, is reduction of CO_2 with water in presence of photocatalyst and sunlight. Where, sunlight along with the photocatalyst can be treated as an attractive and renewable solution that can be used to produce fuels from the mixture of the carbon dioxide and water. These products include a wide variety of chemicals such as carbon monoxide, formic acid, methane oxalate or even higher hydrocarbons depending upon the type of catalyst and chemical environment. The reactions involve a complex multi-electron chemistry, which can either be achieved directly in a photo-reactor or indirectly by using solar derived hydrogen as a “reductant”. It is an essential part of the artificial photosynthesis, where the electrochemical or photochemical reduction of carbon dioxide is used to produce clean, green, and sustainable fuels (Figure 1.8). There are two types of catalytic processes for photocatalytic carbon fixation i.e. heterogeneous (Figures 1.9a and 1.9b) and homogeneous catalysis. A few of the prominent products of carbon dioxide reduction (Sullivan, 1989) along with their energetic parameters are mentioned in Equations 1.1 - 1.7 (Scibioh and Viswanathan, 2004).

$$CO_2 + 2e^- + 2H^+ \rightarrow CO + H_2O \quad E = -0.76\,V \left(\Delta G_F^0 = -137\,\frac{kj}{mol}\right) \quad 1.1$$

$$CO_2 + 2e^- + 2H^+ \rightarrow HCOOH \quad E = -0.85\,V \left(\Delta G_F^0 = -361\,\frac{kj}{mol}\right) \quad 1.2$$

$$2CO_2 + 2e^- \rightarrow (COO)_2^{2-} \quad E = -1.14\,V \left(\Delta G_F^0 = -671\,\frac{kj}{mol}\right) \quad 1.3$$

$$2CO_2 + 2e^- \rightarrow CO + CO_3^{2-} \quad E = -0.79\,V \left(\Delta G_F^0 = -527\,\frac{kj}{mol}\right) \quad 1.4$$

$$CO_2 + 4e^- + 4H^+ \rightarrow HCHO + H_2O \quad E = -0.72\,V \left(\Delta G_F^0 = -102\,\frac{kj}{mol}\right) \quad 1.5$$

$$CO_2 + 6e^- + 6H^+ \rightarrow CH_3OH + H_2O \quad E = -0.62\,V \left(\Delta G_F^0 = -166\,\frac{kj}{mol}\right) \quad 1.6$$

$$CO_2 + 8e^- + 8H^+ \rightarrow CH_4 + H_2O \quad E = -0.48\,V \left(\Delta G_F^0 = -51\,\frac{kj}{mol}\right) \quad 1.7$$

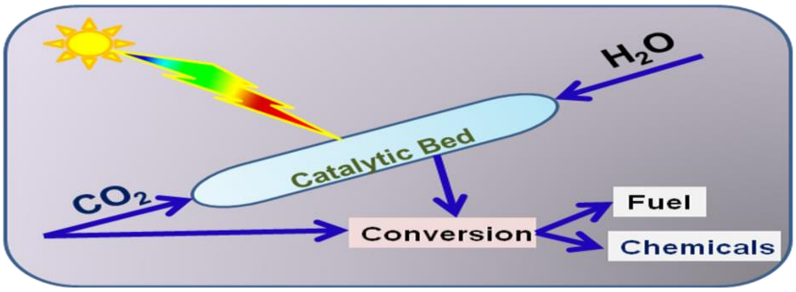

Figure 1.8 Schematic representation of the light induce photocatalytic reduction of carbon dioxide for fuel or reduction products.

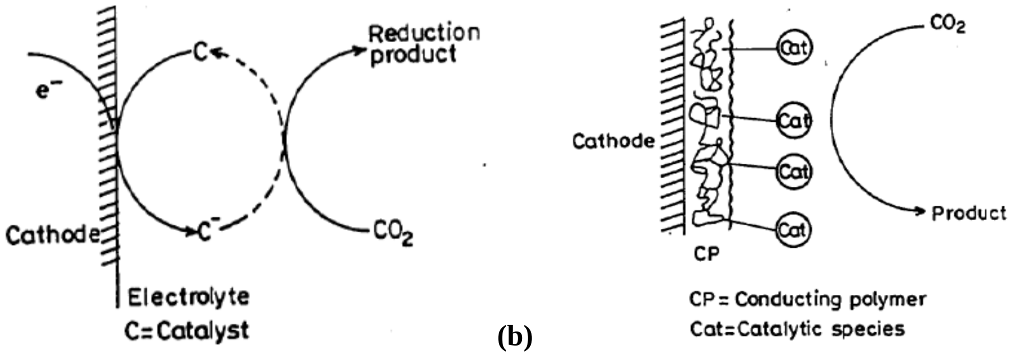

(a) **(b)**

Figure. 1.9 Reduction of CO_2 into chemical products using heterogeneous electrocatalyst i.e. **(a)** Noble metal group of metallic cathode and **(b)** catalytic species loaded conducting polymer. (Hori et al., 1987)

The second class of CO_2 reduction is homogeneous catalysis, which found to be more efficient than heterogeneous catalysis that attracts major interest of the future researchers. But the full potential of the homogeneous catalytic carbon fixation is yet to be explored. Therefore, the research on efficient and highly selective photocatalyst for the reduction of carbon dioxide has been a gigantic scientific challenge. Some of the prominent photocatalysts used for CO_2 reduction are Fe-supported MY-zeolite (M = Li, Na, K, Rb and Y = Lanthanum; Fe-K/La/$A1_2O_3$) for hydrocarbon production (Nam, 2000), titanium oxide for CH_4 and CH_3OH production (Mori, 2012), CdSe (Anpo 1995; Wang, 2002) titanium oxide/ Y- zeolite for MeOH and CH_4 (Yamashita, 1998) production.

1.8.2 Photocatalytic Water Splitting

Fujishima and Honda, opened a gate of new era in hydrogen generation method in1972 by successfully production of hydrogen and oxygen by using solar light via cleavage of water, using biological (plants, algae and certain bacteria) and physical (semiconductors) systems. There were many major breakthroughs in search of better catalytic material for water splitting including the TiO_2 discovered by Fujishima and Honda in 1972. Although, the cost, efficiency or durability of the TiO_2 system was not enough for large scale usages of system (Gary 2008; Walter et al., 2010) but has an important role in guiding path for futuristic approach. A large number of photocatalyst of the following class such as metal oxides, sulfides, nitrides, oxysulfides, and oxynitrides that contains either representative transition metal cation (M^{n+}) of d^0 (e.g. W^{2+}, Mo^{2+}, Nd^{2+}, Ti^{4+}, Ce^{4+}, Zr^{4+}, V^{5+}, Nb^{5+}, Ta^{5+}, etc) or d^{10} (e.g., Ag^{+}, Cd^{2+}, Zn^{2+}, Cu^{2+}, In^{3+}, Ga^{3+}, Ge^{4+}, Sb^{4+}, Sn^{4+}, etc) electronic configuration or the combination of both type cations had been reported as active photocatalyst for overall water splitting. Figures 1.10 a-c exhibits some of the important paradigms of man-made photocatalytic material that accustomed to split the water into hydrogen and oxygen in 2:1 ratio, respectively, during artificial photosynthesis. There are three ways to split water, these are photocatalytic (Figure 1.10a), photo electrochemical (PEC) using a photoanode (Figure 1.10b) and PEC using photoanode and photocathode (Tandem) (Figure 1.10c).

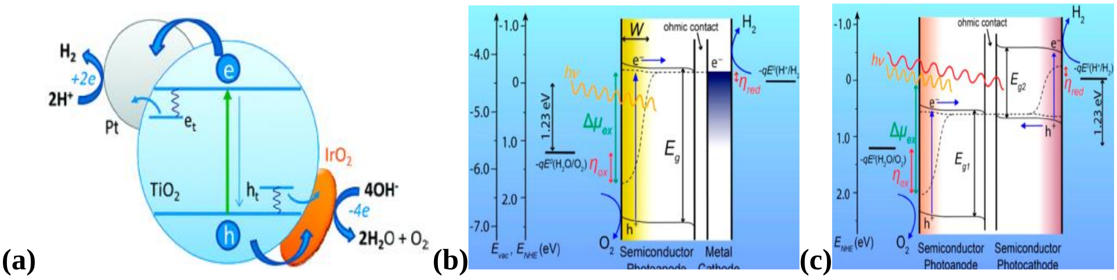

Figure 1.10 One semiconductor-assisted photocatalytic water-splitting reaction aided by Pt and IrO_2 cocatalysts (Kamat, 2012) (b) two photon assisted Photoelectrochemical water splitting using a photoanode and (c) Four photon assisted Photoelectrochemical water splitting using a photoanode and photocathode in tandem. (Sivula, 2013)

All three types of the water splitting processess includes three basic steps: (1) absorption of one or more photon energy (sunlight) by photocatalyst than the band gap energy by photocatalyst that used to generates the photoexcited electron-hole pairs (charge carrier); (2) the photoexcited charge carriers travelled toward opposite sites (cocatalyst’s surface and groove of photocatalyst) of the photocatalyst’s surface without reunification of carriers; and (3) at these sites, water get reduced by situ - generated photoelectrons and in situ oxidized by photoholes, to produce H_2 and O_2, respectively. The above steps are based upon the structural and optoelectronic chracteristices of the photocatalyst and co-catalyst (Figure 1.10a) used to attract charge carriers. The cocatalysts can be either a typical noble metal or transition metal oxide or a combination of the both (eg. Pt, NiO_x, RuO_x, RhO_x, IrO_2, $RhCr_2O_3$) loaded onto the surface of a photocatalyts to produce active sites and reduce the activation energy for gaseous product evolution in photocatalytic overall water splitting.

1.9 Terms Used in Water Splitting

1.9.1 Band Gap and Band Edge Positions of Photocatalytic Material

In material science, the electronic band structure (with band edge positions and band gap) of a solid describes those energy ranges where an electron present between the solid bands *(*called CB/VB) might be treated as a free carrier. On the basis of their band gap and band edge positions the solids can be classified into the four main parts: metals (metals have a partially filled CB that conduct electrons), semimetals (no band gap and negligible electron density at Fermi level), semiconductors (band gap < 5eV; p-type, n-type and intrinsic, zero electron density at Fermi level) and insulators (band gap > 5eV; zero electron density at Fermi level), exhibited in Figure 1.11.

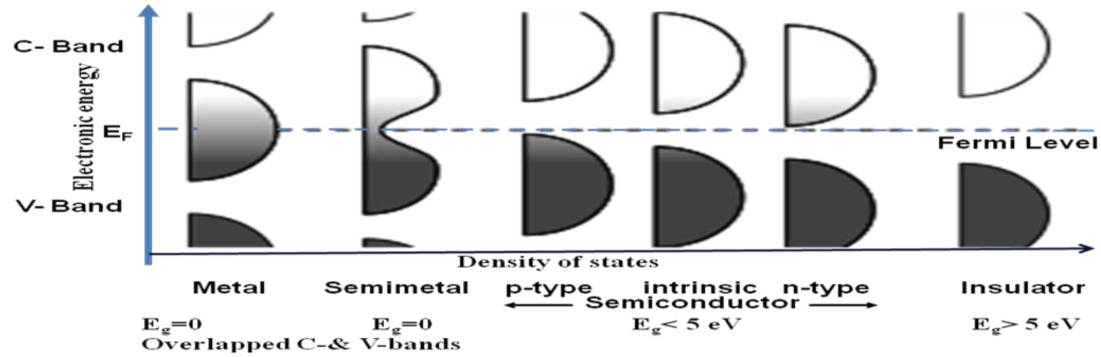

Figure 1.11. Fermi level, conduction-bands and valance-bands positions and electronic density of states in metal, semimetal, semiconductors (p-type, intrinsic, n-type) and insulators at equilibrium along with their energy levels. (Size, 1981)

Therefore, metals had a considerable electron density of states at the Fermi level (Kittel, 1996) unlike semimetals (with no band gap). However, semimetals had a very small overlap between ground level of the CB and the upper level of the VB and both had charge carriers (electrons and holes) but semimetal has carriers in smaller number than the metals. But the semiconductors or insulators possess the Fermi level of electron in forbidden zone of the band gap and has zero conductivity at zero Kelvin temperature unlike metals or semimetals. And insulatorshow zero conductivity at all temperature due to high band gap between VB and CB. In semiconductors, if the Fermi level is closer to the CB then the semiconductor is known as n-type, on the other hand if the semiconductor has Fermi level close to the VB are of p-type. And if the Fermi level resides at the middle of the CB and VB, are intrinsic semiconductors. The band gap (distance between CB and VB; Eg) widths of the compound depends on the overlapping degree among the constitutes atomic orbitals. (Perry 1969). A few of the representative examples of the above categories are: metals (Au, Ag, Na, Al, Cu, etc.), semimetals (antimony, bismuth, arsenic, tin or graphite and the alkaline earth metals, HgTe, conductive polymers) (Bubnova 2014), semiconductors (Si, ZnO, TiO_2, Ge, GaN, InN, WO_3, etc) and insulators (wood, paper, polymer, glass, etc).

Semiconductors are further divided into two parts i.e. direct band gap and indirect band gap semiconductors. In direct band gap materials, the space momentum (*k*) are same for the top of the VB and bottom of the CB under the band gap. But in case of the indirect band substances, the *k* value for the both states, are different as depicted in Figures 1.12. The direct or indirect band gaps are the one of the major parameters in application of the photoconduction and electroluminescence processes of inorganic materials. Few of the prominent examples of the direct band gap semiconducting materials are GaAs, CdTe, GaN, GaAs, ZnO, InAs, $CuInSe_2$, and so on. On the other hand the example of the indirect band gap semiconductor are: Si, Ge and so on. Whereas, the metal or semimetal or metal alloys are generally employed for the reduction process and semiconductors used to exploit the oxidation and reduction process at different sites of the catalytic surface.

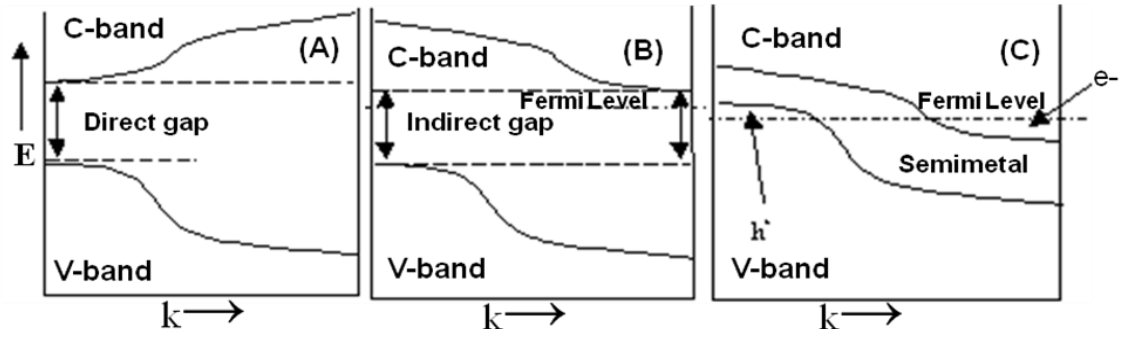

Figure.1.12 Schematic representation of the one dimension lowest-energy conduction band and the highest-energy valence band in a plot momentum space (or k-space)

Versus energy (E) diagram for **(A)** a direct semiconductor**, (B)** an indirect semiconductor and **(C)** a semimetal. (Burns,1985)

Band gap E_g governs the optical absorption range and play an important role in deciding the efficiency of the optoelectronic materials. Various parameters such as UV spectroscopy (transmittance/reflectance) (Change and Wand, 2009), voltammeter study (Shaukatali, 2008), soft x-ray spectroscopic (absorption/ refelectance) techniques (Dong et al., 2004) (Singh 2013) are used to estimate the band gap of the compound (E_g).

1.9.1.1Transmittance/reflectance of UV-Vis spectroscopy: In crystalline semiconductors, the following equation has been used to relate the absorption coefficient (α) with the incidental photos energy (hυ) (Tauc and Menth, 1972).

$$\alpha(V)hv = B(hv - E_{gap})^m \quad \text{...(1.8)}$$

Where, α(υ), $E_{gap,}$ B and hυ are the absorption coefficient, band gap, constant and photon energyof the incident light, respectively. Usually, the factor m is equal to 2 for an indirect band gap and ½ for direct band gap substance. The absorption coefficient α(υ) defined by Beer-Lambert's law as:

$$\alpha(v) = \frac{(2.303 \times \mathrm{Abs}\ (\lambda))}{d} \quad \text{...(1.9)}$$

Where, the coefficients d and Abs (λ) are the observed thickness of film and absorbance of film at the given wavelength λ, respectively.

1.9.1.2Voltammetry Study: Voltammetry tests such as cyclic Voltammetry, ampheometric titration and differential pulse Voltammetry are used to determine the anodic peak of oxidation potiential $V_{ox,}$ and the cathodic peak of reduction potential V_{red} of the studied material. Usually, band gap for organic semiconductors was determined by the difference in HOMO and LUMO. Where, HOMO represents the energy required to extract an electron from a molecule, which is an oxidation process, and LUMO is the energy necessary to inject an electron to a molecule, thus implying a reduction process. Ferrocence is used as a known reference to calculate the energy of the HOMO and LUMO levels, including the ferrocene value of -4.4 eV. The energy levels were calculated using the following empirical (Bredas et al., 1983) equations:

$$E\ (HOMO) = -e\ [E_{ox}^{onset} + 4.4] \quad \text{... (1.10)}$$

$$E\ (LUMO) = -e\ [E_{red}^{onset} + 4.4] \quad \text{... (1.11)}$$

$$E(\text{eV}) = e(V_{red} - V_{ox})\text{(Shaukatali,2008)} \quad \text{....(1.12)}$$

The flat-band potential V_{fb} [V vs NHE] for the metal oxide can be calculated by equation 1.13.

$$V_{fb} = E_0 - \chi + \tfrac{1}{2} E_G \quad \text{.... (1.13)}$$

Here, χ is the geometric mean of the Mulliken electronegativities of the semiconductor constituents, E_G is band gap [eV] of the semiconductor and E_0 (+4.44 eV) is the energy of a free electron, measured on the H_2 redox scale. (Pleskov et al., 1986)

1.9.1.3Soft spectroscopy for band gap determination: The conduction band and valence band character of nanoparticles can be investigated by using X ray-absorption and emission spectroscopy spectrum. The observed results used to calculate the band gap energy of ZnO i.e. 3.3 eV from the X-ray absorption and emission spectrum. (Dong et al., 2004)

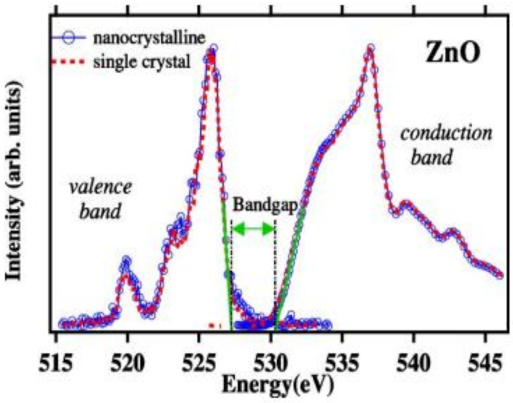

Figure 1.13 Oxygen x-ray absorption-emission spectrum reflected conduction band and valence band near the Fermi level of ZnO nanoparticles in comparison with bulk ZnO.

1.9.2 Quantum Efficiency

Quantum efficiency (QE_λ) is often associated with the term spectral responsivity, which is the measured in term of the current measured for the device for the incoming photon of the light of given energy and wavelength. The unit of spectral responsivity measurement is amperes per watt (A/W). Responsivity (R_λ in A/W) and QE_λ (of gold (on a scale of 0-1)) hold the following relationship (Equation 1.14):

$$QE_\lambda = \frac{R_\lambda}{\lambda} \times \frac{hc}{e} \approx \frac{R_\lambda}{\lambda} \times (1240\, W.\frac{nm}{A}) \qquad \ldots(1.14)$$

Where c = the speed of light in a vacuum, λ = wavelength in nanometers, h = Planck's constant, and e = the elementary charge.

1.9.3 Excitonic Binding Energy

To know the perceptive of the fabrication, functioning, and performance of the developed optoelectronic devices, the knowledge of the excitonic movement at different levels is very essential. Solar energy used to excite the electron that generates excitons (i.e. photoelectron and photoholes) rather than free carrier. Therefore, to produce free charge carriers the extra amount of energy (excitonic binding energy (E_{ex})) is needed. As generated free carriers moved towards the co-catalyst and groove site of the photocatalytic surface of molecule, for the system's synergy. The concept of exciton's movement in semiconductors crystals was first explained by Sir Nevil Francis Mott (Wannier, 1937; Mott, 1938), by considering that the rate of electrons / holes hopping in crystals is always greater than their Coulomb coupling strength. The excitonic pair has finite lifetime and binding energy of the order of 100-300 MeV. As per Frenkel veiw, the perturbation in Coulombic interaction between the excitons, generates crystal potential. Crystal potential generated between the hole and electron presented at r space is shown below by the Equation 1.15:

$$E_{coul} = \sum \frac{q_e q_h}{\in r} \qquad \ldots (1.15)$$

The coulombic potential E_{coul} used to calculate the excitonic binding energy by using following expression given in Equation 1.16.

$$E_{ex} = E_{ION} - \frac{E_{coul}}{n^2}$$
... (1.16)

Where, q_e or q_h = elementary charge of electrons or hole, ε = the electrical permittivity (space), E_{coul} = coulombic potential (13.6 $eV; M_{red}/M_e$), n (excitonic level) = 1, 2, 3, 4, E_{ION} = ionization energy of the molecule, M_h = effective mass of hole, M_e = effective mass of electron, and M_{red} = reduced mass of the exciton pair, expressed by following Equation 1.17.

$$M_{red} = \frac{M_e M_h}{M_e + M_h}$$
... (1.17)

Similar to a hydrogen atom, an exciton also has a couple of the positive and negative charge carrier that differ from the exciton because proton of positive charge is heavier in mass than the hole and the exciton can only exist in a solid. Equation 1.18 used to measure the excitonic energy, which derived from the solution of the Schrodinger equation for H_2 atom by taking presumptuous that the mass of electron is not neglected with respect to the mass of the hole.

$$E_{ex}(k) = E_{gap} - \frac{M_{red} \cdot q^4}{8(n \cdot n \in_0 \in_r \cdot h)^2} + \frac{h^2 \cdot k^2}{8\pi^2 (M_e + M_h)}$$
...(1.18)

Where, ΔE_{ex} is a free excitonic energy (measure in a MeV), which used to move exciton through the crystal and can be treated as the transporting energy without charge, in compare to the typical donor levels and it will not live very long at room temperature. E_{gap} simply accounts for the crystal energy, the second term belong to the hydrogen atom, and the third term is a correction term for the two particles which are not at the same place in k-space (for most direct semiconductors it is zero for ke = –kh or ke = kh =0). In total, we have a system with energy levels just below the CB with the “deepest” level defined by the energy differences, as shown in Figure 1.14a.

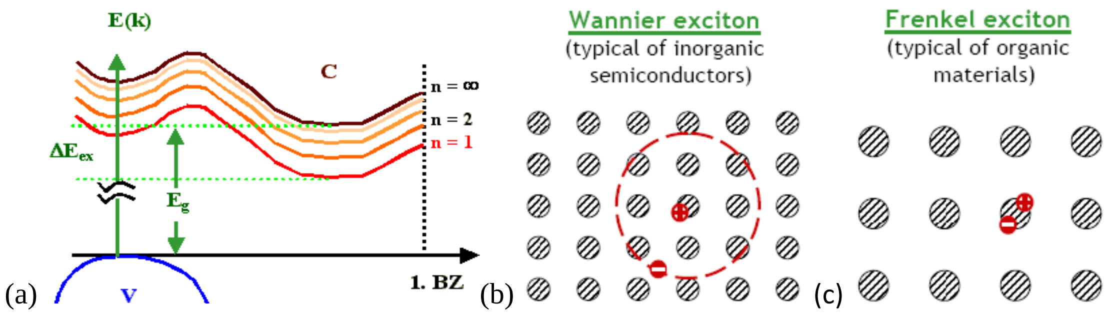

Figure 1.14 (a) Excitation of electron from V-band to C-band and their respective excitonic energy and band gap E_g and different energy levels beneath to C-band, in an indirect band semiconductor. Where, BZ = Birillouin zone, (b) Schematic excitonic binding energy for (a) Wannier-Mott excitons in inorganic semiconductors and (c) Frenkel excitons in organic materials. (Knupfer M., 2003)

Excitonic binding energy for a nonspherical object is calculated by using the following Equation 1.19.

$$\Delta E_{ex} = \frac{M_{red} \cdot q^4}{2 \ \epsilon_0 \epsilon_r \cdot h} \qquad ...(1.19)$$

Inorganic and organic semiconductors can be differentiated on the basis of their excitionic energy (Figures1.14b and 1.14c), which is depend upon the binding force (covalent / Vander Waals forces), dielectric constant and oscillator strength of inter band transitions. Thereafter, the excitonic binding energy utilized to take out the electron form a bound state (excition) and utilised onto another molecular unit far away (Knupfer, 2003).

Usually, the dielectric constants of the inorganic compounds are higher than the organic compound because organics are insulators and lacking the enough charge to be induced under the effect of an electric field. Here, the dielectric constant used to shield the repulsion between the holes and electrons due to the coulombic interaction. Furthermore, the increase in the size of QDs weakened the dielectric constant. Similarly, Zhou and Majumdar reported that the excitonic binding energy of the CNT increases with the shortening of the tube diameter (Zhou and Majumdar, 2004). Figure 1.14b illustrates the role of the exciton in determining the binding energy of inorganics. Where, the bounded hole and electron pairs are confined in the molecule at initial state. These molecules have Wannier-type exciton states whose binding energies are of the order of 10 meV, dependent on the reduced mass of the e^-/h^+ -pair and the dielectric constant. On the other hand, organic molecular solids (Pope and Swenberg, 1984) had Frenkel excitonic states along with their valence and conduction band's (as well as exciton bands) energy lie between 10–100 meV (Coropceanu, 2007) due to the structural elements held together by only weak van der Waals forces result of the weak electronic intermolecular coupling, very small oscillator strength of inter band transitions and (3) the dielectric constant (ε_r) is in the range of 3–4, because of the weak dielectric screening and coulomb effects. This suggests a molecular approach for describing their optoelectronic properties starting from the properties of a molecule in the gas phase.

1.9.4 Diffusion length

The charge carriers are not sitting still in the lattice (they are only "sitting still" in ***k***-space!), but move around with some average velocity due to some thermal energy and the associated random motion of the carriers. We will refer to this transport mechanism as carrier diffusion. An external applied voltage on charged carriers generate the electric field that results in the motion of the charged carriers. This transport mechanism is known as carrier mobility (drift). Furthermore, the carriers can also moves from the high carrier density region to the low carrier density region. When excess of the carriers are generated at the semiconductor surface then the minority carriers diffused up to a certain distance, before recombining with majority carriers, is called as a diffusion length. Usually, the diffusion length of electron is much greater than the same of holes. The minority carrier lifetime and the diffusion length depend strongly upon the type and magnitude of the recombination processes, which govern by the method of fabricate the semiconductor wafer and the processing. Heavily doped semiconductor materials possess the greater rate of recombination and consequently, the shorter diffusion lengths. Higher diffusion lengths are indicative of the materials with longer lifetimes, is therefore an important quality to be considered for selection of semiconductor materials for PWS.

1.10 Water Splitting Techniques for Hydrogen Production

Hydrogen gas not only plays a primary role of the highest efficient fuel (75%) among the presently available fuels but also work fine as an energy carrier. Moreover, it rarely exists in elemental form, cannot be found free even holding the position of most abundant element (95%) of Earth. Therefore, can't be mined due to its high reactivity, always found in compound form and. Moreover, the hydrogen always found in the form of the metal hydride, water or organic compounds. Therefore, we need to take out the hydrogen by cleavage of the different available resources. Currently, most of the hydrogen is produced from the conventional fuels sources i.e. natural gas and coal that added a lot of carbon dioxide release into the atmosphere. Hence, hydrogen production from the benign and abundant source at large scale from zero-carbon compound; water is a good choice. The big question is how to break water for hydrogen generation. Here, we deal with the most popular methods that used to cleave water.

1.10.1 Electrolytic Water Splitting

Hydrogen production at the as low as cost of ~ \$2.00-3.00 Kg^{-1} H_2 as gasoline for the transportation vehicles is the main target of the researchers. For this, the electrolysis of water is the standard commercially used technology (Turner, 2008) from ages. The electrolytic splitting of water shows the potential of this for generation of H_2 and O_2 by applying electricity. This technique produces hydrogen almost 0.25 % worldwide by using from water and electricity at zero greenhouse gas emissions by electrolysis world-wide is the beauty of this method. If the electricity can be produced from the sustainable sources of energy for instance: solar, biomass, hydropower, wind, etc, than the process became extra environmental protective. Researchers, who working on clean energy had been attracted towards the process of electrolysis because of the hydrogen economy involved in the process. Pure water is highly resistive to electricity and we need the acidic or alkaline water for its electrolysis (Kreuter and Hofmann, 1998). Thus, for conducting electricity in pure water the the presence of ions in the water is crucial requirement. The hydrogen production through the electrolysis of water will be estimated in terms of their cost, the electricity production efficiency and the rate of GHGs discharged in environment during electricity creation. Therefore, due to the low efficiency and higher discharge rate of GHGs in atmosphere during electricity production, this method is not a good option for electricity provider. But if the renewable and nuclear energy used for electricity generation for the water electrolysis, result in zero GHGs emissions. Which is the most promising way of hydrogen production by using water with high efficiency of conversion with low energy consumption in compared to the photocatalytic, biolysis, and thermochemical method.

The electrolysis of water done in the device known as electrolyzer, which consists of an anode and a cathode that connected through external circuit, dipped in an electrolyte solution. Where, the oxidation of water takes place at anode for oxygen production, as shown by Equation 1.20. The reduction of water takes place at cathode by using four positively charged hydrogen ions (protons) that selectively move across the polymer electrolyte membrane (PEM) towards the cathode electrode to react with electron and to librate hydrogen gas, as shown in Equation 1.21.

Anode reaction (oxidation): $2H_2O \rightarrow O_2 + 4H^+ + 4e^-$ ... (1.20)

Cathode reaction (reduction): $4H^+ + 4e^- \rightarrow 2H_2$ ... (1.21)

The complete electrolysis of water occured at 298 K (25^0C), which requires enthalpy ΔH = 285.83 kJ/mol (Gibb's free energy [ΔG]) = 237.2 kJ/mol and heat energy [$T\Delta S$] = 48.6 kJ/mol at $\Delta G = 163.14$ J/mol/K). Here, entropy of the system ΔS_0 (H_2) = 130.6 ΔS_0 (O_2) = 205.1, ΔS_0 (H_2O) (1) = 70J/mol/K, ΔS_0 (total) = 130.6 + ½ (205.1 X 70) = 163.14 J/mol/K and ΔS_0 = 233.1 kJ/mol. Therefore, the minimum voltage is E_{cell} = 1.23 V required for water splitting (Neagu, 2000). In the case of an open cell $E_{cell} = \Delta G_0/nF$ = 1.23 V with Gibb's free energy $\Delta G_0 = \Delta H_0 - T\Delta S_0$ = 237.2 kJ/mol at STP (1 bar pressure and 25^0C temperature). The conjectural value of reversible potential for water electrolysis is written by using below mentioned Equation 1.22:

$$E_r = E_0 - \frac{RT}{2F} log \frac{P}{P_0}$$ ...(1.22)

Where, E_0 is the standard potential for electrolysis of water, R = gas constant and T = absolute temperature of electrolysis, P_0 and P are the respective vapour pressures of the pure water and water in electrolyte, respectively. The electrolysis energy of water required is 2.94 kWh (theoretical) for 1 litre H_2 production and to acquire ohmic losses developed by the electrolytes/diaphragms and over voltage (over potential) due to the side electrode reactions (Equations 1.20 and 1.21). Actually, the current efficiency is expected quite high (around 95 %) and treated as the high voltage efficiency.

In order to start reaction, it is essential to overcome this energy barrier (extra). The activation energy E_{act} and number of molecules are the prime controlling factors that able to overcome the energy barrier and the rate of reaction (r) expressed by the Maxwell-Boltzmann distribution law: $r = r_0 \exp(-E_{act}/RT)$. So, the speed of a reaction can be expressed in term of the activation energy. The maximum possible efficiency of an electrochemical cell can be ideally expressed by the Equation 1.23.

$$\epsilon_{MAX} = \frac{\Delta H}{\Delta G} = -\frac{\Delta H}{nFE_{cell}}(theoretical) = -\frac{\Delta H}{nFE_{elec}}\ (real) \quad \text{.... (1.23)}$$

Where, ΔE_{elec} = voltage, required to drive the electrochemical reactions at current I and express by the below mentioned Equation 1.24.

$$\Delta E_{elec} = \Delta A + IR + \Sigma_{\eta} \quad \text{... (1.24)}$$

ΔA= activation energy, R= the total resistance of the cell, which includes the external circuit resistance, electrodes and membrane material and Σ_{η} = over potentials (the activation- or concentration- over potentials). The energy balance acquired during the water electrolysis for per mole is illustrated in Figure 1.6 (Neagu, 2000). It was found that the activation over potentials rose by enhancing current density that will be lowered by the catalytic action of electrodes, such as platinum.

At reversible situations, the maximum electrolysis efficiency of the water with respect to the electrical energy, would be ε_{max} = 120 %. Therefore, heat flow from the surroundings into the cell. With the value of ΔG =1.48 nF (in the denominator) in Equation 1.23 (with over potential ~ 0.25 V), the electrolysis device would show the 100 % performance by maintaining the cell temperature constant. Actually the IR drop is equal to 0.25 V. The overpotential η should be kept low for maximizing the efficiency and minimizing the heat production. But when the overpotential is low then the reaction is slow. Therefore a balance should be maintained between the overpotential (IR) and thermoneutral potential. The most convenient way to enhance the current without increasing the overpotential is by enhancing the contact areas (with active sites) between the electrodes and the solution with electrolyte (Neagu, 2000). The electrolyzers cell are commonly classified on the basis of the electrolyte material used in the cell.

1.10.2 Plasmolytic Water Splitting

Thermolysis of water needs the quite high temperature (3000^0C) and a very specific material (catalayst), which can sustain its integrity at high temperature. To avoid the problems associated with the thermolysis of water, the use of electric discharge of plasma in place of heat is an extremely useful technique for water splitting. This technique is known as plasmolysis of water or plasmolytic water splitting that can carried out water splitting without acquiring the high temperature. It is also a thermodynamically non-impulsive reaction ($\Delta G > 0$) (Bockris, 1985). The electric energy (microwave frequency or direct current) of plasma state transformed into the kinetic energy of the molecules and electrons (responsible for ionisation) due to their molecular excitations and translation of the heavy particles. Plasma discharge is basically categorized into hot (thermal or arc) discharges and cold (low temperature flash) discharges with the electron temperature ranging from 1-10 thousand degree for both classes. Interactions between the electron and molecule are responsible for dissociation and ionization process of plasma. The velocity of electron-molecule reaction depend upon the average electron energy and the energy distribution function of electron that expressed by the Equation 1.25.

$$f_e = f_{LM} \exp\left(\frac{e\phi}{K_B T_e}\right) \qquad \text{...(1.25)}$$

The electron energy distribution function (f_e) was described in term of Maxwellian velocity distribution function, which can be specified by an electron temperature (T_e) and Boltzmann constant (K_B), energy per degree of freedom (e), which is equal to ½ mv^2 = ½ K_BT_e. Due to the variation in the mobility rate of the electron and molecule/ions species the electric fields generated in the plasma state. And as created electric field influence the spatial distribution of particle velocities through the Lorentz force that induced extra mobility in the electrons.

Degree of ionization the number of free electrons = nJN (where, n = the electrons density, J = the current density and *N* = an Avogadro number) is the important parameter for the plasmolysis of the water (Givotov et al., 1981). During the cleavage of water vapor in irreversible plasmonic stage, the discharge energy distribute in form of vibrational excitation process and dissociative energy. The thermal discharges process attained with the local thermodynamic equilibrium in the arc method. Though, the chemical and transport kinetics of discharge controlled by the lowering of the temperature (high) of the reacting species. There are two methods for hydrogen production by plasmolysis of water is either performed in one step or in multiple step- plasmolysis of CO_2 and water plasma then plasmolysis of CO occurred in presence of water (Figure 1.15 a and b), respectively (Hensen and Sanden, 2017).

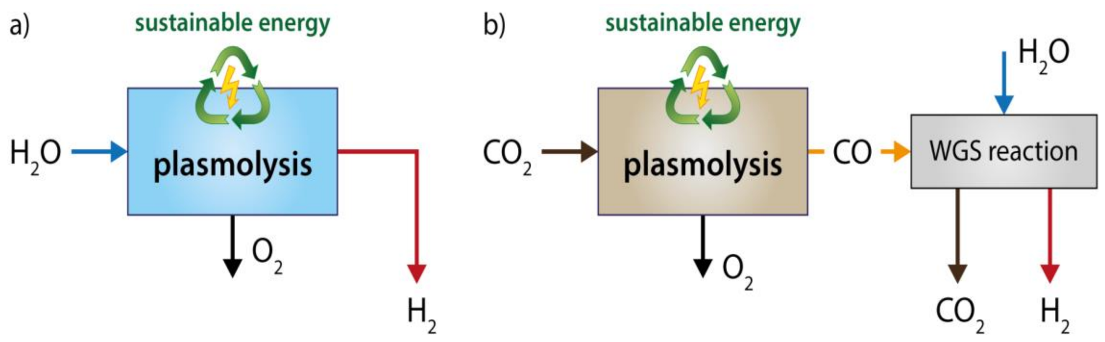

Figure 1.15 Hydrogen production of by plasmolysis of (a) water and (b) CO_2 and water. (Hensen and Sanden, 2017).

Bochin et al. had proposed the reaction mechanism involved in splitting of water process through different vibrational excited states, as shown by Equations 1.26 to 1.30.

$$H_2O^* + H_2O^* \rightarrow H + OH + H_2O \qquad ...(1.26)$$

$$H + H_2O^* \rightarrow H_2 + OH \qquad ...(1.27)$$

$H + H_2O^* \rightarrow H + H_2O_2$ ...(1.28)

$OH + H_2O \rightarrow H_2 + HO_2$ ...(1.29)

$HO_2 + H_2O \rightarrow H_2O_2 + OH$ ...(1.30)

The mechanism of the water plasmolysis via dissociative path is shown by the following Equations 1.31 to 1.35:

$H_2O + e^- \rightarrow H^- + OH$ ...(1.31)

$H^- + e^- \rightarrow H + 2e^-$ ... (1.32)

$H_2O + H^- \rightarrow H_2 + OH$ ...(1.33)

$H_2O + H^- + M \rightarrow H + H_2 + M^-$ ... (1.34)

$OH + H_2 \rightarrow H + H_2O$ ... (1.35)

Here, in the latter set of reactions (Equations 1.31 to1.35) the yield of H_2 decreases irrespective of the actual reaction sequence the problem because of the high requirement for higher degree of ionization which is difficult to attain. However, CO has been found to be a catalyst in the direct production of hydrogen form water by plasma since it lower the need of high degrees of ionization and reduces the free radical OH* concentration.

1.10.3 Photocatalytic Water Splitting

Photosynthesis process naturally observed in plants that gives us a clue of cost-effective requisite route for the solar water cleavage. Investigators had invested their diligent efforts to mimic photosynthesis reactions since 1972 (when water splitting discovered by Fujishima and Honda). Here, we discuss the different aspects of photocatalytic water splitting. During the water splitting process, when the semiconductor (photocatalyst) suspended in water under the light exposure, the oxidation and reduction process of water was observed at the interface region without supply of any electricity. The valence band and conduction band positions of the particulate material should be straddle between the hydrogen and oxygen evolution potential for the overall splitting of the water. Photocatalyst may satisfy some conditions simultaneously as discussed are: stability in water and light, band positions of catalyst straddle between redox potential of water and optoelectric properties i.e. light absorption, charge separation, charge transport, (Maeda and Domen, 2007; Rajeshwar 2007; Osterloh 2008; Maeda 2011; Osterlog and Parkinson, 2011). In short one has to look after the following points: light adsorption, surface structure, interface, charge diffusion, charge trapping, particle size, surface electronic states, dark reactions and photoreactions, all together that may enhanced the complexity of the molecular device Figure 1.16.

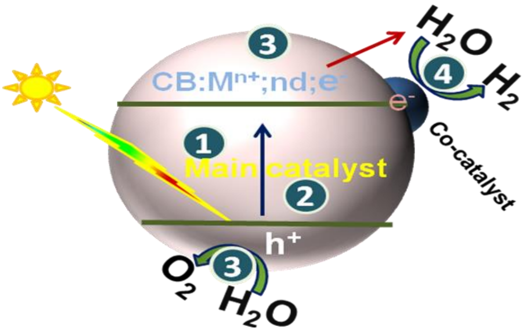

Figure 1.16 Illustrate the operating principle of the photocatalytic reactions (1. light absorption, 2. charge separation, 3. charge transport and 4. reduction of water at co-catalytic site and oxidation of water at catalytic groove on the main catalyst site.

All of the above needs are related with each other and altogether depends on the chemical, electrical, physical and optical characteristics of the semiconductors. Basically, the water splitting reaction is quite active, mechanistically multifaceted, kinetically time-consuming and chemically sarcastic reaction than the simple electron transfer procedure. Even though, the photoelectrochemical electrolysis of water is extremely efficient reaction and the hydrogen production rate by this course of reaction is fairly good. Therefore, we are looking for the material with the high efficiency and low cost are the major challenges in the scaling hydrogen production at large scale. It was found the PV water cleavage including thermo chemical, PEC and photo biological techniques, is a costlier than the single photocatalysis process. On the other hand, the parting of the likely to explode mixture of hydrogen and oxygen gases had needed the extra energy that cuts down the efficiency of the overall water splitting. This method had the few merits, these are: (1) good solar to hydrogen conversion (STH) efficiency; (2) small handing out price; (3) no separation of evolved hydrogen and oxygen gases during the reaction.

1.10.4. Photoelectrocatalytic Water Splitting

Henri Becquerel recorded the initial testimony of a PEC event in 1839. (Becquerel, 1839) with silver chloride- coated platinum electrodes in various electrolytes, in terms of the photocurrent and photovoltage produced by the reaction of sunlight with semiconductor and pure water. Because pure water can absorb the IR region of the solar radiation but at that region the photon energies are too small to generate photochemical reactions. Hence, the water splitting process is derived by utilising the electrical and solar energy in the company of photocatalysts of quite small band gaps ranging between1.6-2.5 eV. If photocatalyst is a wide band gap semiconductor material than a sensitizer or co-catalysts or both should be loaded on the surface of the photocatalyst to make the absorption of sunlight easy and to excite the photochemical reactions to enforce the cleavage of water that lead to the production of hydrogen and oxygen gases. In the photoelectron-cleavage process of the water, initially the sunlight absorbed by the as synthesized molecular assembly or biogenic materials (chloroplast or algae in a configuration coupled with a hydrogen generating enzyme) or hybrid systems that swings in an aqueous electrolyte solution. The systems (semiconductors or enzymes) are either used as the suspended particles or as a electrode unit in a PV or an electrochemical cell, is merged in the electrolyte solution, are used for the electron hole relay. A good photocatalytic material may have some characteristics such as efficiency, durability or stability in water and light (photocorrosion), apt band gap, good lifetime of charge carriers, low defects concentration, free path way for charge carrier, low fabrication price and many more. It is quite tough to observe the all characteristics in a single material. Besides these integrated devices, the high tech systems are required with rigorous development activities in strong synergy with PEC materials and devices by use of nanotechnology and computation systems. Currently, the Nuclear Energy Research Initiative (NERI) place the PEC H_2 manufacturing goal of 15 % conversion efficiency for 900 hours' replacement lifetime (1/2 year at 20 % capacity factor) for commercial hydrogen production cost of \$2.10 kg (material) and \$300/m^2 (PEC electrode cost) (Deutsch, 2013).

Photoelectrochemical water splitting used to adapt light energy into the more useful energy products i.e. electrical (current density) or chemical (H_2 and O_2) or both. In addition, on absorption of solar light by one or more fabricated electrodes (photoanode and photocathode; at least one of the electrodes is fabricated by semiconductor) that dipped in aqueous electrolyte solution that not only produced hydrogen and oxygen gases but also the current density by splitting of water. In principle, the as generated internal electrical field at the semiconductor-electrolyte interface used to separate of the photogenrated electron-hole pairs (exctions).

1.11 Quantum Dot –Sensitized Metal oxide photo catalysts

To promote wide band oxides for harvesting more visible light, use of some photosensitive dyes and semiconductor quantum dots(QDs), have been adopted. Semiconductor QDs have many significant advantages over synthetic / natural dyes such as: better optical stability, large extinction coefficients, and adaptability to the large range solar spectrum with major drawback that the almost every high-quality QD comprises of highly toxic elements. However, recently less-toxic alternatives like InP or CIS are available that seem to solve this problem. Moreover, $CuInX_2$, $CuGaX_2$, $AgInX_2$, $AgGaX_2$ (X=S, Se), and similar materials are alternatives to InP because they are composed of abundand, readily available, non-toxic elements (no class A and B elements of QDs) that form an effective hetero-junction with solid hole/electron conductors, are used to improve the matching of the solar spectrum with their absorption spectrum by controlling the particle size, which can also be used to increase the visible light absorption of large BG metal oxide-based photoelectrodes. By controlling the particle size of QDs, one can vary the energetic of the QDs and the light harvesting capacity of the wide band oxides. For examples, small BG metal sulfides or selenides such as CdS and CdSe QDs have been used to sensitize the wide BG metal oxides such as ZnO and TiO_2 for PEC/PC hydrogen generation. QDs use to demonstrate the size-dependent quantization of the electronic energy levels as dependent upon particle size and shape, particle-particle interaction, particle spacing, and nature of the outer shell. These types of heterojunction allow the rapid separation of electron-hole pair and transfer of photoexcited electron-hole. Quantum confinement and electron tunnelling properties used to differentiate QDs from the same sized nanomaterials. Bohr diameter (r_n) is one another useful parameter that used to determine the type of confinement that to decide which particle will be the QD among the same sized nanodot of different materials.

$$r_n = \frac{n^2 h^2 \epsilon_0}{\pi e^2 m_e}$$

Where, n is energy level, h is plank's constant (6.023x $10^{-23}m^2Kgs^{-1}$), ε dielectric constant ($8.84x10^{-12}$ $m^2Kgs^{-2}J^{-1}$), e charge of electron (1.6x $10^{-19}C$) and me is mass of electron (9.1 x 10^{-31}). Usually, the particles having size smaller than 3 Bohr diameter (the radius of an excition in PbSe is as large as 46 nm, possess strong confinement), are QDs. As the nanocrystals becomes more confined, the peak shrinks, on the basis of the free movement of the particles in 3D, 2D, 1D and 0D space, the nanoparticles are defined as bulk, quantum well, quantum wire and QDs, as shown in Figure 1.17.

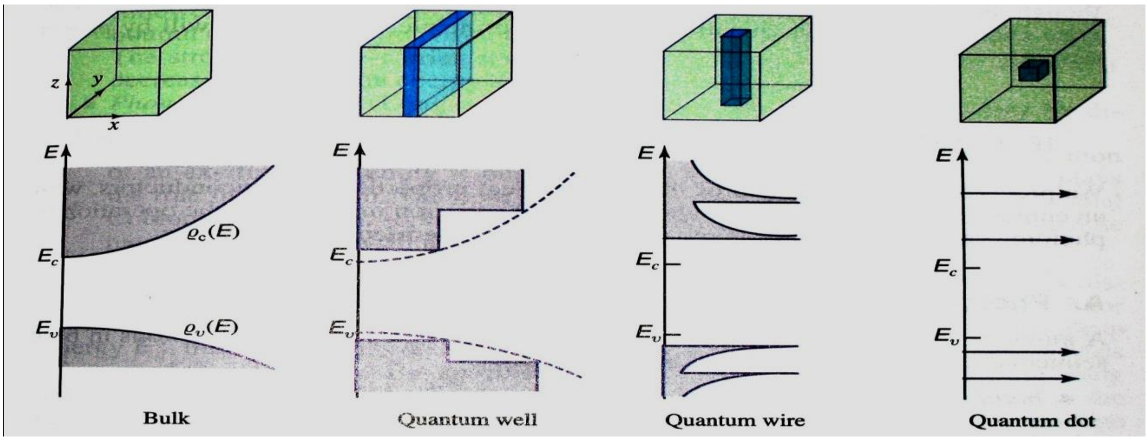

Figure 1.17 Schematic representation of the different sized particles of the same material (a) bulk;3-D all carriers act as free carriers in all 3-directions (b) quantum well; 2-D carriers are 1D-confined but act as free carriers in a plane (c) quantum wire;1-D carriers are 2D-confined but free to move along direction of the wire (d) quantum dot; 0-D carriers are confined in all 3-directions (no free carriers).

Due to the strong confinement in QDs, several novel quantum phenomena emerges, such as Shortened carrier collection pathways, Improved light distribution, Quantum size confinement, Potential determining ions (PDI), Surface area-enhanced charge transfer, phonon bottlenecks and coulomb or spin blockades and Multiple exciton generation, (Nozik, 2001) predicted a novel multiple exciton generation (MEG) phenomenon in QDs, and many more. In MEG process, the multiple electron−hole pairs or excitons produced on absorption of a single photon in semiconductor. (Schaller and Klimov, 2004) provided the strong experimental proof of MEG for PbSe QDs, where MEG of up to seven excitons per single phonon has been reported (Schaller, 2006). Later on other QDs with MEG capacity were observed for the compounds: PbS, PbTe, CdS, CdSe, InAs, Si, single-walled carbon nanotubes (SWNTs, efficiency 130%), graphene, and InP, etc. (Ashok Kumar, 1984; Kudo et al., 2004; Takata, 1998) Besides the several microscopic evidences of the MEG phenomenon is still enigmatic and several mechanisms have been suggested that to be applicable for this process, including impact ionization, an inverse Auger process, direct carrier multiplication (Califano, 2004a and Califano, 2004b), and MEG (Wang, 2003). In MEG, the excitons are generated in a decoherent process. The Auger mechanism assumes an incoherent process and requires a faster decoherence time than for the time in creation of multiple excitons (Ellingson, 2005). Direct carrier multiplication relies on multiexcition coupling to virtual single-excition states and the coherent superposition of these during an optical pulse. The discovery of the MEG process of QDs apparently became important as promising building blocks in solar devices and intensive research is going on involving the fabrication of dye-sensitized solar cells (DSSCs) or photocatalytic devices for water splitting. When irradiated with visible light then several excitons can form per photon in a semiconductor QDs, which gives us a solid assurance for high efficiency up to the Shockley-Quiesser limit (estimated maximum efficiency limit is 31% for photo-devices). The photon absorbed in the VB of the semiconductor promotes an electrons to jump from VB to CB. If the difference between the photon energy and BG will be dissipated as heat and cools down the hot electrons, the phenomenon is known as Auger cooling. It has been shown that QDs need to possess the hydrophilic surface properties in order to adsorb onto metal oxide surfaces efficiently (QDs with hydrophobic surface do adsorb with the same degree, but not as readily as hydrophilic ones).

The two major strategies to obtain hydrophilic QDs are; first, synthesis of QDs in aqueous solution; second, synthesis of QDs in organic solution with subsequent ligand exchange. Both methods lead to the similar results (Murphy et al., 2006b).

QD-sensitized PEC cells have the potential to convert more solar energy than dye-sensitized cells. The sensitization of semiconductor metal oxide for PEC cells using CdS, CdSe, and CdTe QDs was recently reported (Kamat, 2008). Although, cadmium chalcogenide QDs have been extensively used as a sensitizer in harversting visible light, the photostability is a major concern for CdSe and CdS based sensitizers due to their self-oxidation reaction; another concern is their toxicity. Furthermore, the sacrificial chemicals are certainly not desirable to generate hydrogen but it is necessary to develop small BG semiconductors to sensitize large BG metal oxides for water splitting. Hole-sacrificial reagent such as SO_3^{2-}/S^{2-} , were added to prevent the self-oxidation of QDs, while the photoanode is no longer oxidizing water. DSSCs made from TiO_2 and CdSe (or PbS) QDs have already been reported in the literature (Kamat, 2008). Their efficiency is around 3% (Niitsoo et al., 2006), which is still smaller than that of conventional DSSCs.

(Nann, 2010) utilized InP QDs in 2010 as a suitable sensitizer for solar water-splitting applications, where they coated with an iron catalyst forming a 3D nanophotocathode on gold material for production of hydrogen and commonly used as n-type semiconductor oxide photocatalysts, as photoanodes. Recently, (Yang et al., 2014) developed a Z-scheme device, which shows the overall water splitting with efficiency of 0.17%, in a non sacrificial environment under visible light illumination. They reported a corrosion-resistant and photostable PEC system that consisting of a CdS QD-modified TiO_2 photoanode and a CdSe QD-Modified NiO photocathode. Layer of ZnS used for passivation to protect the cadmium chalcogenide QDs and can be used as co-catalyst for H_2 gas evolution. Another interesting example of QD-sensitised overall water splitting under visible light irradiation is demonstrated by (Yeh, 2014) by using nitrogen-doped graphene oxide QDs, where a nitrogen-rich site exhibited n-type and a nitrogen-deficient site show p-type conductivities and overall device served as p-n type photochemical diodes, in which the carbon sp^2 clusters of graphene serve as the interfacial junction for H_2 and O_2 evolution from their p-and n-domains, respectively. Similarly, the mesoporous TiO_2 layer is on the top of CdSe/H-TiO_2 exhibits a maximum photocurrent density of ~16.2 mA/cm^2, which is 35% greater than that of the optimized sample i.e. CdSe/P25 (control), which exhibits a current density of -14.2 mA/cm^2, (Kim et al., 2013) under the same conditions. Enhanced PEC water splitting was demonstrated by Si QDs/ TiO_2 nanotube array electrodes under visible light illumination with the photocurrent density was 1.6 times higher than that of pristine TiO_2 electodes (Li, 2015). Photocatalytic H_2-production rate over Co_3O_4-QDs and over Co_3O_4-SSr with 420 nm visible light cut off filter is estimated as 1.10 and 0.80 $\mu molg^{-1}h^{-1}$, respectively (Zhang, 2014b). The most efficient QDs-based photocatalyst tadem electrode TiO_2/CdZnS/CdZnSe with different batches to provide a remarkable photon-to-hydrogen efficiency of 7.3 ± 0.1% (with the rate 172.8 mmol/h/g of the photocatalytically produced H_2 by water splitting) (Wang 2013). The five fold photocurrent responses of the rGO-CdS-H_2W_2 composite film was observed in compared to the pure CdS film (Wang, 2014). Branched CdS QDs sensitized TiO_2 nanoarrayed anode was used for PEC water splitting with the remarkable photocurrent density (4mA/cm^2 at a potential of 0 V s. Ag/AgCl) and high STH efficiency (Su, 2013). The photoelectrode of InN/$In_{0.54}Ga_{0.46}N$ QDs reveals a maximum IPCE of up to 56% at a wavelength of 600 nm with a hydrogen generation rate of 133 mmol/h/cm^2 at zero voltage under illumination of a 1000W Xenon are lamp. Where the layered InN/$In_{0.54}Ga_{0.46}N$ photoelectrode show the low IPCE of 24% with hydrogen generation rate of 59 mmol/h/cm^2 (Alvi, 2015; Trevisan, 2013) demonstrated the in-situ growth of CdS and PbS QDs on mesoporous TiO_2 aiming for harvesting light in both visible and near-infrared (NIR) regions of light for hydrogen generation through water splitting.

1.12. Plasmonic Material induced Metal Oxide Photocatalysts

Ebbesen et al., (Barnes, 2003) first time established a novel class of optoelectronic materials, i. e. plasmonic photocatalyst. This new class of material inspired the researchers to use them with photocatalysts due to their good light-producing qualities along with their apt band gap breaking effect and sensitizer effect. This new class had a wide range of applications such as wastewater treatment, air purification, water splitting, enhancing computational power of electronic gadgets , breast cancer treatment, manufacturing of light-emitting diodes (LEDs), rendering a satellite object invisible, and so on (Atwater, 2007), During the water-splitting process, the studied photocatalytic materials (oxides, oxynitride, nitrides, sulfides, oxysulfides, etc.) faced two main problems: (1) low efficiency (due to the unification of photo-carriers) and (2) lack of satisfactory number of visible light responsive photocatalytic materials because the most commonly available are stable oxides materials had a wide BG, that make them eligible to harvest UV light and short BG materials vulnarableto be oxdise in light on long time light exposure (Hashimoto, 2005; Wang, 2012). Both of the deficiencies would be overcome by the use of plasmonic photocatalytic materials. These novel metamaterials have two prime parts: (1) localized surface plasmonic resonance (LSPR) in nanoparticles of noble metals; and (2) Schottky junction results of the contact between the noble metal and semiconductor/polar material (support/carrier). The prominent benefits associated with plasmonic material in terms of LSPR are given as follows:

1. Tunable resonating wavelength: (UV, near UV, visible, or IR) of the metal nanoparticles can control the size, shape and surrounding environment (Kelly, 2003).
2. Enhanced light absorption effect: The LSPR can drastically enhance the absorption of visible light (low BG photocatalysts)/UV light (Thomann, 2011) (large BG materials) (Awazu, 2008).
3. Reduced diffusion length: This is compatible to the minority carrier diffusion length of 10 nm (Zhdanov, 2005; Linic, 2011; Mubeen, 2011); with the strong absorption of the incident light in a thin layer, it will be beneficial to materials that present poor electron transport.
4. Enhanced local electric field: The LSPR creates an intensive local electric field, which favors photocatalytic reactions by excitation of the electrons and holes (Wu, 2010; Torimoto, 2011) or by increasing in the number of photoexcited electron and holes that heats up the surrounding environment to enhance the redox reaction rate and the mass transfer (Sun 2009; Christopher, 2011), and polarized the nanopolar molecules for better adsorption (Mubeen, 2011).
5. Other contributory effects: In addition to the aforementioned effects in photocatalysis, plasmonic photocatalysis enjoys some other benefits also such as higher light utilization efficiency, better temperature dependence, and enhanced molecule adsorption, polarization, the catalytic effect of the noble metal (e.g. Pt for hydrogen evolution), and the quantum tunneling effect (Wang, 2012).

6. Benefits of Schottky junction: Electrons and holes are compelled to move in different directions once they are created inside or near the Schottky junction (Thimsen, 2011) and the phenomena prevent the recombination of the photocarrier.

1.13 Adverse effect of Metal nanoparticles

Beside aforesaid goodness of the nanoparticles, there are few bad effects associated with nanostructures, which are listed below:

1. **Shading effect**: metal nanoparticles loaded on the surface of the semiconductor reduce the light-receiving area of the semiconductor. The shading effect affects the photocatalytic systems that require irradiation of the semiconductor part.
2. **Block active sites of semiconductors**: Some area of the semiconductor surface i.e. pores (active areas) may even blocked by plasmons, results in reduction of the specific surface area of the semiconductor and thus affects adversely the photocatalytic activity.
3. **Recombination centre**: The noble metal nanoparticles could act as a recombination centre. Due to the contact between the metal and the semiconductor could from surface states at the interface, which promotes charge trapping, recombination, and Fermi level pinning processes (Nakato, 1975; Nakato and Tsubomura, 1985; Primo, 2011).
4. **Stability**: Few problems are related with the stability of the metal/semiconductor mixture. The metal nanoparticles might undergo photocorrosion and leaching, result in a gradual loss of the photocatalytic performance over time (Herrmann, 2005); the encapsulated from of molecular system can avoid this problem, at the cost of losing the “fast lane” transfer of the charge carriers to their semiconductors.

Heterogeneous photocatalysis has five basic independent steps, (Sun, 2009) which can be benefited by the aforementioned phenomena as follows:

1. Transfer of the carriers onto the photocatalytic surface to reactant may be boosted by fluid mixing.
2. Adsorption of the reactants was improved by polarization (Awazu, 2008).
3. Redox reactions at the adsorbed phase were facilitated by the metals fast transfer, charge carrier trapping, and high contact surface area would significantly enhance

the creation and separation of active electrons/holes associated with the localized heating effect to raise the reaction rate (Yu, 2009).

4. Desorption rate of the production from the surface (transfer of the products away from the surface) was increased by the localized heating effect that increases the reaction rate (Chen, 2008; Adleman, 2009) and boost fluid mixing.

In usual practice, metallic structures are known for high optical losses, which is not good for transmitting light signals. Because the electrons use to oscillate in the electromagnetic field and collide with the electrons present in the close vicinity of atomic lattice and soon dissipated the field energy. However, when the plasmonic material exposed to sunlight, free electrons of the noble metal nanoparticles integrated with the photon energy of sunlight and produces subwaves and to propagate electrons in oscillating mode, result in to enhance optical properties and to lower the energy losses due at the interface (Low electron density zone) between the nanometals and the bulk semiconducting material, where there are no free electrons to collide or to dissipate the energy. Hence, plasmons can be propagated at interface (semidconductor and noble metal surface) for several centimeters before dying. This propagation length can be maximized if the waveguide employs in an asymmetric mode, which pushes the greater portion of the electromagnetic energy away from the guiding metal film and into the surrounding dielectric, thereby lowering energy losses. Thus, electrons of noble metals act as LSPR systems (Figure 1.18) and produces the active thermal redox reaction centers on the catalyst surface that can scatter, trap, and concentrate the light, and to enhance the number of active sites and rate of electron-hole production through fast charge transfer process at the photocatalyst‘s surface.

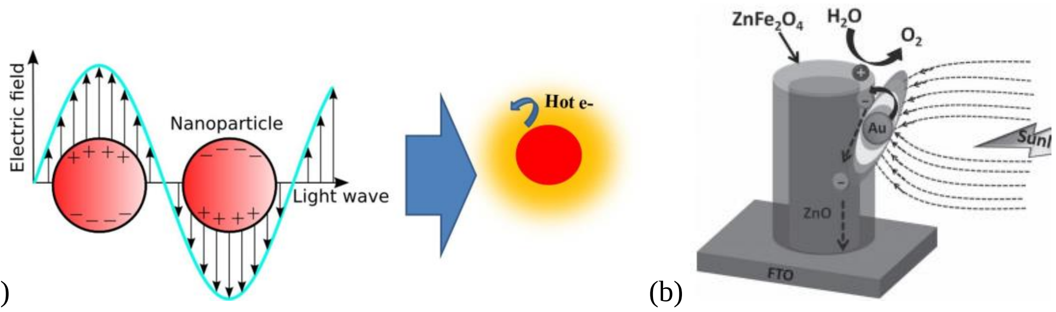

(a) (b)

Figure.1.18 (a) Scheme for the localized surface plasmonic hot electrons of a noble metal and (b) light harvesting oxide-oxide heterojunctions for efficient solar photo electrochemical water splitting by using the material AuNP/ZnFe$_2$O$_4$/ZnO.

The material systems will be mainly grouped based on the structure of the metal and photo catalyst for example, nanoparticles in the sole-metal form, nanocomposites in the embedded form, nanocomposites in the encapsulated form, and nanocomposites in the isolated form.

The charged chemical compound are selectively attracted or repelled by the accumulated charges on the surfaces of the metal nanoparticles and the semiconductor. In addition, the dipole nature of the local electric field of the surface Plasmons attracts the polar molecules that can polarizes the nonpolar molecules. Au@$ZnFe_2O_4$/ZnO is a classical representative of the plasmonic photocatalysis, in which a hot electron of the plasmonic Au nanoparticles transfered to the CB of the $ZnFe_2O_4$ and ZnO for facilitating the absorbance of the light to increase the efficiency of the device (Figures 1.18b) (Sheikh, 2013). Au@TiO_2 is an another good example, the presence of Au nanoparticale induces a space charge region (i.e. Schottky junction) in the TiO_2. Plosmonic nanoparticles can build up an internal energy field E pointing from the TiO_2 to the Au. The LSPR was created in response to the electromagnetic field of the incident light on small sized Au nanoparticles drives the collective oscillation of the electrons, which excites more electrons and holes. Such internal field forces induce the separation of electrons and holes, which suppress their recombination and let the excited electrons of Au NPs LSPR to have sufficient energy to go across the space charge region to fed them into the CB of TiO_2 as depicted by (Zhang, 2013) under 633-nm light irradiation along with the experimental support. Some prominent systems that used for water splitting with their hydrogen generation oxygen efficiency, are listed in following Table no.1.

Table 2 Prominent systems used for hydrogen and oxygen generation via water splitting with light source and electrolyte

S.N.	Main system	Light source	Electrolyte	Hydrogen production (g-1 h-1)	Oxygen Production	Ref.
1.	Au/CeO$_2$	visible light (λ > 400 nm)	aqueous AgNO$_3$ suspension	---	10.5 μmol h^{-1})	Primo A. et al., 2011
2.	(ZnO)$_{1-x}$(CdS)$_x$ core–shell nanorods/RuO$_2$ co-catalyst,	irradiation of solar light	S^{2-} and SO$_3^{2-}$ as sacrificial reagents	6.18 mmol	---	Wang et al., 2010
3.	Ag/TiO$_2$	UV and visible light irradiation.	Alcohol sacrificial Agent	1.05 μmol	------	Wu F. et al., 2013
4.	Au-ZnO Photoelectrode	Solar simulator with 100 mW/cm^2 light.	0.5M Na$_2$SO$_4$ aqueous solution	11.2 μmol	4.4 μmol	Chen H. et al., 2012
5.	CdS nanorods/ ZnS nanoparticale	Visible light Irradiation (λ > 420 nm)	aqueous 0.75 M Na$_2$S and 1.05 M Na$_2$SO$_3$ in 20mL.	239,000 μmol	--	Jiang J.D. et al., 2016
6.	Ni/CdS/g-C3N$_4$	300 W Xe lamp(≥420 nm	10 mL triethanolamine	1258.7 μmol	--	Yue X. et al., 2016
7.	Ru/SrTiO$_3$:Rh PRGO(BiVO$_4$)	light source, 300 W Xe lamp (λ > 420 nm)	H2SO4(aq)	11 μmol.	5.5	Iwase A.et al., 2011
8.	Pt–Co/g-C$_3$N$_4$	UV (l > 300 nm)	sacrificial reagents	12.2 mmol	--	Zhang G.et al., 2016
9.	2wt%Au/TiO$_2$-P25	150W metal halide lamp, intensity 30 mWcm-2	Methanol	7.20 mmol	---	Maeda K., Domen K. 2007
10.	LaTiO$_2$N	Visible light (ì > 400 nm)	methanol (10vol %) as sacrificial reagent.	30 μmol	41 μmol	Wang Q. et al., 2016
11.	SrTiO$_2$:La,Rh/Au/BiVO$_4$:Mo	300W Xe lamp fitted with a Cut off filter(λ>420nm)	aqueous methanol (10 vol%) and NaIO$_3$ (4 mM) solution	90 μmol	---	Ingram D. B., Linic S.et al., 2011

1.14 Typical examples of the plasmonic materials used for water splitting

1.14.1 Gold Supported on Nanoparticulate CeO_2

(Primo et al., 2011) evident the 1 wt % gold-supported ceria nanoparticles generate oxygen from photocatalytic water splitting (10.5 $\mu mol \cdot h^{-1}$) even more competently from the standard WO_3 (1.7 $\mu mol \cdot h^{-1}$) under the visible light ($\lambda > 400$ nm) even in UV irradiation (9.5 $\mu mol \cdot h^{-1}$). The extraordinary photocatalytic activity attributed to the reduced particle size of ceria (5 nm) by means of electrostatic binding of Ce^{4+} to alginate gel, localised spin plasmonic resonance effect associated with gold nanoparticle, subsequent supercritical CO_2 drying, and calcination.

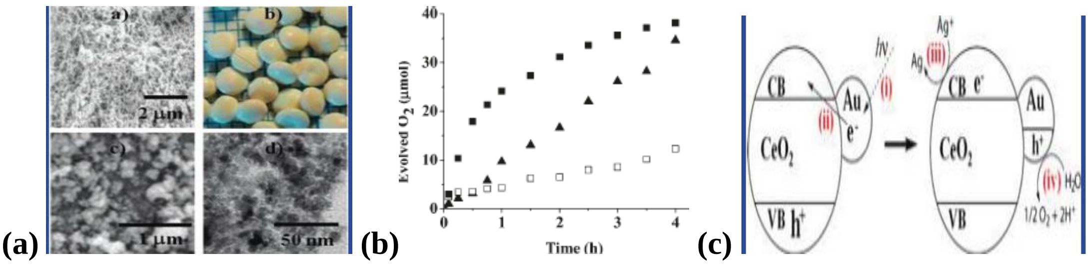

Figure 1.19 (a) SEM images of uncalcined CeO_2; uncalcined CeO_2 spheres; calcined CeO_2(A); TEM Au (1.0 wt%)/CeO_2. (b) Evolution of O_2 upon visible light irradiation of an aqueous suspension of $AgNO_3$ containing: 9WO_3, 2CeO_2, and 0CeO_2 and (c) elementary steps proceed during the photocatalytic oxygen. (Primo et al., 2011)

1.14.2 ZnO–CdS core–shell nanorods

(Wang et al., 2010) studied $(ZnO)_{1-x}(CdS)_x$ core–shell nanorods, where (x =0.1, 0.2, 0.3, 0.4, 0.5, 0.6) for photocatalytic hydrogen evolution from water splitting under measurement conditions: 0.2 g sample, 300 mL aqueous 0.1 M Na_2S and 0.1 M Na_2SO_3 solution as sacrificial reagent, and 300 W Xe light source.[129] It was found that the photocatalytic activity and stability of ZnO–CdS core–shell nanorods with RuO_2 co-catalyst is superior to that of ZnO–CdS core–shell nanorods with Pt co-catalyst.

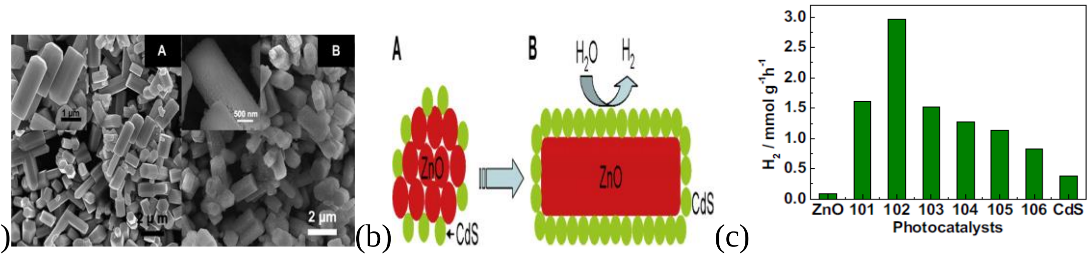
a) (b) (c)

Figure 1.20 (a) SEM images of (A) ZnO nanorods and (B) $(ZnO)_{0.8}(CdS)_{0.2}$ core–shell nanorods, (b) Schematic of (A) ZnO–CdS heterostructured nanoparticles used for (B) hydrogen generation through core–shell nanorods and (c) Comparative photocatalytic H_2 evolution rate of CdS particles, ZnO nanorods, and the $(ZnO)_{1-x}(CdS)_x$ core–shell nanorods, where (x =0.1, 0.2, 0.3, 0.4, 0.5, 0.6) are denoted as 101, 102, 103, 104, 105 and 106, respectively, prepared at 400°C for 1 h in H_2S atmosphere. (Wang et al., 2010)

1.14.3 Ag/TiO_2 Nanotube Arrays

The Au/TiO_2 (Wu et al., 2013) system with surface plasmon resonance (SPR) effect was employed to study the photocatalytic water splitting to produce the renewable solar hydrogen gas. Where, silver nanoparticles loaded on TiO_2 nanotubes surface behaved as electron trapping centre retard the recombination of electron−hole pairs, result in improved reaction activity. However, the electron trapping phenomenon along with the SPR effects are responsible for the photoactivity enhancement. The intensified electric field at the interface between the Au particles and the subdomain TiO_2, is used for photocatalytic degradation of methylene blue and photocatalytic water splitting performed on Au/TiO_2, prepared by the photodeposition method (Figures 1.21).

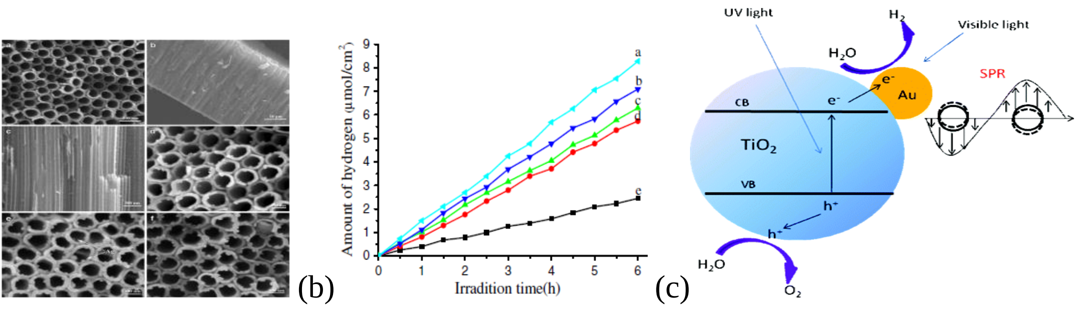
(a) (b) (c)

Figure 1.21 (a) Morphological images of the plasmonic Au particles loaded on TiO_2 nanotubes used (b) for photocatalytic hydrogen generation using water splitting and (c) their electron transfer mechanism (Wu et al., 2013)

1.14.4 Plasmonic Au@ZnO

(Wu et al., 2013) Artificial photosynthesis attracts investigators to use same phenomena for transferring solar energy into chemical fuels. Study concern about how the effect of plasmon excitation and other factor dominates the solar splitting of water in photovoltaic devices that to experimentally demonstrate (The finite-difference time-domain (FDTD) program with MEEP, photolectrochemical current density measured as a function of the wavelength of light, density function theory, X-ray absorption near edge spectroscopy, simulated heat generation distribution map of Au nanospheres-ZnO nanorod) the effects of plasmons upon an Au nanostructure–ZnO nanorods array as a photoanode. About 11.2 and 4.4 μmol h^{-1} of H_2 and O_2 gas molecules were generated by the Au-ZnO photoanodes and platinum cathode under irradiation by AM 1.5 illumination in 0.5 M Na_2SO_4 (pH=6.8) aqueous solution with the Faraday efficiencies: 86% and 69%, respectively. (Jiang et al., 2016)

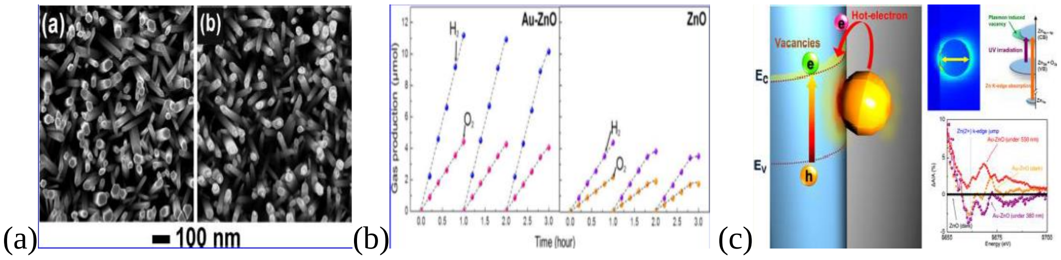

Figure 1.22 (a). SEM images of bare ZnO (a) and Au@ZnO photoelectrodes with nanoparticles deposited for 12 h deposition (b) Time courses of H_2 and O_2 evolution using Au@ZnO and ZnO photoelectrodes under AM 1.5G solar simulator and (c) electron transfer mechanism of Au@ZnO system with evident of plasmonic phenomena by X-ray absorbtion spectroscopy. (Yue et al., 2016)

1.14.5 Z-Scheme ($Ru/SrTiO_3:Rh$)/($PRGO/BiVO_4$)

(Iwase et al., 2011) During the Z-scheme photocatalysis system, the photoreduced graphene oxide can shuttle the photogenerated electrons from an O_2-evolving photocatalyst ($BiVO_4$) to a H_2-evolving photocatalyst ($Ru/SrTiO_3:Rh$) Here, the reduced graphene oxide played a role of solid electron mediator for water splitting in the Z-scheme photocatalysis process that tripled the consumption of electron–hole pairs in the water splitting process to generate 11.0 μmol $g^{-1}h^{-1}$ hydrogen and 5.5

μmol $g^{-1}h^{-1}$ oxygen gas under the visible-light irradiation in acidic medium (pH=3.5), as demonstrated by (Iwase et al., 2011) (Figure 1.23).

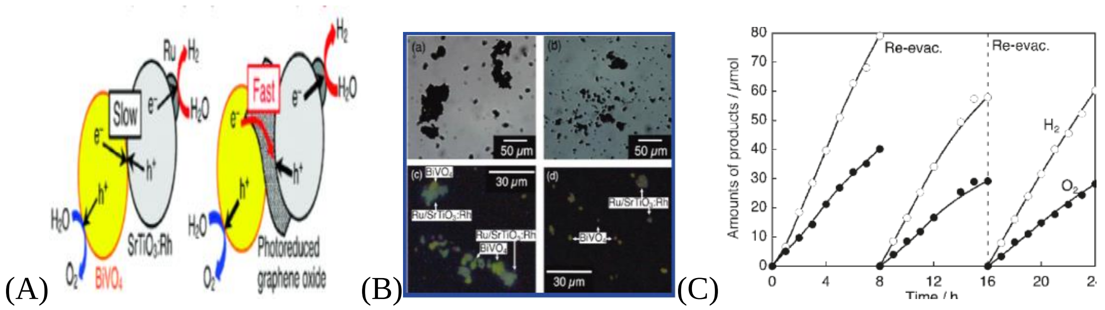

Figure 1.23 (a) Schematic representation of a mechanism of water splitting in a Z-scheme photocatalysis system consisting of Ru/$SrTiO_3$:Rh/$BiVO_4$ and Ru/$SrTiO_3$:Rh/PRGO/$BiVO_4$ under visible-light irradiation, (b) electronic microscopic images of Ru/$SrTiO_3$: Rh and PRGO/$BiVO_4$ suspended in water at pH 3.5 (adjusted by H_2SO_4) and pH 7.0 and (c) **o**verall water splitting under visible-light irradiation by the (Ru/$SrTiO_3$:Rh)/(PRGO/$BiVO_4$) system under the experimental conditions: catalysts (0.03 g each) in H_2SO_4(aq) (pH 3.5, 120 mL); light source:300 W Xe lamp with a 420 nm cutoff filter; top-irradiation cell with a Pyrex glass window.(Wang et al., 2016)

1.14.6 Nanocomposite Ag/N-TiO_2

In photocatalytic reactions such as photocatalytic water splitting with oxide semiconductors, the high rate of charge-carrier recombination is a critical factor that limiting the rate. Therefore, (Ingram and Linic, 2011) demonstrated the effect by combining a semiconductor photocatalyst with the tailored plasmonic-metal nanostructures by the support of the formation of resonant surface plasmons in response to a photon flux, localizing electromagnetic energy close to their surfaces (Figure 1.24). The advantage of the formation of e^-/h^+ pairs near the semiconductor surface is that these charge carriers are readily separated from each other and easily migrate to the surface for performing photocatalytic transformations.

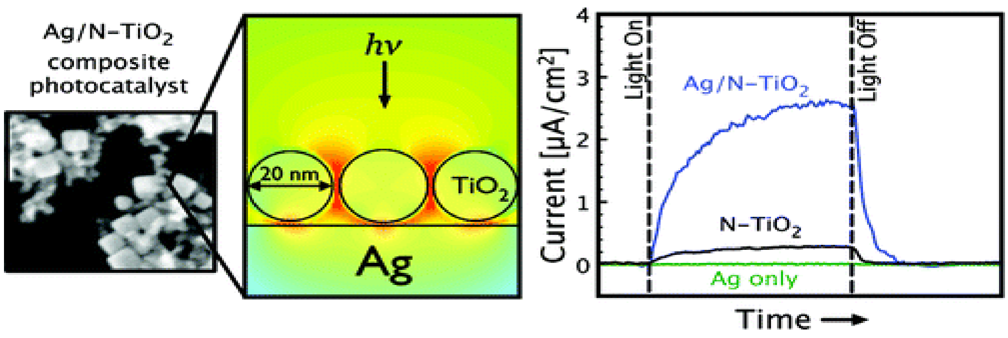

Figure 1.24. Illustration of the Ag/N-TiO_2 nanocomposites photoanode used for the measurement of the photocurrent density curve.(Ingram and Linic, 2011)

1.14.7 Au Nanostructure-Decorated TiO_2 Nanowires

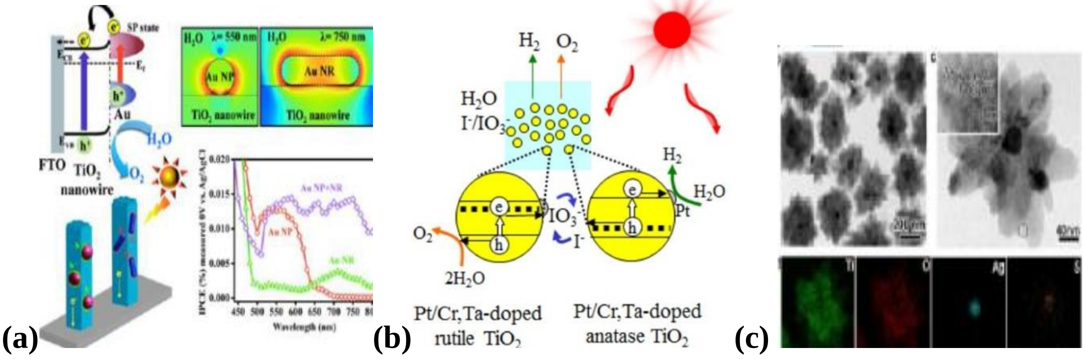

Figure 1.25 (a) TiO_2 nanowire- decorated with Au NP and Au NR and their respective UV-visible absorbance plot(b) electronic transition for the Z-scheme system with Pt/Cr, Ta doped -rutile (O_2) and -anatase (H_2) TiO_2 system and (c) TEM images along with elemental mapping of Au NPs and NRs -TiO_2. (Pu et al., 2013)

(Pu et al., 2013) demonstrated that the photoactivity of Au NPs and NRs -decorated TiO_2 electrodes were used for photo electrochemical water oxidation in the entire UV−visible region from 300 to 800 nm. The samples with Au nanoparticles (NPs), Au nanorods (NRs), and a mixture of Au NPs and NRs were deposited on the surface of TiO_2 nanowire arrays along with bare TiO_2. And it is found that the bare TiO_2, Au NP decorated TiO_2 nanowire electrodes exhibited significantly enhanced photoactivity in both the UV and visible regions of sunlight. Mixture of Au NPs and NRs-decorated TiO_2 electrodes showed the maximum photoactivity enhancement was, however, observed in the visible region only (maximum at 710 nm). Monochromatic incident photon-to-electron conversion efficiency (IPEC) measurements indicated that the excitation of surface plasmon resonance of Au is responsible for the enhanced photoactivity. The work could provide a insight view for designing an appropriate plasmonic metal/semiconductor composite systems to harvest the entire UV−visible light for solar fuel production.

1.14.8 Quantum Dot CdTe Monolayer Sensitized ZnO Nanowire

One-dimensional nanostructures of ZnO offer the additional potential advantage of improved charge transport when they were associated with the zero-dimensional nanostructures (quantum dots; CdTe) such as nanocrystals. (Chen et al., 2010) The electron donors, or hole scavengers such as sulfide ions or selenium ions, photogenerated holes irreversibly oxidize the reductant rather than the water. Use of CdTe QDs is advantageous due to more favourable conduction band energy (ECB=-1.0 V vs. NHE) that can inject electrons into ZnO faster than CdSe (ECB= -0.6 V vs. NHE). Monolayer of CdTe QDs deposited on the surface of ZnO nanowires would further improve the stability of the system in electrochemical reactions of course by avoiding anodic decomposition/ corrosion of CdTe, result in enhancing the overall water splitting performance.

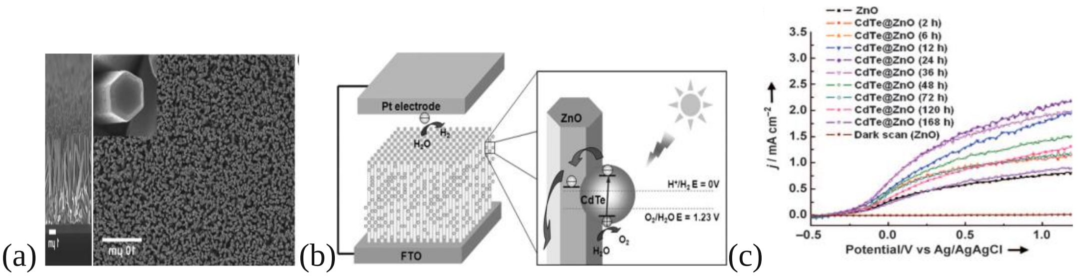

Figure 1.26. (a) SEM images of quantum dots CdTe loaded ZnO nanowires on FTO substrate (cross sectional and topical view), (b) schematics of the photocatalytic water splitting and CdTe QDs loaded ZnO nanowires under irradiation sunlight and (c) current density-voltage plots for different composition of CdTe loaded ZnO nanowires after different deposition time. (Chen et al., 2010)

1.15 Summary

In this chapter we discuss the current energy status and its future perspectives. Water and solar are established as a good renewable sources of energy. And by using artificial photosynthesis process we discussed water splitting phenomenon for hydrogen production using large number of photocatalyst. Out of these different type of photocatalysts we focused on plasmonic nanocomposite Ag/AgX@ZnO photocatalyst made of Ag, AgX (X= Cl, CO_3^{-2}, PO_4^{-3}, NO_3^-, SO_3^{2-}) and ZnO by using microwave and conventional single pot refluxing method. After characterisation we used these photocatalytic material for hydrogen production via water splitting. These systems discussed in detail in Chapter 3.

1.16 Reference

1. Adleman J.R., Boyd D.A., Goodwin D.G., Psaltis D., "Heterogenous catalysis mediated by Plasmon heating" Nano Lett. (2009), 9: 4417-23.
2. Alvi N. ul H., Eduardo P., Rodriguez D.S., "InN/InGaN quantum dot photo electrode: Efficient hydrogen generation by water splitting at zero voltage" Nano Energy (2015), 13: 291-97.
3. Anpo M., Yamashita H., Ichihashi Y., Ehara S., "Photocatalytic reduction of CO_2 with H_2O on various titaniunm oxide catalysts" J. Electroanal. Chem. (1995), 396:21-6.
4. Ashok Kumar M., "An overview of semiconductor particulate system for photo production of hydrogen" Int. J. Hydrogen Energy (1998), 23:427−38.
5. Atwater H.A., "The promises of plasomonics" Sci. Am. (2007), 296(4): 56-63.
6. Awazu K., Fujimaki M., Rockstuhl C., "A plasmonic photo catalyst consisting of silver nanoparticles embedded in titanium dioxide" J. Am. Chem. Soc. (2008), 130: 1676-80.
7. Barber I.J., "Photosynthetic energy conversion: Natural and artificial" Chem. Soc. Rev. (2009), 38:185-96.
8. Barnes W., Dereux L.A., Wbbesen T.W., "Surface plasmon subwave length optics Nature" (2003), 424: 824-30.
9. Bochin V.P., Fridman A. A, Egasov V.A.L, Rusanov V.D., Sholin G.V., "Hydrogen Energy Systems" (eds T.N. Veziroglu and W. Seifritz), Vol.3. London, UK: Pergamon Press, (1978), pp. 1183.
10. Bockris J.O.M., Dandapani B., Cocke D., Ghorogchian J., "On the splitting of water" Int. J. Hudrogen Energy (1985), 10: 179-201.
11. Bredas J.L., Silbey R., Boudreux D.S. and Chance R.R., 'Chain-length dependence of electronic and electrochemical properties of conjugated systems: polyacetylene, polyphenylene, polythiophene, and polypyrrole" J. Am. Chem. Soc. (1983), 105: 6555.
12. Bubnova, O., Khan Z.U., Wang H. et al., "Semi-metallic polymer". Nat. Mat., (2014), 13: 190-94.

13. Burns G. “Solid State Physics” New York, NY: Academic Press, (1985), Inc. pp. 339-40.

14. Califano M., Zunger A., Franceschetti A., “Direct carrier multiplication due to inverse Auger scattering in CdSe quantum dots” Appl. Phys. Lett. (2004), 84(13): 2409
15. Califano M., Zunger A., Franceschetti A., “Efficient inverse Auger recombination at threshold in CdSe nanocrystals” Nano Lett. (2004), 4(3): 525.
16. Chen H. M., Chen C. K., Chang Y.C., Tsai C.W., Liu R.S., Hu S.F., Chang W.S. Chen KH., “Quantum Dot Monolayer Sensitized ZnO Nanowire-Array Photo electrodes: True Efficiency for Water Splitting” Angewandte Chemie. Int. Ed. (2010), 49: 5966 –69.
17. Chen H.M., Chen C.K., Chen C.J. Cheng L.C., Wu P.C., Cheng B.H., Ming Y.Z., Tseng L., Hsu Y.Y., Chan T.S., Lee J.F., Liu R.S., Tsai D.P., “Plasmon Inducing Effects for Enhanced Photoelectrochemical Water Splitting: X-ray Absorption Approach to Electronic Structures” ACS Nano (2012), 6(8): 7362–72.
18. Chen J., Wu F., “Review of hydrogen storage in inorganic fullerene-like nanotubes” Appl. Phys. A (2004), 78: 989-94.
19. Chen X., Zhuo H., Zheng Z., Gao X., “Visible-light-driven oxidation of organic contaminants in air with gold nanoparticle catalysts on oxide supports” Angew. Chem. Int. Edn. Engl. (2008), 47: 5353-56
20. Cheng, K.W., Wang S.C., “Efffects of complex agents on the physical properties of Ag-In-S ternary semiconductor films using chemical bath deposition” Mat. Chem. Phys. (2009), 115: 14-20.
21. Chouhan N., Liu R.S. Zhang, J., “Photochemical Water Splitting: Materials and Applications; Series Name: Electrochemical Energy Storage and Conversion” Series Editor: Jiujun Zhang, CRC Press, Taylor & Francis Group, Florida-USA, (2017), pp: 358.

22. Christopher P., Xin H., Linic S., “Visible light enhanced catalytic oxidation reactions on plasmonic silver nanostructures” Nature Chem. (2011), 3: 467-72.
23. Cogdell, R.J., Brotosudarmo T.H.P., Gardiner A.T., Sanchez P.M., Cronin L., “Artificial photosynthesis-solar fuels: Current status and future prospects” Biofuels (2010), 1(6): 861-76.

24. Coley G.D., Field J.E., “Role of Cavities in the Initiation and Growth of Explosions in Liquids.” Proeedings of the. Royal Society of London Series A, (1973), 335 (1600): 67-86.
25. Coropceanu V., Cornil J., da Silva Filho D.A., Olivier Y., Silbey R. and Brédas, J.L., “Charge transport in organic semiconductors” Chemical reviews, (2007),107(4):.926-952.
26. Coward H.F., Jones G.W., “Limits of Flammability of Gases and Vapours” Bureau of Mines Bulletin (1952), 503: N70-74476; AD-701575.
27. Derwent, R., Simmonds P., Doherty S. O’, Manning A., Collins W., Stevenson D., “Global environmental impacts of the hydrogen economy” In. J. Nucl. Hydrogen Prod. Appl. (2006), 1(1): 57-67.
28. Deutsch T., Turner J., Wang H., Dinh H., “Annual Progress Report, National Renewable Energy Laboratory” (NREL), accessed 9 July, (2013), pp. II-70-II-74.
29. Dillon A.C., Jones K.M., Bekkedhal T.A., Kiang C.H., Bethune D.S., Heben M. J., “Letters to nature. Storage of hydrogen in single wall carbon nanotubes” Nature (1997), 386: 377-79.
30. Dong C.L., Persson C., Vbayssieres L. et al., “Electronic structure of nanostructured ZnO from x-ray absorption and emission spectroscopy and the local density approximation’ Phys. Rev. B (2004), 70: 195325.
31. Edwards P.P., Kuznetsov V.L., David W.I.F., “Hydrogen energy” Phil. Trans. R. Soc. A (2007), 365: 1043–1056.
32. Ellingson R.J. Beard M.C., Johnson J.C., “Highly efficient multiple excition generation in colloidal PbSe and PbS Quantum dots” Nano Lett. (2005), 5: 865.
33. Energy Information Administration. International Energy Outlook. Washington, DC, EIA. (2003), 1605.
34. Fujishima A., Honda K., “Electrochemical photolysis of water at a semiconductor electrode” Nature (1972), 238:37-38.
35. Gary H., “Solar fuel II: The quest for catalysts” Eng. Sci. (2008), 46: 26-31.
36. Givotov V.K., Fridman A.A., Frotov M.F., “Plasmochemical methods of hydrogen production” Int. J. Hydrogen Energy (1981), 6:441-49.
37. GM. Fuel cell technology: Prospects, Promises and Challenges. (2007).

38. Hairston D., “Hail hydrogen” Chem. Eng. (1996), 103: 59.
39. Hashimoto K., Irie H., Fujishima A., “TiO_2 photo catalysis: A historical overview and future prospects. Japan” J. Appl. Phys. (2005), 44: 8269.
40. Hensen E., Sanden R. van de., “Solar Fuels: The Scientific Challenges” Eindhoiven, the Naterlands: University of Technology. (2014).
41. Herrmann J.M., “Hetrogeneous photo catalysis: State of the art and present application” Top. Catal. (2005), 34: 49-65.
42. Hirano S., Young K.S., Kwqabena A., Schwarz J.A., “The high surface area activated carbon hydrogen storage system. In: Proceedings of the First International Conference on New Energy Systems and Conversions” Frontiers Science Series No.7, June (1993), pp. 67-72.
43. Hori Y., Murata A., Kikuchi K., Suzuki S., “Electrochemical reduction of carbon dioxides to carbon monoxide at a gold electrode in aqueous potassium hydrogen carbonate” J. Chem. Sco. Chem. Commun. (1987), 728-9.
44. Hubbert M.K., “The energy resources of the Earth” Sci. Am. (1971), 225:60-70.
45. Hubbert M.K., “Nuclear Energy and Fossil Fuels” Paper presented before the spring meeting of the Southem District Division of Production, American petroleum Institute Plaza Hotel, (1956), 95: 22-27.
46. Ingram D.B., Linic S., “Water Splitting on Composite Plasmonic-Metal/Semiconductor Photo electrodes: Evidence for Selective Plasmon-Induced Formation of Charge Carriers near the Semiconductor Surface” J. Am. Chem. Soc., (2011), 133 (14): 5202–05.
47. Iwase A., Ng Y.H., Ishiguro Y., Kudo A. and Amal R., “Reduced Graphene Oxide as a Solid-State Electron Mediator in Z-Scheme Photocatalytic Water Splitting under Visible Light” J. Am. Chem. Soc. (2011),133(29): 11054-57.
48. Jiang J.D., Sun Z., Jia H., Lu D., Du P., “A cocatalyst-free CdSnanorod/ZnS nanoparticle composite for high performance visible-light-driven hydrogen production from water” Mater. Chem. A Mater. Energy Sustain. (2016), 4: 675-83.
49. Jiang L., Neill B.C.O., “The energy transition in rural China” Int. J. Global Energy (2004), 21(1-2): 2-26

50. Jones L.W., “Toward a liquid hydrogen fuel economy” Presented at the University of Michigan Environmental Action for Survival Teach In. Ann Arbor, MI: University of Michigan, (1970).
51. Kamat P.V. Manipulation of Charge Transfer Across Semiconductor Interface. A Criterion that Cannot Be Ignored in Photocatalyst Design. J. Phys. Chem. Lett. (2012),3(5): 663−72.
52. Kamat P.V., “Quantum dot solar cells. Semiconductor nanocrystals as light harvester” J. Phys. Chem. C (2008), 112: 18737.
53. Kelly K.L., Coronado E., Zhao L.L., Schatz G.C., “The optical properties of metal nanoparticles: The influence of size, shape and dielectric environment” J. Phys. Chem. B (2003), 107: 668-77.
54. Kim K., Kim M.J., Kim S.I, Jang J.H., “Towards visible light hydrogen generation: Quantum dot-sensitization via efficient light harvesting of hybrid-TiO_2” Sci. Rep. (2013), 3: 3330.
55. Kittel C., “Indroduction to Solid State Physics” New York, NY: Wiley, (1996).
56. Knupfer M., “Exciton binding energies in organic semiconductors” Applied Physics A: Materials Science & Processing (2003), 7(5): 623–26.
57. Ktreuter W., Hofmann H., “Electrolysis: The important energy transformer in a world of sustainable energy” Int. J. Hydrogen Energy (1988), 23 (8) :661-66.
58. Kudo A., Kato H., Tsuji I., “Strategies for the development of visible-light-driven photocatalysts for water splitting” Chem. Lett. (2004), 33:1534-39.
59. Li Z., Cui X., Hao H., Lu M., Lin Y., “Enhanced photo electrochemical water splitting from Si quantum dots/TiO_2 nanotube arrays composite elecrtrodes” Mater. Res. Bull. (2015), 66: 9-15.
60. Linic S., Christopher P., Ingram D.B., “Plasmonicmetal nanostructures for efficient conversion of solar to chemical energy” Nat. Mater. (2011), 10: 911-21.
61. Maeda K., Domen K., “New non-oxide photo catalysts designed for overall water splitting under visible light” J. Phys. Chem. C (2007), 111: 7851-61.
62. Maeda, K., “Photocatalytic water splitting using semiconductor particles: History and recent developments” J. Photochem. Photobiol. C (2011), 12: 237-68.
63. Mauna Loa Observatory in Hawaii, NOAA-ESRL), (2018).

64. McCarty R.D., Hord J., Roder H.M., “Selected Properties of Hydrogen” (Engineering Design Data) NBS Monograph 168, National Bureau of Standards, Boulder, CO. (1981).
65. Mori K., Yamashitaand H., Anpo, M., “Photocatalytic reduction of CO_2 with H_2O on various titanium oxide photocatalysts” RSC Adv. (2012), 2: 3165-72.
66. Mott N.F., “Conduction in polar crystals. 2. The conduction band and ultra-violrt absorption of alkali-halide crystals” Trans. Farad. Soc. (1938), 34: 500-506.
67. Mubeen S., Hernandez-Sosa G., Moses D., Lee J., Moskovits M., “Plasmonic photosensitization of a wide band gap semiconductor: converting plasmons to chargecarriers” Nano Lett. (2011), 11: 5548-52.
68. Murphy J.E., Beard M.C., Norman A.G., “PbTe colloidal nanocrystals: Synthesis, characterization, and multiple exciton generation” J. Am, Chem. Soc. (2006), 128: 3241.
69. Nakato Y., Ohnishi T., Tsubomura H., “Photo-electrochemical behaviours of semiconductor electrodes coated with thin metal films” Chem. Lett. (1975), 4: 883-92.
70. Nakato Y., Tsubormura H., “Structures and functions of thin metal layers on semiconductor electrodes” J. Photo Chem. (1985), 29(1-3): 257-66.
71. Nam S.S., Kishan G., Lee M.W., Choi M.J., Lee K.W., “Effect of lanthanum loading in Fe-K/La/$A1_2O_3$ catalyst for CO_2 hydrogenation to hydrocarbons” Appl. Organometallic Chem. (2000), 14: 794-98.
72. Nann T., Ibrahim S.K., Woi P.M., Xu S., Ziegler C.J., Pickett J., “Water splitting by visible light: A nano-photocathode for hydrogen production” Angew. Chem. Inter. Ed. (2010), 49: 1574-77.
73. Neagu C., Jansen H., Gratrdeniers H., Elwenspock M., “The electrolysis of water: An actuation principle for MEMS with a big opportunity” Mechatronics. (2000), 10 (4-5) :571-81.
74. Newton E., Haletter T.H., Hottinger P., Roth F. VonSchetter W.H., Schuan T.H., “Seasonal storage of hydrogen in stationary systems with liquid organic hydrides” Int. J. Hydrogen Energy (1998), 23(10): 904-09.
75. Nezhad H. "Software Tools for Managing Project Risk: Management Concepts. Vienna, VA” Management Concepts (2007), 1037-55.

76. Nezhad H. "World Energy Scenarios to 2050: Issues and Options. Minnesota" MN: State University of Minneapolis (2009).

77. Niitsoo O., SarkarS. K., Pejoux C., "Chemical bath deposited CdS/CdSe sensitized porous TiO_2 solar cells" J. Photo Chem. Photo Bio. A (2006), 181: 306.
78. Nozik A.J., "Spectroscopy and hot electron relaxation dynamics in semiconductor quantum wells and quantum dots" Annual Rev. Phys. Chem. (2001), 52: 193.
79. Oak Ridge National Laboratory, carbon dioxide information analysis center.
80. Osterloh F.E. and Parkinson B.A., "Recent developments in solar water-splitting photo catalysis" MRS. Bull. (2011), 36: 17-22.
81. Osterloh F.E., "Inorganic materials as catalysts for photochemical splitting of water" Chem. Mater, (2008), 20:35-54.
82. Perry T.R., "Washington, DC: U.S. Patent and Trademark Office" (1969), U.S. Patent No. 3,436,611.

83. Pleskov Y.Y.; Gurevich, Y.V., "Semiconductor photoelectrochemistry" Consultants Bureau: New York, (1986), pp 422 and b Kim, Y.I.; Atherton, S.J.; Brigham, E.S.; Mallouk, T.E.J. Phys. Chem. (1993), 97 (45): 11802–10.
84. Pope M., Swenberg C.E., "Electronic processes in organic solids" Annual Review of Physical Chemistry (1984), 35(1): 613-655.

85. Primo A., Corma A., Garcia H., "Titania supported gold nanoparticles as photo catalyst" Phys. Chem. Chem. Phys. (2011), 13: 886-910.
86. Primo A., Marino T., Corma A., Molinari R., García H., "Efficient Visible-Light Photocatalytic Water Splitting by Minute Amounts of Gold Supported on Nanoparticulate CeO_2 obtained by a Biopolymer Templating Method" J. Am. Chem. Soc. (2011),133 (18): 6930–33.
87. Pu Y.C., Wang G., Chang K.D., Ling Y., Lin Y.K., Fitzmorris B.C., Liu C.M., Lu X., Tong Y., Zhang J.Z., Hsu Y.J., Li Y., "Au Nanostructure-Decorated TiO_2 Nanowires Exhibiting Photoactivity Across Entire UV-visible Region for Photoelectrochemical Water Splitting" Nano Lett. (2013), 13: 3817−23.
88. Rahlwes H., Teske R.S., Wijnhoven J., Energy [R] evolution: "A sustainable Netherlands energy outlook" Report 2013 Netherlands energy scenario. Utrecht, the Netherland: Utrecht University Repository. (2013).

89. Rajeshwar K., “Hydrogen generation at irradiated oxide semiconductor-solution interfaces” J. Appl. Electrochem. (2007), 37: 765-87.
90. Rogner H.H., “United Nations Development World Energy Assessment” United Nations, Geneva, (2004), pp: 162.
91. Ruhl C., Appleby P., Fennema, J., Naumov, A. Schaffer M.E., “Economic development and the demand for energy: A historical perspective on the next 20 years” Energy Policy (2012),50: 109-16.
92. Ruijven B. Van, Lamarque J.F., Vuuren D.P. van “Emission scenarios for a global hydrogen economy and the consequences for global air pollution” Glob. Environ. Chang. (2011), 21: 983-94.
93. Schaller R.D., Klimov V.I., “High efficiency carrier multiplication in PbSe nano-crystals: Implications for solar energy conversion” Phys. Rev. Lett. (2004), 92(18): 186601.
94. Schaller R.D., Sykora M., Pietryga J.M., Klimov V.I., “Seven excitons at a cost of one: Redefininh the limits for conversion efficiency of photons into charge carriers” Nano Lett. (2006), 6:424.
95. Schlaphach L., Zuttel A., “Hydrogen-stroage materials for mobile applications” Nature (2001), 141: 353-54.
96. Schmitt M.L, Shelby J.E., Hall M.M., “Preparation of hollow glass microspheres from sol-gel derived glass for application in hydrogen gas storage” J. Non Crystalline Solids. (2006), 352:626-31.
97. Scibioh M.A. Vishwanathan B., “Electrochemical reduction of carbon dioxide: A status report” Proc. Indn. Natl. Acad. Sci. (2004), 70 A (3): 407-62.
98. Shaukatali N.I., Inngole P.P., Haram, S.K., “Determination of band structure parameters and the quasi-paraticle gap of CdSe quantum dots by cyclic voltammetry” Chem. Phys. Chem. (2008), 9: 2574-79.
99. Shaukatali N. Inamdar, Pravin P., Ingole, and Santosh K. Haram, “Determination of Band Structure Parameters and the Quasi-Particle Gap of CdSe Quantum Dots by Cyclic Voltammetry” Chem. Phys. Chem. (2008), 9: 2574 – 79.
100. Sheikh A., Yengantiwar A., Deo M., Kelkar S., Ogale S.C., “Near-field plasmonic functionalization of light harvesting oxide-oxide heterojunctions for efficient solar

photo electrochemical water splitting: The AuNP/$ZnFe_2O_4$/ZnO system" Small (2013), 9(12): 2091-96.

101. Shell V., "Lighthouse for Hydrogen" Shell. (2004).
102. Shing P., Harbola M.K., Sanyal B., Mookerjee A., "Accurate determination of bad gaps within density functional formalism" Phys. Rev. B (2013), 87:235110.
103. Sivul K., "Metal Oxide Photo-electrodes for Solar Fuel Production, Surface Traps, and Catalysis" J. Phys. Chem. Lett. (2013), 4 (2013): 1624−33.)
104. Size S.M., "Physics of Semiconductor Devices" 2nd edition Awiley Inter-science John wiley and Sons (1981), pp 33-37.
105. Sorensen B., "Energy and resources" Science (1975), 189: 255-60.
106. Su F., Lu J., Tian Y., Ma X., Gong J., "Branched TiO_2 nano arrays sensitized with CdS quantum dots for highly efficient photo electrochemical water splitting" Phys. Chem. Chem. Phys. (2013), 15: 12026-32.
107. Sullivan, B.P., "Reduction of carbon dioxide with platinum metals electro catalysts: A potentially important route for the future production of fuels and chemicals" Platin. Met. Rev. (1989), 33(1): 2-9.
108. Sun S., Wang W., Zhang L., Shang M., Whag L., "Ag@C cote/shell nanocomposite as highly efficient plasmonic photo catalyst" Catal. Commun. (2009), 11: 290-93.
109. Takata T., Tanaka A., Hara M., Kondo J.N., Domen K., "Recent progress of photocatalysts for overall water splitting" Catal. Today (1998), 44:17−26.
110. Tauc J., Menth A., "States in the gap" J Non-Cryst. Solids. (1972), 569:8-10.
111. Thimsen E., Formal F. Le, Gratzel M, Warren S.C., "Influence of plasmonic Au nanoparticles on the photoactivity of Fe_2O_3 electrodes for water splitting" Nano Lett. (2011), 11: 35-43.
112. Thomann I., Pinaud B.A., Chen Z., Lemens B.M.C., Jaramillo T.F., Bronggersma M.L., "Plasmon enhanced solar-to-fuel energy conversion" Nano Lett. (2011), 11: 3440-46.
113. Trevisan R., Rodena P., Pedro V.G., "Harnessing infrared photons for photo electrochemical hydrogen generation. A PbS quantum dot based "quasi-artificial leaf". J. Phys. Chem. Lett. (2013), 4(1): 141-46.

114. Trimoto T., Horibe H., Ameyama T.K., "Plasmon-enchanced photocatalytic activity of cadmium sulfide nanoparticles immobilized on silica-coated gold particles" J. Phys. Chem. Lett. (2011), 2: 2057-62.
115. Turner J., Sverdrup G., Mann M.K., et al., "Renewable hydrogen production" Int. J. Energy Res. (2008), 32(5): 379-407.
116. U.S. Environmental protection agency light-duty automotive technology carbon dioxide emissions and fuel economy trend 1975 through 2012, March 2013.
117. Walter M.G., Warren E.L., McKone J.R., "Solar water splitting cell" Chem. Rev. (2010), 110: 6446-73
118. Wang B., Kanhere P., Chen Z., Nisar J., Pathak B., Ahuja R., "Anion-doped $NaTaO_3$ for visible light photocatalysis" J. Phys. Chem. C (2013), 117: 22518-24
119. Wang H.Y., Wang G.M., Ling Y.C., "Photochemical study of oxygen deficient TiO_2 nanowire arrays with CdS quantum dot sensitization" Nanoscale (2012), 4: 1463-66.
120. Wang L.G., Pennycook S.J., Pantelides S.T., "The role of the Nanoscale in surface reactions: CO_2 on CdSe" Phys. Rev. Lett. (2002), 89(7): 075506.
121. Wang L.W., Califano M., Zunger A., Franceschetti A., "Pseudopotential theory of auger processes in CdSe quantum dots. Phys. Rev. Lett. (2003), 91(5): 0564047.
122. Wang M., Shang X., Yu X., "Graphene-CdS quantum dots-poly oxometalatc composite films for efficient photo electrochemical water splitting and pollutant degradation" Phys. Chem. Chem. Phys. (2014), 16(47): 26016-23.
123. Wang Q., Hisatomi T., Jia Q., Tokudome H., Zhong M., Wang C., Pan Z., Takata T., Nakabayashi M., Shibata N., "Scalable water splitting on particulate photocatalyst sheets with a solar-to-hydrogen energy conversion efficiency exceeding" Nature Mater. (2016), 15: 611-15.
124. Wang X., Liu G., Lu G.Q., Cheng H.M., "Stable photocatalytic hydrogen evolution from water over ZnO–CdS core–shell nanorods" International Journal of Hydrogen Energy (2010), 35:8199 – 205.
125. Wannier G. H., "The structure of electronic excitation levels in insulating crystals" Phys. Rev. (1937), 52(3): 191.
126. Wu F., Hu X., Fan J., Liu E., Sun T., Kang L., Hou W., Zhu C., Liu H., "Photocatalytic Activity of Ag/TiO_2 Nanotube Arrays Enhanced by Surface

Plasmon Resonance and Application in Hydrogen Evolution by Water Splitting" Plasmonics (2013), 8:501–08.

127. Wu Z.C., Zhang Y., Tao T.X., Zhang L., Fong H., "Silver nanoparticles on amidaximefibers for photocatalytic degradation of organic dyes in waste water" Appl. Sci., (2010), 257: 1092-97.

128. Yamashita H., Fujii Y., Ichihashi Y. et al., "Selective formation of CH_3OH in the photo- catalytic reduction of CO_2 with H_2O on titanium oxides highly dispersed within zeolites and mesoporous molecular sieves" Catal. Today (1998),45: 221-27.

129. Yang H.B., Miao J., Hung S.F., Huo G., Chen H.M., Liu B., "Stable quantum dot photo electrolysis cell for unassisted visible light solar water splitting" ACS Nano (2014), 8(10): 10403-413.

130. Yeh T.F., Teng C.Y., Chen S.J., Teng H., "Nitrogen-doped grapheme oxide quantum dots as photo catalysts for overall water-splitting under visible light illumination" Adv. Mater. (2014), 26(20): 3297-303.

131. Yu J., Dai G., Huang B., "Fabrication and characterization of visible light driven plasmonic photo catalyst Ag/AgCl/TiO_2 nanotube arrays" J. Phys. Chem. C (2009), 113:16394-40.

132. Yue X., Yi S., Wang R., Zhang Z. and Qiu S., "Cadmium Sulfide and Nickel Synergetic Co-Catalysts Supported on Graphitic Carbon Nitride for Visible-Light-Driven Photocatalytic Hydrogen Evolution" Sci. Rep. (2016), 6: 22268:1-9.

133. Yuksel I., "Global warming and renewable energy sources for sustainable developments in Trukey" Renewable Energy (2008), 33(4): 802-12.

134. Zhang G., Lan Z-A., Lin L., Lin S., Wang X. "Overall water splitting by Pt/g-C_3N_4 photo catalysts without using sacrificial agents" Chem. Sci., (2016), 7: 3062–66.

135. Zhang N, Shi J., Mao S.S., Guo L., "Co_3O_4 quantum dots: Reverse micelle thesis and visible light driven photocatytic overall water splitting" Chem. Commun (2014), 65401.

136. Zhang X., Chen Y. L., Liu R.S, Tsai D.P., "Plasmonic photo catalysis" Rep. Phys. (2013), 76:046401.

137. Zhdanov V. P., Haggland C., Kasemo B., "Relaxation of plasmons in non-siged metal particles located on or embedded in an amorphous semiconductor" Surf. Sci. (2005), 599: L372-75.

138. Zhou H., Mazumdar S., “Electron-electron interaction effects on the optical excitations of semiconducting single-walled carbon nanotubes” Phys. Rev. Lett. (2004), 93: 157402.

Chapter-2

Instrumentation

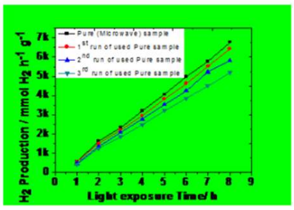

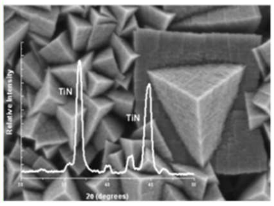

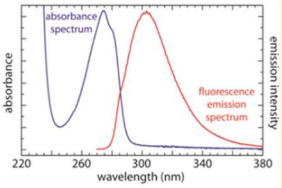

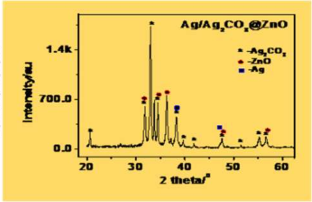

ABSTRACT

This chapter explains the elementary instrumentation knowledge and their usages in our studies. It describes the various analytical techniques, which was utilized for analyses of the samples and water splitting application of the as-synthesized nanophotocatalysts. This chapter also describes the basic theories and main working principles behind the important characterization tools i.e. XRD, FTIR, UV-Vis spectrophotometr Specrofluorimeter, ATR, microwave synthesizer, electron microscopy, centrifuge, digital pH meter, water splitting assembly, GC with TCD, etc that were used for investigation.

2.1. Instrumental techniques

This part of the thesis describes various major instrumental techniques such as UV-VIS spectrophotometer, X ray diffractometer, FTIR spectrophotometer, SEM, EDX, TEM, etc. along with other minor analytical techniques had been adopted to study the various properties such as phase purity, crystallinity, optical properties, bonding, functional groups, shape, size, surface morphology, elemental composition and binding energy of the as prepared nanocatalysts.

2.1.1. Ultraviolet -Visible Spectrophotometer

Ultraviolet-visible (UV-Vis) Spectroscopy is an ideal technique for determining the electronic transition in different levels that used for calculating the band gap and particle size of both organic and inorganic materials. Double beam UV-Vis analyses of the samples can be performed on samples either dispersed in a solvent or embedded in the insulating solid matrix with $BaCl_2$. Existence of the surface plasmon resonance (SPR) effect of the nanometal particles can be traced for the nanocomposite with Ag nanoparticle. Surface plasmon resonance is related to the light waves that are trapped on the metal surface due to the interaction of electrons with light, resulted hot electrons at metal surface (Brans et al., 2003) in presence of the supporting material ZnO/AgCl.

The UV-Vis spectrum of metal nanoparticles embedded in dielectric media used to reveal the characteristic absorption peaks at a specific wavelength depending upon the nature of substance, its matrix, shape of the particles and their distribution (Bullen and Mulvaney, 2006; Templeton, 2000; Strelow, 1994) in lattice/surface. Furthermore, the observed optical properties are size-dependent and observed in the nano and atomic range, resulted in the peak broadening or shifting in the absorption wavelength. The excitation in such higher order modes can be explained by the homogeneous polarization phenomena of the nanoparticles in the electromagnetic field of light that intract with the nanoparticles of different size compatible to the wavelength of the incoming light radiation (Kreibig and Vollmer, 1995).

For the present work UV-Vis absorption spectra were analyzed by using (LABINDIA UV- Visible 3000+) spectrophotometer situated at the Department of Pure & Applied Chemistry, University of Kota, Kota (Raj.) by using the quartz cuvette of light path length 1.0 cm and 5cm height. The compound was dissolved in methanol before place in cuvette.

Possible electronic transitions of π, σ and n electrons due to light absorption are:

(1) The energy required for the excitation of an electron from the bonding s orbital to the corresponding antibonding orbital, is quite large. For example, methane with C-H bonds, can undergo $\sigma \rightarrow \sigma^*$ transitions that show an absorbance maximum at 125 nm. But the absorption maxima due to $\sigma \rightarrow \sigma^*$ transitions are not for our samples.

(2) Saturated samples with lone pairs (non-bonding electrons) are capable of transition $n \rightarrow \sigma^*$ transitions, which required the energy less than $\sigma \rightarrow \sigma^*$ transitions and need light energy of wavelength ranging in 150-250 nm. The number of organic functional groups, which has $n \rightarrow \sigma^*$ transition peaks in the UV region are low.

(3) Most of organic compounds show transitions: n or π electrons to the n* excited state in absorption spectroscopy because the absorption peaks for above transitions fall in a convenient experimental region of the spectrum (200-700 nm). molecule (having unsaturated group) with π electrons are suitable for these transitions. Molar absorbance for $n \rightarrow n^*$ transitions are quite low, found in the range from 10 to 100 L $Mol^{-1}cm^{-1}$. Where, $\pi \rightarrow n^*$ transitions normally give molar absorbance between 1000 and 10,000 L $Mol^{-1}cm^{-1}$.

2.1.2. X-RAY Diffraction

X-ray diffraction was performed on well grind powder samples using the X-ray diffractometer (PANalytical system diffractometer; Model: *XPERT-3*) with Nickel filter for K_β radiation. X-Ray diffraction patterns were recorded for the 2θ angle = 20° to 90° with a using Cu K_α (λ=1.542Å) radiation with an accelerating 40 KV voltage. Experimental data were collected at the scanning rate of 1°/min. The K_α doublets were well resolved with Ge filter. From XRD, the crystallite particle size of the sample can be measured by using the following Scherer's formula,

$$P = 0.9\ \lambda / \beta \cos \theta$$

Where:

P = Crystallite size in nm

λ = Wavelength of X ray (1.540 nm),

β = Full maxima half width in degree,

θ= Diffraction angle in degree

Figure 2.1 PANalytical system diffractometer (Model: *XPERT-3*)

And, it was found that the crystallite size of the nanostructure sample measured by Scherer's formula is similar to the value determined by the another instrument i.e. particle size analyzer.

2.1.3. Fourier Transform Infrared (FTIR) Spectrophotometer

FTIR is a technique based on the principle that the most of the molecules absorb the infra-red region of the electromagnetic spectrum of light in the wave numbers over the range 4000–600 cm^{-1}. These absorptions correspond to the specific bonds present in the molecule which vibrates in a particular mode (inter-atomic bond vibration in stretching or bending mode). When IR radiation passing through a sample, then an infrared spectrum is obtained depending upon the factor, which fraction of the incident radiation was absorbed by a particular system. The energy of peak in an IR spectrum matches to the vibration frequency of a sample molecule (Stuart and Ando, 1996). In IR spectrum, the frequencies of the infrared radiation absorbed (peaks or signals) can be directly correlated to the bonds present in the compound due to inter-atomic bond vibration in different motions (stretching or bending) therefore one individual bond may absorb at more than one IR frequency. Usually stretching absorptions produce stronger peaks than bending absorption. However, these weaker bending absorptions are useful in discriminating the similar types of bonds mostly for aromatic substitution.

Attenuated total Reflectance FTIR (ATR-FTIR) technique used to study the surface of materials. It is a modified version of FTIR, in which IR radiations are not transmitted through the sample but reflected by the sample. Consequently, a specimen is not placed between two IR windows, but against an IR crystal (ZnSe, diamond or Ge). ATR requires very little or no sample preparation for the most samples and is one of the most versatile sample analysis technique (Settle, 1997). It is used for observing IR spectra of difficult samples, which cannot be readily examined by the normal transmission method, such as thick or highly absorbing solid and liquid materials such as: powders, films, coatings, adhesive, polymers, threads, and dense aqueous samples. During analysis process, the analysing sample was pressed into the optical contacts with the top surface of the IR crystal. Here, we record FTIR spectra in diffuse reflectance mode using FTIR spectrophotometer (Bruker- model Tensor -27 Model), located at Department of Pure & Applied Chemistry, University of Kota, Kota (Raj.) The FT-IR spectrum was recorded in the range of 400-4000 cm^{-1} by mixing the sample with dried KBr (in 1: 20 weight ratio) with a resolution of 4 cm^{-1}. The powder sample was placed on a sample holder and the spectrum was recorded.

Figure 2.2 Bruker -Tensor FT-IR Spectrophotometer

2.1.4. Scanning Electron Microscopy (SEM)

The Scanning electron microscope (SEM) is an advance version of optical microscope with higher and better magnification and resolution that can be used to produce the high resolution surface morphological images of sample’s surface. far superior to optical systems. The main principle of SEM is focused on the interaction of an accelerated electron’s beam (which carry extra kinetic energy) with the specimen (Grundy and Jones, 1976). Due to the excess energy of electron that decelerated in the solid sample and give a variety of signals produced surface image of the sample and is found useful for judging the surface structure of the sample. The electron microscope is well equipped with a field emission gun, operated at an accelerating voltage vary from 0.2 to 30kV, with a resolution of images of 2 nm. A schematic diagram of an SEM apparatus is given below in Figure 2.3**.**

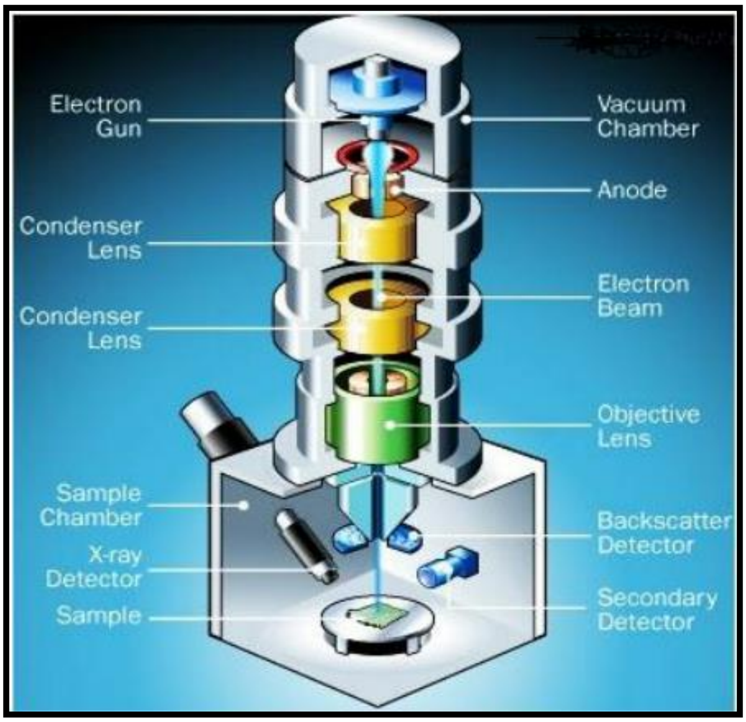

Figure 2.3 Ray diagram of the Scanning Electron Microscope (Goldstein, 1992) with its essential elements.

SEM images can be collected in two modes: these are: 1) front specimen imaging mode that used the intensity of the incident illuminating electrical beam, dissipated in the sample to produce an image. 2) Backscattering image mode, that usages the high-energy electrons offered from 180 degrees angle from the incident electron beam’s direction.

In our study, SEM analyses was performed with an FESEM instrument from FEI Nova Nano Lab combined with focused ion beams, located at Material Research Centre (MRC) MNIT, Jaipur (Raj.). For sample preparation, the dispersed nanoparticles were centrifuged and ultrasonicated by probe sonicator in solvent for 40 minutes. 30µl aliquots were then extracted and deposited on stub for FESEM analysis.

2.1.5. Transmission Electron Microscopy (TEM)

Transmission Electron Microscopy (TEM) is one of the most significant electron microscopic technique that often used to image nanomaterial with in sub-nanometer resolution (High resolution TEM) limit by transmitting electron beam through the analysing sample to get the image of sample. Here, a image of the thin specimen is obtained when the electrons tramismitted through the sample with an electron beam at uniform current density (Reimer, 1989) and acceleration voltage of 80-200 KV. These electrons are emitted from a target (tungsten or lanthanum hexaboride filament) or field emission (tungsten filament) electron guns. The illuminated area of specimen was controlled by a set of condenser lenses and objective lenses (see Figure 2.4 for ray diagram).

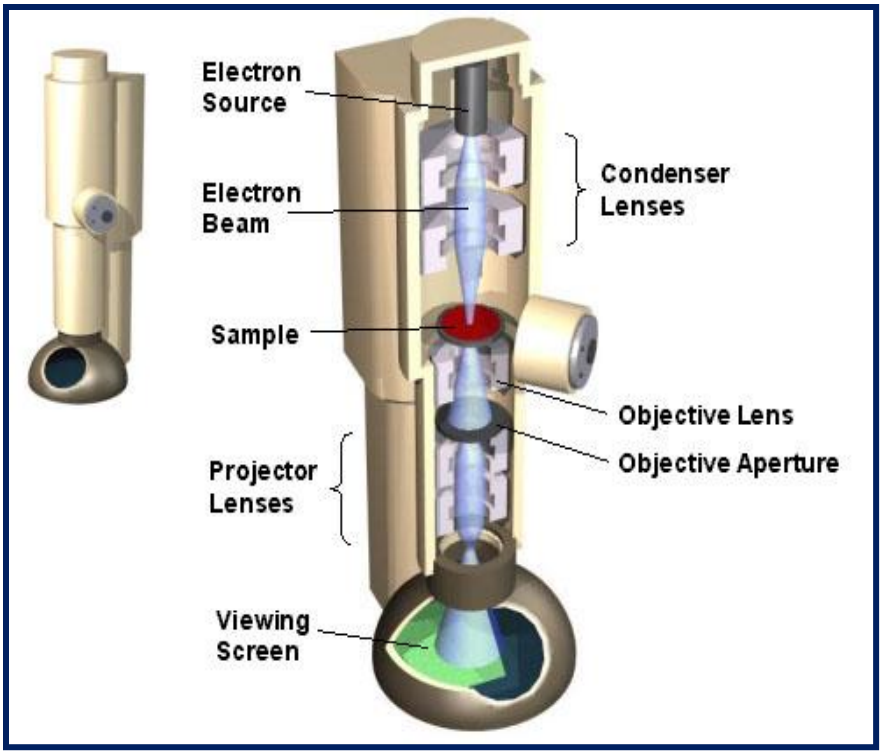

Figure 2.4 Transmission electron microscope with all important parts required for analyzing sampled in both imaging and diffraction modes. (Williams and Carter, 1996)

TEM images are used to characterise the crystallographic surface of the analysing material in image or diffraction mode. The particle size and distribution of nanoparticles was analysed in the image mode, while the crystalline arrangement was observed in diffraction mode. The morphological images of the sample are recorded either by using CCD camera or photographic plate. Besides a high-voltage magnification, various other factors (TEM column alignment and selection of the optimum focus) should be well managed for acquiring the good quality HRTEM image. TEM column alignment needs electron gun and condenser lens alignment, and astigmatism correction of condenser and objective lens. HRTEM atomic image of a crystal is possible by the fulfilment of the certain conditions such as assortment of the optimum focus, etc are required.

TEM Model- JEOL-2010F, located at Material Research Centre (MRC) MNIT, Jaipur (Raj.) has been used and operated with 200 kV energised electron beam. Under samples preparation 3–4 drops of the well ultrasonicated dissolved samples into alcohol was placed on to a 300-mesh carbon-coated Cu grid (EM sciences) and allowing the liquid to evaporate in air. The sample was twinned with CCD camera and plate film camera instrument, to get required information. The samples were prepared by using small amount of nanoparticles separated by centrifugation then ultrasonicated to disperse the suspensions, which was mounted on carbon coated copper grids.

2.1.6. ENERGY DISPERSIVE X-RAY (EDX)

Energy Dispersive X-ray Analysis (EDX) corresponding to the Scanning Electron Microscopy (SEM) and Transmission Electron Microscopy (TEM) technique was used to get information of the elemental composition of the sample. The analytical data acquired in the form of spatial peaks with resolution of approximately 1 μm for SEM imaging and less than 10 nm for TEM imaging. This technique recognized the elements present in concentration of 0.1% or higher but elements with low atomic numbers are difficult to identify by using this method. An electron beam with energy in the range of 10-20 keV strikes the surface of a conducting sample that results in X-rays emission from the irradiated material that used for examine the sample. Lithium drifted Silicon detector is usually used in EDX. As generated X-ray strikes the detector surface to generate the photoelectron, which travel within Si detector to generate electron-hole pairs. The experiment must be performed at liquid nitrogen temperatures. As produced electrons and holes, are attracted to opposite ends of the detector in presence of strong electric field. The height of the current pulse peak generated depends on the number of electron-hole pairs crafted or on the energy of the emitted X-ray.

2.1.7. Spectrofluorimeter

Basically spectrofluorimeter (Figures 2.5 and 2.6) comprises of two light sources of different wavelength selectors. One for excitation wavelength from the source i.e. low-pressure Hg vapor lamp, which generates intense emission lines share out throughout the ultraviolet and visible region (254, 312, 365, 405, 436, 546, 577, 691, and 773 nm). And another source i.e. high-pressure Xe arc lamp for generating continuous emission spectrum for the sample. Both contain a monochromator for selecting particular wavelength of light.

Figure 2.5 Instrument picture of the Spectrofluorimeter (Simazdu; RF)

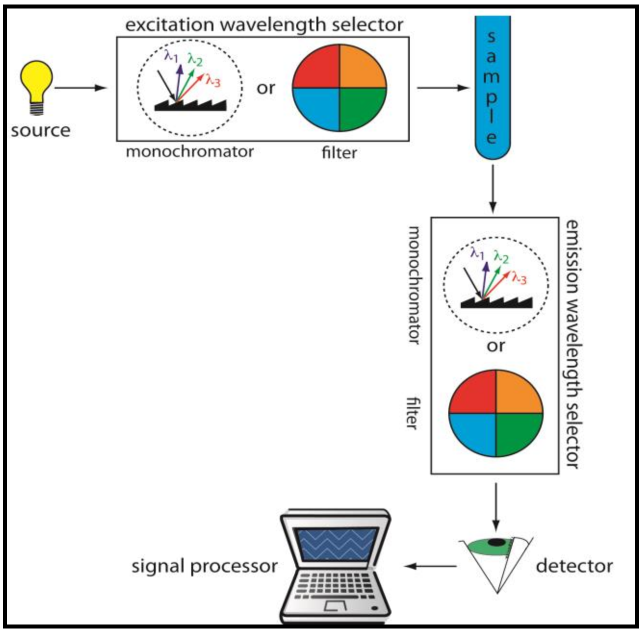

Figure 2.6 Sketch of fluorescence measuring instrumentation used with the wavelength selectors for excitation and emission**.**

In fluorimeter a filter is used where a monochromator is used in a spectrofluorimeter instrument. As resulted fluorescence, observed promote lowest energy absorption ($\pi \rightarrow \pi^*$ transition) in a studied molecule. Usually, the unsubstituted or nonheterocyclic aromatic compounds show the good fluorescence quantum yields.

Photoluminescence spectra were recorded in two steps by measuring the emitted radiation as a function of either the excitation wavelength or the emission wavelength. An excitation spectrum can be obtained by keeping fixed emission wavelength and varying the excitation wavelength. Mostly wavelength of excitation spectrum is nearly identical to its absorbance spectrum. The best excitation spectrum selected by changing various excitation wave length for a quantitative or qualitative analysis.

For obtaining the emission spectrum (Figure 2.7), a fixed excitation wavelength used by varying intensity of emitted radiation. A molecule can give only a single excitation spectrum, to get two emission spectra: one belongs to fluorescence and another belongs to phosphorescence.

Major classes of application of fluorimeter include the following:

1. Detection and quantification of trace-level species, especially in biological-clinical and environmental samples.
2. Detection is separation techniques, especially liquid and thin-layer chromatography and electrophoresis. Coupling of laser-induced fluorescence to electrophoresis for rapid base sequencing of DNA fragments may have considerable significance in biotechnology.
3. On-line analyses and remote sensing, using fiber optic sensors or laser-induced fluorescence.
4. Identifying, sorting, and counting particles (most notably biological cells) via fluorescence flow cytometry.
5. In-situ imaging mapping and quantification of species in biological systems such as tissue and single cells.

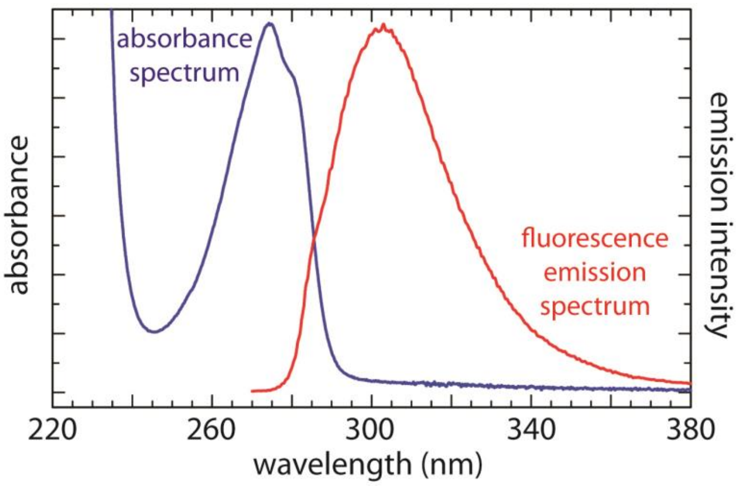

Figure 2.7 Absorbance spectrum and fluorescence emission spectrum

2.1.8. GC with TCD

Gas chromatography is a term used to describe the group of analytical separation techniques used to analyze volatile substances in the gas phase. In gas chromatography, the components of a sample are dissolved in a solvent and vaporized in order to separate the analytes by distributing the sample between two phases: a stationary phase and a mobile phase. The mobile phase is a chemically inert gas that serves to carry the molecules of the analyte through the heated column. The stationary phase is either a solid adsorbent, or a liquid on an inert support. The combination of gas chromatography and mass spectrometry is an invaluable tool in the identification of molecules. A typical gas chromatograph consists of an injection port, a column, carrier gas flow control equipment, ovens and heaters for maintaining temperatures of the injection port and the column, an integrator chart recorder and a detector. To separate the compounds in gas-liquid chromatography, a solution sample that contains organic compounds of interest is injected into the sample port where it will be vaporized. The vaporized samples that are injected are then carried by an inert gas. This inert gas goes through a glass column packed with silica that is coated with a liquid. Materials that are less soluble in the liquid will increase the result faster than the material with greater solubility.

2.1.9. Ultrasonic Processor

Ultrasonic processor (Coleparmer, Model EI-250UP) working at power 250 W (average) and frequency 20 KHz with a microprocessor based timer ranging from 0 to 20 minutes was used to prepare the sample (few steps of the synthesizing) and analysing the prepared nanoparticles for electron microscopy TEM and SEM and other methods.

2.1.10. Centrifuge

Centrifuge (MAX model 8X15) instrument work on the principle of the centrifugal acceleration that results in the movement of the denser matters/ particles to move away from surface in the radial direction. Instrument includes Rotar with swings out heads was used to obtain solid nano substances out of colloidal solution of the nanoparticles. The instrument is located at Department of Pure & Applied Chemistry, University of Kota, Kota (Raj.).

2.1.11. pH-Meter

pH Meter, ERMA model pH-035 and Systronics digital pH meter, model MAC (MSW-552) were used for acquiring the required pH (for synthesis purpose) with the maximum uncertainty in pH of ±0.01 unit. After reduction the pH of sample was found to increase and move towards the basic range. The pH meter used for the study are situated at our department.

2.2 Water splitting Instrumentation

The nanocomposite Ag/AgX@ZnO catalyst (0.3 g) was suspended in 120 mL of 20% aqueous CH_3OH in reaction cell (volume ~220 mL, a double walled Pyrex glass with water jacket). The cell used a rubber septum to cover / sealed the cell. Experimental setup of the instrumentation for water splitting is exhibited by Figure 2.8. For ejecting the air content of the solution, the sample was purged with Argon gas for almost 1 h before the photochemical reaction about to perform. To expel the dissolve gases, Argon gas purged in inner jacket, to uphold the 1 atm. pressure of the solution. Temperature of the outer jacket was set at 25^oC. The nanocomposite suspension was exposed with a 300 W Xe light source (>420 nm, light intensity $1x10^{22}$ photons per hour Xe lamp-HX1, Model: PE300UV). Photocatalytic responses of the photocatalyst in term of the water splitting ability was hourly monitoring was done in terms of the amount of the hydrogen expelled during the reaction time interval 2-4 h, using gas chromatograph (Shimazdu, Japan, equipped with thermal conductivity detector (TCD) and molecular sieve with 5 A columns) during the course of the experiment.

Figure 2.8 Instrumentation of the water splitting during experimental.

2.3 Reference

1. (a)Bullen C., Mulvaney P., “The effects of chemisorption on the luminescence of CdSe quantum dots Langmuir” (2006),22:3007. (b) Henglein A., “Chemisorption effects on colloidal lead nanoparticles” J. Phys. Chem. B (1999),103:9302.
2. Brans W.L., Dereux A., Ebbesen T.W., “Surface plasmon subwavelength optics Nature”, (2003), 424:824.
3. Goldstein J., “Scanning electron microscopy and X-ray microanalysis” A text book for biologist, material scientist, geologist, Plenum Press, New York, (1992).
4. Grundy P.J., Jones G.A., “Electron microscopy in the study of materials" Edward Arnold, London, (1976).
5. http://commons.wikipedia.org/wiki/File:TEM_ray_Diag.basic.en.png, visited June, (2010).
6. Kreibig U., Vollmer M., “Optical properties of metal clusters” Springer, Berlin: New York, (1995).
7. Reimer L., “Transmission electron microscopy: physics of image formation and microanalysis” Springer–Verlag, Berlin: New York. (1989).

8. Settle F.A., “Handbook of instrumental techniques for analytical chemistry” Prentice Hall, Upper saddle River, N. J., (1997).
9. Strelow F., Fojtik A., Henglein A., “Chemisorption of phosphine on colloidal silver in aqueous solution” J. Phys. Chem., (1994),98:3032.
10. Stuart B., Ando D. J., “Modern infrared spectroscopy” Wiley, Chichester, New York, (1996).
11. Templeton A.C., Pietron J.J., Murray R.W., Mulvaney P., “Solvent refractive index and core charge influences on the surface plasmon absorbance of alkanethiolate monolayer-protected gold clusters” J. Phys. Chem. B(2000),104:564.
12. Williams D.B., Carter C.B., “Transmission electron microscopy: A textbook for material science” Plenum Press, New York, (1996).

Chapter- 3

Experimental

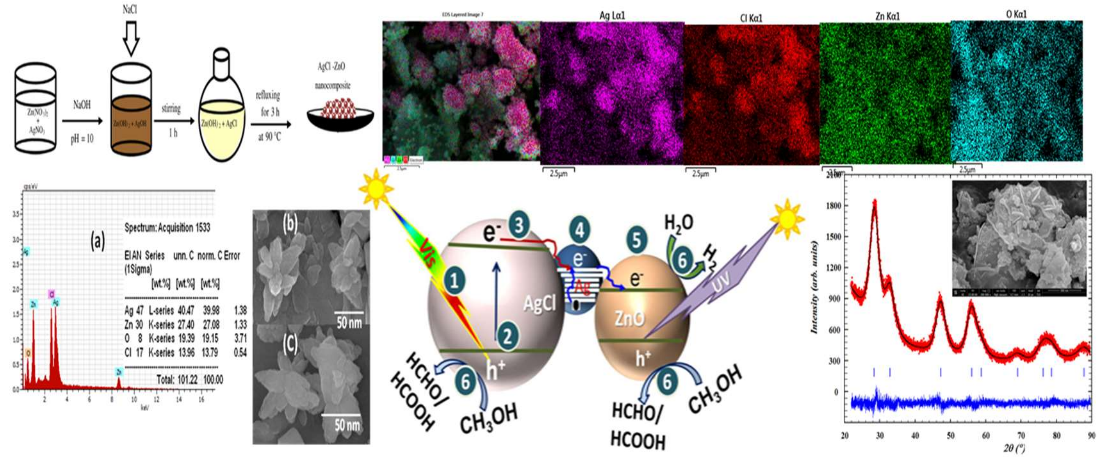

ABSTRACT

We had successfully prepared microwave assisted lotus shaped Ag/AgCl@ZnO nanocomposites (NCs) of size 57.72 nm, in aqueous media at 90 ^{o}C for 7 min. heating. The conventional single pot refluxing method was also used to prepare NCs with diffrent shaped-nanoparticles (NPs) Ag/AgX@ZnO (X= Cl, CO_3^{-2}, PO_4^{-3}, NO_3^{-}, SO_3^{2-}) of size 45-60 nm at 90 ^{o}C heating for 3 h. X-ray diffraction (XRD) data of the Ag/AgX@ZnO NCs synthesized by the both methods, confirmed that the nanocomposite crystallized in three phases i.e. face-centered cubic (AgX), nano silver and wurtzite hexagonal (ZnO) phases. Electron microscopy and corresponding energy dispersive X-rays (EDX) analyses and their corresponding elemental mapping, envisioned the surface morphology and percentage elemental composition i.e. Zn, O, X, and Ag in the NC. The Ag/AgX@ZnO NCs exhibited the visible light harvesting ability with visible band gap i.e.2.5- 2.75 eV. All samples had shown the photoluminescence emission in yellow light region. However, the mode of heating affects the degree and types of defects generated in crystals. Therefore, the conventional sample represented more defects than microwave assisted samples. FTIR spectra was taken at different stages of the formation of the nanocomposites that visualized the gradual changes occur in bonding positions of NCs. We utilized this molecular system as an efficient visible-light harvesting optical devices for hydrogen production through water splitting. Microwave assisted Ag/AgCl@ZnO NCs and conventionally synthesised Ag/AgX@ZnO NCs samples librates hydrogen with time, through photocatalytic water splitting under AM 1.5G irradiation.

Key words: Nanocomposite, Ag/AgXl@ZnO, plasmonics silver nanopartcles, one pot synthesis, microwave assisted synthesis, water splitting, hydrogen generation.

3.1 Introduction

Nanomaterials are superior to their bulk counter substances due to their properties such as mechanical strength, thermal stability, catalytic activity, electrical conductivity, magnetic properties, optical properties, etc. These superb materials can be utilised in several fields because of their magnificent properties such as nanofabrication of nanodevices, nanobiology, and nanocatalysis for LED display, PV film making, self-cleaning window, temperature control fabrics, health monitoring clothes, solution to energy crisis, environmental problem, artificial joints, CNT chair, biocompatible materials, nanoparticle paint, smart window, data memory, CNT fuel cells, nano-engineered cochlear and many more. Therefore, we can say nanotechnology is gradually changing our life, but not enough. But the major challenges associated with the dealing with nanomaterials are to achieve monodispersity, size and shape control, reproducibility, scale up at industrial level, building up of the complex nanostructures. That can be sort out by making variation in synthesis process by changing pH, temperature, time, concentration of reagents, concentration of catalyst and precursors, phase transition materials, etc.

3.2 Nanomaterial Synthesis Method

There are two main approaches for synthesis of nanomaterials these are: Bottom-Up and Top-Down. **(**Hahn,1997)

3.2.1 Top-Down

In top-down approach, fabrication of nanoscale structures by making a bulk material short with various physical/ chemical techniques-lithography, cutting, etching, grinding as shown by Figure 3.1.

3.2.2 Bottom-Up

In this approach (Figure 3.1), nanomaterials can be assembled from building blocks (such as atoms and molecules) by compiling atom-by-atom, molecule-by molecule, or cluster-by-cluster using chemical synthesis, self assembly, positional assembly method.

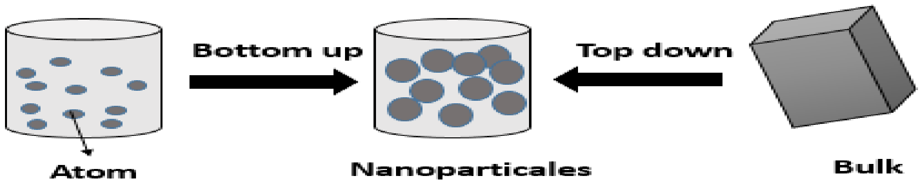

Figure 3.1 Schematic representation of the top to down and bottom to up approaches. (Hahn, 1997)

Different synthesis techniques of the nanomaterial syntheses are classified by the Figure 3.2 and some of the important methods are discussed below.

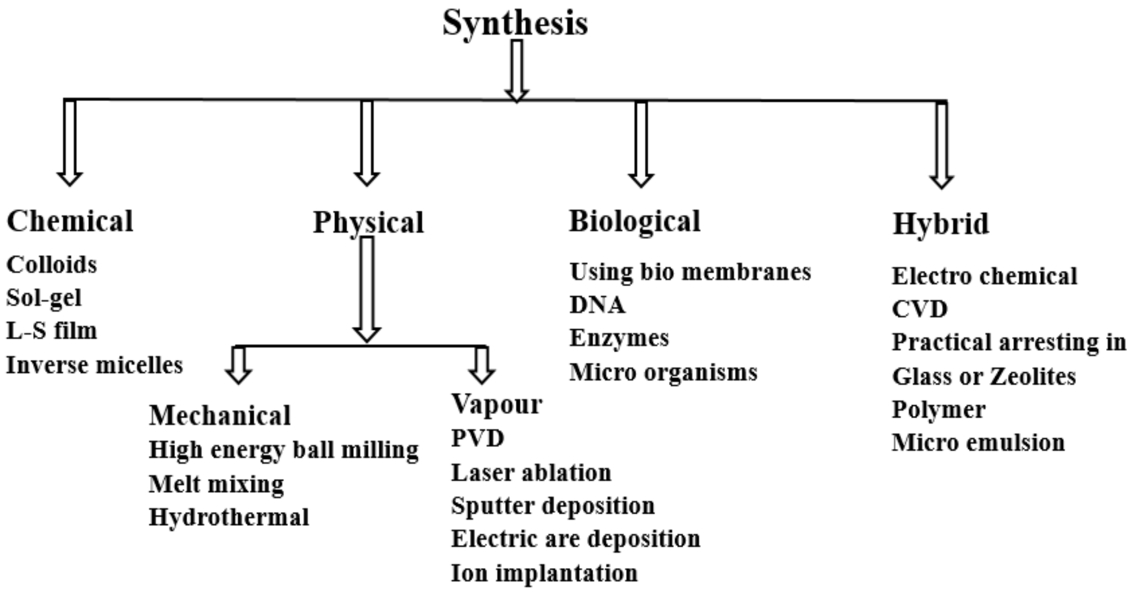

Figure 3.2 Sundry methods used for synthesis of nanomaterials.

3.3 Chemical Methods

3.3.1 Liquid phase synthesis

Precipitating nanoparticles from a solution of chemical compounds can be classified in following categories: colloidal methods, sol–gel processing, water/oil micro-emulsions method, hydrothermal/solvothermal synthesis, microwave synthesis, sono-chemical synthesis, template synthesis, biomimetic synthesis, co-precipitation and polyol method (Barabaszova, 2006)

3.3.2 Colloidal Method

Colloidal methods are the most useful, easiest, and cheapest ways to create nanoparticles of different metal and metal oxides gold, molybdenum iron, silver, ZnO, TiO_2, etc. Colloidal methods may utilize both organic and inorganic reactants. In a typical colloidal method, a metal salt reduced in to evenly dispersed nanoparticles in a liquid. Aggregation is of particles can be prevented by electrostatic repulsion or the introduction of a stabilizing reagent that coats the particle surfaces. Particle sizes range from 1-200 nm, are controlled by the initial concentrations of the reactants and the action of the stabilizing reagent.

3.3.3 Sol-gel Method

Sol-gel technology is a well established colloidal chemistry technology, which used to offer the possibility to produce various materials with novel, predefined properties in a simple process and at relatively low process cost. The sol named a colloidal solution, which made of the solid particles (of few hundred nm in diameter) that suspended in a liquid phase. The gel can be considered as a solid macromolecule immersed in a solvent. Sol-gel process consists in the chemical transformation of a liquid (the sol) into a gel state and with subsequent post-treatment and transition into solid oxide material. The main benefits of sol–gel process are the high purity and uniform nanostructure can be obtained at low temperature. Figure 3.3 brief the step by step process of nanomaterial synthesis using sol-gel technique. (Fernandez-Garcia et al., 2004)

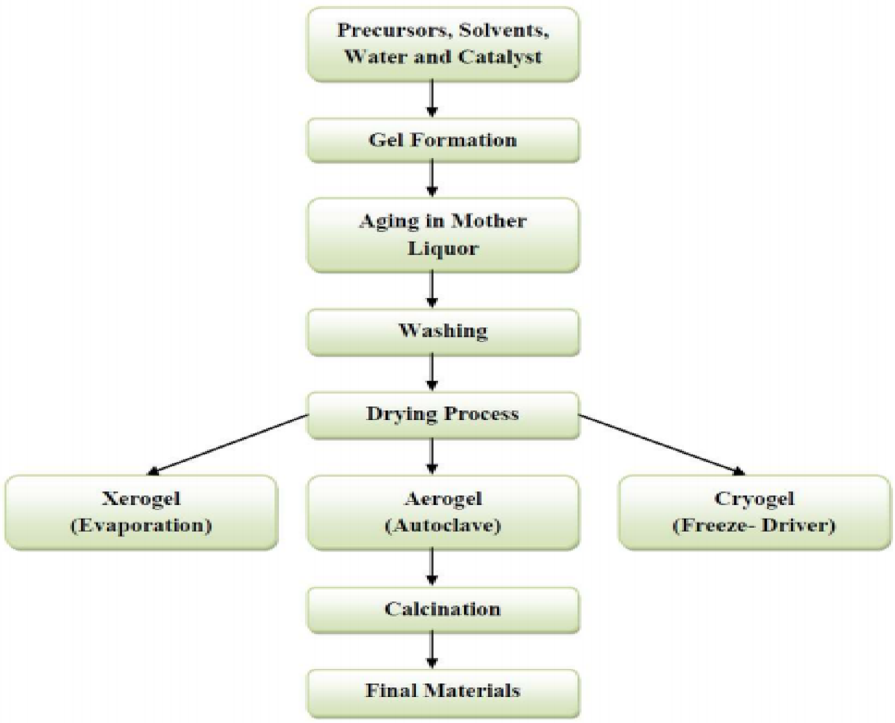

Figure 3.3 Flow chart of nanomaterial synthesis using sol-gel technique. (Pierre, 1998),

3.3.4 Micro emulsion-based methods

Ultrafine metal nanoparticles of diameter between 5 nm and 50 nm can be prepared by water-in-oil micro emulsions. Where, water nanodroplets are dispersed in the oil phase. The reactant metal salts and reducing agents are mostly soluble in water. One microemulsion contains the metal salt and the other microemulsion contains the reducing agent. The size of the water droplets can be varied in the range of 5–50 nm depending upon the water/surfactant ratio. Here, the role of the surfactant molecules is to provide the sites for particle nucleation and to stabilize the growing particles. Therefore, in the microemulsion process the nanodroplets acts as a micro reactor and the nucleation of particles proceeds in the water pools of the microemulsion. (Ghosh,1999; Kumar and Mittal, 1999).

water-in-oil microemulsion method are extensively used in synthesis of iron, platinum, cadmium, palladium, silver, copper, nickel and gold nanoparticles.

3.3.5 Hydrothermal synthesis

Hydrothermal synthesis includes the crystallization of the fabricating substances from high-temperature aqueous solutions at high vapour pressure. Hydrothermal method based on the principle that an insoluble material could be made soluble by imposing high temperature and pressure. The crystal growth proceeds in a steel vessel called an autoclave, in which a reactants are supplied along with water. A temperature gradient is well preserved between the both (opposite) ends of the growth chamber. The reactants/solute got dissolved at the hotter end while seed crystal start growing in the desire shaped crystal at the cooler end. (Yang et al.,2001)

Advantage of the hydrothermal method is that one can grow the crystals of the compounds (with high melting points) at lower temperature using aqueous medium. The method is suitable for the growth of large good-quality crystals by maintaining their composition. The main disadvantage of this method is the use of expensive autoclaves and hard to observe the minute to minute crystal growth process. (Carp et al., 2004).

3.3.6 Microwave synthesis

Microwave assisted synthesis for the production of inorganic compounds has been studied since 1986. The interaction of dielectric materials (liquids or solids from) with microwaves leads to the dielectric heating. Electric dipoles of the above materials respond to the applied electric field. In liquids, constant reorientation leads to the friction between molecules, which subsequently generate heat. Microwave irradiation is a heating method that includes the thermal effect along with the nonthermal effects (Galema, 1997). It has a number of applications in chemistry. The microwave assisted heating frequencies lies between 918 MHz to 2.45 GHz, with the latter frequency being most often used. The simple household multimode microwave ovens to large-scale batch as well as continuous multimode oven are used for microwave chemistry. In comparison to the conventional oven heating microwave heating (volumetric) of liquids, is an alternative heating approach with specific advantages (fast and homogeneous heating effects) in the synthesis of inorganic nanoparticles and keeps growing its utility to materials science. Therefore, microwave assisted heating method are more advantageous with short reaction time, high energy efficiency and the ability to induce the particles formation with small size particles with narrow particle-size distribution and high purity. (Ma et al., 2005; Wu et al., 2005)

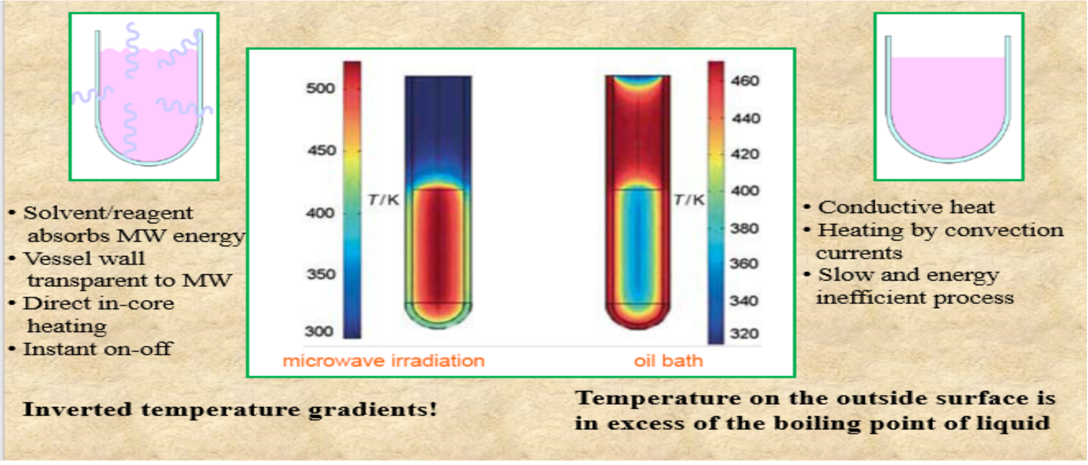

Figure 3.4 Comparison between the microwave *Vs* oil-bath (conventional) heating.

3.3.7 Photochemical Synthesis

Presently, the photo energy is greatly used in synthesis of variety of molecules and to induce a variety of photochemical reactions. This method has the potential advantage of mild reaction conditions, convenient operations and use of the simple and cheap equipments. Usually, a low-pressure mercury pillar lamp and a high-pressure column-like indium lamp are used as the ultraviolet irradiation and visible photo irradiation sources, respectively. This technique may be extended to prepare other sulfide semiconductor nanoparticles, including ZnS, Ag_2S, PbS, NiS, CuS, nanocrystalline CdS with different morphologies. This method provides a mild chemical route to fabricate the semiconducting nanowires, which can be applied in many fields.

3.4 Physical Methods

3.4.1 Physical Vapour Deposition (PVD)

PVD includes several technological processes like, pulse Laser deposition, cathodic arc deposition from the cathode, plasma method, electron beam vapour deposition, sputtering deposition, and many more. (Barabaszova, 2006)

3.4.2 Plasma method

Plasma is a forth state of matter and consists of a hot ionized gas having the approximately equal numbers of positively charged ions and negatively charged electrons. In the plasma method, reactions of elements or molecules occurred in the gaseous state. An essential part of the plasma processes is evaporation of key in material through high temperature to achieve its plasma state that followed by the cooling that leads to the re-nucleation of products in a form of highly dispersed nanoparticles of various sizes. It is widely used and environmentally acceptable chemical procedure for preparation of nanomaterials. Highly dispersed nanopowders of nitrides, carbides, borides and oxides of metals and pure metals, can be made using this technique. The synthesis of powder materials on the basis of gaseous phase reactions is based on random processes of formation of particles. Plasma can occur in the equilibrium or non-equilibrium state. In the former case, all components of plasma (ions and neutral gas) having the same thermal energy and known as a high-temperature plasma. Where, in latter case the plasma components have different thermal energy levels. In the non-equilibrium plasma, electrons have the highest thermal energy, ions have lower and the neutral gas has the lowest thermal energy. This state is designated as a low-temperature plasma. (Barabaszova, 2006)

3.5 Study of nanocomposite Ag/AgCl@ZnO

3.5.1 Experimental Material and Methods

3.5.1.1 Materials

All chemical used as-purchased (of make Sigma Aldrich) in the synthesis of nanocomposites and their application in water splitting without further purification. These chemicals are: hexahydrated-zinc nitrate, sodium chloride, sodium hydroxide, and silver nitrate, etc.

3.5.1.2 Synthesis

3.5.1.2.1 Conventional Synthesis

Ag/Zn- nano particles supported ZnO/AgCl NCs were fabricated by the one-pot refluxing method, described at somewhere else (Pirhashemi and Habibi-Yangjeh, 2014). In which, 5.220 g hexahydrated zinc nitrate and 2.110 g silver nitrate were mixed in 50 mL of deionised water (DIW) and stirred at room temperature and followed by the addition of aqueous NaOH (5 M) to adjust the pH of the solution 10. Above mixture was treated with 1.450 g NaCl in 20 mL of water. Then, the suspension was refluxed at 90 ^{o}C for 3 h. Resulting product was centrifuged and washed several times with DIW and ethanol mixture and dried in an oven at 60 ^{o}C for 24 h.

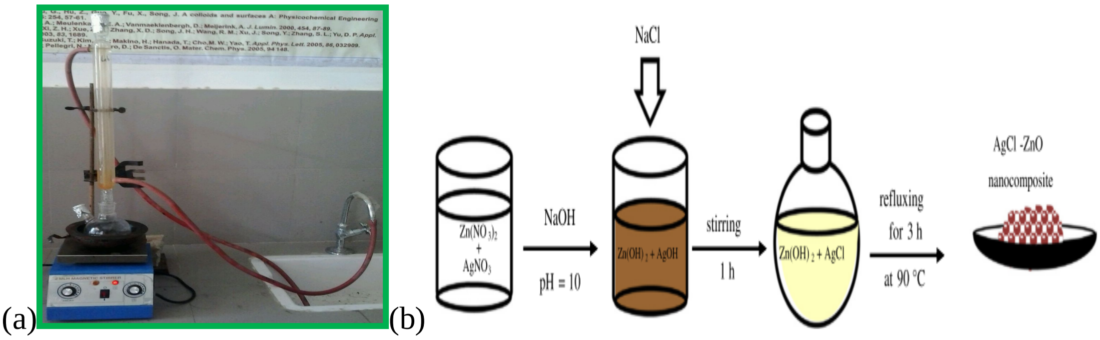

Figure 3.5 Schematic presentation of fabrication of nanocomposite Ag/AgCl/ZnO using one pot conventional method.

3.5.1.2.2 Microwave Synthesis

Microwave synthesizer (CEM, Model-Discover) was opted to prepare the Ag/Zn NPs embedded ZnO/AgCl NCs with 0.383 mol fraction of silver chloride with respect to ZnO. A solution of 5.220 g $Zn(NO_3)_2.4H_2O$ and 2.110 g $AgNO_3$, were made in 50 mL of deionised water (DIW) and stirred at room temperature. Thereafter the aqueous NaOH (5 M) was added in the solution to adjust the pH of the solution 10. Above solution was treated with 1.450 g NaCl in 20 mL of water. Then, the suspension was heated in microwave at 90 ^{o}C for 7 min. Resulted product was centrifuged and washed several times with DIW and ethanol mixture and dried in an oven at 60^{o}C for 24 h.

3.5.2 Analysis of hydroxyl radical ($^{\bullet}$OH) in photocatalytic solution

The hydroxyl radicals ($^{\bullet}$OH) formed during the photo-illumination of the samples/water interface, can be traced by the use of basic terephthalic acid (as a probe molecule) solution in the photoluminescence (PL) method using double beam spectrofluorimeter (Yu et al., 2009). In this method, the hydroxylation of the terephthalic acid was taken place when it reacted with $^{\bullet}$OH radical and as-synthesized 2-hydroxyterephtalic acid at the water/catalyst interface, exhibited the PLE signal around 425 nm at the excitation wavelength of 315 nm. The intensity of the PLE peak of 2-hydroxyterephtalic acid is directly proportional to the amount of $^{\bullet}$OH radicals produced in the water. Under the experimental procedure 0.3 g of the sample was added to 110 mL of 5×10^{-4} M terephthalic acid (pH=10) that was prepared in aqueous 2×10^{-3} M NaOH. Afterwards the solution was exposed to the 300 W Xe light source, by keeping the other experimental conditions same as used in measurement of photocatalytic water splitting activity. Spectrofluorimeter (Simandzu; Model: RF-5301) of the department was used to measure the PLE spectrum of the above mentioned solution at room temperature.

3.5.3 Water splitting analysis

Photocatalytic H_2 evolution power of the as synthesised samples was carried out in a 20% methanolic (hole-scavenger) solution of Ag/AgCl@ZnO samples at RT. Where, 0.3 g of the Ag/AgCl@ZnO in an aqueous methanolic solution (160 mL H_2O and 40 mL CH_3OH) was suspended in a double wall reaction cell of Pyrex glass, equipped with a quartz window. Reaction cell was connected to a closed gas circulation (argon) of 1 atmosphere pressure to evacuate the solution several times up to the complete removal of the air from the reaction vessel and then system was irradiated by a light source (300 W Xe lamp) for the photocatalytic observations. The amount of H_2 evolved during the photocatalytic experiment, was monitored in the graduated tube connected directly through the reactor over the water tank. Hydrogen gas was detected using the gas chromatography that was equipped with a thermal conductivity detector (TCD, GC-8A, China gas chromatograph; and Ar as carrier gas).

3.5.4 Characterization

Several techniques were used to characterize the nanocomposite Ag/AgCl@ZnO using technical tools such as: UV-Vis absorption spectroscopy, FE-SEM, EDX, spectroflurometery, XRD, PLE and FT-IR, etc. Crystalline nature of the nanocomposites was characterized by XRD, using PANalytical Xpert-Pro diffractometer of MNIT, Jaipur, well equipped with Ni-K_β filter for CuK_α radiation at 40 kV voltage and 30 mA current. Morphology of the sample was evaluated by using FESEM (JEOL JSM-6700F). The UV-Vis spectra were recorded with multimode microplate reader (Lab India Model 3000^+ with Diffuse Reflectance Spectroscopy) in the wavelength range between 200 and 800 nm. An FT-IR spectrum was recorded using spectrophotometer (Bruker Model Tensor 27) available at our institute. Furthermore, photoluminescence emission (PLE) spectrum of the Ag/AgCl@ZnO nanocomposite material was characterized by using spectrofluorimeter (Simandzu; Model: RF-5301) of our department.

By using above methods we had synthesized total six systems, these are: Ag/AgCl(NaCl)@ZnO, Ag/AgCl($BaCl_2$)@ZnO, Ag/$AgPO_4$@ZnO, Ag/$AgNO_3$ ($NaNO_3$)@ZnO, Ag/$AgCO_3$($NaCO_3$)@ZnO and Ag/Ag_2SO_3@ZnO, nanocomposite systems.

3.5.5 Results

3.5.5.1 XRD

The phase purity of the Ag/AgCl@ZnO NC was tested using XRD profile, depicted in Figure 3.6. Diffraction patterns of the studied samples are found at 27.942 °(111), 32.34 °(200), 46.34 °(220), 54.94 °(311), 57.58 ^{o}(222), 67.54 °(400), 74.76

°(331) and 76.82 °(420) attributed to the highly crystalline two prominent phases that corresponds to the face-centered cubic (chlorargyrite) phase (reference JCPDS card No.31-1238) of the AgCl with their cell parameters : a=b=c= 5.545 Å, $\alpha=\beta=\gamma=90^{o}$ at z=4, and space group *Fm3m* (225) along with FCC (zinc blende) crystalline phase (reference JCPDS card No. 80-0020) of ZnS (Ai et al., 2013; Fang et al., 2013) with their cell parameters: a=b=c=5.345 Å, $\alpha=\beta=\gamma=90^{o}$ at z= 4 and space group *F4-3m*(216). The careful examination of diffraction peaks exhibits tiny peaks at 38.56° (111), 46.34° (200), 67.54° (220), 76.82° (311) position that belongs to the standard JCPDS card No.04-0783 of pure silver (cell constants a=b=c= 4.0857 Å, $\alpha=\beta=\gamma=90\ ^{o}$ at z= 4 and space group *Fm3m* (225) that also confirmed the presence of the small particles of silver and their size was calculated by using the Scherrer formula.

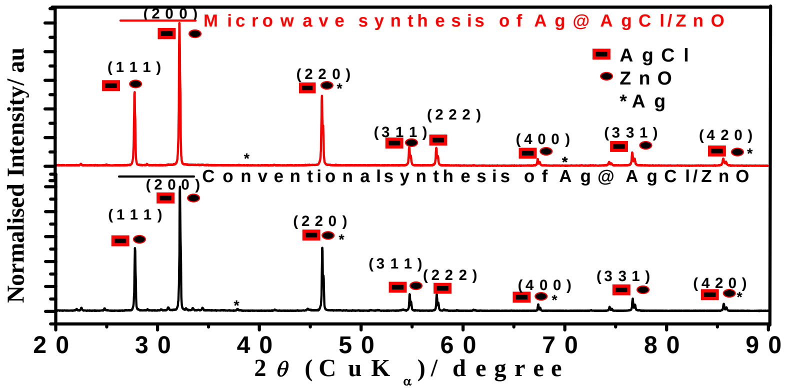

Figure. 3.6 Diffraction patterns of the nanocomposite Ag/AgCl@ZnO, synthesized by one pot conventional and microwave method. The XRD peaks are exactly matched to those of the bulk *FCC* chlorargyrite phase (JCPDS card No.31-1238) of the AgCl with cell parameters: a=b=c= 5.548 and $\alpha=\beta=\gamma=90^{o}$ at z=4 with space group *Fm3m* (225), FCC zinc blende crystalline phase (JCPDS card No.80-0020; ZnS) of ZnO with cell parameters: a=b=c= 5.345 Å, $\alpha=\beta=\gamma=90^{o}$ at z= 4 and space group *F4-3m* (216) and standard JCPDS card No.04-0783 of pure silver (cell constants a=b=c= 4.0857 Å, $\alpha=\beta=\gamma=90\ ^{o}$ at z= 4 and space group *Fm3m* (225).

3.5.5.2 FESEM & EDX

Surface morphology Nanolotus (Microwave synthesize), Spherical (one plot synthesize) metallic composition and particle size 57.72 nm (Microwave synthesize) and 59.12 nm (one plot synthesize) of the nanocomposite was confirmed by the FESEM, FESEM elemental mapping and corresponding EDX analyses, as represented by Figures 3.7a, 3.7b, 3.7c, 3.7d and 3.7e. No characteristic peaks for the elements other than Zn (27.08%), Ag (39.98%), Cl (13.79%) and O (19% actual concentration can't be determined due to the presence of the oxygen in air) were found in the EDX profile of the Ag/AgCl@ZnO, as illustrated by the Figure 3.7a.

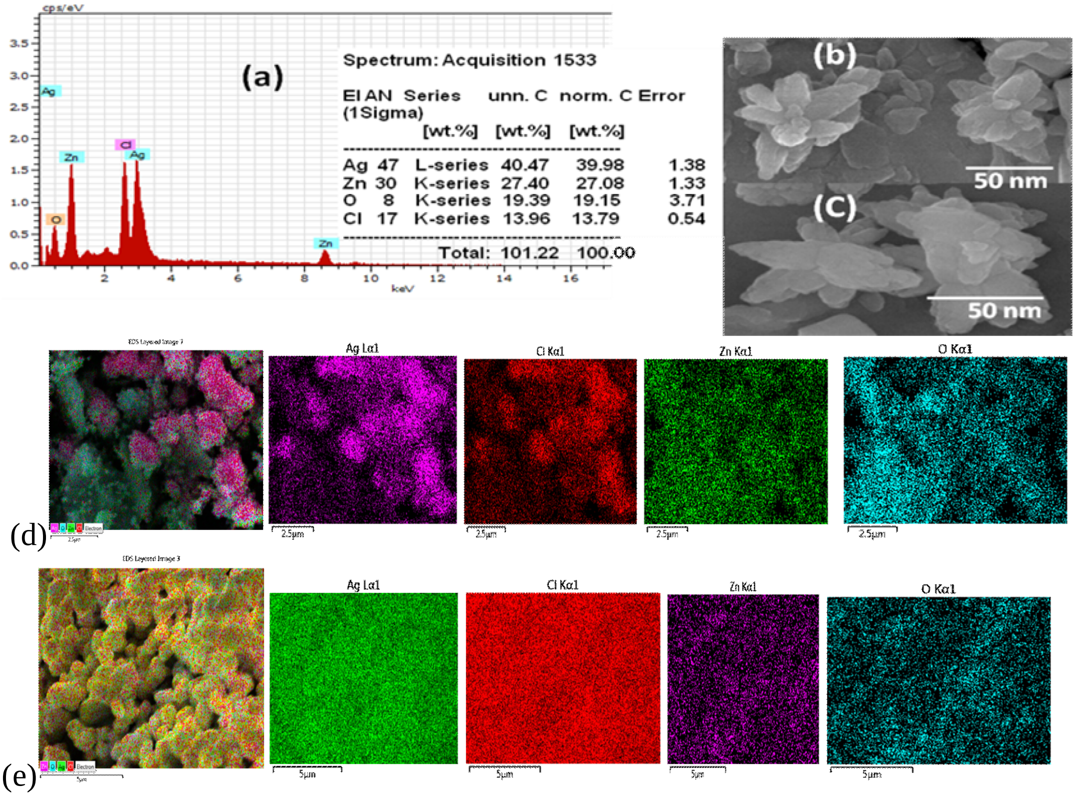

```
Spectrum: Acquisition 1533

El AN  Series    unn. C  norm. C Error
(1Sigma)
                 [wt.%]  [wt.%]  [wt.%]
---------------------------------------
Ag 47  L-series  40.47   39.98        1.38
Zn 30  K-series  27.40   27.08        1.33
O   8  K-series  19.39   19.15        3.71
Cl 17  K-series  13.96   13.79        0.54
---------------------------------------
         Total:  101.22  100.00
```

(d)

(e)

Figure 3.7. Nanolotus Ag/AgCl@ZnO (microwave) with corresponding (a) FESEM supported EDX showing elemental presence of Ag, Zn, O and Cl, (b) and (c) are FESEM images of nanocomposite, prepared by one pot synthesis and microwave route. FESEM Elemental mapping of Ag, Cl, Zn and O elements in Ag/AgCl@ZnO for corresponding (d) one pot (conventional) and (e) Microwave synthesized nanocomposite.

3.5.5.3 UV-Vis Diffuse Reflectance Spectra

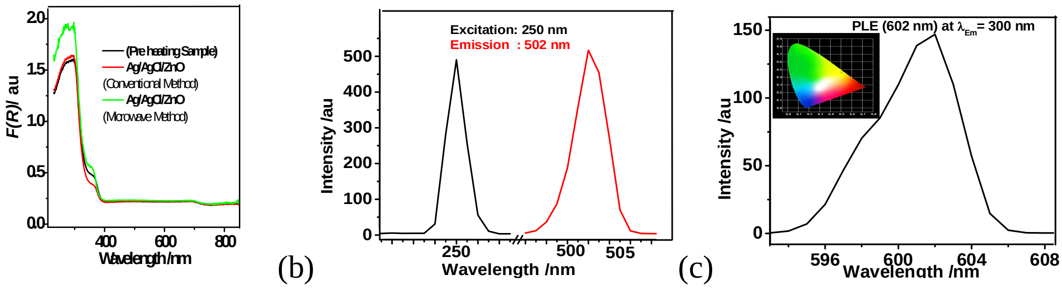

(a) (b) (c)

Figure. 3.8 (a) λ_{ex}UV-Vis diffuse reflectance spectra of the pre heated sample along with conventional- and microwave- prepared Ag/AgCl@ZnO nanocomposites with first excitonic peak around 340.4 nm. (b) PLE spectra with maxima at 502 nm under the excitation light wave length $\lambda_{max}^{ex} = 250$ nm of the sample prepared by one pot reflux method and (c) photoluminescence emission spectra with maxima at 602 nm under the excitation light wave length λ^{ex}_{max} = 300 nm, for the sample prepare through microwave. In inset CIE plot of the same sample exhibit the yellow emission.

Figure 3.8a exhibited the UV-Vis spectra of the pre heated sample along with conventional- and microwave- prepared Ag/AgCl@ZnO nanocomposites with first excitonic peak around 284.4 nm and band gap around 338.186 for ZnO 417.14 nm(conventional) 418.78 nm (microwave) 831.27 nm (almost same for conventional and microwave sample) for Ag@AgCl part of the composite.

3.5.5.4 PL Spectrum

Ag/AgCl@ZnO that exhibited the Photoluminescence emission (PLE) spectra of Ag/AgCl@ZnO are revealed by Figures 3.8(b) and 3.8(c), which were taken for the samples prepared by one pot reflux- and microwave assisted- methods. Figures 3.8(b) exhibited the excitation peak at the wavelength of 250 nm under the exposure of emission light of the wavelength λ^{em}_{max} = 502 nm and green light emission spectra was found at 502 nm under the excitation light of wavelength λ^{ex}_{max} = 250 nm, respectively. Similarly, the strong PLE peak was observed for microwave assisted sample at 602 nm under the excitation light wavelength 300 nm, as shown by the Figure 3.8c.

3.5.5.5 Determination of the presence of the OH* radical

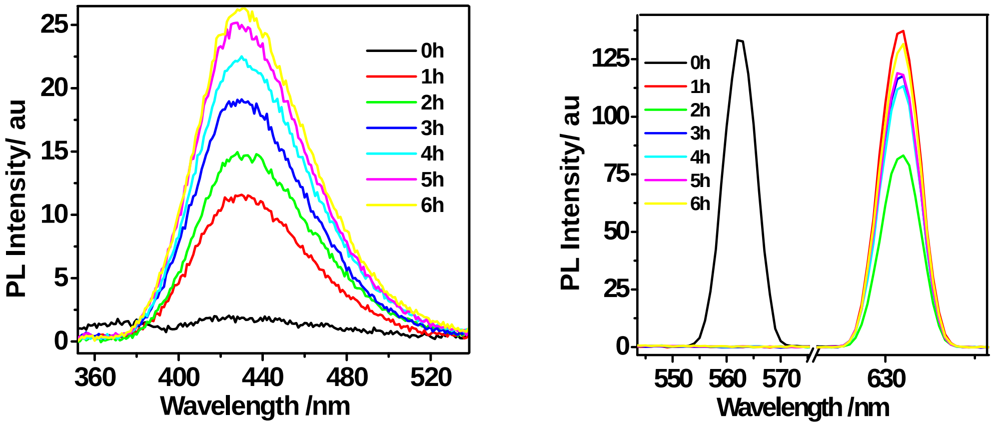

(a) (b)

Figure 3.9 PL spectral changes at (a) 428 nm and (b) 562.8 nm and 632.9 nm wavelength with visible-light irradiation time (0h,1h,2h,3h,4h,5h and 6h) for the Ag/AgCl@ZnO (microwave) nanocomposite powder dispersed in alkaline terephthalic acid solution for checking the OH ion concentration during photocatalytic water splitting reaction.

Figure 3.9a illustrated the PLE spectra of the conventionally prepared sample to check the presence of OH^* radical in alkaline terephthalic acid under light. Rest of the PLE peaks positioned at 562.8 nm and 632.9 nm are associated with the *Soret*-band and *Q*-bands, respectively as shown in Figure 3.9 b.

3.5.5.6 FTIR

Figures 3.10a, 3.10b and 3.10c**,** exhibits the FTIR profiles of the Ag/AgCl/@ZnO at various stages of synthesis i.e. pre-heated stage of the sample, final product one pot refluxing method and final product microwave assisted method, respectively.

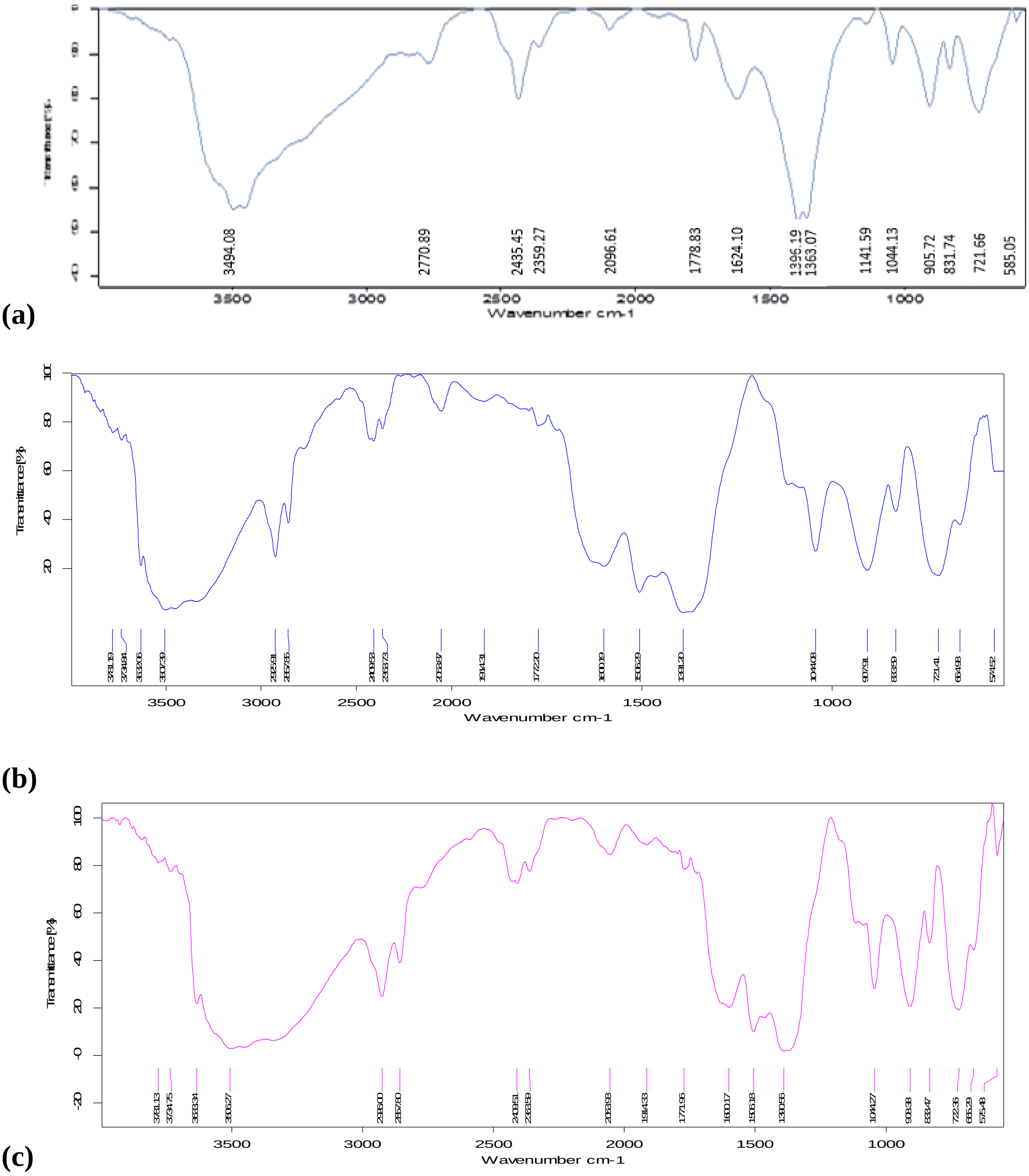

Figure 3.10. FTIR profile of the Ag/ZnO@AgCl synthesized at various stages: (a) pre-heated stage of the sample, (b) final product one pot refluxing method and (c) final product microwave assisted method, respectively.

On careful observation of the FTIR profile of the samples prepared by microwave and one pot reflux method, it was found that both final products are having almost same environment with presence of the OH, Cl^- group, Ag-Cl and Zn-O bonding. The width of infrared bands for the samples, reflected the chemical environments which is related to the strength of intermolecular and intramolecular interactions such as hydrogen bonding and free OH group. The peak intensities are true representations of the values of $\delta\mu/\delta x$ for different vibrations.

Table 3.1 IR Vibrational frequencies for few selected inorganic anionic groups of a complex. (Nyquist,1968)

Anion	**Stretching vibration (cm^{-1})**	**Bending vibration (cm^{-1})**
Water of hydration	3800-3200	1700-1 600
Carbonate	1550-1 350	900-650
Nitrate	1500-1 250	850-700
Sulfate	1200-1 050	680-600
Phosphate	1300-900	600-550
Silicate	1200-800	800-400
Formates, acetates, and oxalates	1700-1 300	1050-700
Cyanates, cyanides, and thiocyanates	2200-200	-------

Table 3.2 FTIR peak positions of nanocomposite sample at various stages: (a) pre heated sample, (b) one pot refluxing method and (c) microwave assisted method, respectively

SL. No.	FTIR Peak of Pre heated sample (cm^{-1})	FTIR Peak one pot reflux Product (cm^{-1})	FTIR Peak Microwave-assist Product (cm^{-1})	Respective functional group
1.	-	3781.19	3781.13	Free OH
2.	-	3734.84	3734.75	Free OH
3.	-	3632.06	3633.34	Free OH
4.	3494.08	3507.39	3506.27	Intra- or inter-molecular bonded –OH
5.	-	2925.91	2926.00	---
6.	-	2857.85	2857.80	-CH_2- stretch (s), C-H str. Methane, symmetric stretching CH_2
7.	2770.89	-		C-H str. , –C(=O)H, aldehyde
8.	2435.45	2409.53	2409.51	
9.	2359.27	2363.73	2363.59	NH_2^+, NH^+ str.
10.	2096.61	2053.87	2053.93	
11.	-	1914.31	1914.33	
12.	1778.83	1722.20	1771.96	Primary amide , carboxylate C-O stretch, conjugated ketones H O-H bending HO-H
13.	1624.10	1600.19	1600.17	C=O group M-Cl stretching
14.	-	1506.29	1506.18	C=N(plus C=C), δ-NH_2 str. Aromatic ring str., M-Cl stretching
15.	1396.19	1391.20	1390.56	
16.	1363.07			S=O str., ν-C–N, wagging vibrations of CH_2 group
17.	1141.59	---	---	C-O, C-N, C-C str.
18.	1044.13	1044.08	1044.27	Alkane, C-O str. P-O str. M-Cl bending
19.	905.72	907.91	908.38	C-H out of the plane bend M-Cl bending
20.	831.74	833.59	833.47	C-O str.
21.	721.66	721.41	722.36	N-H bonded, secondary amide
22.	-	664.98	665.29	C-S str.
23.	585.05	574.52	575.48	M- X out of plane bending P-O bending

3.5.5.7 Water Splitting

Molecular devices of Ag/AgCl@ZnO NC (prepared via one pot conventional and microwave method), produced hydrogen in 20% methanolic water, under visible light exposure of 300 W Xe light. Amount of the released hydrogen, was significantly enhanced with increasing exposure time (i.e. 1, 2, 3, 4, 5, 6, 7 and 8 h) viz. 536.71 and 556.8, 1404.41 and 1621.21, 2207.86 and 2325.37, 2835.26 and 3203.09, 3554.11 and 4053.44, 4359.24 and 4987.66, 5221.07 and 5761.86, 6082.9 and 6782.32 μmol H_2 h^{-1} g^{-1}, corresponding to the conventional and microwave prepared nanocomposite samples under 300 W Xe light irradiation (Figure 3.11a), at RT. Figure 3.11b, Figure 3.11c, Tables 3.2 and Table 3.3 represent the reproducibility experiments for the first time used, second time used- and third time used conventionally and microwave synthesized samples for the time ranging from 1h to 8h. It was found that the hydrogen production activity of the above samples decreased to almost 94%, 86% and 74%, respectively.

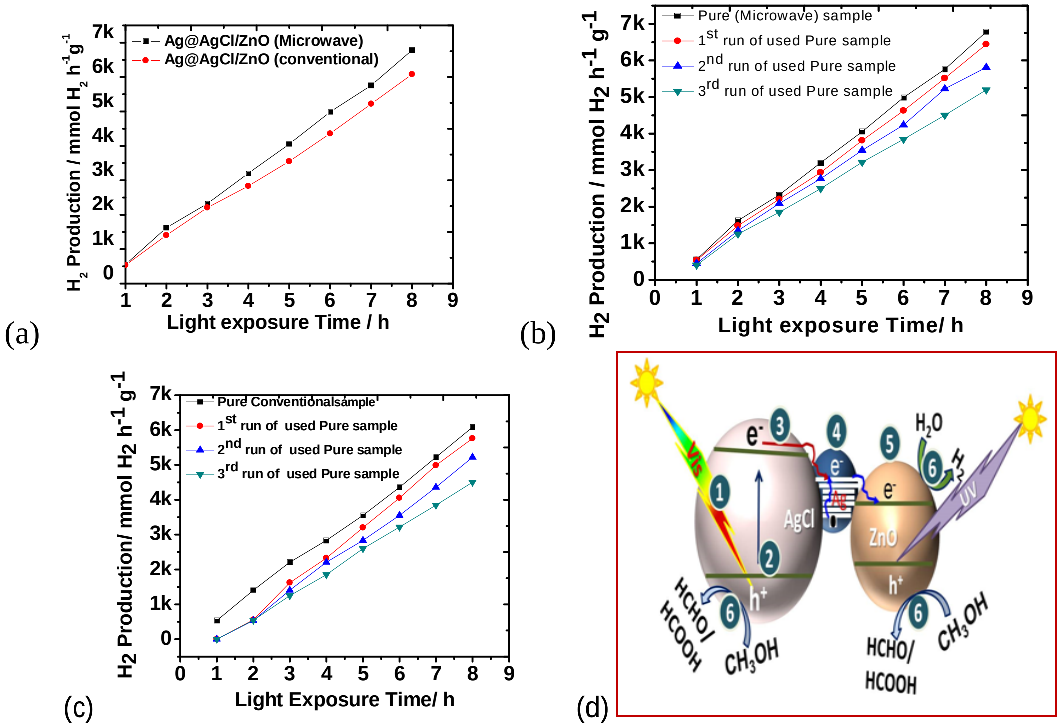

Figure 3.11 Photocatalytic hydrogen production by (a) pristine NC(Ag/AgCl@ZnO) prepared by the conventionally (red)- and microwave (black)- method. Reproducibility of pristine checked for the first time used, second time used- and third time- used (b) microwave (c) conventionally -synthesized samples, with respect to the time (1 h to 8 h) under 300 W Xe-light exposure. (d) The proposed representative electron transfer mechanism for nanocomposites.

Table 3.3 Hydrogen production form pristine, first time used, second time used- and third time- used conventionally synthesized samples.

Time in hour	**H_2 Production of Pure sample** µmol H_2 h^{-1} g^{-1}	**H_2 Production of I time used sample** µmol H_2 h^{-1} g^{-1}	**H_2 Production of II time used sample** µmol H_2 h^{-1} g^{-1}	**H_2 Production of III time used sample** µmol H_2 h^{-1} g^{-1}
1	536.71	0000.00	0000.00	0000.00
2	1404.41	0556.80	0536.71	0544.40
3	2207.86	1621.21	1404.41	1250.50
4	2835.26	2325.37	2207.86	1850.80
5	3554.11	3203.09	2835.26	2597.06
6	4359.24	4053.44	3554.11	3218.02
7	5221.07	4987.66	4359.24	3844.89
8	6082.90	5761.86	5221.07	4504.55

Table 3.4 Hydrogen production form pristine, first time used, second time used- and third time- used microwave synthesized samples.

Time / hour	**H_2 Production Pure sample /** µmol H_2 h^{-1} g^{-1}	**H_2 Production in I time used sample /** µmol H_2 h^{-1} g^{-1}	**H_2 Production in II time used sample /** µmol H_2 h^{-1} g^{-1}	**H_2 Production in III time used sample** / µmol H_2 h^{-1} g^{-1}
1	0556.80	0540.71	0450.00	0404.40
2	1621.21	1480.41	1345.78	1250.50
3	2325.37	2207.87	2086.50	1850.80
4	3203.09	2935.26	2765.98	2497.06
5	4053.44	3810.81	3542.11	3218.02
6	4987.66	4626.13	4235.60	3844.89
7	5761.86	5511.95	5223.34	4504.55
8	6782.32	6441.08	5809.67	5196.90

3.6 Study of nanocomposite System Ag/AgCl($BaCl_2$)@ZnO

3.6.1 Experimental: Materials and Synthesis Methods

3.6.1.1 Materials

All chemicals such as tetrahydrated zinc nitrate, barium chloride, sodium hydroxide, and silver nitrate, etc, were purchased from Sigma Aldrich and used without purification.

3.6.1.2 Synthesis (Conventional Method)

Under synthesis procedure 5.220 g tetrahydrated zinc nitrate and 2.110 g silver nitrate in 50 mL of DIW were added and the resulted mixture was stirred at room temperature for half an hour. Afterwards, it was followed by the addition of 5 M NaOH solution to adjust the pH of the solution 10 and above mixture was treated with 1.450 g $BaCl_2$ in 20 mL of water. Then, the suspension was refluxed at 90^{o}C for 3h. Resulted product was centrifuged, washed several times with DIW and ethanol and dried in an oven at 60^{o}C for 24 h.

3.6.2 Characterisation

3.6.2.1 Results

3.6.2.1.1 XRD

The phase purity of the Ag/AgCl($BaCl_2$)@ ZnO NC was studied using XRD profile, as shown in Figure1. Diffraction peaks of the studied samples are found at 27.942 °(111), 32.34 °(200), 46.34 °(220), 54.94 °(311), 57.58 ^{o}(222), 67.54 °(400), 74.76 °(331) and 76.82 ^{o}(420) attributed to the highly crystalline phases that corresponds to the face-centered cubic (chlorargyrite) phase (reference JCPDS card No.31-1238) of the AgCl with cell parameters: a=b=c= 5.548 and $\alpha=\beta=\gamma=90^o$ at z=4 and space group *Fm3m* (225), FCC zinc blende crystalline phase (JCPDS card No.80-0020; ZnS) of ZnO, and reflection peaks 31.79(100), 34.45(002), 31.61°(111), 34.26°(101), 36.10°(102), 47.37°(110), 56.40°(103), 62.68°(004) and 67.72° (112)correspond to the hexagonal structure of ZnO (JCPDS: 03-065-3411) with cell parameters: a=b=c= 5.345 Å, $\alpha=\beta=\gamma=90^o$ at z= 4 and space group *F4-3m* (216).The careful examination of diffraction peaks exhibits small peaks at 38.56° (111), 46.34°

(200), 67.54° (220), 76.82° (311) position that belongs to the standard JCPDS card No.04-0783 of pure silver (cell constants a=b=c= 4.0857 Å, $\alpha=\beta=\gamma=90\ ^{o}$ at z= 4 and space group *Fm3m* (225) that also confirmed the presence of the small silver particles and with minute traces of hexagonal(space group P62m, 189) $BaCl_2$ (PDF#45-1313) (Pfau et al., 2011) at 23.09°, 24.27°, 29.39°, 32.35°, 38.82°, 44.90°, 46.47°, 56.48° and 62.87°, 2 θ angles. The particle size (53.67nm) was calculated by using the Scherer’s formula.

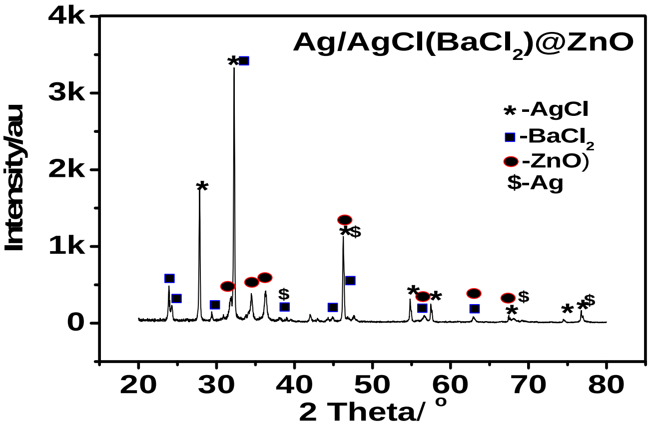

Figure 3.12 pattern of the nanocomposite Ag/AgCl($BaCl_2$)@ZnO NC shown as the combination of the XRD peaks equivalent to the bulk *FCC* chlorargyrite phase (JCPDS card No.31-1238) of the AgCl with cell parameters: a=b=c= 5.548 and $\alpha=\beta=\gamma=90^{o}$ at z=4 and space group *Fm3m* (225), FCC zinc blende crystalline phase (JCPDS card No. 03-065-3411 of ZnO) of ZnO with cell parameters: a=b=c= 5.345 Å, $\alpha=\beta=\gamma=90^{o}$ at z= 4 and space group *F4-3m* (216) and Ag content resemble to the standard JCPDS card No.04-0783 of pure silver(cell constants a=b=c= 4.0857 Å, $\alpha=\beta=\gamma=90\ ^{o}$ at z= 4 and space group *Fm3m* (225) and with minute traces of hexagonal $BaCl_2$ (PDF#45-1313) (Pfau et al., 2011)

3.6.2.1.2 FESEM & EDX

Surface morphology (2D-flax shape- particles), elemental composition and particle size (32.0 nm) of the nanocomposite was confirmed by the FESEM, EDX, FESEM elemental mapping. Nanocomposite crystallised in the form of flaxes that was confirmed from the corresponding FESEM analyses, illustrated by Figures 13a, 13b, 13c, 13d,13e, 13f and 13g.

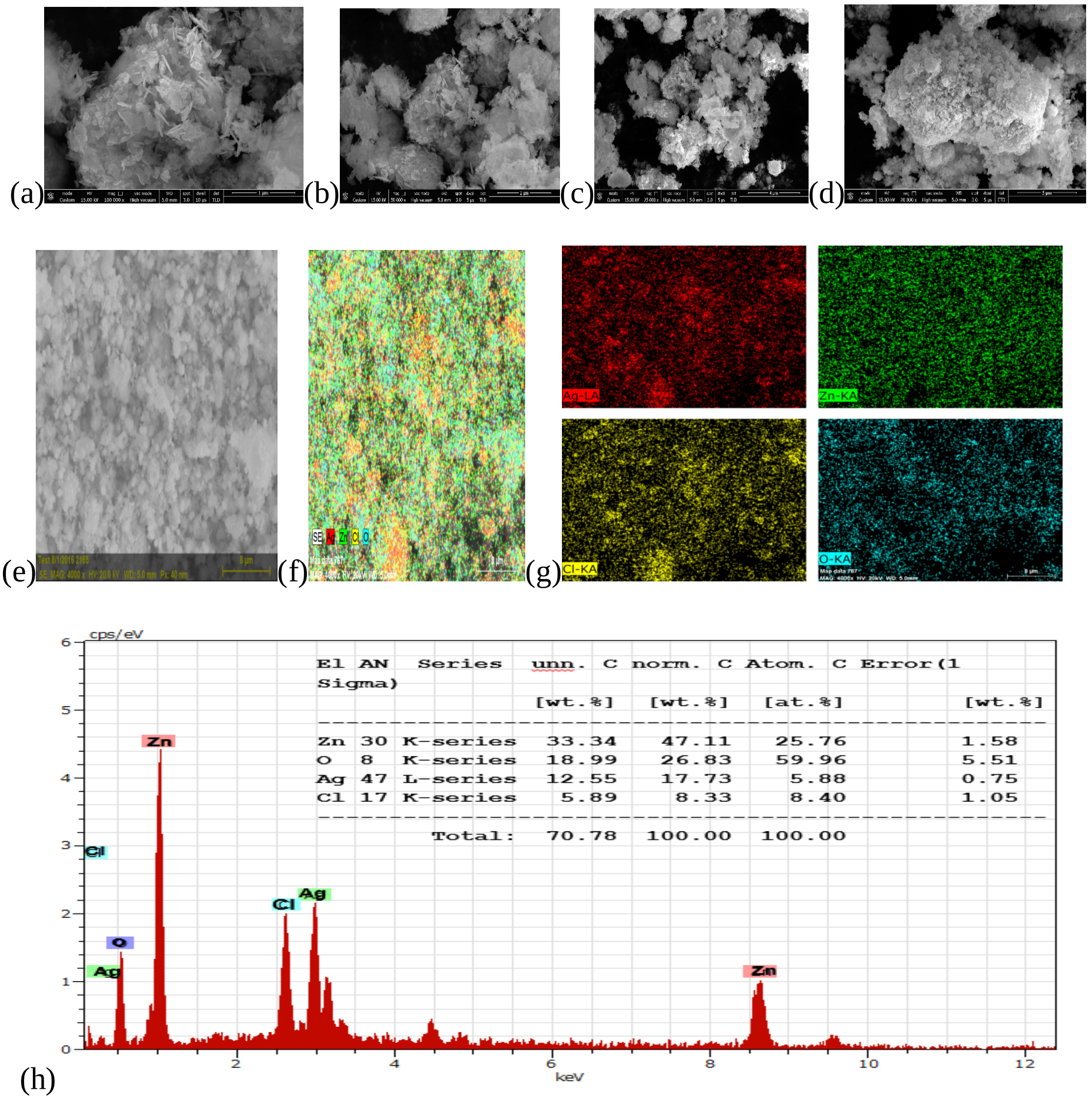

```
El AN  Series   unn. C norm. C Atom. C Error(1
Sigma)
                [wt.%]  [wt.%]  [at.%]          [wt.%]
--------------------------------------------------------
Zn 30 K-series  33.34   47.11   25.76            1.58
O  8  K-series  18.99   26.83   59.96            5.51
Ag 47 L-series  12.55   17.73    5.88            0.75
Cl 17 K-series   5.89    8.33    8.40            1.05
--------------------------------------------------------
         Total: 70.78  100.00  100.00
```

Figure 3.13. NC Ag/AgCl($BaCl_2$)@ZnO with corresponding (a), (b), (c) and (d) are FESEM images of nanocomposite at different scale. Micrographs (e), (f) and (g) represents the FESEM elemental mapping of Ag, Cl, Zn and O elements in nanocomposite Ag/AgCl($BaCl_2$)@ZnO. Corresponding EDX represented by (h).

No characteristic peaks for the elements other than Zn (25.76%), Ag (05.88%), Cl (08.40%), Ba (1.08%) and O (59.96%) actual concentration can't be determined due to the presence of the oxygen in air) were found in the EDX profile (Figure 13h) of the Ag/AgCl($BaCl_2$)@ZnO. That shows nanocomposite is rich in Ag (K_α= 2.984 KeV), Zn (K_α= 8.63 KeV; L_α=1.012 KeV), O (K_α= 0.525 KeV) and Cl (K_α= 2.621 KeV) compounds along with the traces of $BaCl_2$ was found around that exhibited by the K_α peak at 4.46 KeV position of abassica (binding energy) due to the element barium.

3.6.2.1.3 FTIR

Figure 3.14 reveals the FTIR peak positions of nanocomposite sample Ag/AgCl($BaCl_2$)@ZnO prepared using one pot refluxing method at 3437.7(b), 2919.2(vw), 1632.6(vw), 1447.40(s), 1384.14(vs), 1025.3(vw), 421.98 (w) cm^{-1} due to the presence of the intra- or inter-molecular bonded –OH groups.

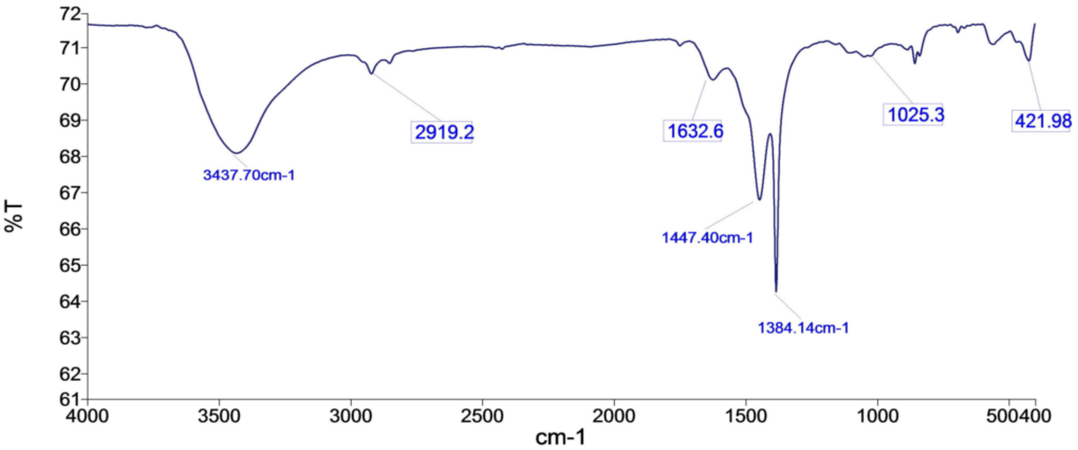

Figure 3.14 FTIR spectrum of the nanocomposite Ag/AgCl($BaCl_2$)@ ZnO.

Where, the general range 3700 – 3440 cm^{-1} may be assigned to asymmetrical and symmetrical O-H stretching vibration modes of hydrated water and the peak at 1632 cm^{-1} belonged to O-H bending vibration mode. 1447.40(s) and 1384.14(vs) cm^{-1} peaks attributed to M-Cl band stretching vibration peak and 1025.3 (vw) reflected the bending vibration peak of M-Cl band and in comparison to pure $BaCl_2$ FTIR, synthesised samples show lower side due to the bulky chemical environment of Ag/AgCl($BaCl_2$)@ZnO to 421.98 (w) cm^{-1} represents the Zn-O bending vibration of ZnO.

3.6.2.1.4 Water Splitting

Table 3.5 and Figure 3.15 represents the hydrogen production activity of the nanocomposite Ag/AgCl($BaCl_2$)@ZnO with time in 20% methanol solution under visible light irradiation. Gradual increase in hydrogen production was observed with the time as illustrated by Figure 3.15.

Table 3.5 Hydrogen generation of nanocomposite Ag/AgCl($BaCl_2$)@ZnO with time duration.

S. No.	Time (min.)	Time (h)	H_2 in mL	No. of moles(n)
1	13	0.21	1.5	0.061×10^{-3}
2	17	0.28	2.0	0.081×10^{-3}
3	22	0.36	2.5	0.10×10^{-3}
4	26	0.45	3.0	0.12×10^{-3}
5	30	0.50	3.5	0.14×10^{-3}
6	34	0.56	4.0	0.16×10^{-3}
7	37	0.61	4.5	0.18×10^{-3}
8	42	0.70	5.0	0.20×10^{-3}
9	47	0.78	5.5	0.22×10^{-3}
10	52	0.86	6.0	0.24×10^{-3}
11	60	1.00	6.5	0.26×10^{-3}
12	65	1.08	7.0	0.28×10^{-3}
13	73	1.21	7.7	0.31×10^{-3}
14	94	1.56	9.7	0.39×10^{-3}

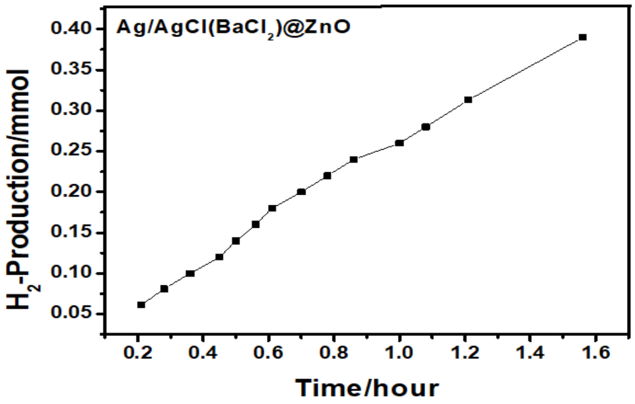

Figure 3.15 Hydrogen generation of nanocomposite Ag/AgCl($BaCl_2$)@ZnO with time.

3.7 Study of nanocomposite System Ag/AgPO$_4$ @ ZnO

3.7.1 Experimental: Materials and Methods:

3.7.1.1 Materials

All chemicals such as tetrahydrated zinc nitrate, Ammonium phosphate, sodium hydroxide, and silver nitrate, etc, were purchased from Sigma Aldrich and used without purification.

3.7.1.2 Synthesis (Conventional Method)

5.220 g tetrahydrated zinc nitrate and 2.110 g silver nitrate in 50 ml DIW were stirred at room temperature, followed by the addition of 5 M NaOH solution to adjust the pH of the solution 10. Above solution was treated with 1.450 g $(NH_4)_3PO_4$ in 20 ml of water. Then, the suspension was refluxed at 90^{o}C for 3h. Resulted product was centrifuged, washed several times with DIW and ethanol and dried in an oven at 60^{o}C for 24h.

3.7.2 Characterization

3.7.2.1 Results

3.7.2.1.1 XRD

XRD profile (Figure 3.16) revealed that nanocomposite Ag/Ag_3PO_4@ZnO consist of three phases i.e.: 24.17,31.22 ^{o} 34.62 ^{o}, 56.30 ^{o}, 62.22 ^{o} correspond to the hexagonal structure FCC zinc blende crystalline phase (JCPDS card No.80-0020; ZnS) of ZnO with cell parameters: a=b=c= 5.345 Å, $\alpha=\beta=\gamma=90^{o}$ at z= 4 and space group *F4-3m* (216). Peaks at 38.15 ^{o}, 43.82 ^{o} and 64.24 ^{o} belongs to pure Ag with cell constants a=b=c= 4.0857 Å, $\alpha=\beta=\gamma=90$ ^{o} at z= 4 and space group *Fm3m* (225) and diffraction peaks 20.89 ^{o}, 29.21 ^{o}, 33.36 ^{o}, 36.64 ^{o}, 46.97 ^{o}, 55.31 ^{o} corresponding to the crystal plane of (110), (200), (210), (211), (220), (310), (222), and (320), (respectively belongs to the body-centered cubic (bcc) structure of Ag_3PO_4 with cell constant of a= 6.013 Å (JCPDS no. 84-512). (P.S. Saud et al./Journal of Colloid and Interface Science 465 (2016) 225–232) Debye- Scherer's equation used to determine the particle size of the nanocomposite Ag/Ag_3PO_4@ZnO i.e. 38.82nm.

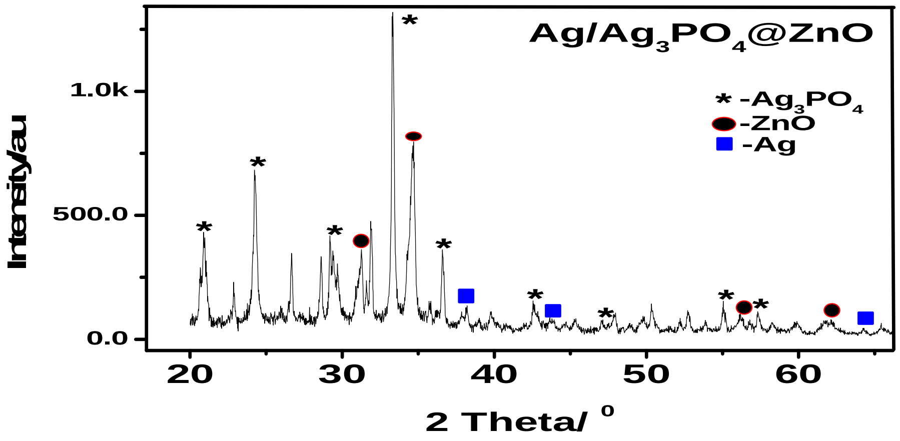

Figure 3.16 X Ray Diffraction profile of the nanocomposite Ag/Ag_3PO_4@ZnO, synthesized by one pot method.

3.7.2.1.2 FESEM & EDX

Figures 3.17a, 3.17b, 3.17c and 3.17d, are FESEM images of Ag/Ag_3PO_4@ZnO that showing the surface morphology (rice grain shape particles and particle size (length= 4.07nm width =0.91nm) of the nanocomposite. FESEM elemental mapping and corresponding EDX analyses, as represented by Figures 3.17(e)-3.17(g) and Figure 3.17(h), respectively. No characteristic peaks for the elements other than Zn (17.13%) K_α and $L_{\alpha-}$ edge at 8.6 KeV and 1.012 KeV respectively, Ag (06.79%) L_α at 2.8396 KeV, P (09.93%) K_α at 2.013 KeV and O (66.16%) K_α at 0.525 KeV position of binding energy, were found. The actual concentration of oxygen can't be determined due to the presence of the oxygen in air, which was found in the EDX profile of the Ag/$AgPO_4$ @ZnO, as illustrated by the Figure 3.17(h).

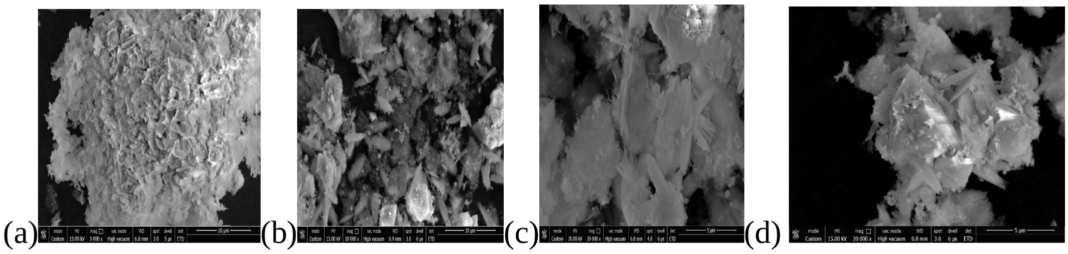

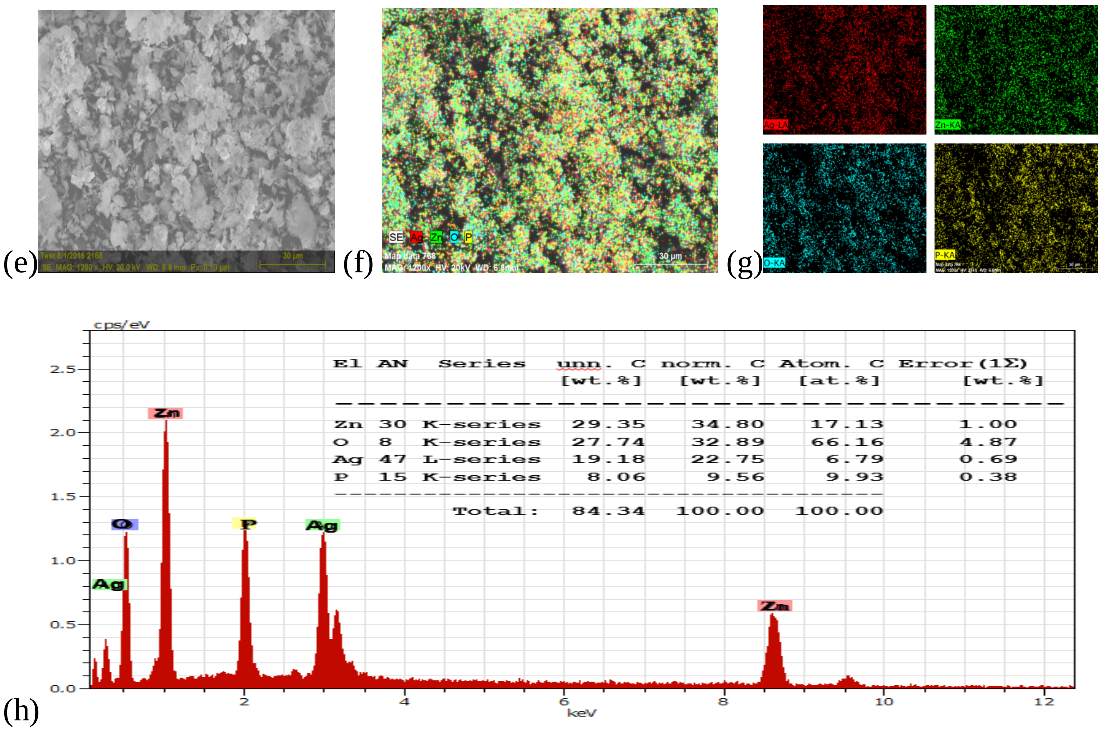

Figure 3.17 Ag/Ag_3PO_4@ZnO with corresponding (a), (b), (c) and (d) are FESEM images of nanocomposite, prepared by one pot synthesis and microwave route. (e), (f) and (g) belongs to the FESEM elemental mapping of Ag, P, Zn and O elements in Ag/Ag_3PO_4@ ZnO. (h) FESEM supported EDX showing elemental composition of Ag, Zn, O and P.

3.7.2.1.3 FTIR

FTIR peak positions of nanocomposite sample Ag/Ag_3PO_4@ ZnO (made by using one pot refluxing method), are exhibited by Figure 3.18, which reveals the vibrations at 3439.46 cm^{-1} (Intra- or inter-molecular bonded OH stretching), 1633.97 cm^{-1} (-OH bending), 1384.31 cm^{-1} (P-O stretching), 1019.77 cm^{-1} (P-O bending) and 588.25 cm^{-1} (out of plane bending P-O bending and Zn-O).

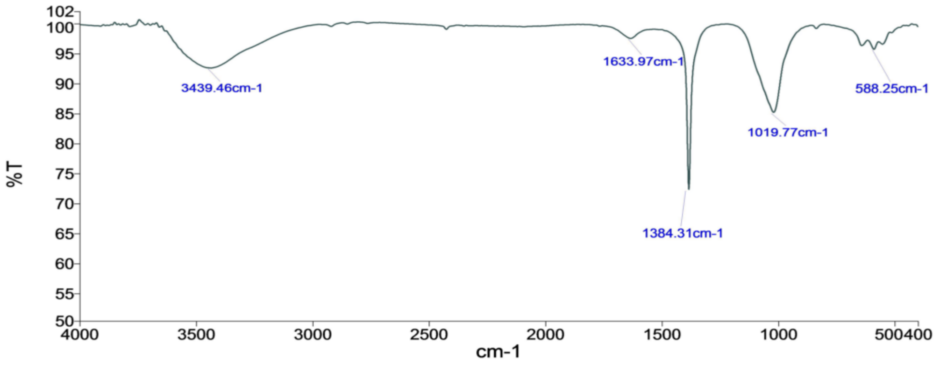

Figure 3.18 FTIR spectrum of nanocomposite Ag/Ag_3PO_4@ ZnO, prepared by conventional one pot method.

Table 3.6 and Figure 3.19 represents the hydrogen production activity of the nanocomposite Ag/Ag_3PO_4)@ZnO with time in 20% methanol solution under visible light irradiation. Gradual increase in hydrogen production was observed with the time as illustrated by Figure 3.19.

3.7.2.1.4 Water Splitting

Table 3.6 Various time and their corresponding hydrogen generation for Ag/Ag_3PO_4@ ZnO.

S. No.	Time (min.)	Time (h)	H_2 in mL	No. of moles(n)
1	20	0.33	1.5	0.061×10^{-3}
2	30	0.50	2.0	0.081×10^{-3}
3	45	0.75	2.5	0.10×10^{-3}
4	62	1.03	3.0	0.12×10^{-3}
5	75	1.25	3.5	0.14×10^{-3}
6	84	1.40	4.0	0.16×10^{-3}
7	94	1.56	4.5	0.18×10^{-3}
8	122	2.03	5.2	0.21×10^{-3}
9	183	3.05	7.3	0.29×10^{-3}

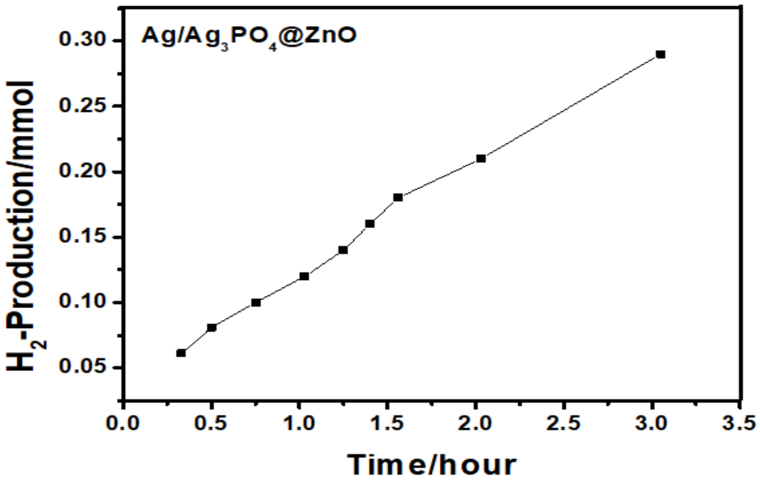

Figure 3.19 Hydrogen generation of nanocomposite Ag/Ag_3PO_4@ZnO with time.

3.8 Study of nanocomposite System Ag/$AgNO_3$@ ZnO

3.8.1 Experimental: Materials and Methods

3.8.1.1Materials

Tetrahydrated zinc nitrate, sodium nitrate, sodium hydroxide, and silver nitrate, etc, were purchased from Sigma Aldrich and used as such.

3.8.1.2 Synthesis (Conventional Method)

5.220 g Tetrahydrated zinc nitrate and 2.110 g silver nitrate were dissolved in 50 mL DIW under constant stirring at room temperature, which was followed by the addition of 5 M NaOH solution to adjust the pH of the solution to 10. Above solution was treated with 1.450 g $NaNO_3$ dissolved in 20 mL of water. Then, the suspension was refluxed at 90°C for 3h. Resulted product was centrifuged, washed several times with the 1:1 mixture of DIW and ethanol and dried in an oven at 60°C for 24 h.

3.8.2 Characterization

3.8.2.1 Results

3.8.2.1.1 XRD

The phase purity of the Ag/$AgNO_3$($NaNO_3$)/ ZnO NC was studied using XRD profile, as shown in Figure3.20. Diffraction peaks of the studied samples are found at 20.58 °, 31.76 °, 34.51 °, 38.22 °, 65.70 ° $AgNO_3$, 38.22 °, 47.65 °, 68.05 ° Ag with cell constants a=b=c= 4.0857 Å, $\alpha=\beta=\gamma=90$ ° at z= 4 and space group *Fm3m* (225) and ZnO 32.92 ° 34.51 °, 36.27 °, 47.64 °, 56.68 °, 62.76 °,68.05 ° corresponding to the hexagonal structure of ZnO of FCC zinc blende crystalline phase (JCPDS card No.80-0020; ZnS) with cell parameters: a=b=c= 5.345 Å, $\alpha=\beta=\gamma=90°$ at z= 4 with space group *F4-3m* (216). The particle size of the NC (32.01nm) was calculated by using the Scherer's formula.

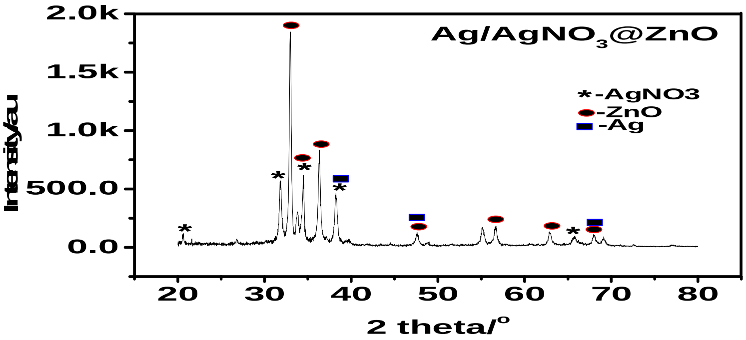

Figure 3.20 Diffraction patterns of the nanocomposite Ag/$AgNO_3$@ ZnO, synthesized by one pot method show three phases i.e. cubic Ag with cell constants a=b=c= 4.0857 Å, $\alpha=\beta=\gamma=90$ ° at z= 4 with space group *Fm3m* (225), FCC zinc

blende crystalline phase (JCPDS card No.80-0020; ZnS) of ZnO with cell parameters: a=b=c= 5.345 Å, $\alpha=\beta=\gamma=90^o$ at z= 4 with space group *F4-3m* (216) and Orthorhombic $AgNO_3$ (JCPDS 01- 0856). Pbca [61] with cell parameters, a=7.086 Å, b=7.447 Å,c=10.300 Å and volume= 543.545 Å.

3.8.2.1.2 FESEM & EDX

Surface morphology (agglomeration of needle shape particles), metallic composition and particle size (34.88 nm) of the nanocomposite Ag/$AgNO_3$@ ZnO was confirmed by the FESEM images by the Figures 3.21(a), 3.21(b), 3.21(c) and 3.21(d) at different scales. FESEM elemental mapping as represented by the Figures 3.21(e), 3.21(f) and 3.21(g).

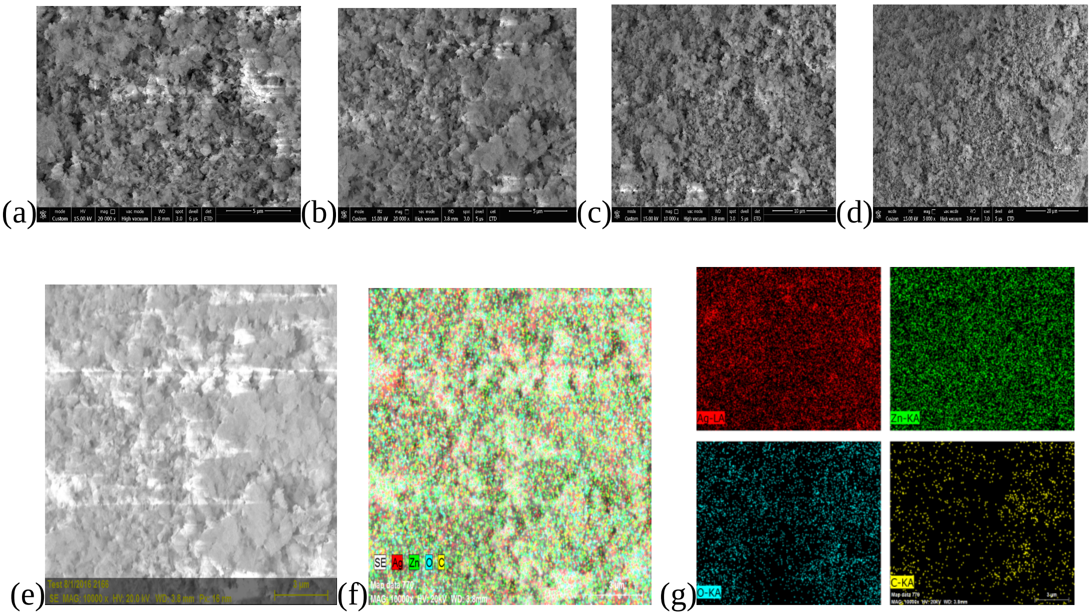

Figure 3.21 Nanocomposites Ag/$AgNO_3$@ ZnO exhibited the FESEM images of nanocomposite, prepared by one pot synthesis in (a), (b), (c) and (d). (e), (f) and (g) represent the corresponding FESEM elemental mapping of Ag, N, Zn and O elements in nanocomposite Ag/$AgNO_3$@ZnO.

And their corresponding EDX analyses are shown in Figure 3.20, where no characteristic peaks for the elements other than Zn (39.46%) K_α and L_α -edge at 8.6 KeV and 1.012 KeV respectively, Ag (13.40%) L_α -edge at 2.8396 KeV, N (2.82%) K_α-edge at 0.392 KeV and O (59.49%) K_α -edge at 0.525 KeV position of binding energy. That confirmed the formation of the nanocomposite Ag/$AgNO_3$@ ZnO.

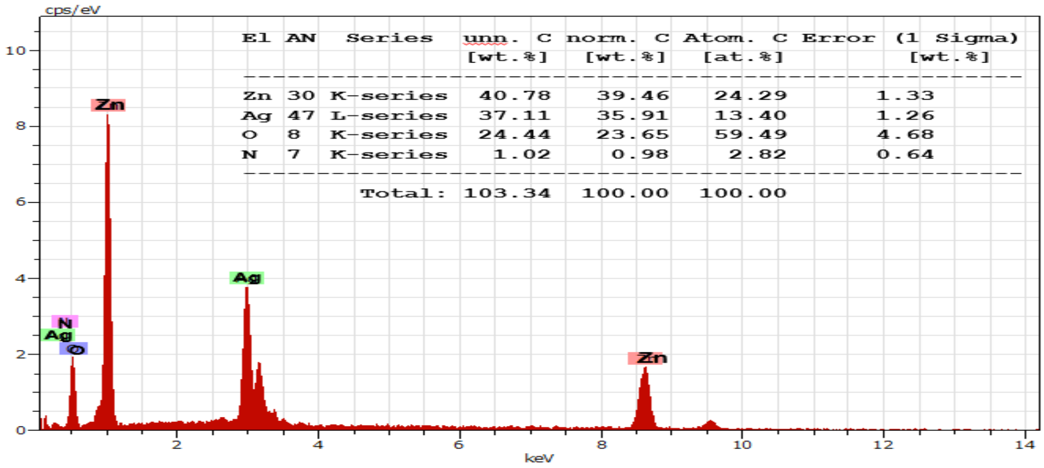

El	AN	Series	unn. C [wt.%]	norm. C [wt.%]	Atom. C [at.%]	Error (1 Sigma) [wt.%]
Zn	30	K-series	40.78	39.46	24.29	1.33
Ag	47	L-series	37.11	35.91	13.40	1.26
O	8	K-series	24.44	23.65	59.49	4.68
N	7	K-series	1.02	0.98	2.82	0.64
		Total:	103.34	100.00	100.00	

Figure 3.22 FESEM supported EDX profile of Ag/AgNO$_3$@ZnO.

3.8.2.1.3 FTIR

FTIR profile of the nanocomposite Ag/AgNO$_3$@ ZnO was exhibited in Figure 3.23 with vibration peaks at 3428.26 (OH-str.), 1648.6(-OH bending),1384.83(NO$_3$ stretching) 881.47(NO$_3$ bending), 549.83, 433.96(ZnO) cm^{-1}

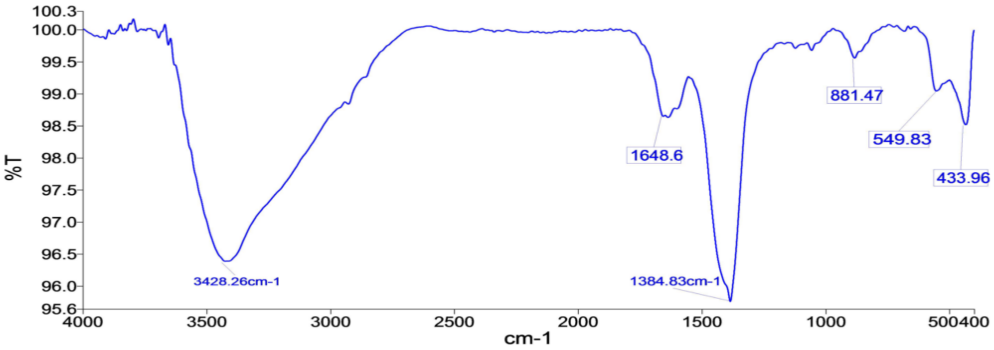

Figure 3.23 FTIR spectrum of the nanocomposite sample Ag/AgNO$_3$@ ZnO prepared by one pot refluxing method

3.8.2.1.4 Water Splitting

Table 3.7 and Figure 3.24 represents the hydrogen production activity of the nanocomposite Ag/AgNO$_3$)@ZnO with time in 20% methanol solution under visible light irradiation. Gradual increase in hydrogen production was observed with the time as illustrated by Figure 3.24.

Table 3.7 Hydrogen generation for Ag/AgNO$_3$@ ZnO with time.

S. No.	Time (min.)	Time (h)	H_2 in mL	No. of moles(n) of H_2 produced
1	19	0.31	1.5	0.061×10^{-3}
2	25	0.41	2.0	0.081×10^{-3}
3	29	0.48	2.5	$0. 10 \times 10^{-3}$
4	35	0.58	3.0	$0. 12 \times 10^{-3}$
5	39	0.65	3.5	0.14×10^{-3}
6	43	0.71	4.0	0.16×10^{-3}
7	50	0.83	4.5	0.18×10^{-3}
8	60	1.00	5.0	0.20×10^{-3}
9	68	1.13	5.5	0.22×10^{-3}
10	79	1.31	6.0	0.24×10^{-3}
11	85	1.41	6.5	0.26×10^{-3}
12	120	2.00	8.2	0.33×10^{-3}
13	137	2.25	9.0	$0..36 \times 10^{-3}$
14	155	2.58	10.2	$0..41 \times 10^{-3}$

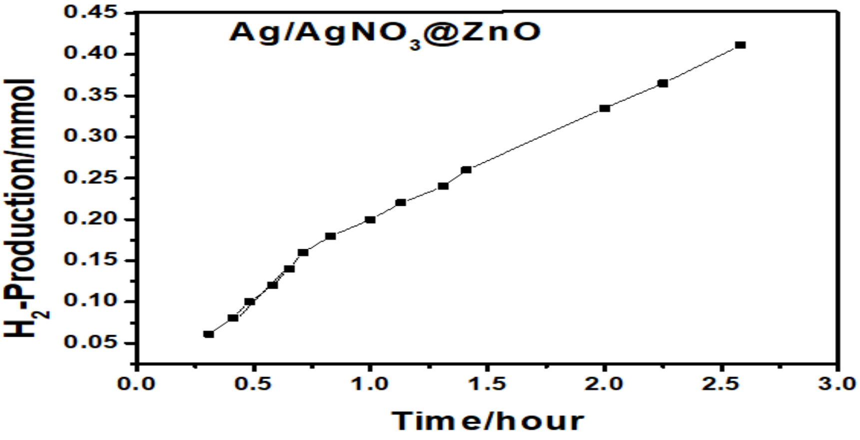

Figure 3.24 Hydrogen generation of nanocomposite Ag/AgNO$_3$@ZnO with time.

3.9 Study of nanocomposite System $Ag/Ag_2CO_3@ZnO$

3.9.1 Experimental: Materials and Methods

3.9.1.1 Materials

Tetrahydrated zinc nitrate, sodium carbonate, sodium hydroxide, and silver nitrate, etc. of Sigma Aldrich were used as purchased from without further purification.

3.9.1.2 Synthesis (Conventional Method)

5.220 g $Zn(NO_3)_2.4H_2O$ and 2.110 g $AgNO_3$ were mixed well in 50 mL of deionized water (DIW) were stirred at room temperature and followed by the addition of 5M NaOH solution to fix the pH at 10. Above solution was treated with 1.450 g Na_2CO_3 in 20 ml of DIW. Then, the suspension was refluxed at $90^{o}C$ for 3h. Resulted product was centrifuged and washed with DIW and ethanol in 1:1 Ratio and afterwards it was dried in an oven at $60^{o}C$ for 24 h.

3.9.2 Characterisation

3.9.2.1 Results

3.9.2.1.1 XRD

Diffraction patterns of the nanocomposite $Ag/Ag_2CO_3@$ ZnO, was synthesized by one pot method, shown by Figure 3.25. The phase purity of the $Ag/Ag_2CO_3@$ ZnO NC was studied using XRD profile, as shown in Figure3.25. Diffraction peaks of the studied samples are found at 2= 20.62 ^{o}, 29.03 ^{o}, 33.74 ^{o}, 34.48 ^{o}, 38.32 ^{o}, 39.56 ^{o}, 41.78 ^{o}, 47.60 ^{o}, 51.42 ^{o}, 55.15 ^{o} and 56.63 ^{o} for Ag_2CO_3.These diffraction peaks could be indexed to the crystallite planes of (110), (101), (130), (200) and (031) of monoclinic Ag_2CO_3 of phase PDF 26-0339. 38.32 ^{o} and 47.66 ^{o} belongs to pure Ag metal with cell constants a=b=c= 4.0857 Å, $\alpha=\beta=\gamma=90$ ^{o} at z= 4 and space group *Fm3m* (225) and ZnO 31.76 ^{o},34.48 ^{o}, 36.34 ^{o}, 47.66 ^{o} and 56.63 ^{o} correspond to the hexagonal structure of ZnO of FCC zinc blende crystalline phase (JCPDS card No.80-0020; ZnS) with cell parameters: a=b=c= 5.345 Å, $\alpha=\beta=\gamma=90^{o}$ at z= 4 and space group *F4-3m* (216) an. The particle size of the NC (29.26nm) was calculated by using the Scherer's formula.

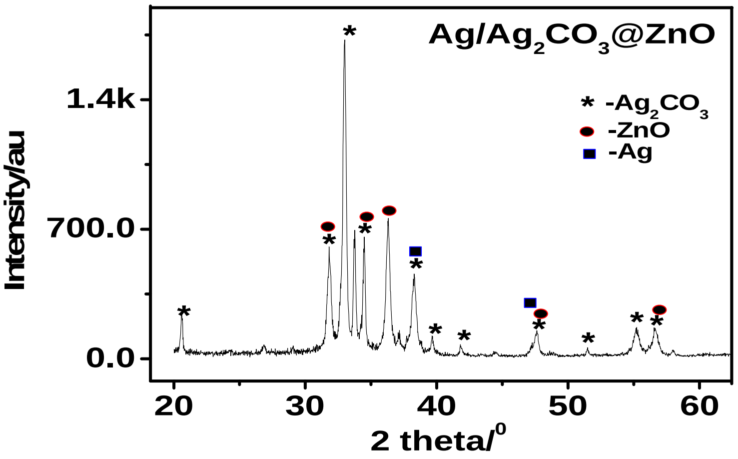

Figure 3.25 XRD patterns of the nanocomposite Ag/Ag$_2$CO$_3$@ZnO, synthesized by one pot method. FCC zinc blende crystalline phase (JCPDS card No.80-0020; ZnS) of ZnO with cell parameters: a=b=c= 5.345 Å, $\alpha=\beta=\gamma=90^o$ at z= 4 and space group *F4-3m* (216) and Ag$_2$CO$_3$ with monoclinic phase PDF# 26-0339.

3.9.2.1.2 FESEM and EDX

FESEM images shown in Figures 3.26(a), 3.26 (b), 3.26 (c) and 3.26 (d) represent the surface morphology (flax of thickness 38.0 nm), and particle size (38.0 nm) of the nanocomposite. FESEM elemental mapping images are represented by Figures 3.23e, 3.23f, and 3.23g.

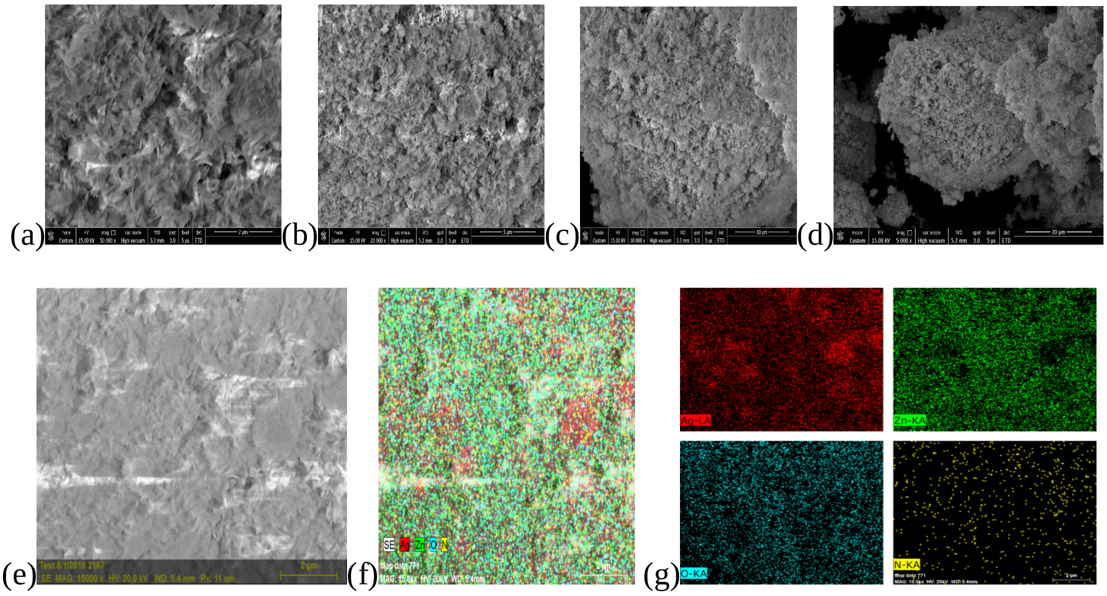

Figure 3.26 Nanocomposite Ag/Ag$_2$CO$_3$@ZnO.corresponds to their FESEM images in (a), (b), (c) and (d), prepared by one pot synthesis route. Images in (e), (f), and (g) showed the FESEM elemental mapping of Ag, C, Zn and O elements present in Ag/Ag$_2$CO$_3$@ZnO.

And their corresponding EDX analyses are shown in Figure 3.24, where no characteristic peaks for the elements other than Zn (27.03%) K_α and L_α -edge at 8.6 KeV and 1.012 KeV respectively, Ag (14.63%) L_α -edge at 2.8396 KeV, C(15.89%) K_α-edge at 0.277 KeV and O (42.45%) K_α -edge at 0.525 KeV position of binding energy. That confirmed the formation of the nanocomposite Ag/Ag_2CO_3@ZnO.

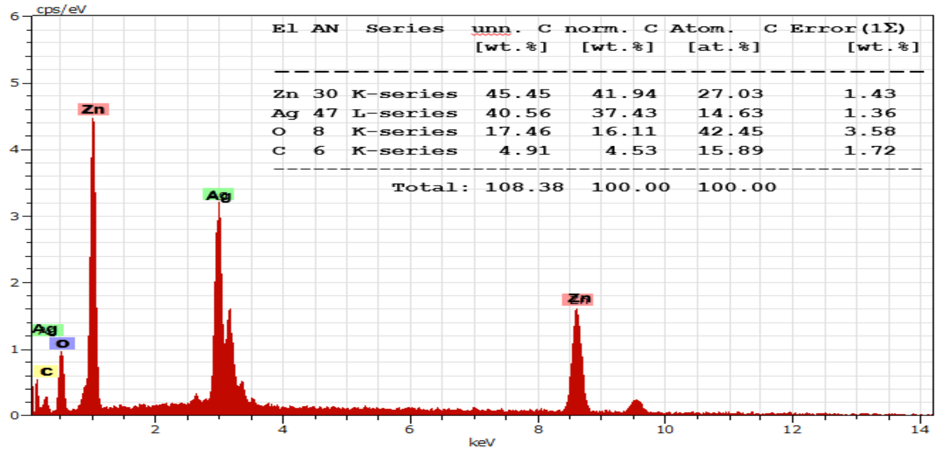

El	AN	Series	unn. C [wt.%]	norm. C [wt.%]	Atom. C [at.%]	Error (1Σ) [wt.%]
Zn	30	K-series	45.45	41.94	27.03	1.43
Ag	47	L-series	40.56	37.43	14.63	1.36
O	8	K-series	17.46	16.11	42.45	3.58
C	6	K-series	4.91	4.53	15.89	1.72
		Total:	108.38	100.00	100.00	

Figure 3.27 FESEM supported EDX showing elemental presence of Ag, Zn, O and C of Ag/Ag_2CO_3@ZnO.

3.9.2.1.3 FTIR

Vibrational peak positions of nanocomposite Ag/Ag_2CO_3@ZnO.sample one pot refluxing method at 3398.31 (OH- Str. band), 1657.98 (OH-bending), 1384.79(carbonate str.), 856.12(CO_3^- bending), 543.74 (ZnO) cm^{-1}, are illustrated by the Figure 3.28

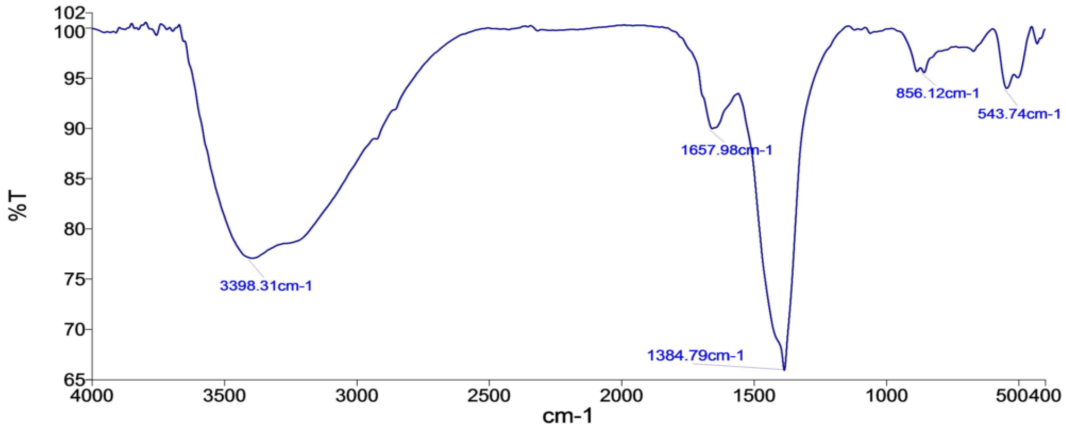

Figure 3.28 FTIR vibration spectrum recorded for Ag/Ag_2CO_3@ZnO.

3.9.2.1.4 Water Splitting

Table 3.8 and Figure 3.29 represents the hydrogen production activity of the nanocomposite Ag/Ag_2CO_3@ZnO with time in 20% methanol solution under visible light irradiation. Gradual increase in hydrogen production was observed with the time as illustrated by Figure 3.29.

Table 3.8 Hydrogen generation for Ag/Ag_2CO_3@ZnO with time.

S. No.	Time (min.)	Time (h)	H_2 in mL	No. of mmoles (n) of H_2 produced with time
1	05	0.08	1.5	0.061×10^{-3}
2	07	0.11	2,0	0.081×10^{-3}
3	12	0.20	2.5	0.10×10^{-3}
4	18	0.30	3.1	0.12×10^{-3}
5	24	0.40	3.5	0.14×10^{-3}
6	28	0.46	4.0	0.16×10^{-3}
7	32	0.53	4.5	0.18×10^{-3}
8	37	0.61	5.0	0.20×10^{-3}
9	42	0.70	5.5	0.22×10^{-3}
10	52	0.86	6.0	0.24×10^{-3}
11	72	1.20	7.0	0.28×10^{-3}
12	102	1.70	9.0	0.36×10^{-3}
13	126	2.10	11.0	0.44×10^{-3}

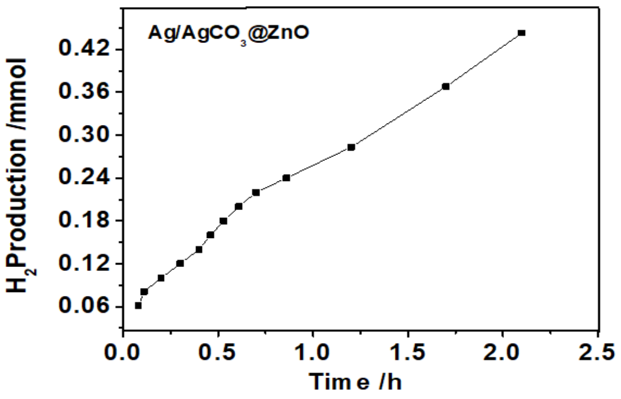

Figure 3.29 Hydrogen generation of nanocomposite Ag/Ag_2CO_3@ZnO with time.

3.10 Study of nanocomposite System Ag/Ag_2SO_3@ZnO system

3.10.1 Experimental: Methods and Materials

3.10.1.1 Materials

All chemicals such as tetrahydrated zinc nitrate, sodium sulphite, sodium hydroxide, and silver nitrate, etc, were purchased from Sigma Aldrich and used without further purification.

3.10.1.2 Synthesis (Conventional Method)

5.220 g tetrahydrated zinc nitrate and 2.110 g silver nitrate were mixed with 50 mL DIW in 250mL round bottom flask and stirred at room temperature, followed by the addition of 5 M NaOH solution to adjust the pH of the solution 10. Above solution was treated with 1.450 g Na_2SO_3 in 20 mL of water. Then, the suspension was refluxed at 90^{o}C for 3h. Resulted product was centrifuged, washed several times with DIW and ethanol and dried in an oven at 60^{o}C for 24 h.

3.10.2 Characterisation:

3.10.2.1 Result

3.10.2.1.1 XRD

The phase purity of the Ag/Ag_2SO_3@ZnO NC was studied using XRD profile, as shown in Figure 3.30. Diffraction peaks of the studied samples are found at $2\theta=24.48^{o}$, 27.12^{o}, 31.88^{o}, 38.15^{o}, 41.16^{o}, 44.30^{o}, 47.56^{o}, 49.93^{o}, 62.85^{o} Ag_2SO_3 matches with the standard JCPDS file no. of 23-0644, Ag Peaks at $2\theta= 38.15^{o}$, 43.82^{o} and 64.24^{o} belongs to pure Ag with cell constants a=b=c= 4.0857 Å, $\alpha=\beta=\gamma=90^{o}$ at z= 4 and space group *Fm3m* (225) and reflections at $2\theta=31.88^{o}$, 34.39^{o}, 36.27^{o}, 47.56^{o}, 56.58^{o}, 62.85^{o}, 66.49^{o} correspond to the hexagonal structure of ZnO with cell parameters: a=b=c= 5.345 Å, $\alpha=\beta=\gamma=90^{o}$ at z= 4 and space group *F4-3m* (216). The particle size of the NC (45.14 nm) was calculated by using the Scherer’s formula.

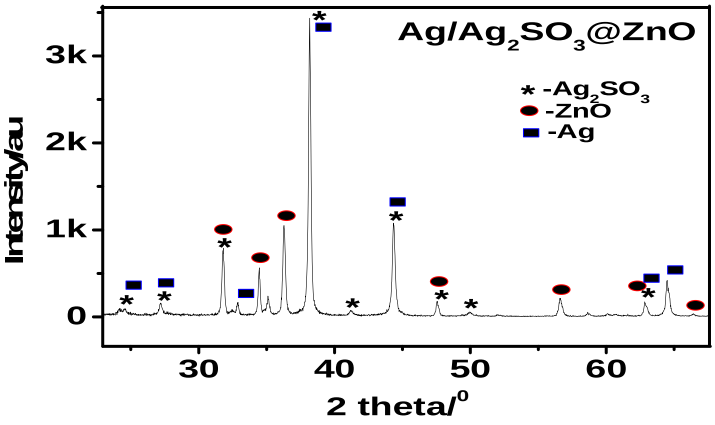

Figure 3.30 Diffraction patterns of the nanocomposite Ag/Ag_2SO_3@ZnO, synthesized by one pot method.

3.10.2.1.2 FESEM and EDX

Surface morphology (rod/needle shape) and particle size (1length=1.13 nm width=0.17 nm) of the nanocomposite Ag/Ag_2SO_3@ZnO was confirmed by the FESEM images shown in Figures 3.31(a), 3.31(b), 3.31(c) and 3.31(d).

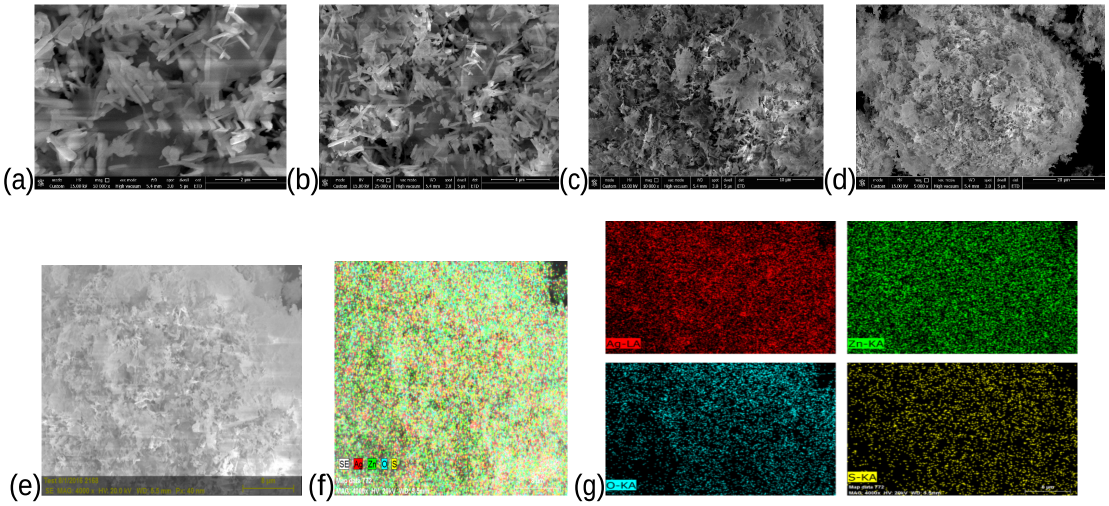

Figure 3.31 Nanocomposite Ag/Ag_2SO_3@ZnO prepared by one pot synthesis, showing the FESEM images (a), (b), (c) and (d) at different scale. (e), (f and (g) are the FESEM elemental mapping of nanocomposite Ag/Ag_2SO_3@ZnO with respect to the elements Ag, Zn, O and S.

FESEM elemental mapping analyses, as represented by Figures 3.31e-3.31g. No characteristic elemental peaks for the elements other than Zn (25.98%) K_{α} and L_{α} -edge at 8.6 KeV and 1.012 KeV respectively, Ag (16.09%) L_{α} -edge at 2.8396 KeV, S(1.17%) K_{α}-edge at 2.307 KeV and O (56.17%; actual concentration can't be determined due to the presence of the oxygen in air) K_{α} -edge at 0.525 KeV position of binding energy. That confirmed the formation of the nanocomposite $Ag/Ag_2SO_3@$ ZnO, were found in the EDX profile of the $Ag/Ag_2SO_3@ZnO$, as illustrated by the Figure 3.32.

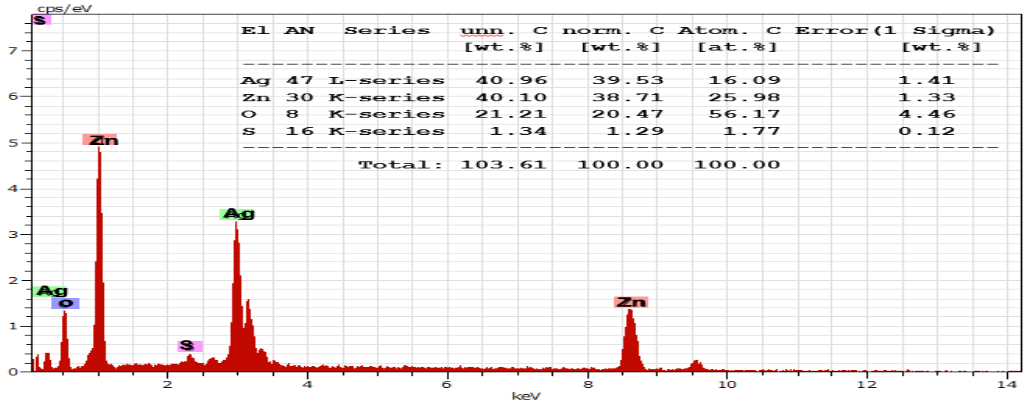

```
El AN  Series   unn. C norm. C Atom. C Error(1 Sigma)
               [wt.%]  [wt.%]  [at.%]          [wt.%]
-----------------------------------------------------
Ag 47 L-series  40.96   39.53   16.09           1.41
Zn 30 K-series  40.10   38.71   25.98           1.33
O  8  K-series  21.21   20.47   56.17           4.46
S  16 K-series   1.34    1.29    1.77           0.12
-----------------------------------------------------
        Total: 103.61  100.00  100.00
```

Figure 3.32 FESEM supported EDX showing elemental presence of Ag, Zn, O and S for the nanocomposite $Ag/Ag_2SO_3@ZnO$.

3.10.2.1.3 FTIR

FTIR vibrational peaks are observed at the frequency 3441.81(Intra- or inter-molecular stretching bonded OH), 2931.2, (bending OH band) 1620.6 (C=O stretching band),1392.9(SO_3 str. band), 1107.7(SO_3 bending band) and 515.10 (Zn—O bending) cm^{-1} for the nanocomposite $Ag/Ag_2SO_3@ZnO$, as shown by the Figure 3.33**.**

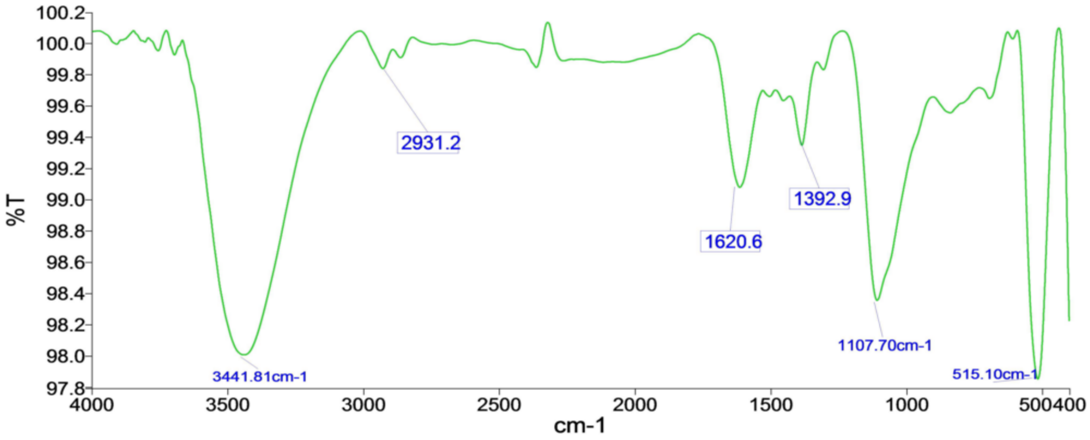

Figure 3.33 FTIR peak positions of nanocomposite sample $Ag/Ag_2SO_3@ZnO$, prepared using one pot refluxing method

3.10.2.1.4 Water Splitting

Table 3.9 and Figure 3.34 represents the hydrogen production activity of the nanocomposite Ag/$AgNO_3$@ZnO with time in 20% methanol solution under visible light irradiation. Gradual increase in hydrogen production was observed with the time as illustrated by Figure 3.34.

Table 3.9 Hydrogen generation of nanocomposite sample Ag/Ag_2SO_3@ZnO at different time intervals.

S. No.	Time (min.)	Time (h)	H_2 in mL	No. of moles(n)
1	15	0.25	1.5	0.061×10^{-3}
2	20	0.33	2.0	0.081×10^{-3}
3	30	0.5	2.5	0.10×10^{-3}
4	33	0.55	3	0.12×10^{-3}
5	38	0.63	3.5	0.14×10^{-3}
6	42	0.70	4	0.16×10^{-3}
7	50	0.83	4.5	0.18×10^{-3}
8	54	0.90	5	0.20×10^{-3}
9	59	0.98	5.5	0.22×10^{-3}
10	63	1.05	6	0.24×10^{-3}
11	68	1.13	6.5	0.26×10^{-3}
12	78	1.30	7	0.28×10^{-3}
13	87	1.45	8	0.32×10^{-3}

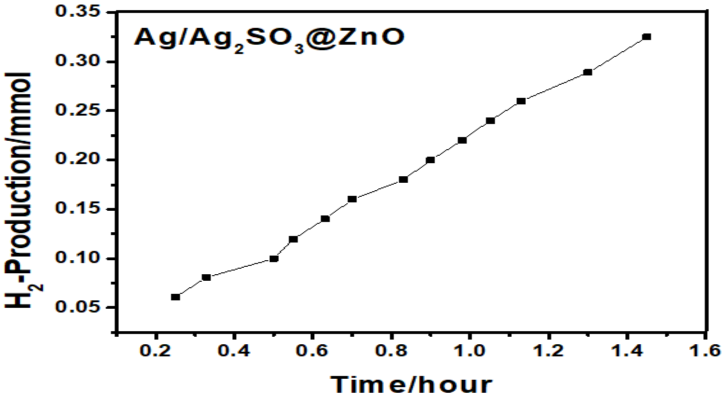

Figure 3.34 Hydrogen generation of nanocomposite Ag/$AgNO_3$@ZnO with time.

3.11 Result and Discussion

World, eventually witnessing the eco-degradation and political hostility on energy lines, which is a matter of prime global concern. Therefore, we all are looking forward to the clean energy sources that can replace the present conventional energy sources, as a fuel or energy carrier. Hydrogen rated as the best option on its merits i.e. high energy density (142 KJ/Kg), high heating value (52,000 Btu/lb), high auto ignition temperature (585 ^oC), high fuel efficiency (75%) and widest range of flammability (4-75%), etc. In contrast to the current hydrogen generation practices (steam reforming of methane), the use of solar energy and carbon-less fuel i.e. water along with a suitable photocatalyst, is an eco-benign way. A wide variety of photocatalytic materials are tested for hydrogen generation via water spitting. Unfortunately, most of them failed on the criteria of stability (in water and light), cost and efficiency (>10%). Recently, silver halides based plasmonic nanoparticles (NPs) have been attracted the attention as a superb class of nanocomposites (NCs) that used for visible-light-harvesting device (Xu et al., 2011; Wang et al., 2011; Li et al., 2013; Adhikari et al., 2013; Guo et al., 2013) Although, due to instability under sunlight (Hamilton JF 1974), silver halides AgX were seldom used as photocatalysts. However, Kakuta et al. studied the Ag^0 supported AgBr dispersed on a silica support that used for continuous H_2 production (1.00 mmol h^{-1} g^{-1} after 2 h) from 20% CH_3OH (as hole scavenger) in H_2O solution (Kakuta et al. 1999). They had observed that Ag NPs deposited on AgBr, which supported by silica, was not destroyed under successive UV/Vis illumination till 200 h (total 445 mmol per g of AgBr), thus assembly Ag/AgBr, was able to act as a stable photocatalyst under visible light, and eventually used to the synthesized the first visible-light plasmonic photocatalyst Ag@AgCl (i.e. Ag–AgCl). Moreover, SchKrch etal. proved that AgCl deposited on a conducting support (Au coated FTO) was used to photocatalyse the water for O_2 production (160 nmol.h^{-1}) in the presence of silver ions (as electron scavenger), under UV/Vis light exposure (Schürch et al., 2002) Similarly, 3D- hierarchical superstructures, concave cubes, and cubes of AgCl, were used as photocatalyst for O_2 generation via water splitting with their activity are 254 mmolg^{-1} for hierarchical superstructures, 187 mmolg^{-1} of concave cubic AgCl and 136 mmolg^{-1} of cubic AgCl in 5 h (Lou et al., 2012). The photoactivity of AgCl in presence of Ag^+ ions, extended from the UV to the visible light region under the process known as self-sensitization, which is due to the formation of silver species during the photoreaction, as follows (Equations 1-7):

$$[nAg^+, \quad mAgCl] + \frac{r}{2}H_2O \xrightarrow{light} [(n-r)Ag^+, \quad mAgCl, rAg^0] + rH^+ + \frac{r}{4}O_2 \qquad ...(1)$$

$$[(n-r)Ag^+, mAgCl, rAg^0] \xrightarrow{light} [nAg^+, mAgCl] + re^- \qquad ...(2)$$

$$[\ mAgCl]\{Ag^+\}_s \xrightarrow{light} [(m-1)AgCl]\ \{Ag^+Ag^0\}_{s,i} + [Cl^{\cdot}_s] \qquad ...(3)$$

$$2Cl^{\cdot}_s \rightarrow Cl_2 \qquad ...(4)$$

$$Cl_2 + H_2O \rightarrow HOCl + H^+ + Cl^- \qquad ...(5)$$

$$2HOCl \xrightarrow{Ag^+} O_2 + 2H^+ + 2Cl^- \qquad ...(6)$$

$$[(m-1)AgCl + Ag^+ + Cl^- \rightarrow [mAgCl] \qquad ...(7)$$

Equations 1 to 7, had been analyzed experimentally and theoretically (Pfanner et al., 1996; Glaus and Calzaferri,1999)

The comparison of experimental and calculated values for the ionization energy for different sized Ag clusters shows that Ag levels are located below the conduction band edge of AgCl. Additional AgCl surface states (SURS), as well as metal induced gap states (MIGS) from Ag/ AgCl cluster composites are also present in the band gap region of silver chloride that induced the self-sensitization in AgCl. Therefore, Ag/AgX on support can be used as good photocatalytic system (Calzaferri et al., 2001; Glaus et al., 2002; Sumi et al., 1980; Yu, 2009)

Table 3.10 Some state of art plasmonic catalyst for hydrogen generation.

SL. No.	**Plasmonic Material /supported photocatalyst**	**Light source**	**Conditions for H_2 generation**	**Amount of H_2 generation** μ mol H_2 h^{-1} g^{-1}	**Amount of O_2 generation** μ mol O_2 h^{-1} g^{-1}	**year**	**Reference**
1	Ag^0 supported -AgBr dispersed on silicadioxide support	100W high-pressure Hg lamp-with IR filter	20% CH_3OH (hole scavenger) in H_2O	1000 after 2 h	-	1999	Kakuta et al.
2	Ag@AgCl deposited on Au coated FTO	UV-Vis light exposure	In presence of Ag^+ ions	-	0.160 mol.h^{-1}	2002	Schürch et al.
3.	3D hierarchical superstructures , concave cubes , and cubes of AgCl	300 W Xe arc lamp	In presence of Ag^+ ions	----	254000, 187000 and 136 000 in 5h	2012	Lou et al.
4.	Au/ZnAlCeLDH and Au/ZnAlLDH	Solar light exposure	20% methanol	127 and 94	-	2013	Carja et al.
5.	Ag/ZnONRs and ZnONRs	Xe light source	20% methanol	8.7 and 4.3	-	2013	Chen et al.
6	Ag/AgCl/ZnO	Xe light source	20% methanol	1706.9		2017	This work

Some of the notable nanocomposite plasmonic materials are Ag@AgBr (Longhui et al., 2012), Au/TiO_2 (Tian and Tatsuma, 2005), gold/layered double hydroxides (Carja et al., 2013), Ag/AgCl@ZnO (Pirhashemi and Habibi-Yangjeh,2014), Ag embedded TiO_2 (Awazu et al., 2008), Au/ZnO (Chen et al., 2012), graphene oxide (GO) enwrapped Ag/AgX (X = Cl, Br) (Zhu et al., 2011), Ag/AgBr@TiO_2 (Zhang et al., 2011), Ag/AgCl@$H_2WO_4 \cdot 3H_2O$ (Wang et al., 2011), and AgBr/WO_3 (Cao et al., 2011), Ag/ZnO nanorods (NRs) (Chen et al., 2013), as plasmonic nanocomposites with support. Most of the above molecular devices used to degraded dye/organic pollutants (methylene blue, methyl orange, VOCs, ethanol/methanol) but only few of the composite plasmonics, were used to produce hydrogen such as gold/layered double hydroxides (127 μmolh^{-1} for Au/ZnAlCeLDH and 94 μmol for Au/ZnAlLDH), Ag/ZnONRs (8.7 μmol h $^{-1}$ of H_2 by ZnO/Ag and 4.3 μmol h $^{-1}$ of H_2 by ZnO) (Carja et al., 2010) In this direction, several advance methods such as ultrasonic assisted deposition-precipitation method (Shi et al., 2013), ployol process (Christopher et al., 2011), single pot refluxing (Pirhashemi and Habibi-Yangjeh, 2014), ionic liquids-assisted hydrothermal method (Im et al., 2005), reconstruction process (Carja et al., 2010), a facile reverse micelle method (Lou et al., 2011), etc, has been used to prepare NCs. Microwave (MW) assisted synthesis is one of the eco-friendly method for molecular assemblies' fabrication, where MW-heating provided faster and uniform heating profile than the conventional thermal heating. Therefore, MW assisted-synthesis leads not only homogenous nucleation but also accelerate the reaction rate, improve yield, shorten the reaction time, produce small sized particle of high purity with narrow particle size distribution, and improve physicochemical properties (Perreux and Loupy, 2001). Some notable materials are SnO_2 (Singh and Nakate, 2013), ZnO (Barreto et al., 2013), Ag (Yamamoto et al., 2004) Pt (Komarneni et al., 2002), CuS (Tadjarodi and Khaledi, 2010), etc, which were fabricated using MW assisted synthesis. but record was not found for MW assisted synthesis of the Ag/AgCl@ZnO NC. Therefore, we employed the microwave assisted synthesis first time for NCs preparation that consist of plasmonic silver NPs embedded in ZnO and AgCl matrix, which was used for water splitting to generate hydrogen. Conventionally, Ag/AgCl@ZnO NC (Pirhashemi and Habibi-Yangjeh, 2014), was synthesized by one pot refluxing method in water. Under sunlight exposure, ZnO and AgCl generates photo electrons and holes and AgCl (with expanded CB energy levels) plays a role of polar carrier for electron-transport to plasmonic material (Ag NPs) from ZnO and whole assembly become capable to harvest visible light, as it schematically illustrated by the Scheme 1a and Energy diagram 1b. Therefore, we can say the nanocomposite Ag/AgCl@ZnO, has the better compatibility for visible light harvesting by suppressing the recombination rate of photo carriers. That will be ultimately enhanced the hydrogen generation efficiency of the device. In addition to above, the advanced technical approaches were used to address the characterization of the device.

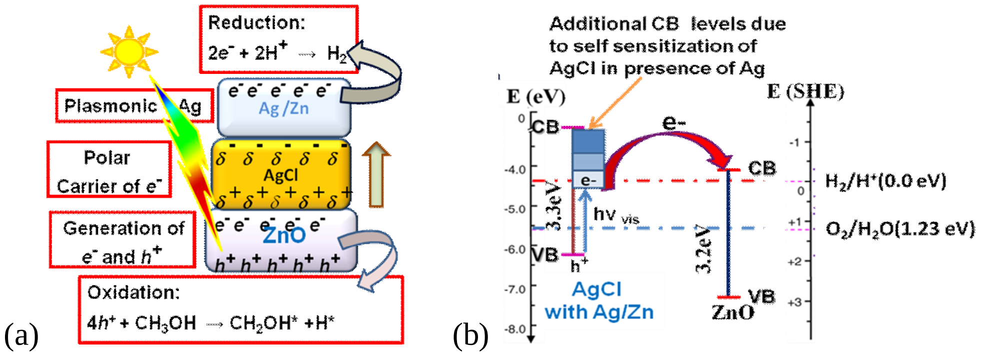

Figure 3.35 (a) Schematic representation of the overall water splitting phenomenon using Ag NPs embedded AgCl-ZnO NCs and (b) comparative energy level diagram of nanocomposite device Ag/AgCl@ZnO with their respective band positions (Calzaferri et al., 2001; Glaus et al., 2002; Sumi et al., 1980).

The XRD study confirms the formation of Ag/AgX@ZnO (X= Cl, CO_3^{-2}, PO_4^{-3} NO_3^-, SO_3^{2-}) nanocomposite with multiple phases. The particle size of these nanocomposites prepared by one pot conventional and microwave synthesis was determined using Scherrer formula given by Equation 8 (Scherrer,1918) along with their corresponding lattice strain.

$$B(2\theta) = \frac{K\lambda}{L\cos\theta} \qquad \ldots(8)$$

Where, B= FWHM (2θ), λ = Wavelength (nm), L =Average crystallite size ($\perp$ to surface of specimen; unit nm), k = 0.94 [k $\in$ (0.89, 1.39)] ~ 1 (the accuracy of the method is only 10%)

Dislocations with in crystal structure could either be caused a crystallographic defects or irregularity in lattice arrangement. These topological defects can be highly influenced by the material’s native properties. The X-ray diffraction profiles can also be used in determination of the dislocation density (δ) for the samples using following expression given in Equation 9 (Venkata Subbaiah et al., 2006).

$$\delta = \frac{15\beta\cos\theta}{4aD} \qquad \ldots(9)$$

Where, dislocation density (δ=3.8019x$10^{13}$$m^{-2}$ (one pot) and 3.9100x$10^{13}$$m^{-2}$ (microwave) is calculated from broadening of diffraction peak i.e. Full width at its half of maximum intensity β (in radian), Bragg's diffraction angle θ (in degree), lattice constant a (in nm) and particle size D (in nm). Higher delocalization density of the microwave synthesized sample in comparison to the sample made by one pot synthesis method, is associated with higher number of active sites on the molecular surface due to lotus shape of the particle. The very minute presence of Zn in Ag lattice is also confirmed from blue shift that observed for Ag XRD peaks due to addition of low weighted element Zn.

FESEM images, FESEM elemental mapping and EDX profile corresponding to the FESEM images of NCs, used to exhibit the morphology and elemental composition of NCs as 20.65/19.00% ZnO, 12.98/13.79% AgCl, 4.73/8.08% Zn and 28.01/26.19% Ag in the NC (one pot/microwave). Above results also predicted that the six petaled-lotus like structures of Ag loaded (nanoparticle of size 30-40 nm)-AgCl (size ≈50-100 nm) was developed on the ZnO rich- surface by microwave samples. Where one pot method used to develop the different shape and sized particle as per anion used for synthesis. Figure 2d reveals that Ag/Zn and AgCl were dispersed on ZnO surface. It was also confirmed by elemental mapping that conventionally prepared samples had more homogeneously dispersed elements than the microwave prepared samples, as represented by the Figures 2d and 2e.

High intense UV-Vis absorption band around 300.4 nm is appeared due to $\pi \rightarrow \pi^*$ electron transition (the charge transfer of excitons from the VB to CB) the host material. $n \rightarrow \pi^*$ Transition is responsible for the broad and small peak at 352.0 nm because the electrons in the n-orbitals are positioned perpendicular to the plane of π bond and hence along the plane of π^* orbital. According to symmetry selection rules, the possibility of the jump of an electron from $n \rightarrow \pi^*$ orbital is very stumpy (~ zero). But, vibrations of atoms result in a partial overlap between these perpendicular planes and so $n \rightarrow \pi^*$ transition does occurred at limited extent. Second broad and small peak around 352.0 nm, is attributed to the *d-d* transition, which were deposited on AgCl/ZnO surface (Suhai 1986). Surface plasmonic effect of the Ag/Zn NPs can be clearly seen for the pre heated-, conventional- and microwave- prepared Ag/AgCl@ZnO samples that boasted to a weak visible light response with an absorption band edge tangent touching to base line at about 404.6 nm (E_g=3.056 eV), 437.2 nm (E_g= 2.831 eV), and 426.8 nm (E_g= 2.901 eV), respectively. On vigilant observation, a broad and very weak plateau observed between 407.9 nm to 700 nm, attributed to the *d-d* orbital interactions of Ag/Zn nanoparticles. The ability of visible light absorption for final nanocomposites was drastically enhanced due to the surface plasmonic resonance (SPR) effect of Ag/Zn NPs that associated with the AgCl surface. This combination (nanoparticles with AgCl) prompts the selfsensitization of AgCl, result in additional CB levels. Ag levels are located below the conduction band edge of AgCl, can develop additional AgCl surface states (SURS), as well as metal induced gap states (MIGS) from Ag@AgCl cluster composites that to present in the band gap region of silver chloride and their presence induce the self-sensitization phenomenon in AgCl (scheme 1b). This arrangement of additional CB layers requires less energy for electron transfer from VB to CB than pristine AgCl. Moreover, this electronic transformation was induced by visible light whether the individual transition in AgCl or ZnO, was exposed to light. Therefore, the presence of NPs on AgCl/ZnO extends the good photoactivity from the UV to the visible light region, via self sensitization of AgCl. The whole system sustains the good photocatalytic activity in AgCl, which used to decompose in light exposure. Close examination of the spectra told us microwave synthesized samples are more active than conventionally prepared sample.

High dislocation density, calculated by XRD profile of the sample is responsible for another important phenomena, occurs in nanocomposites i.e. photoluminescence. Excitation and emission (PLE) spectra of sample produced by one pot reflux- and microwave methods, corresponded to the Figures 3b and 3c. Inset of Figure 3c, exhibit the CIE plot of the Ag/AgCl@ZnO that confirms that the material emits yellow light. The change in preparation method result in shifting of PLE peak from 502 to 602 nm, attributed to the high concentration of the delocalization defects in microwave -prepared sample than conventionally (one pot) – prepared sample. Moreover, the photoluminescence phenomena associated with the degree of deviation from the balance between two competing effects i.e. lattice and local coordination effects, around the studied element. The deviation found more for microwave synthesized sample. Therefore, microwave synthesized samples are prone to possess more delocalized defects.

As the pure water has inefficient energy to decompose all alone but presence of photocatalyst promote this decomposition. Therefore, the study focused on photocatalytic water splitting by using of semiconductor NC i.e. Ag/AgCl@ZnO.

Minimum four electrons required to stimulate the multistep-water reduction and oxidation reactions of overall water splitting process for H_2 and O_2 production, respectively. The sacrificial molecules (20% methanol in this case) act as an electron donor/ hole-acceptor and enhance the efficiency of the H_2 production by consuming the holes. Various organic compounds such as alcohols, carboxylic acids, and hydrocarbons, etc, can act as an efficient hole-scavengers (or electron donors) for the photocatalytic H_2 generation. Here, we used methanol as sacrificial electron donor. And result in a significant drop in the charge carrier-recombination process, enhance the hydrogen gas production in presence of the hole-scavenger and also avoid a subsequent gaseous product (H_2 and O_2) separation stage. Accumulative all process, leads to increase the overall H_2 yield. It irreversibly encountered the photo-generated holes to enhance the photocatalytic electron/hole-separation efficiency and give rise to high quantum yields for hydrogen generation (Schneider and Bahnemann, 2013).

Therefore, photocatalytic water splitting experiments was performed for the hydrogen generation from the molecular nanocomposite Ag/AgCl@ZnO that well dispersed in 20% aqueous methanol scavenger at pH =7, under 1.5AM G light irradiation as demonstrated by Figures 5a, 5b and 5c. The hydrogen generation from water in presence of nanocomposite Ag/AgCl@ZnO might follow the below mentioned reaction mechanism, expressed by Equations 9 to17:

Generation of Hydrogen

$Ag@AgCl \xrightarrow{\text{Visible light}} (CV)e^- + (VB)h^+$ (photocarriers (e^-/h^+) generation) ...(09)

$Ag@AgCl\ (CV)e^- \rightarrow ZnO\ (CV)e^-$ (transfer of photoelectron) ...(10)

$ZnO(CV)e^- + H_2O \rightarrow H^* + OH^-$ (generation of free radical H*) (Schwarz, 1992)...(11)

$h^+ + OH^- \rightarrow OH^*$ (generation of free radical OH*) ...(12)

$H^* + H^* \rightarrow H_2$ (0.00 eV) (generation of H_2) ...(13)

Consumption of h^+ using CH_3OH

$ZnO\ or AgCl\ (VB)h^+ + CH_3OH \rightarrow CH_2OH^* + H^+$ (-0.126 eV) (Seetula, 1994) ...(14)

$CH_2OH^* + OH^* \rightarrow HOCH_2OH^* \rightarrow HCHO + H_2O$ (-0.3848 eV) ...(15)

$CH_2OH^* + O \rightarrow OCH_2OH^* \rightarrow HCHO + OH^*$ (-3.180 eV) ...(16)

$CH_2OH^* + O \rightarrow OCH_2OH^* \rightarrow HCOOH + H^*$ (-4.125 eV) ...(17)

While the first two reactions (Equations 9 and 10) devoted to increase the concentration of photoelectrons on surface of molecular device, are thus to favor for reduction of water in presence of the sunlight and catalyst. The reactions (Equations 11, 13 and 17), involve in generation of free radical H^* and the formation of the H_2 gas. These reactions had a large negative Gibbs energy, thus it intrinsically provides a barrier for the undesired reverse consumption of the H_2. Furthermore, two possible mechanisms are proposed for photocatalytic oxidation of methanol: (1) the direct oxidation by photogenerated holes and (2) the indirect oxidation via interfacial $^{\bullet}OH$ radicals. To distinguish the two mechanisms in practice is still a challenge due to the lack of suitable probe techniques. Although, we traced the presence of the *OH radicals on the surface of the catalyst under visible-light exposure by using alkaline terephthalic acid solution (initial pH=10.5) in NaOH as the probe in the photoluminescence method (Xiang et al., 2010; Xiang et al., 2011). Figure 4a exhibited the gradual increase in PLE intensity at 428 nm with increasing irradiation exposure time. Furthermore, experiments show that no PL signals for the Ag/AgCl@ZnO NC impregnated terephthallic acid solution in dark (0 h-PLE curve) because pure molecular device is activated by visible light and result in no production of OH^* radicals. Other PLE peaks situated at 562.8 nm and 632 .9 nm are associated with the *Soret*-band and *Q*-bands, respectively. The trapping of valence band holes by surface $–OH^-$ groups of the adsorbed water molecules, result in the production of $–OH^*$ radical along with the decrease in its pH=8.14 with reaction. The production of $–OH^*$ radical, is not only reflected from the decrease in pH (from 10.5 to 8.14) of the alkaline terephthalic acid solution impregnated with the molecular device but also from the raise in a global absorption maximum for PLE peak at 425 nm (*Soret*-band) with increasing exposure time along with the *Q*-bands, which are appear at 567 and 618 nm. The molar absorption coefficient for the Soret-band is 155- 500 $M^{-1}\,cm^{-1}$ shown in Figures 4a and 4b. In the PLE spectrum of catalyst in alkaline terephallic acid, the intense soret band is attributed to the S_0 to S_2 transition whereas the q bands are attributed to the S_0 to S_1 transition. In free base terephalate solution, the *Q* band further split owing to vibrational excitations. Therefore, two bands are produced due to transition from ground state to two vibrational states of the excited state [*Q*(0,0) and *Q*(1,0)] (Zhang et al. 2011; Spellane et al., 1980) This implies that the fluorescence evident the chemical reactions between terephthalic acid and ${}^{\bullet}OH$ formed during photocatalytic reactions (Xiang et al., 2011). Therefore, the experiments hydroxyl ions converted into hydroxyl radicals under the light exposure, which degrade the methanol and result in production of HCHO or HCOOH, as shown by Equations 14-17. Finally, the hydrogen production occurs through photocatalytic hassle-free reduction of the water.

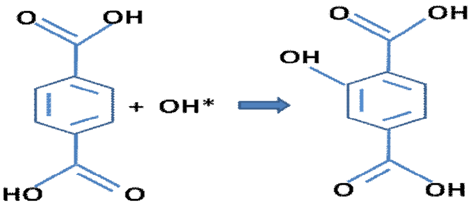

Terephthalic acid + hydroxyl radical→ 2-hydroxy Terephthalic acid

Figure 3.36 Reaction of the terephthalic acid with hydroxyl radical to form 2-hydroxy terephthalic acid

It was found that no detectable amount of hydrogen production was observed even after the 72 h exposure of water with or without catalyst in dark. The H_2 generation capacity of the catalyst was continuously estimated for 20% methanol solution in an argon atmosphere via Gas Chromatograph (Agilent, TCD (8A column; model: 2780).

Experimentally observed rate of hydrogen evolution are in good agreement with state of art nanocomposite Ag/AgBr/TiO_2 that releases 1.00 mmol h^{-1} g^{-1} H_2 after 2 h, under the irradiation of 100W high-pressure Hg lamp-with IR filter (Yu et al., 2009). Catalytic activity of the nanocomposite Ag/AgCl@ZnO was rejuvenated during the photocatalysis process, as it exposed by Equations 1 to 7 (Pfanner et al. 1996; Glaus S, Calzaferri G., 1999). After photocatalytic activity of H_2 production-measured, the catalyst (pinkish grey) was thoroughly washed with distilled water and reused after drying at 80 ^{o}C for 12 h. It was found there is no significant lost in catalytic activity even after three time use as shown in Figs 5b and 5c. Above spectroflurometric and photocatalytic study gives us hint about the electron transfer mechanism of the photocatalytic water splitting for the H_2 production process, which is well illustrated by the Figure 5c. when the light falls upon the surface of the NC Ag/AgCl@ZnO then electron of VB jumped over to the CB and transferred to CB of ZnO though Ag metallic electronic pool. Where this photoelectron reduces the water to liberate H_2 and holes consumed to generate HCHO or HCOOH by OH^* radicals.

Table 3.11 Comparative hydrogen production efficiency of the all studied systems.

S. No.	System	Particle shape	Particle Size(nm)	H_2 Production in mmol	H_2 Production mmol H_2 h^{-1} g^{-1} at 2h
1.	Ag/AgCl(NaCl)@ ZnO (microwave synthesis)	Nanolotus	57.72 nm	0.97	1.62121
2.	Ag/AgCl(NaCl)@ ZnO (one pot synthesis)	Spherical	59.12 nm	0.84	1.40441
3.	Ag/AgCl($BaCl_2$)@ ZnO (one pot synthesis)	2D-flax shaped particles	53.67nm	0.49	0.8166
4.	Ag/Ag_3PO_4@ZnO (one pot synthesis)	Rice grain shaped	38.82nm	0.21	0.3491
5.	Ag/$AgNO_3$@ ZnO (one pot synthesis)	needle shaped	32.01nm	0.33	0.5500
6.	Ag/Ag_2CO_3@ZnO (one pot synthesis)	Flax shaped	29.26 nm	0.42	0.7140
7.	Ag/Ag_2SO_3/ZnO (one pot synthesis)	Rod/ needle shaped	45.14 nm	0.44	0.7330

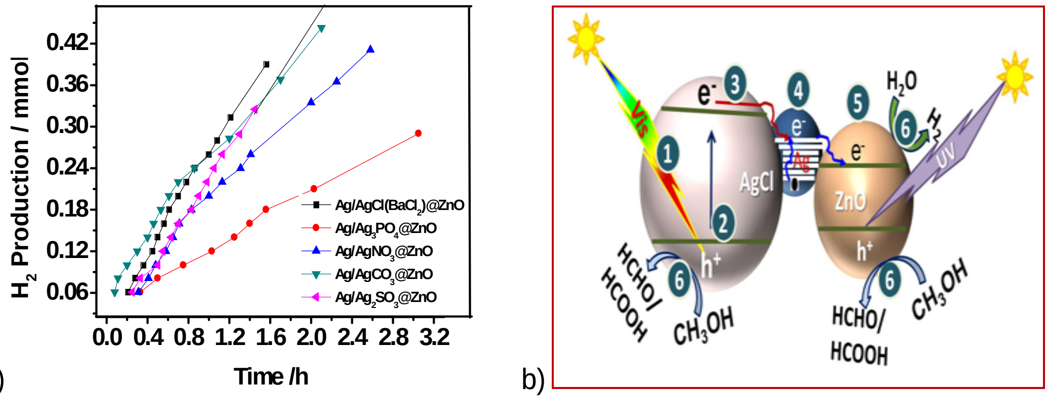

(a) b)

Figure 3.37 (a) Comparative hydrogen production rate for the all studied systems Ag/AgX@ ZnO (b) schematic representation of the electron transfer mechanism for hydrogen production through water splitting in 20% methanolic Ag/AgX@ ZnO NC.

3.12. Conclusion

We explored nanocomposite Ag/AgCl@ZnO NC as a smart material (fabricated by two ways i.e. microwave and conventional) that can be utilized as a photocatalyst for hydrogen generation through water splitting under visible light exposure. The molecular device exhibits highest activity towards photocatalytic hydrogen generation among the state of art photocatalyst of the same class. Moreover, it was established for the molecular device that the photo electrons generated during the light irradiation was used as a photocatalyst for better hydrogen production and photo-holes reacted with OH^- to form OH^* radicals, which used as a scavenger to degrade the methanol into HCHO or HCOOH. Furthermore, advancement in the molecular device is in progress by replacing halides with other anions and other plasmonic materials.

3.13 Reference

1. Adhikari R., Gyawali G., Sekino T., Lee SW., “Microwave assisted hydrothermal synthesis of Ag/AgCl/WO_3photocatalyst and its photocatalytic activity under simulated solar light’ J Solid State Chem. (2013), 197: 560–565.
2. Ai L., Zhang C., Jiang J., “Hierarchical porous AgCl@Ag hollow architectures: Self-templating synthesis and highly enhanced visible light photocatalytic activity” Appl. Catal. B (2013), 142–143: 744–751.
3. Awazu K., Fujimaki M., Rockstuhl C., Tominaga J., Murakami H., Ohki Y., Yoshida N., Watanabe T., “A plasmonics photocatalyst consisting of silver nanoparticle esembedded in titaniumdioxide” J Am Chem. Soc. (2008), 130: 1676-1680.
4. Barabaszová, K., “Nanotechnologie a nanomateriály” VŠB-Tu Ostrava,158 p., in Czechlanguage. (2006), ISBN 80-248-1210-X.

5. Barreto G.P, Morales G., Quintanilla M.L.L, “Microwave assisted synthesis of ZnO nanoparticles: effect of precursor reagents, temperature, irradiation time, and additives on Nano-ZnO morphology development”. J. Mater (2013): 478681 (11 pages).
6. Calzaferri G., Bru¨hwiler D., Glaus S., Schu¨rch D., Currao A., Leiggener C., “Quantum-sized silver, silver chloride and silver sulfide clusters” J. Imaging Sci.Technol (2001),45: 331-339.
7. Cao J., Luo B.D., Lin H.L., Chen S.F., “Photocatalytic activity of novel AgBr/WO_3 composite photocatalyst under visible light irradiation for methyl orange degradation” J Hazard Mater (2011), 190: 700−706.
8. Carja G., Birsanu M., Okadac K., Garcia H., “Composite plasmonic gold/layered double hydroxides and derived mixed oxides as novel photocatalysts for hydrogen generation under solar irradiation” J. Mater Chem. (2013), A1: 9092–9098.
9. Carja G., Nakajima A., Dranca S., Dranca C., Okada K., “Nanoparticles of nickel oxide: growth and organization on zinc substituted anionic clay matrix by one-pot route at room temperature” J. Phys. Chem. C (2010), 114:14722–14728.
10. Carp O., Huisman C.L., Reller A., “Progress in Solid State” Chem., (2004), 32:33.
11. Chen H.M., Chen C.K., Chen C.J., Cheng L.C., Wu P.C., Cheng B..H, Ho Y.Z., Tseng M.L., Hsu Y.Y., Chan T.S., Lee J.F., Liu R.S., Tsai D.P., “Plasmon inducing effects for enhanced photoelectrochemical water splitting: X-ray absorption approach to electronic structures”ACS Nano(2012), 6: 7362–7372.
12. Chen H.M., Chen C.K., Tseng M.L., Wu, P.C., Chang C.M., Cheng L.C., Huang H.W., Chan T.S., Huang D.W., Liu R.S., Tsai D.P., “Plasmonic ZnO/Ag embedded structures as collecting layers for photogenerating electrons in solar hydrogen generation photoelectrodes” Small (2013),2926–2936.
13. Christopher P., Xin H., Linic S.., “Visible-light-enhanced catalytic oxidation reactions on plasmonic silver nanostructures” Nat Chem. (2011), 3: 467.

14. Fang Y., Li Z., Xu S., Han D., Lu D., “Optical properties and photocatalytic activities of spherical ZnO and flower-like ZnO structures synthesized by facile hydrothermal method” J. Alloys Compound (2013), 575: 359–363.
15. Fernandez-Garcia M., Martinez-Arias A., Hanson J.C., Rodriguez J.A., “Nanostructured Oxides in Chemistry: Characterization and Properties” Chem. Rev., (2004), 104(9):4063-4104.
16. Ghosh P., “Preparation of Nanomaterials” NPTEL Chemical Engineering, Interfacial Engineering (1999) Module 9: Lecture 2.
17. Glaus S, Calzaferri G., “Silver chloride clusters and surface states.” J. Phys. Chem. B. (1999), 103: 5622-5630.
18. Glaus S., Calzaferri G., Hoffmann R., “Electronic properties of the silver–silver chloride cluster interface” Chem. Eur. J. (2002),8: 1785-1794.
19. Guo R., Zhang G., Liu J., “Preparation of Ag/AgCl/$BiMg_2VO_6$ composite and its visible-light photocatalytic activity” Mater Res Bull (2013), 48: 1857–1863.
20. Hahn H., “Nanostructured Materials” Elsevier Ltd. (1997),9:3-12
21. Hamilton J.F., “Physical-properties of silver-halide microcrystals” Photogr. Sci. Eng. (1974), 18: 493–500.
22. Im S.H., Lee Y.T., Wiley B., Xia Y., “Large-scale synthesis of silver nanocubes: the role of HCl in promoting cube perfection and monodispersity” Angew. Chem. Int. Ed. (2005), 44: 2154.
23. Kakuta N, Goto N, Ohkita H, Mizushima T., “Silver bromide as a photocatalyst for hydrogen generation from CH_3OH/H_2O solution” J Phys. Chem. B (1999), 103: 5917–5919.
24. Komarneni S., Li D.S., Newalkar B., Katsuki H., Bhalla, A.S., “Microwave−Polyol process for Pt and Ag nanoparticles” Langmuir (2002), 18: 5959.
25. Kumar P. and Mittal K. L. (Editors), “Handbook of Microemulsion Science and Technology” Marcel Dekker, New York, (1999) Chapters-2
26. Li W., Hua F., Yue J., Li J., “Ag@AgCl plasmon-induced sensitized ZnO particle for high-efficiency photocatalytic property under visible light” Appl. Surf Sci. (2013), 285: 490–497.

27. Longhui N., Zhengqing H., Hongtao X., Wangxi Z., Borui Y., Lei F., Shuaihua L., "Synthesis of Ag@AgBr photocatalyst and its performance for degradation of methylene blue under visible-lightirridiation" Chinese J Catal. (2012), 33: 1209-1216.
28. Lou Z., Huang B., Ma X., Zhang X., Qin X., Wang Z., Dai Y., Liu Y.A., "3D AgCl hierarchical superstructure synthesized by a wet chemical oxidation method' Chem. Eur. J. (2012), 18:16090 – 16096.
29. Lou Z.Z., Huang B.B., Qin X.Y., Zhang X.Y., Wang Z.Y, Zheng Z..K, Cheng H.F., Wang P., Dai Y., "One-step synthesis of AgBr microcrystals with different morphologies by ILs-assisted hydrothermal method" Crystal Eng. Comm. (2011), 6: 1789–1793.
30. Ma G., Zhao X., Zhu J., Int. J. Mod. Phys. B, (2005), 19.
31. Nyquist R.A., Richard A., "Factors affecting infrared group frequencies: Carbonyl stretching absorption bends" Applied Spectroscopy (1968), 40(3):336-39.
32. Perreux L., Loupy A., "A tentative rationalization of microwave effects in organic synthesis according to the reaction medium, and mechanistic considerations" Tetrahedron (2001), 7: 9199-9223.
33. Pfanner K., Gfeller N., Calzaferri G., "Photochemical oxidation of water with thin AgCl layers" J. Photoch Photobio A. (1996), 95: 175-180.
34. Pfau C., Bohley C., Miclea P.T. and Schweizer S, "Low phonon energy $BaCl_2$ nanocrystals in Nd^{3+-}doped fluorozirconate glasses and their influence on the photoluminescence properties" J. Appl. Phys. (2011), 109:083545.
35. Pierre A.C., "Introduction to sol-gel processing" Kluwer Academic Publishers, Boston, (1998) 394.
36. Pirhashemi M., Habibi-Yangjeh A., "Preparation of AgCl–ZnO nanocomposites as highly efficient visible-light photocatalysts in water by one-pot refluxing method" J. Alloys Compound (2014), 601: 1–8.
37. Saskia A. Galema., "Microwave chemistry" Chem. Soc. Rev., (1997), 26: 233-238
38. Scherrer P., "Bestimmung der Grösse und der innerenStruktur von Kolloidteilchenmittels Röntgenstrahlen" Nachr. Ges. Wiss. Göttingen (1918), 26: 98-100

39. Schneider J., Bahnemann D.W., “Undesired Role of Sacrificial Reagents in Photocatalysis” J. Phys. Chem. Lett. (2013), 4: 3479-3483.
40. Schürch D., Currao A., Sarkar S., Hodes G., Calzaferri G., “The silver chloride photoanode in photoelectrochemical water splitting” J Phys. Chem. B (2002), 106:12764–12775.
41. Schwarz H.A., “Reaction of the hydrated electron with water” J. Phys. Chem. (1992), 96: 8937–8941.
42. Seetula J.A., Kalinovski I.J., Slagle I.R, Gutman D., “Kinetics of the reaction of CH_2OH radical with oxygen atoms” Chem. Phys. Lett.(1994), 224: 533-538.
43. Shi H., Chen J., Li G., Nie X., Zhao H., Wong P.K., An T., “Synthesis and Characterization of Novel Plasmonic Ag/AgX-CNTs (X = Cl, Br, I) Nanocomposite photocatalysts and dynergetic degradation of organic pollutant under visible light” ACS Appl. Mater Interfaces (2013),5: 6959–6967.
44. Singh A.K., Nakate U.T., “Microwave synthesis, characterization and photocatalytic properties of SnO_2 nanoparticles” Advances in Nanoparticles (2013), 2: 66-70.
45. Spellane P.J., Gouterman M., Antipas A., Kim S., Liu Y.C., “Porphyrins 40. Electronic spectra and four-orbital energies of free-base, zinc, copper, and palladium tetrakis (Perfluorophenyl) porphyrins” Inorganic Chem. (1980), 19: 386-91.
46. Suhai S., “On the excitonic nature of the first UV absorption peak in polyene” Int. J. Quantum Chem. (1986), 29: 469–476.
47. Sumi S., Watanabe T., Fujishima A., Honda K., “Effect of Cl^- and Br^- ions and pH on the flatband potentials of silver halide sheet crystal electrodes. Bull Chem. Soc. Japan. (1980), 53: 2742-2747.
48. Tadjarodi A., Khaledi D., “Preparation of CuS nanoparticles by microwave irradiation” 14th International electronic conference on synthetic organic chemistry, (2010), (C010).
49. Tian Y., Tatsuma T., “Mechanisms and applications of plasmon-induced charge separation at TiO_2 films loaded with gold nanoparticles” J. Am. Chem. Soc. (2005), 127: 7632-7637.

50. Venkata Subbaiah Y.P., Prathap P., Ramakrishna Reddy K.T., “Structural, Electrical and Optical Properties of ZnS Films Deposited by Close-Spaced Evaporation” Appl. Surf Sci. (2006), 253: 2409-2415.
51. Venkata Subbaiah Y.P., Prathap P., Ramakrishna Reddy K.T., “Structural Electrical and Optical Properties of ZnS Films Deposited by Close-Spaced Evaporation” Appl. Surf Sci. (2006), 253: 2409-2415.
52. Wang D., Duan Y., Luo Q., Li X., Bao L., “Visible light photocatalytic activities of plasmonic Ag/AgBr particles synthesized by a double jet method” Desalination (2011), 270: 174–180.
53. Wang X.F., Li S.F., Ma Y.Q., Yu H.G., Yu J.G., “$H_2WO_4{\cdot}H_2O$/Ag/AgCl Composite nanoplates: aplasmonic Z-scheme visible-light photocatalyst” J. Phys. Chem. (2011), C 115: 14648−14655.
54. Wu X., Jiang Q. Z., Ma Z.F., Fu M., Shangguan W.F., “Synthesis of titania nanotubes by microwave irradiation” Sol. State Comm. (2005), 136.
55. Xiang Q., Yu J., Wong P.K., “Quantitative characterization of hydroxyl radicals produced by various photocatalysts” J Colloid Interface Sci. (2011), 357: 163-167.
56. Xiang Q.J., Yu J.G, Cheng B., Ong H.C., “Microwave-Hydrothermal Preparation and Visible-Light Photoactivity of Plasmonic Photocatalyst Ag/TiO_2 Nanocomposite Hollow Spheres” Chem. Asian J. (2010), 5: 1466-1474.
57. Xu Y., Xu H., Li H., Xia J., Liu C., Liu L., “Enhanced photocatalytic activity of new photocatalyst Ag/AgCl/ZnO” J Alloys Compound (2011), 509: 3286–3292.
58. Yamamoto T., Wada Y., Sakata T., Mori H., Goto M., Hibino S., Yanagida S., “Microwave-assisted preparation of silver nanoparticles” Chem. Lett. (2004), 33:158.
59. Yang J., Mei S., Ferreira J.M.F., “Hydrothermal synthesis of TiO_2 nanopowders from tetraalkylammonium hydroxide peptized sols” Mater. Sci. Eng. B, (2001), C:15.
60. Yu G., Dai G.P, Huang B.B., “Fabrication and characterization of visible-light-driven plasmonic photocatalyst Ag/AgCl/TiO_2 nanotube arrays” J. Phys. Chem. C (2009), 113:16394-16401.

61. Zhang Y.H., Tang Z.R., Fu X.Z., Xu Y., “Nanocomposite of Ag–AgBr–TiO_2 as a photoactive and durable catalyst for degradation of volatile organic compounds in the gas phase” J. Appl. Catal. (2011), B106: 445−452.

62. Zhu M.S., Chen, P.L., Liu M.H., “Graphene oxide enwrapped Ag/AgX (X= Br, Cl) nanocomposite as a highly efficient visible-light plasmonic photocatalyst”ACS Nano (2011) 5: 4529− 4536.

Conclusion

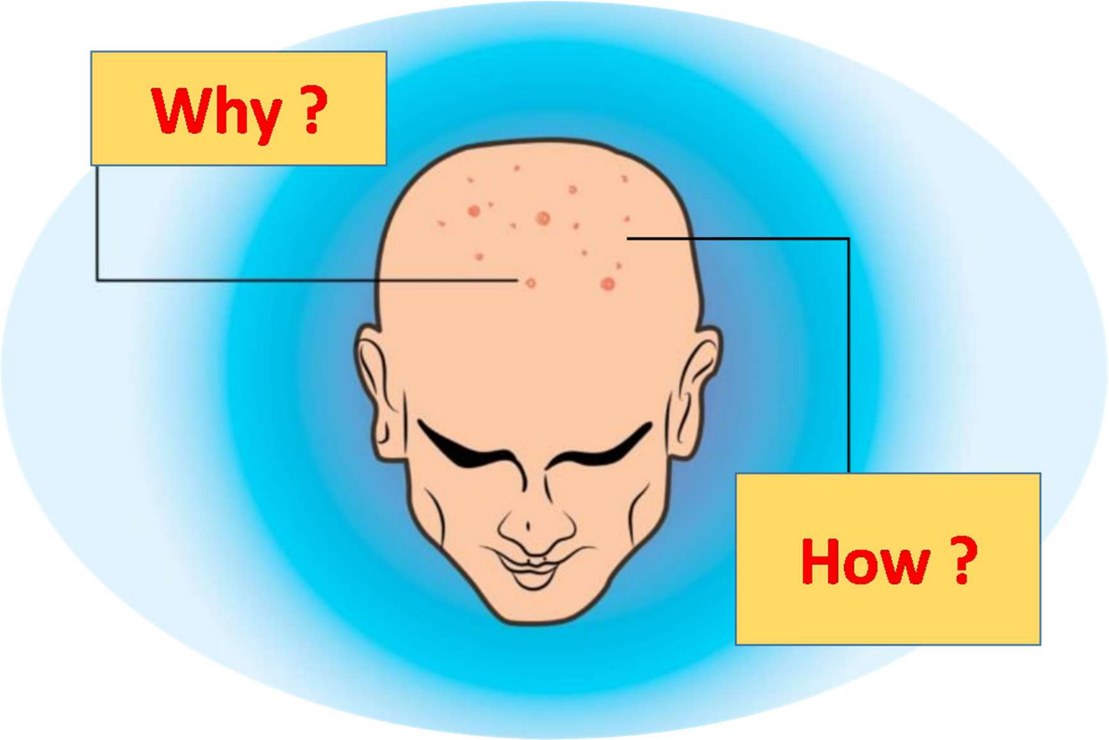

CONCLUSION

We had synthesised silver halides and ZnO based plasmonic nanoparticles (NPs) of Ag nanocomposites (NCs) by conventional one pot refluxing method and microwave heating that was utilised in visible-light-harvesting molecular devices for hydrogen creation via breaking of water. Formation of the nanocomposite Ag/AgX@ZnO (X (anion)= Cl, CO_3^{2-}, PO_4^{3-} NO_3^{-}, SO_3^{2-}) in many phases was confirmed by XRD and UV-Visible spectra of the compound. In the nanocomposite, silver halides AgX are unstable under sunlight (Hamilton JF 1974) and seldom used as photocatalysts. But with plasmonic silver nanoparticles and support, AgX become quite stable due to the additional SURS states and used for continuous H_2 production in 20% CH_3OH solution (Kakuta et al. 1999) under successive UV/Vis illumination. Thus, assembly Ag/AgX@ZnO, become able to act as a stable photocatalyst under visible light irradiation. On the behalf of the experimental and theoretical assessments in the form of the ionization energy of the diverse size -Ag clusters along with AgCl, it was established that Ag levels are located below the conduction band edge of AgCl. These additional AgCl surface states (SURS), as well as metal induced gap states (MIGS) present in the band gap region of AgCl of the Ag/ AgCl cluster composites, provoked the self-sensitization process in AgCl. Therefore, Ag/AgX supported mZnO can be employed as good photocatalytic system (Calzaferri et al., 2001; Glaus et al., 2002; Sumi et al., 1980; Yu, 2009) that can work fine under the UV-Visible light region. Rejuvenation of the AgCl in presence of Ag^{+} occurred due to the formation of the various silver species during the photoreaction, as follows (Equations 1-7), which had been analyzed experimentally and theoretically (Pfanner et al., 1996; Glaus and Calzaferri,1999).

$$[\mathrm{nAg^{+},\ mAgCl}] + \tfrac{r}{2}\mathrm{H_2O} \xrightarrow{\text{light}} [\mathrm{(n-r)Ag^{+},\ mAgCl, rAg^{0}}] + \mathrm{rH^{+}} + \tfrac{r}{4}\mathrm{O_2} \quad ...(1)$$

$$[\mathrm{(n-r)Ag^{+}, mAgCl, rAg^{0}}] \xrightarrow{\text{light}} [\mathrm{nAg^{+}, mAgCl}] + \mathrm{re^{-}} \quad ...(2)$$

$$[\mathrm{\ mAgCl}]\{\mathrm{Ag^{+}}\}_{s} \xrightarrow{\text{light}} [\mathrm{(m-1)AgCl}]\ \{\mathrm{Ag^{+}Ag^{0}}\}_{s,i} + [\mathrm{Cl}_{s}^{-}] \quad ...(3)$$

$$2Cl^{\cdot}_{s} \rightarrow Cl_2 \qquad ...(4)$$

$$Cl_2 + H_2O \rightarrow HOCl + H^+ + Cl^- \qquad ...(5)$$

$$2HOCl \xrightarrow{Ag^+} O_2 + 2H^+ + 2Cl^- \qquad ...(6)$$

$$[(m-1)AgCl + Ag^+ + Cl^- \rightarrow [mAgCl] \qquad ...(7)$$

Therefore, Ag embedded in ZnO and AgX (X(anion)= Cl^-, CO_3^{-2}, PO_4^{-3}, NO_3^-, SO_3^{-2} with SURS) matrix Ag/AgX@ZnO nanocomposites (Pirhashemi and Habibi-Yangjeh, 2014), were made by one pot refluxing method(conventional) and microwave assisted method in aqueous media that to be used for generating hydrogen via water splitting. Where, ZnO site and AgX site of the nanocomposite generates photo electrons and holes, respectively and therefore, AgX (with expanded CB energy levels) works as polar carrier segregator for charge carrier as shown in Scheme 1. These charge carriers: the electrons used to reduce water and holes: oxidised CH_3OH by transporting electrons to plasmonic material (Ag NPs) from ZnO (hole rich). The whole assembly become capable for exploiting visible light by repressing the rate of photo carriers- union. Therefore, the nanocomposite Ag/AgCl@ZnO, became capable for the hydrogen generation with good efficiency of the molecular device. In addition to above, the advance analytical physicochemical methods were used to define the pact of the NC.

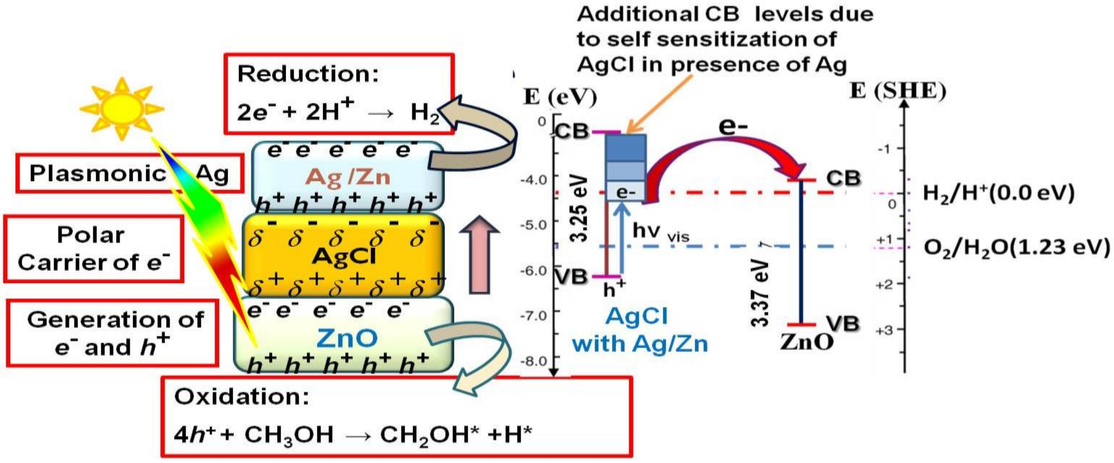

Scheme 1. Components of the mocelular device (Ag NPs embedded AgCl-ZnO NCs) used for the overall water splitting phenomenon along with their comparative energy level diagram.

The pure water did not decomposed by itself because of its inefficient energy. Therefore, the presence of the photocatalyst is necessary required to speed up the decomposition process. In this study, we focused on semiconductor NC i.e. Ag/AgCl@ZnO (photocatalyst) that to be applied for photocatalytic water splitting. Minimum four electrons required to stimulate the multi-steps of water oxidation reactions and two electrons required for reduction of water for overall water splitting, required for O_2 and H_2 elvolution, respectively. To avoid the complication of the separation of gases and recombination of the photoelectrons and holes, water splitting proceed with in presence of the scavengers (for H_2 production hole-scavengers and for O_2 production electron-scavengers). Some of the efficient organic hole-scavengers are: alcohols, carboxylic acids, and hydrocarbons etc, that can act as electron donors in the photocatalytic H_2 generation process. For this particular case, we had used 20% methanol act as sacrificial agent (electron donor/ hole-acceptor) to increase the H_2 production efficiency of photocatalyst by eating the holes. It irreversibly enhanced the separation efficiency of the photocatalytically generated electron/hole- and boost the high quantum yields for hydrogen production (Schneider and Bahnemann, 2013).

Hence, the photocatalytic water splitting experimentation was performed by using the molecular nanocomposite Ag/AgX@ZnO that was well spread in 20% aqueous methanol (hole-scavenger) at pH =7, under exposure of 1.5AM G light, as illustrated by Figures 5a, 5b and 5c. The hydrogen generation from water in presence of particular case: nanocomposite Ag/AgCl@ZnO follow the below mentioned reaction mechanism, expressed by Equations 8 to17:

Generation of Hydrogen

$Ag@AgCl \xrightarrow{\text{Visible light}} (CV)e^{-} + (VB)h^{+}$ (photocarriers (e^{-}/h^{+}) formation) ...(8)

$Ag@AgCl\ (CV)e^{-} \rightarrow ZnO\ (CV)e^{-}$ (photoelectron transfer) ...(9)

$ZnO(CV)e^{-} + H_2O \rightarrow H^{*} + OH^{-}$ (production of free radical H*) ...(10)

$h^{+} + OH^{-} \rightarrow OH^{*}$ (production of free radical OH*) ...(11)

$H^{*} + H^{*} \rightarrow H_2$ (0.00 eV) (production of H_2) ...(12)

Consumption of h^+ using CH_3OH

$\text{ZnO orAgCl (VB)}h^+ + CH_3OH \rightarrow CH_2OH^* + H^+$ (-0.126 eV) (Seetula, 1994) ...(13)

$CH_2OH^* + OH^* \rightarrow HOCH_2OH^* \rightarrow HCHO + H_2O$ (-0.3848 eV) ...(14)

$CH_2OH^* + O \rightarrow OCH_2OH^* \rightarrow HCHO + OH^*$ (-3.180 eV) ...(15)

$CH_2OH^* + O \rightarrow OCH_2OH^* \rightarrow HCOOH + H^*$ (-4.125 eV) ...(16)

Equations 8 and 9 induce the concentration of photoelectrons on surface of the catalyst to favour the reduction of water under Xe -light irradiation. The free radical H^* generation and formation of the H_2 gas are shown by the Equations 10, 12 and 16. Due to the large negative Gibbs energy of above reaction, a barrier formed for the using up of the H_2 in any reaction. There are two most probable reaction mechanisms are proposed for the photocatalytic oxidation of methanol i.e.: (1) the direct oxidation by photogenerated holes and (2) the not-direct oxidation through interfacial $^\bullet OH$ radicals. To distinguish above mechanisms in practice, is still a great challenge due to the lack of suitable techniques to trace the reaction in-situ. Although, we can marked out the presence of the *OH radicals at the catalyst surface on visible-light exposure in presence of the alkaline terephthalic acid solution (initial pH=10.5) by using photoluminescence method (Xiang et al., 2010; Xiang et al., 2011). Figure 4a presented the gradual augment in PLE intensity at 428 nm (as a result of the production of $–OH^*$ radical along) with increasing irradiation exposure time along with *Soret*-band and *Q*-bands at 562.8 nm and 632 .9 nm, respectively. Where, the intense Soret band, associated to the S_0 to S_2 changeover, whereas the Q-bands are trait of the S_0 to S_1 transition. Furthermore, experimental proof show that no PL peaks received for the Ag/AgCl@ZnO NC permeated terephthallic acid solution in dark (0 h-PL emission plot) because this molecular device get activated in light and without light there is no manufacturing of OH^* radicals.

In dark no detectable amount of hydrogen produced even after the 72 h disclosure of water either with or without catalyst. The H_2 generation capacity of the nanocomposite was continuously measured in 20% methanol solution in an argon atmosphere via Gas Chromatograph (Agilent, TCD (8A column; model: 2780) for 7h.

Experimental hydrogen evolution rate of Ag/AgBr/TiO_2 is foud 1.00 mmol h^{-1} g^{-1} H_2 after 2 h, under the exposure of 100W high-pressure Hg lamp-with IR filter (Yu et al., 2009), which was in good agreement with state of art nanocomposites. Photocatalytic activity of the nanocomposite Ag/AgCl@ZnO was rejuvenated under the light exposure, as shown by Equations 1 to 7 (Pfanner et al. 1996; Glaus S, Calzaferri G., 1999). After the measurement of the H_2 production- activity of the nanocomposite systems (pinkish grey), the compound was properly washed with distilled water and reused after dehydrated at 80 ^{o}C for 12 h. It was found that there is no noticeable lost in catalytic activity even after thrice use as shown in Figures 5b and 5c. The spectrofluorometric and photocatalytic measurement gives experimental proof of the electron transfer mechanism for the H_2 production process in photocatalytic water splitting, as illustrated in the Figure 5c. It reveals that when the light falls upon the surface of the NC Ag/AgCl@ZnO than electron of VB jumped to the CB and afterwards transferred to CB of ZnO through Ag metallic electronic pool. Where, this electron utilized to reduce the water into H_2 and holes to produce HCHO or HCOOH by OH^* radicals. Table 4.1 represent the hydrogen generation capacity of the samples that may vary with anion of AgX, preparation technique, particle shape and size of the nanocomposite.

Table 4.1 **H**ydrogen production efficiency recorded for the all observed systems.

S. No.	**System**	**Particle shape**	**Particle Size(nm)**	**H_2 Production in mmol**	**H_2 Production mmol H_2 h^{-1} g^{-1} at 2h**
1.	Ag/AgCl(NaCl)@ ZnO (microwave synthesis)	Nanolotus	57.72 nm	0.97	1.62121
2.	Ag/AgCl(NaCl)@ ZnO (one pot synthesis)	Spherical	59.12 nm	0.84	1.40441
3.	Ag/AgCl($BaCl_2$)@ ZnO (one pot synthesis)	2D-flax shaped particles	53.67nm	0.49	0.8166
4.	Ag/Ag_3PO_4@ZnO (one pot synthesis)	Rice grain shaped	38.82nm	0.21	0.3491

5.	Ag/$AgNO_3$@ ZnO (one pot synthesis)	needle shaped	32.01nm	0.33	0.5500
6.	Ag/Ag_2CO_3@ZnO (one pot synthesis)	Flax shaped	29.26 nm	0.42	0.7140
7.	Ag/Ag_2SO_3@ZnO (one pot synthesis)	Rod/ needle shaped	45.14 nm	0.44	0.7330

Smaller the particle, higher the efficiency (L=29.26 nm; η =0.7140), large surface area (L=57.72 nm; η =1.62121). Among the series of anions (CO_3^{-2}, PO_4^{-3} NO_3^-, SO_3^{2-}), nanocomposite with SO_3^{2-} anion group show the maximum efficiency (needle shape with L=45.14 nm; η =0.7330). There is no single reason behind the efficiency but there are several factors which has decisive role for efficiency of hydrogen generation. It can be result as the nanocomposite Ag/AgCl(NaCl)@ZnO (lotus shape particles synthesised by microwave method) which shown maximum efficiency. These systems can be optimised by varying various synthesis parameters (pH, composition, temperature, anions, addition of surfactant Ag/AgX and ZnO ratio) and supporting material (ZnO) and plasmonic material (Au, Cu, Na etc). Furthermore, the efforts will be made in improving the efficiency of the molecular device.

Summary

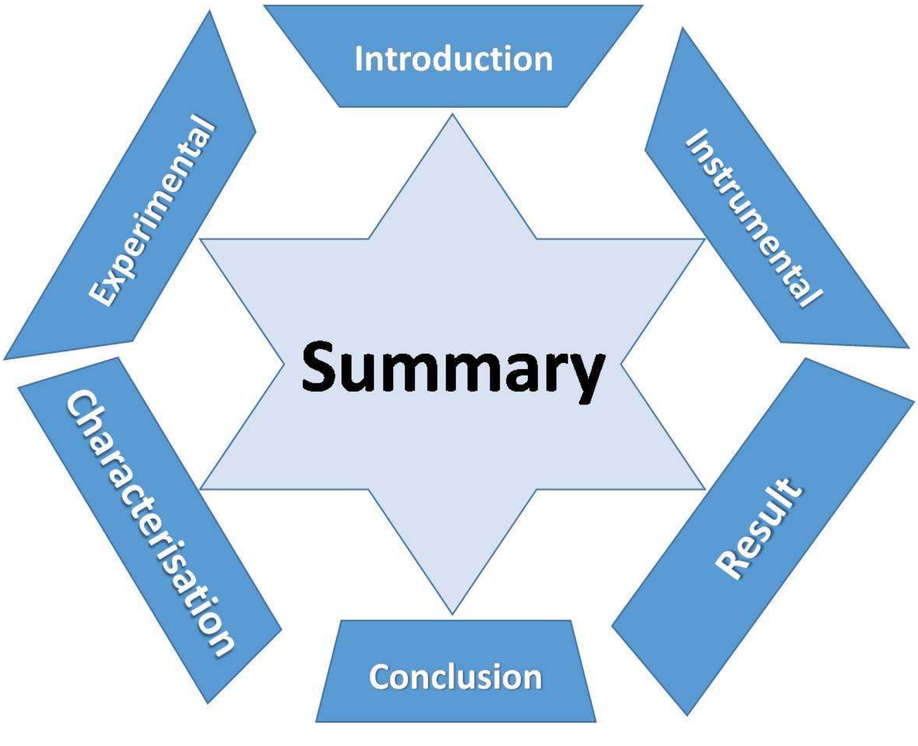
Introduction
Instrumental
Result
Conclusion
Characterisation
Experimental
Summary

SUMMARY

Energy is very important issue in looking to the current energy scenario, where conventional fuels not are only depleting with very fast speed but their consumption keeps polluting our environment with high speed. Therefore, clean energy is the demand of the time. Hydrogen is pretty good energy source and carrier. However, hydrogen is abundantly available element on our planet but mostly associated either with carbon or metals. Therefore, we had selected water as the carbon free source of hydrogen, which give hydrogen after breaking it with renewable source like solar power (sunlight) in presence of photocatalytic material. The present thesis had taken up the nanocomposites Ag/AgX@ZnO as the photocatalytic material for hydrogen production by splitting water. For this the six metal nanocomposites Ag/AgX@ZnO consist of the metal oxide (ZnO) as supporting material, noble metals (Ag) as plasmonic material and MX (X= Cl^-, CO_3^{-2}, PO_4^{-3}, NO_3^-, SO_3^{-2} with SURS) was synthesised using microwave and one pot refluxing method. As synthesized nanocomposite molecular devices were well characterised using advance techniques before and after being used for hydrogen production through water splitting. Which, strengthen our technological competence in the field of designing the photocatalyst for proficient water splitting with a assurance of giving reasonable solution for the production of clean fuel i.e. hydrogen at large scale. That will resolve the present current energy tight situation without spoiling our valuable environment any longer. The entire research work is divided into three chapters.

The **first chapter** deals with introduction of this research work by including literature survey, objective, scope and previous application of the title. Hydrogen can be considered as the most clean and storable energy carrier of the future and has good capability to substitute the conventional fossil fuel to address the problem of environment pollution. Hydrogen can be generated by the using renewable (hydro, wind, wave, solar, biomass and geothermal) and non-renewable (coal, natural gas and nuclear) source of energy for splitting of water. Other methods used for hydrogen production i.e. steam reforming, pyrolysis /plasma reforming of the natural gas, gasification/partial oxidation of coal or oil, by utilizing the solar energy for thermal, electrolysis by photocatalytical splitting of water, were also discussed.

Different classes of photocalalysts (plasmonic material induced-, quantum dot sensitized- materials and other systems of similar category) were well conversed in this chapter in the light of their synthesis, efficiency of water splitting for hydrogen generation efficiency.

The **second chapter** illustrates the fundamental experimental techniques conducted to analyses the as prepared photocatalytic samples. This chapter deals with the description and their application of various advance characterization techniques which are important to characterize the as-synthesized nanocomposites. It also discussed the detailed instrumentation method with emphasis on sample preparation and analyses techniques. These characterization apparatus deals with the characterization of the synthesized nanocatalyst with the knowledge of the basic theories and principles associated with instruments such as electron microscopes, UV-Visible spectrophotometer, FTIR spectrophotometer, XRD, SEM, EDX, electronic balance, pH meter, used for the study.

The **third chapter** well discussed the different synthesis methods and successfully prepared the microwave assisted lotus shaped and conventional single pot refluxing method for spherical Ag/AgCl(NaCl)@ZnO nanocomposites (NCs) along with five other nano composites of different shaped-nanoparticles (NPs) Ag/AgX@ZnO (X= Cl, CO_3^{-2}, PO_4^{-3}, NO_3^{-}, SO_3^{2-}). As synthesised compounds was characterised using advance analysis techniques such as: X-ray diffraction (XRD), UV-Vis absorption spectroscopy, energy dispersive X-rays (EDX) analyses, scanning electron microscopy and their corresponding elemental mapping, FTIR spectra was taken at different stages of the formation of the nanocomposites. Photolumeniscence emission technique used to identify the defects in crystal lattice. These molecular assemblies exploit the visible-light for hydrogen production through water splitting under the exposure of 300 W Xe light source. All synthesized samples show quite good efficiency towards hydrogen production through water splitting.

In conclusion session all synthesised sample were compare on the basis of their water splitting capability and their various characteristics.

Bibliography

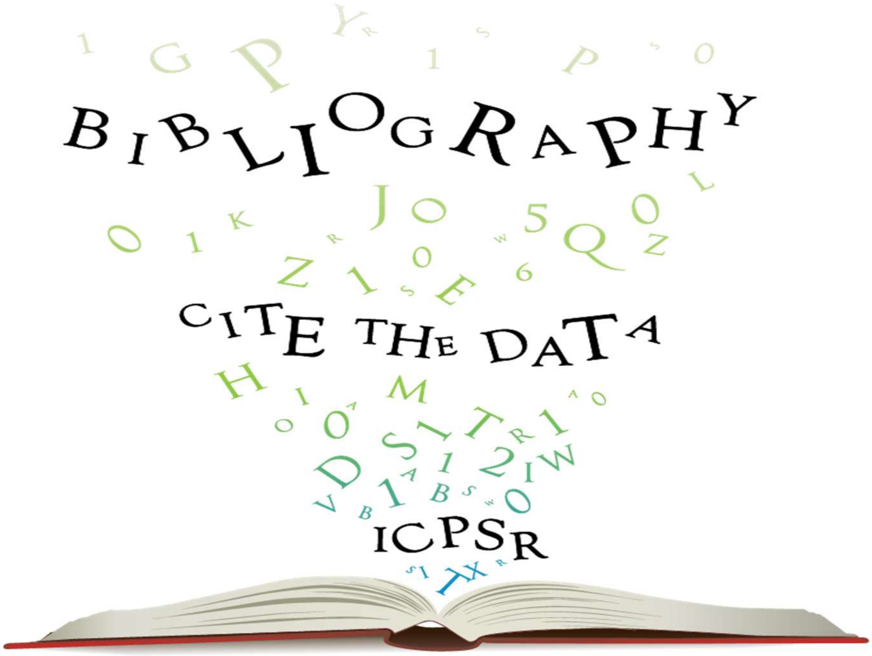

BIBLIOGRAPHY

1. Adhikari R., Gyawali G., Sekino T., Lee S.W., “Microwave assisted hydrothermal synthesis of Ag/AgCl/WO_3 photocatalyst and its photocatalytic activity under simulated solar light’ J Solid State Chem. (2013), 197: 560–565.
2. Adleman J.R., Boyd D.A., Goodwin D.G., Psaltis D., “Heterogenous catalysis mediated by Plasmon heating” Nano Lett. (2009), 9: 4417-23.
3. Ai L., Zhang C., Jiang J., “Hierarchical porous AgCl@Ag hollow architectures: Self-templating synthesis and highly enhanced visible light photocatalytic activity” Appl.Catal. B (2013), 142–143: 744–751.
4. Alvi N. ul H., Eduardo P., Rodriguez D.S., “InN/InGaN quantum dot photo electrode: Efficient hydrogen generation by water splitting at zero voltage” Nano Energy (2015), 13: 291-97.
5. Anpo M., Yamashita H., Ichihashi Y., Ehara S., “Photocatalytic reduction of CO_2 withH_2O on various titaniunm oxide catalysts” J. Electroanal. Chem. (1995), 396:21-6.
6. Ashok Kumar M., “An overview of semiconductor particulate system for photo production of hydrogen” Int. J Hydrogen Energy (1998), 23:427−38.
7. Atwater H.A., “The promises of plasomonics” Sci. Am. (2007), 296(4): 56-63.
8. Awazu K., Fujimaki M., Rockstuhl C., “A plasmonic photo catalyst consisting of silver nanoparticles embedded in titanium dioxide” J. Am. Chem. Soc. (2008), 130: 1676-80.
9. Awazu K., Fujimaki M., Rockstuhl C., Tominaga J., Murakami H., Ohki Y., Yoshida N., Watanabe T., “A plasmonics photocatalyst consisting of silver nanoparticles embedded in titaniumdioxide” J Am. Chem. Soc. (2008), 130: 1676-1680.
10. Barabaszová, K., “Nanotechnologie a nanomateriály” VŠB-Tu Ostrava,158 p., in Czechlanguage. (2006), ISBN 80-248-1210-X.
11. Barber I.J., “Photosynthetic energy conversion: Natural and artificial” Chem. Soc. Rev. (2009), 38:185-96.

12. Barnes W., Dereux L.A., Wbbesen T.W., "Surface plasmon subwave length optics Nature" (2003), 424: 824-30.
13. Barreto G..P, Morales G., Quintanilla M.L.L, "Microwave assisted synthesis of ZnO nanoparticles: effect of precursor reagents, temperature, irradiation time, and additives on Nano-ZnO morphology development". J. Mater (2013): 478681 pp 11
14. Bochin V.P., Fridman A.A, Egasov V.A.L, Rusanov V.D., Sholin G.V., "Hydrogen Energy Systems" (eds T.N. Veziroglu and W. Seifritz), Vol.3. London, UK: Pergamon Press, (1978), pp. 1183.
15. Bockris J.O.M., Dandapani B., Cocke D., Ghorogchian J., "On the splitting of water" Int. J. Hudrogen Energy (1985), 10: 179-201.
16. Brans W.L., Dereux A., Ebbesen T.W., "Surface plasmon subwavelength optics Nature", (2003), 424:824.
17. Bredas J.L., Silbey R., Boudreux D.S. and Chance R.R., 'Chain-length dependence of electronic and electrochemical properties of conjugated systems: polyacetylene, polyphenylene, polythiophene, and polypyrrole" J. Am. Chem. Soc. (1983), 105: 6555.
18. Bubnova, O., Khan Z.U., Wang H. et al., "Semi-metallic polymer". Nat. Mat., (2014), 13: 190-94.
19. Bullen C., Mulvaney P., "The effects of chemisorption on the luminescence of CdSe quantum dots Langmuir" (2006),22:3007.
20. Burns G. "Solid State Physics" New York, NY: Academic Press, (1985), Inc. pp. 339-40.
21. Califano M., Zunger A., Franceschetti A., "Direct carrier multiplication due to inverse Auger scattering in CdSe quantum dots" Appl. Phys. Lett. (2004), 84(13): 2409
22. Califano M., Zunger A., Franceschetti A., "Efficient inverse Auger recombination at threshold in CdSe nanocrystals" Nano Lett. (2004), 4(3): 525.
23. Calzaferri G., Bru¨hwiler D., Glaus S., Schu¨rch D., Currao A., Leiggener C., "Quantum-sized silver, silver chloride and silver sulfide clusters" J Imaging Sci.Technol(2001),45: 331-339.

24. Cao J., LuoB.D., Lin H.L., Chen S.F., "Photocatalytic activity of novel AgBr/WO_3 composite photocatalyst under visible light irradiation for methyl orange degradation" J Hazard Mater(2011), 190: 700−706.
25. Carja G., Birsanu M., Okadac K., Garcia H., "Composite plasmonic gold/layered double hydroxides and derived mixed oxides as novel photocatalysts for hydrogen generation under solar irradiation" J Mater Chem. (2013), A1: 9092–9098.
26. Carja G., Nakajima A., Dranca S., Dranca C., Okada K., "Nanoparticles of nickel oxide: growth and organization on zinc substituted anionic clay matrix by one-pot route at room temperature" J. Phys. Chem.C(2010), 114:14722–14728.
27. Carp O., Huisman C.L., Reller A., "Progress in Solid State" Chem., (2004), 32:33.
28. Chen H.M., Chen C.K., Chang Y.C., Tsai C.W., Liu R.S., Hu S.F., Chang W.S. Chen K.H., "Quantum Dot Monolayer Sensitized ZnO Nanowire-Array Photo electrodes: True Efficiency for Water Splitting" Angewandte Chemie. Int. Ed. (2010), 49: 5966 –69.
29. Chen H.M., Chen C.K., Chen C.J. Cheng L.C., Wu P.C., Cheng B.H., Ming Y.Z., Tseng L., Hsu Y.Y., Chan T.S., Lee J.F., Liu R.S., Tsai D.P., "Plasmon Inducing Effects for Enhanced Photo electrochemical Water Splitting: X-ray Absorption Approach to Electronic Structures" ACS Nano (2012), 6(8): 7362–72.
30. Chen H.M., Chen C.K., Chen C.J., Cheng L.C., Wu P.C., Cheng B..H, Ho Y.Z., Tseng M.L., Hsu Y.Y., Chan T.S., Lee J.F., Liu R.S., Tsai D.P., "Plasmon inducing effects for enhanced photo electrochemical water splitting: X-ray absorption approach to electronic structures"ACS Nano(2012), 6: 7362–7372.
31. Chen H.M., Chen C.K., Tseng M.L., Wu, P.C., Chang C.M., Cheng L.C., Huang H.W., Chan T.S., Huang D.W., Liu R.S., Tsai D.P., "Plasmonic ZnO/Ag embedded structures as collectin glayers for photo generating electrons in solar hydrogen generation photoelectrodes" Small (2013),2926–2936.
32. Chen J., Wu F., "Review of hydrogen storage in inorganic fullerene-like nanotubes" Appl. Phys. A (2004), 78: 989-94.
33. Chen X., Zhuo H., Zheng Z., Gao X., "Visible-light-driven oxidation of organic contaminants in air with gold nanoparticle catalysts on oxide supports" Angew. Chem. Int. Edn. Engl. (2008), 47: 5353-56

34. Cheng, K.W., Wang S.C., "Efffects of complex agents on the physical properties of Ag-In-S ternary semiconductor films using chemical bath deposition" Mat. Chem. Phys. (2009), 115: 14-20.
35. Chouhan N., Liu R.S. Zhang, J., "Photochemical Water Splitting: Materials and Applications; Series Name: Electrochemical Energy Storage and Conversion" Series Editor: Jiujun Zhang, CRC Press, Taylor & Francis Group, Florida-USA, (2017), pp: 358.
36. Christopher P., Xin H., Linic S., "Visible light enhanced catalytic oxidation reactions on plasmonic silver nanostructures" Nature Chem. (2011), 3: 467-72.
37. Cogdell, R.J., Brotosudarmo T.H.P., Gardiner A.T., Sanchez P.M., Cronin L., "Artificial photosynthesis-solar fuels: Current status and future prospects" Biofuels (2010), 1(6): 861-76.
38. Coley G.D., Field J.E., "Role of Cavities in the Initiation and Growth of Explosions in Liquids." Proeedings of the. Royal Society of London Series A, (1973), 335 (1600): 67-86.
39. Coropceanu V., Cornil J., da Silva Filho D.A., Olivier Y., Silbey R. and Brédas, J.L., "Charge transport in organic semiconductors" Chemical reviews, (2007),107(4):.926-952.
40. Coward H.F., Jones G.W., "Limits of Flammability of Gases and Vapours" Bureau of Mines Bulletin (1952), 503: N70-74476; AD-701575.
41. Derwent, R., Simmonds P., Doherty S.O', Manning A., Collins W., Stevenson D., "Global environmental impacts of the hydrogen economy" In. J. Nucl. Hydrogen Prod. Appl. (2006), 1(1): 57-67.
42. Deutsch T., Turner J., Wang H., Dinh H., "Annual Progress Report, National Renewable Energy Laboratory" (NREL), accessed 9 July, (2013), pp. II-70-II-74.
43. Dillon A.C., Jones K.M., Bekkedhal T.A., Kiang C.H., Bethune D.S., Heben M. J., "Letters to nature. Storage of hydrogen in single wall carbon nanotubes" Nature (1997), 386: 377-79.

44. Dong C.L., Persson C., Vbayssieres L. et al., “Electronic structure of nanostructured ZnO from x-ray absorption and emission spectroscopy and the local density approximation’ Phys. Rev. B (2004), 70: 195325.
45. Edwards P. P., Kuznetsov V. L., David W. I. F., “Hydrogen energy” Phil. Trans. R. Soc. A (2007), 365: 1043–1056.
46. Ellingson R.J. Beard M.C., Johnson J.C., “Highly efficient multiple excition generation in colloidal PbSe and PbS Quantum dots” Nano Lett. (2005), 5: 865.
47. Energy Information Administration. International Energy Outlook. Washington, DC, EIA. (2003), 1605.
48. Fang Y., Li Z., Xu S., Han D., Lu D., “Optical properties and photocatalytic activities of spherical ZnO and flower-like ZnO structures synthesized by facile hydrothermal method” J. Alloys Compound (2013), 575: 359–363.
49. Fernandez-Garcia M., Martinez-Arias A., Hanson J.C., Rodriguez J.A., “Nanostructured Oxides in Chemistry: Characterization and Properties” Chem. Rev. (2004), 104(9):4063-4104.
50. Fujishima A., Honda K., “Electrochemical photolysis of water at a semiconductor electrode” Nature (1972), 238:37-38.
51. Gary H., “Solar fuel II: The quest for catalysts” Eng. Sci. (2008), 46: 26-31.
52. Ghosh P., “Preparation of Nanomaterials” NPTEL Chemical Engineering, Interfacial Engineering (1999) Module 9: Lecture 2.
53. Givotov V.K., Fridman A.A., Frotov M.F., “Plasmochemical methods of hydrogen production” Int. J. Hydrogen Energy (1981), 6:441-49.
54. Glaus S, Calzaferri G., “Silver chloride clusters and surface states.” J. Phys. Chem. B. (1999), 103: 5622-5630.
55. Glaus S., Calzaferri G., Hoffmann R., “Electronic properties of the silver–silver chloride cluster interface” Chem. Eur. J. (2002),8: 1785-1794.
56. GM. Fuel cell technology: Prospects, Promises and Challenges. (2007).
57. Goldstein J., “Scanning electron microscopy and X-ray microanalysis” A text book for biologist, material scientist, geologist, Plenum Press, New York, (1992).
58. Grundy P.J., Jones G.A., “Electron microscopy in the study of materials" Edward Arnold, London, (1976).

59. Guo R., Zhang G., Liu J., "Preparation of Ag/AgCl/$BiMg_2VO_6$ composite and its visible-light photocatalytic activity" Mater Res Bull (2013), 48: 1857–1863.
60. Hahn H., "Nanostructured Materials" Elsevier Ltd. (1997),9:03-12
61. Hairston D., "Hail hydrogen" Chem. Eng. (1996), 103: 59.
62. Hamilton J.F., "Physical-properties of silver-halide microcrystals" Photogr. Sci. Eng. (1974), 18: 493–500.
63. Hashimoto K., Irie H., Fujishima A., "TiO_2 photo catalysis: A historical overview and future prospects. Japan" J. Appl. Phys. (2005), 44: 8269.
64. Henglein A., "Chemisorption effects on colloidal lead nanoparticles" J. Phys. Chem. B (1999),103:9302.
65. Hensen E., Sanden R. van de., "Solar Fuels: The Scientific Challenges" Eindhoiven, the Naterlands: University of Technology. (2014).
66. Herrmann J.M., "Hetrogeneous photo catalysis: State of the art and present application" Top. Catal. (2005), 34: 49-65.
67. Hirano S., Young K.S., Kwqabena A., Schwarz J.A., "The high surface area activated carbon hydrogen storage system. In: Proceedings of the First International Conference on New Energy Systems and Conversions" Frontiers Science Series No.7, June (1993), pp. 67-72.
68. Hori Y., Murata A., Kikuchi K., Suzuki S., "Electrochemical reduction of carbon dioxides to carbon monoxide at a gold electrode in aqueous potassium hydrogen carbonate" J. Chem. Sco. Chem. Commun. (1987), 728-9.
69. http://commons.wikipedia.org/wiki/File:TEM_ray_Diag.basic.en.png,visited on June, (2010).
70. Hubbert M. K., "The energy resources of the Earth" Sci. Am. (1971), 225:60-70.
71. Hubbert M.K., "Nuclear Energy and Fossil Fuels" Paper presented before the spring meeting of the Southem District Division of Production, American petroleum Institute Plaza Hotel, (1956), 95: 22-27.
72. Im S.H., Lee Y.T., Wiley B., Xia Y., "Large-scale synthesis of silver nanocubes: the role of HCl in promoting cube perfection and monodispersity" Angew. Chem. Int. Ed. (2005), 44: 2154.

73. Ingram D.B., Linic S., "Water Splitting on Composite Plasmonic-Metal/Semiconductor Photo electrodes: Evidence for Selective Plasmon-Induced Formation of Charge Carriers near the Semiconductor Surface" J. Am. Chem. Soc., (2011), 133 (14): 5202–05.
74. Iwase A., Ng Y.H., Ishiguro Y., Kudo A. and Amal R., "Reduced Graphene Oxide as a Solid-State Electron Mediator in Z-Scheme Photocatalytic Water Splitting under Visible Light" J. Am. Chem. Soc. (2011),133(29): 11054-57.
75. Jiang J.D., Sun Z., Jia H., Lu D., Du P., "A cocatalyst-free CdSnanorod/ZnS nanoparticle composite for high performance visible-light-driven hydrogen production from water" Mater. Chem. A Mater. Energy Sustain. (2016), 4: 675-83.
76. Jiang L., Neill B.C.O., "The energy transition in rural China" Int. J. Global Energy (2004), 21(1-2): 2-26
77. Jones L.W., "Toward a liquid hydrogen fuel economy" Presented at the University of Michigan Environmental Action for Survival Teach In. Ann Arbor, MI: University of Michigan, (1970).
78. Kakuta N, Goto N, Ohkita H, Mizushima T., "Silver bromide as a photocatalyst for hydrogen generation from CH_3OH/H_2O solution" J Phys. Chem. B (1999), 103: 5917–5919.
79. Kamat P.V. Manipulation of Charge Transfer Across Semiconductor Interface. A Criterion that Cannot Be Ignored in Photocatalyst Design. J. Phys. Chem. Lett. (2012),3(5): 663−72.
80. Kamat P.V., "Quantum dot solar cells. Semiconductor nanocrystals as light harvester" J. Phys. Chem. C (2008), 112: 18737.
81. Kelly K.L., Coronado E., Zhao L.L., Schatz G.C., "The optical properties of metal nanoparticles: The influence of size, shape and dielectric environment" J. Phys. Chem. B (2003), 107: 668-77.
82. Kim K., Kim M.J., Kim S.I, Jang J.H., "Towards visible light hydrogen generation: Quantum dot-sensitization via efficient light harvesting of hybrid-TiO_2" Sci. Rep. (2013), 3: 3330.
83. Kittel C., "Indroduction to Solid State Physics" New York, NY: Wiley, (1996).

84. Knupfer M., “Exciton binding energies in organic semiconductors” Applied Physics A: Materials Science & Processing (2003), 7(5): 623–26.

85. Komarneni S., Li D.S., Newalkar B., Katsuki H., Bhalla, A.S., “Microwave–Polyol process for Pt and Ag nanoparticles” Langmuir (2002), 18: 5959.

86. Kreibig U., Vollmer M., “Optical properties of metal clusters” Springer, Berlin: New York, (1995).

87. Ktreuter W., Hofmann H., “Electrolysis: The important energy transformer in a world of sustainable energy” Int. J. Hydrogen Energy (1988), 23 (8) :661-66.

88. Kudo A., Kato H., Tsuji I., “Strategies for the development of visible-light-driven photocatalysts for water splitting” Chem. Lett. (2004), 33:1534-39.

89. Kumar P. and Mittal K.L. (Editors), “Handbook of Microemulsion Science and Technology” Marcel Dekker, New York, (1999), Chapters-2

90. Li W., Hua F., Yue J., Li J., “Ag@AgCl plasmon-induced sensitized ZnO particle for high-efficiency photocatalytic property under visible light” Appl. Surf Sci. (2013), 285: 490–497.

91. Li Z., Cui X., Hao H., Lu M., Lin Y., “Enhanced photo electrochemical water splitting from Si quantum dots/TiO_2 nanotube arrays composite elecrtrodes” Mater. Res. Bull. (2015), 66: 9-15.

92. Linic S., Christopher P., Ingram D.B., “Plasmonic metal nanostructures for efficient conversion of solar to chemical energy” Nat. Mater. (2011), 10: 911-21.

93. Longhui N., Zhengqing H., Hongtao X., Wangxi Z., Borui Y., Lei F., Shuaihua L., “Synthesis of Ag@AgBr photocatalyst and its performance for degradation of methylene blue under visible-lightirridiation” Chinese J Catal. (2012), 33: 1209-1216.

94. Lou Z., Huang B., Ma X., Zhang X., Qin X., Wang Z., Dai Y., Liu Y.A**.,** “3D AgCl hierarchical superstructure synthesized by a wet chemical oxidation method’ Chem. Eur. J**.** (2012)**,** 18:16090 – 16096.

95. Lou Z.Z., Huang B.B., Qin X.Y., Zhang X.Y., Wang Z.Y, Zheng Z.K, Cheng H.F., Wang P., Dai Y., “One-step synthesis of AgBr microcrystals with different

morphologies by ILs-assisted hydrothermal method” Crystal Eng. Comm. (2011), 6: 1789–1793.

96. Ma G., Zhao X., Zhu J., Int. J. Mod. Phys. B, (2005), 19.
97. Maeda K., Domen K., “New non-oxide photo catalysts designed for overall water splitting under visible light” J. Phys. Chem. C (2007), 111: 7851-61.
98. Maeda, K., “Photocatalytic water splitting using semiconductor particles: History and recent developments” J. Photo chem. Photo biol. C (2011), 12: 237-68.
99. Mauna Loa Observatory in Hawaii, NOAA-ESRL), (2018).
100. McCarty R.D., Hord J., Roder H.M., “Selected Properties of Hydrogen” (Engineering Design Data) NBS Monograph 168, National Bureau of Standards, Boulder, CO. (1981).
101. Mori K., Yamashitaand H., Anpo, M., “Photocatalytic reduction of CO_2 with H_2O on various titanium oxide photocatalysts” RSC Adv. (2012), 2: 3165-72.
102. Mott N.F., “Conduction in polar crystals. 2. The conduction band and ultra-violrt absorption of alkali-halide crystals” Trans. Farad. Soc. (1938), 34: 500-506.
103. Mubeen S., Hernandez-Sosa G., Moses D., Lee J., Moskovits M., “Plasmonic photosensitization of a wide band gap semiconductor: converting plasmons to chargecarriers” Nano Lett. (2011), 11: 5548-52.
104. Murphy J.E., Beard M.C., Norman A.G., “PbTe colloidal nanocrystals: Synthesis, characterization, and multiple exciton generation” J. Am, Chem. Soc. (2006), 128: 3241.
105. Nakato Y., Ohnishi T., Tsubomura H., “Photo-electrochemical behaviours of semiconductor electrodes coated with thin metal films” Chem. Lett. (1975), 4: 883-92.
106. Nakato Y., Tsubormura H., “Structures and functions of thin metal layers on semiconductor electrodes” J. Photo Chem. (1985), 29(1-3): 257-66.
107. Nam S. S., Kishan G., Lee M. W., Choi M. J., Lee K. W., “Effect of lanthanum loading in Fe-K/La/$A1_2O_3$ catalyst for CO_2 hydrogenation to hydrocarbons” Appl. Organometallic Chem. (2000), 14: 794-98.

108. Nann T., Ibrahim S.K., Woi P.-M., Xu S., Ziegler C. J., Pickett J., “Water splitting by visible light: A nano-photocathode for hydrogen production” Angew. Chem. Inter. Ed. (2010), 49: 1574-77.
109. Neagu C., Jansen H., Gratrdeniers H., Elwenspock M., “The electrolysis of water: An actuation principle for MEMS with a big opportunity” Mechatronics. (2000), 10 (4-5) :571-81.
110. Newton E., Haletter T. H., Hottinger P., Roth F. VonSchetter W. H., Schuan T.H., “Seasonal storage of hydrogen in stationary systems with liquid organic hydrides” Int. J. Hydrogen Energy (1998), 23(10): 904-09.
111. Nezhad H. "Software Tools for Managing Project Risk: Management Concepts. Vienna, VA” Management Concepts (2007), 1037-55.
112. Nezhad H. “World Energy Scenarios to 2050: Issues and Options. Minnesota” MN: State University of Minneapolis (2009).
113. Niitsoo O., Sarkar S. K., Pejoux C., “Chemical bath deposited CdS/CdSe sensitized porous TiO_2 solar cells” J. Photo Chem. Photo Bio. A (2006), 181: 306.
114. Nozik A.J., “Spectroscopy and hot electron relaxation dynamics in semiconductor quantum wells and quantum dots” Annual Rev. Phys. Chem. (2001), 52: 193.
115. Nyquist R.A., Richard A., “Factors affecting infrared group frequencies: Carbonyl stretching absorption bends” Applied Spectroscopy (1968), 40(3):336-39.
116. Oak Ridge National Laboratory, carbon dioxide information analysis center.
117. Osterloh F.E. and Parkinson B.A., “Recent developments in solar water-splitting photo catalysis” MRS. Bull. (2011), 36: 17-22.
118. Osterloh F.E., “Inorganic materials as catalysts for photochemical splitting of water” Chem. Mater, (2008), 20:35-54.
119. Perreux L., Loupy A., “A tentative rationalization of microwave effects in organic synthesis according to the reaction medium, and mechanistic considerations” Tetrahedron (2001), 7: 9199-9223.
120. Perry T.R., “Washington, DC: U.S. Patent and Trademark Office” (1969), U.S. Patent No. 3,436,611.
121. Pfanner K., Gfeller N., Calzaferri G., “Photochemical oxidation of water with thin AgCl layers” J. Photoch Photo bio A. (1996), 95: 175-180.

122. Pfau C., Bohley C., Miclea P.T. and Schweizer S., “Low phonon energy $BaCl_2$ nanocrystals in Nd^{3+}-doped fluorozirconate glasses and their influence on the photoluminescence properties” J. Appl. Phys. (2011), 109:083545.
123. Pierre A.C., “Introduction to sol-gel processing” Kluwer Academic Publishers, Boston, (1998), 394.
124. Pirhashemi M., Habibi-Yangjeh A., “Preparation of AgCl–ZnO nanocomposites as highly efficient visible-light photocatalysts in water by one-pot refluxing method” J. Alloys Compound (2014), 601: 1–8.
125. Pleskov Y.Y.; Gurevich, Y.V., “Semiconductor photoelectron chemistry” Consultants Bureau: New York, (1986), pp 422 and b Kim, Y. I.; Atherton, S. J.; Brigham, E. S.; Mallouk, T. E. J. Phys. Chem. (1993), 97 (45): 11802–10.
126. Pope M., Swenberg C.E., “Electronic processes in organic solids” Annual Review of Physical Chemistry (1984), 35(1): 613-655.
127. Primo A., Corma A., Garcia H., “Titania supported gold nanoparticles as photo catalyst” Phys. Chem. Chem. Phys. (2011), 13: 886-910.
128. Primo A., Marino T., Corma A., Molinari R., García H., “Efficient Visible-Light Photocatalytic Water Splitting by Minute Amounts of Gold Supported on Nanoparticulate CeO_2 obtained by a Biopolymer Templating Method” J. Am. Chem. Soc. (2011),133 (18): 6930–33.
129. Pu Y.C., Wang G., Chang K.D., Ling Y., Lin Y-K., Fitzmorris B.C., Liu C.M., Lu X., Tong Y., Zhang J. Z., Hsu Y.J., Li Y., “Au Nanostructure-Decorated TiO_2 Nanowires Exhibiting Photo activity Across Entire UV-visible Region for Photo electro chemical Water Splitting” Nano Lett. (2013), 13: 3817−23.
130. Rahlwes H., Teske R.S., Wijnhoven J., Energy [R] evolution: “A sustainable Netherlands energy outlook” Report 2013 Netherlands energy scenario. Utrecht, the Netherland: Utrecht University Repository. (2013).
131. Rajeshwar K., “Hydrogen generation at irradiated oxide semiconductor-solution interfaces” J. Appl. Electrochem. (2007), 37: 765-87.
132. Reimer L., “Transmission electron microscopy: physics of image formation and microanalysis” Springer–Verlag, Berlin: New York. (1989).

133. Rogner H.H., “United Nations Development World Energy Assessment” United Nations, Geneva, (2004), pp: 162.
134. Ruhl C., Appleby P., Fennema, J., Naumov, A. Schaffer M. E., “Economic development and the demand for energy: A historical perspective on the next 20 years” Energy Policy (2012),50: 109-16.
135. Ruijven B. Van, Lamarque J.F., Vuuren D.P. van “Emission scenarios for a global hydrogen economy and the consequences for global air pollution” Glob. Environ. Chang. (2011), 21: 983-94.
136. Saskia A. Galema., ”Microwave chemistry” Chem. Soc. Rev., (1997), 26: 233-238
137. Schaller R.D., Klimov V.I., “High efficiency carrier multiplication in PbSe nano-crystals: Implications for solar energy conversion” Phys. Rev. Lett. (2004), 92(18): 186601.
138. Schaller R.D., Sykora M., Pietryga J.M., Klimov V.I., “Seven excitons at a cost of one: Redefininh the limits for conversion efficiency of photons into charge carriers” Nano Lett. (2006), 6:424.
139. Scherrer P., “Bestimmung der Grösse und der inneren Struktur von Kolloidteilchenmittels Röntgenstrahlen” Nachr. Ges. Wiss. Göttingen (1918), 26: 98-100
140. Schlaphach L., Zuttel A., “Hydrogen-stroage materials for mobile applications” Nature (2001), 141: 353-54.
141. Schmitt M.L, Shelby J.E., Hall M.M., “Preparation of hollow glass microspheres from sol-gel derived glass for application in hydrogen gas storage” J. Non Crystalline Solids. (2006), 352:626-31.
142. Schneider J., Bahnemann D.W., “Undesired Role of Sacrificial Reagents in Photocatalysis” J Phys. Chem. Lett. (2013), 4: 3479-3483.
143. Schürch D., Currao A., Sarkar S., Hodes G., Calzaferri G**.**, **“**The silver chloride photoanode in photoelectron chemical water splitting” J Phys. Chem. B (2002), 106:12764–12775.
144. Schwarz H.A., “Reaction of the hydrated electron with water” J. Phys. Chem. (1992), 96: 8937–8941.

145. Scibioh M.A. Vishwanathan B., “Electrochemical reduction of carbon dioxide: A status report” Proc. Indn. Natl. Acad. Sci. (2004), 70 A (3): 407-62.

146. Seetula J.A., Kalinovski I.J., Slagle I.R, Gutman D., “Kinetics of the reaction of CH_2OH radical with oxygen atoms” Chem. Phys. Lett.(1994), 224: 533-538.

147. Settle F.A., “Handbook of instrumental techniques for analytical chemistry” Prentice Hall, Upper saddle River, N. J., (1997).

148. Shaukatali N. Inamdar, Pravin P., Ingole, and Santosh K. Haram, “Determination of Band Structure Parameters and the Quasi-Particle Gap of CdSe Quantum Dots by Cyclic Voltammetry” Chem. Phys. Chem. (2008), 9: 2574 – 79.

149. Shaukatali N.I., Inngole P.P., Haram, S.K., “Determination of band structure parameters and the quasi-paraticle gap of CdSe quantum dots by cyclic voltammetry” Chem. Phys. Chem. (2008), 9: 2574-79.

150. Sheikh A., Yengantiwar A., Deo M., Kelkar S., Ogale S.C., “Near-field plasmonic functionalization of light harvesting oxide-oxide heterojunctions for efficient solar photo electrochemical water splitting: The AuNP/$ZnFe_2O_4$/ZnO system” Small (2013), 9(12): 2091-96.

151. Shell V., “Lighthouse for Hydrogen” Shell. (2004).

152. Shi H., Chen J., Li G., Nie X.,Zhao H., Wong P.K., An T., “Synthesis and Characterization of Novel Plasmonic Ag/AgX-CNTs (X = Cl, Br, I) Nanocomposite photocatalysts and dynergetic degradation of organic pollutant under visible light” ACS Appl. Mater Interfaces (2013),5: 6959–6967.

153. Shing P., Harbola M.K., Sanyal B., Mookerjee A., “Accurate determination of bad gaps within density functional formalism” Phys. Rev. B (2013), 87:235110.

154. Singh A.K., Nakate U.T., “Microwave synthesis, characterization and photocatalytic properties of SnO_2 nanoparticles” Advances in Nanoparticles (2013), 2: 66-70.

155. Sivul K., “Metal Oxide Photo-electrodes for Solar Fuel Production, Surface Traps, and Catalysis” J. Phys. Chem. Lett. (2013), 4 (2013): 1624−33.)

156. Size S.M., “Physics of Semiconductor Devices” 2nd edition Awiley Inter-science John wiley and Sons (1981), pp 33-37.

157. Sorensen B., “Energy and resources” Science (1975), 189: 255-60.
158. Spellane P.J., Gouterman M., Antipas A., Kim S., Liu Y.C., “Porphyrins 40. Electronic spectra and four-orbital energies of free-base, zinc, copper, and palladium tetrakis (Perfluorophenyl) porphyrins” Inorganic Chem. (1980), 19: 386-91.
159. Strelow F., Fojtik A., Henglein A., “Chemisorption of phosphine on colloidal silver in aqueous solution” J. Phys. Chem., (1994),98:3032.
160. Stuart B., Ando D.J., “Modern infrared spectroscopy” Wiley, Chichester, New York, (1996).
161. Su F., Lu J., Tian Y., Ma X., Gong J., “Branched TiO_2 nano arrays sensitized with CdS quantum dots for highly efficient photo electrochemical water splitting” Phys. Chem. Chem. Phys. (2013), 15: 12026-32.
162. Suhai S., “On the excitonic nature of the first UV absorption peak in polyene” Int. J. Quantum Chem. (1986), 29: 469–476.
163. Sullivan, B. P., “Reduction of carbon dioxide with platinum metals electro catalysts: A potentially important route for the future production of fuels and chemicals” Platin. Met. Rev. (1989), 33(1): 2-9.
164. Sumi S., Watanabe T., Fujishima A., Honda K., “Effect of Cl^- and Br^- ions and pH on the flatband potentials of silver halide sheet crystal electrodes. Bull Chem. Soc. Japan. (1980), 53: 2742-2747.
165. Sun S., Wang W., Zhang L., Shang M., Whag L., “Ag@C cote/shell nanocomposite as highly efficient plasmonic photo catalyst” Catal. Commun. (2009), 11: 290-93.
166. Tadjarodi A., Khaledi D., “Preparation of CuS nanoparticles by microwave irradiation” 14th International electronic conference on synthetic organic chemistry, (2010), (C010).
167. Takata T., Tanaka A., Hara M., Kondo J.N., Domen K., “Recent progress of photocatalysts for overall water splitting” Catal. Today (1998), 44:17−26.
168. Tauc J., Menth A., “States in the gap” J Non-Cryst. Solids. (1972), 569:8-10.

169. Templeton A.C., Pietron J.J., Murray R.W., Mulvaney P., “Solvent refractive index and core charge influences on the surface plasmon absorbance of alkanethiolate monolayer-protected gold clusters” J. Phys. Chem. B (2000),104:564.

170. Thimsen E., Formal F. Le, Gratzel M, Warren S.C., “Influence of plasmonic Au nanoparticles on the photoactivity of Fe_2O_3 electrodes for water splitting” Nano Lett. (2011), 11: 35-43.
171. Thomann I., Pinaud B.A., Chen Z., Lemens B.M.C., Jaramillo T.F., Bronggersma M.L., “Plasmon enhanced solar-to-fuel energy conversion” Nano Lett. (2011), 11: 3440-46.
172. Tian Y., Tatsuma T., “Mechanisms and applications of plasmon-induced chargeseparation at TiO_2 filmsloaded with gold nanoparticles” J. Am. Chem. Soc. (2005), 127: 7632-7637.
173. Trevisan R., Rodena P., Pedro V.G., “Harnessing infrared photons for photo electrochemical hydrogen generation. A PbS quantum dot based “quasi-artificial leaf”. J. Phys. Chem. Lett. (2013), 4(1): 141-46.
174. Trimoto T., Horibe H., Ameyama T.K., “Plasmon-enchanced photocatalytic activity of cadmium sulfide nanoparticles immobilized on silica-coated gold particles” J. Phys. Chem. Lett. (2011), 2: 2057-62.
175. Turner J., Sverdrup G., Mann M.K., et al., “Renewable hydrogen production” Int. J. Energy Res. (2008), 32(5): 379-407.
176. U.S. Environmental protection agency light-duty automotive technology carbon dioxide emissions and fuel economy trend 1975 through 2012, March 2013.

177. Venkata Subbaiah Y.P., Prathap P., Ramakrishna Reddy K.T., “Structural Electrical and Optical Properties of ZnS Films Deposited by Close-Spaced Evaporation” Appl. Surf Sci. (2006),253: 2409-2415.
178. Venkata Subbaiah Y.P., Prathap P., Ramakrishna Reddy K.T., “Structural, Electrical and Optical Properties of ZnS Films Deposited by Close-Spaced Evaporation” Appl. Surf Sci. (2006), 253: 2409-2415.
179. Walter M. G., Warren E. L., McKone J. R., “Solar water splitting cell” Chem. Rev. (2010), 110: 6446-73

180. Wang B., Kanhere P., Chen Z., Nisar J., Pathak B., Ahuja R., “Anion-doped $NaTaO_3$ for visible light photocatalysis” J. Phys. Chem. C (2013), 117: 22518-24

181. Wang D., Duan Y., Luo Q., Li X., Bao L., “Visible light photocatalytic activities of plasmonic Ag/AgBr particles synthesized by a double jet method” Desalination (2011), 270: 174–180.

182. Wang H. Y., Wang G.M., Ling Y.C., “Photochemical study of oxygen deficient TiO_2 nanowire arrays with CdS quantum dot sensitization” Nanoscale (2012), 4: 1463-66.

183. Wang L. W., Califano M., Zunger A., Franceschetti A., “Pseudopotential theory of auger processes in CdSe quantum dots. Phys. Rev. Lett. (2003), 91(5): 0564047.

184. Wang L.G., Pennycook S.J., Pantelides S.T., “The role of the Nanoscale in surface reactions: CO_2 on CdSe” Phys. Rev. Lett. (2002), 89(7): 075506.

185. Wang M., Shang X., Yu X., “Graphene-CdS quantum dots-poly oxometalatc composite films for efficient photo electrochemical water splitting and pollutant degradation” Phys. Chem. Chem. Phys. (2014), 16(47): 26016-23.

186. Wang Q., Hisatomi T., Jia Q., Tokudome H., Zhong M., Wang C., Pan Z., Takata T., Nakabayashi M., Shibata N., “Scalable water splitting on particulate photocatalyst sheets with a solar-to-hydrogen energy conversion efficiency exceeding” Nature Mater. (2016), 15: 611-15.

187. Wang X., Liu G., Lu G.Q., Cheng H.M., “Stable photocatalytic hydrogen evolution from water over ZnO–CdS core–shell nanorods” International Journal of Hydrogen Energy (2010), 35:8199 – 205.

188. Wang X.F., Li S.F., Ma Y.Q., Yu H.G., Yu J.G., “$H_2WO_4{\cdot}H_2O$/Ag/AgCl Composite nanoplates: aplasmonic Z-scheme visible-light photocatalyst” J. Phys. Chem. (2011), C 115: 14648−14655.

189. Wannier G.H., “The structure of electronic excitation levels in insulating crystals” Phys. Rev. (1937), 52(3): 191.

190. Williams D.B., Carter C.B., “Transmission electron microscopy: A textbook for material science” Plenum Press, New York, (1996).

191. Wu F., Hu X., Fan J., Liu E., Sun T., Kang L., Hou W., Zhu C., Liu H., "Photocatalytic Activity of Ag/TiO_2 Nanotube Arrays Enhanced by Surface Plasmon Resonance and Application in Hydrogen Evolution by Water Splitting" Plasmonics (2013), 8:501–08.
192. Wu X., Jiang Q. Z., Ma Z. F., Fu M., Shangguan W. F., "Synthesis of titania nanotubes by microwave irradiation" Sol. State Comm. (2005), 136.
193. Wu Z.C., Zhang Y., Tao T.X., Zhang L., Fong H., "Silver nanoparticles on amidaxime fibers for photocatalytic degradation of organic dyes in waste water" Appl. Sci., (2010), 257: 1092-97.
194. Xiang Q., Yu J., Wong P.K., "Quantitative characterization of hydroxyl radicals produced by various photo catalysts" J Colloid Interface Sci. (2011), 357: 163-167.
195. Xiang Q.J., Yu J.G, Cheng B., Ong H.C., "Microwave-Hydrothermal Preparation and Visible-Light Photo activity of Plasmonic Photo Catalyst Ag-TiO_2 Nanocomposite Hollow Spheres" Chem. Asian J. (2010), 5: 1466-1474.
196. Xu Y., Xu H., Li H., Xia J., Liu C., Liu L., "Enhanced photocatalytic activity of new photocatalyst Ag/AgCl/ZnO" J Alloys Compound (2011), 509: 3286–3292.
197. Yamamoto T., Wada Y., Sakata T., Mori H., Goto M., Hibino S., Yanagida S., "Microwave-assisted preparation of silver nanoparticles" Chem. Lett. (2004), 33:158.
198. Yamashita H., Fujii Y., Ichihashi Y. et al., "Selective formation of CH_3OH in the photo- catalytic reduction of CO_2 with H_2O on titanium oxides highly dispersed within zeolites and mesoporous molecular sieves" Catal. Today (1998),45: 221-27.

199. Yang H.B., Miao J., Hung S.F., Huo G., Chen H. M., Liu B., "Stable quantum dot photo electrolysis cell for unassisted visible light solar water splitting" ACS Nano (2014), 8(10): 10403-413.
200. Yang J., Mei S., Ferreira J.M.F., "Hydrothermal synthesis of TiO_2 nanopowders from tetraalkylammonium hydroxide peptized sols" Mater. Sci. Eng. B, (2001), C:15.

201. Yeh T.F., Teng C.Y., Chen S.J., Teng H., “Nitrogen-doped grapheme oxide quantum dots as photo catalysts for overall water-splitting under visible light illumination” Adv. Mater. (2014), 26(20): 3297-303.
202. Yu G., Dai G.P, Huang B.B., “Fabrication and characterization of visible-light-driven plasmonic photocatalyst Ag/AgCl/TiO_2 nanotube arrays” J Phys. Chem. C (2009), 113:16394-16401.
203. Yu J., Dai G., Huang B., “Fabrication and characterization of visible light driven plasmonic photo catalyst Ag/AgCl/TiO_2 nanotube arrays” J. Phys. Chem. C (2009), 113:16394-40.
204. Yu J., Dai G., Huang B., “Fabrication and characterization of visible-light-driven plasmonic photocatalyst Ag/AgCl/TiO_2 nanotube arrays” J Phys. Chem. C. (2009), 113: 16394-16401.
205. Yue X., Yi S., Wang R., Zhang Z. and Qiu S., “Cadmium Sulfide and Nickel Synergetic Co-Catalysts Supported on Graphitic Carbon Nitride for Visible-Light-Driven Photocatalytic Hydrogen Evolution” Sci. Rep. (2016), 6: 22268:1-9.
206. Yuksel I., “Global warming and renewable energy sources for sustainable developments in Trukey” Renewable Energy (2008), 33(4): 802-12.
207. Zhang G., Lan Z.A., Lin L., Lin S., Wang X. “Overall water splitting by Pt/g-C_3N_4 photo catalysts without using sacrificial agents” Chem. Sci., (2016), 7: 3062–66.
208. Zhang N, Shi J., Mao S.S., Guo L., “Co_3O_4 quantum dots: Reverse micelle thesis and visible light driven photocatytic overall water splitting” Chem. Commun (2014), 65401.
209. Zhang X., Chen Y.L., Liu R.S, Tsai D.P., “Plasmonic photo catalysis” Rep. Phys. (2013), 76:046401.
210. Zhang Y.H., Tang Z.R., Fu X.Z., Xu Y., “Nanocomposite of Ag–AgBr–TiO_2 as a photoactive and durable catalyst for degradation of volatile organic compounds in the gas phase” J Appl. Catal. (2011), B106: 445−452.
211. Zhdanov V.P., Haggland C., Kasemo B., “Relaxation of plasmons in non-siged metal particles located on or embedded in an amorphous semiconductor” Surf. Sci. (2005), 599: L372-75.

212. Zhou H., Mazumdar S., “Electron-electron interaction effects on the optical excitations of semiconducting single-walled carbon nanotubes” Phys. Rev. Lett. (2004), 93: 157402.

213. Zhu M.S., Chen, P.L., Liu M.H., ”Graphene oxide enwrapped Ag/AgX (X= Br, Cl) nanocomposite as a highly efficient visible-light plasmonic photocatalyst”ACS Nano(2011),5: 4529− 4536.

Published Paper
&
Seminar / Symposiums / Conferences

Research Article

Nanocomposite Ag@AgCl/ZnO for efficient hydrogen generation through water splitting

Niranjan Kumar Mandawat[1] · Hari Shankar Sharma[2] · Neelu Chouhan[1]

© Springer Nature Switzerland AG 2019

Abstract

We had successfully prepared the microwave assisted lotus shaped Ag@AgCl/ZnO nanocomposite (NC) of size 57.72 nm, in aqueous media at 90 °C for 7 min heating. The conventional single pot refluxing method was also used to prepare NCs with spherical shaped nanoparticles of size 59.12 nm at 90 °C heating for 3 h. X-ray diffraction data of the Ag@AgCl/ZnO NCs synthesized by the both methods, confirmed that the nanocomposite crystallized in three phases i.e. face-centered cubic (AgCl), cubic (nanosilver) and wurtzite hexagonal phase (ZnO). Energy dispersive X-rays corresponding to the electron microscopy analysis with their elemental mapping, envisioned the surface morphology and elemental composition i.e., 19% ZnO, 13.79% AgCl, 8.08% Zn and 26.19% Ag in the NC. The Ag@AgCl/ZnO NCs exhibited the visible light harvesting ability with band gap i.e. 3.02 and 2.96 eV with SURS selfsensitization of AgCl. Conventionally made sample and microwave assisted sample emits green and yellow-photoluminescence emissions, respectively. FTIR spectra at different stages of the formation of the nanocomposites, visualized the gradual changes in bonding positions of NCs. We utilized this molecular system as an efficient visible-light harvesting optical devices for water splitting. Conventionally and microwave assisted Ag@AgCl/ZnO samples, librated 6082.9 and 6782.32 μmol H_2 h^{-1} g^{-1}, optimum hydrogen in 8 h, respectively, through photocatalytic water splitting under AM 1.5G irradiation.

Graphical abstract

SN Applied Sciences

ARTICLE IN PRESS

Available online at www.sciencedirect.com

ScienceDirect

Visible light harvesting Pt/CdS/Co-doped ZnO nanorods molecular device for hydrogen generation

Neelu Chouhan[a,*], Rakshit Ameta[b], Rajesh Kumar Meena[a,1], Niranjan Mandawat[a,1], Rahul Ghildiyal[c]

ARTICLE INFO

ABSTRACT

Introduction

LIST OF RESEARCH PAPERS

1. Neelu Chouhan, Rakshit Ameta, Rajesh Kumar Meena, **Niranjan Kumar Mandawat** and Rahul Ghildiyal, “Visible light harvesting Pt/CdS/Co-doped ZnO nanorods molecular device for hydrogen generation” **International Journal of Hydrogen Energy** (2016), 41(4): 2298-2306.

2. Rajesh Kumar Meena, **Niranjan Kumar Mandawat**, Neeta Gurbani and Neelu Chouhan, “Synthesis of ZnO Nanoparticles for Organic Pollutant Degradation” **International Journal of Advance Research inscience and Engineering** (2017), 6: 802-808.

3. **Niranjan Kumar Mandawat,** Harishanker Sharma and Neelu Chouhan, “Nanocomposite Ag@AgCl/ZnO for Efficient Hydrogen Generation through Water Splitting” **Springer Nature: Applied Sciences** (2019),1:571

INTERNATIONAL JOURNAL OF HYDROGEN ENERGY XXX (2015) 1–9

Available online at www.sciencedirect.com

ScienceDirect

journal homepage: www.elsevier.com/locate/he

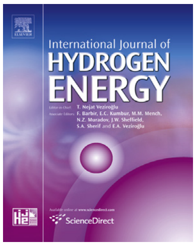

Visible light harvesting Pt/CdS/Co-doped ZnO nanorods molecular device for hydrogen generation

Neelu Chouhan [a,*], *Rakshit Ameta* [b], *Rajesh Kumar Meena* [a,1], *Niranjan Mandawat* [a,1], *Rahul Ghildiyal* [c]

[a] *Department of Pure and Applied Chemistry, University of Kota, MBS Road, Near Kabir Circle, Kota 324005, Rajasthan, India*

[b] *Department of Chemistry, PAHER University, Udaipur 313003, Rajasthan, India*

[c] *Display Materials Laboratory, Applied Physics Department, Faculty of Technology and Engineering, M. S. University of Baroda, Baroda 390002, Gujarat, India*

A R T I C L E   I N F O

Article history:
Received 11 September 2015
Received in revised form
31 October 2015
Accepted 2 November 2015
Available online xxx

Keywords:
CTAB
Micelles
Co-doped ZnO nanorods
Structural disorders
Photocatalytic water splitting

A B S T R A C T

Co-doped ZnO nanorods (Co–ZnO NRs) were synthesized by hydrothermal method using cationic surfactant cetyltrimethylammonium bromide (CTAB). Their physical growth mechanism was traced in the light of FESEM and HRTEM studies. A strong correlation between their electronic structural arrangement and photocatalytic activity was established. Broad and uniform peaks were found between 525 and 700 nm in UV–Vis. diffuse reflectance spectra, which were attributed to the d–d transition of Co^{2+} ion. Successful loading of the nano-sized sensitizer CdS onto the Co–ZnO NRs' surface, contributes to the band gap reduction in CdS/Co–ZnO NRs (Eg = 2.25 eV) sample. X-ray absorption spectroscopy confirms the presence of the lower degree structural disorders in CdS/Co–ZnO NRs with respect to the pristine ZnO and Co–ZnO NRs. Gradual modification in pristine ZnO NRs enhances the photocatalytic activity. Hetero-assembly of 1.5% Pt/CdS/Co–ZnO NRs, exhibited excellent photocatalytic responses in terms of quantum efficiency (1.98%) and hydrogen generation capacity (67.20 mmol/H_2 g) under 1 Sun (1.5AM G) light exposure.

Copyright © 2015, Hydrogen Energy Publications, LLC. Published by Elsevier Ltd. All rights reserved.

Introduction

Hydrogen is the most compatible and clean fuel on the planet in terms of energy economy and ecological health of the planet [1–3]. Unfortunately, the large amount of the H_2 is produced by the carbon containing resources that release enormous amount of CO_2 in atmosphere. Beside this, nature has provided us a carbon-free abundant source of hydrogen in form of water almost free of cost. Cleavage of water in presence of the photocatalyst (a semiconductor of appropriate band gap) and sunlight, can produce hydrogen in an eco-friendly manner. Although, sunlight and water, comes free of cost to us but the cost, stability and efficiency of the

---

[*] Corresponding author. Tel.: +91 744 2471722; fax: +91 744 2471742.
E-mail address: neeluchouhan@uok.ac.in (N. Chouhan).

[1] Tel.: +91 744 2471722; fax: +91 744 2471742.

http://dx.doi.org/10.1016/j.ijhydene.2015.11.019

0360-3199/Copyright © 2015, Hydrogen Energy Publications, LLC. Published by Elsevier Ltd. All rights reserved.

Please cite this article in press as: Chouhan N, et al., Visible light harvesting Pt/CdS/Co-doped ZnO nanorods molecular device for hydrogen generation, International Journal of Hydrogen Energy (2015), http://dx.doi.org/10.1016/j.ijhydene.2015.11.019

photocatalysts are the main thrust areas for the large scale hydrogen production. At some extent oxide photocatalysts (ZnO, TiO_2, Ga_2O_3, Nb_2O_3, In_2O_3 Fe_2O_3, SnO_2, WO_3, NiO, etc.) were found fit in above criteria. Out of the commercially available wide range of oxide semiconductors, ZnO [4,5] has been selected for the study because of its superb and unique inherent qualities such as low cost, wide availability, viability to change in morphology, large excitonic binding energy (60 meV), deep photon penetration, short diffusion length, low reflectivity, high carrier mobility, good bio-compatibility, etc. Usually, the nanostructures of ZnO have a large degree of charge transfer over their bulk counterparts that is due to their large surface area to volume ratio, short lateral diffusion length and low reflectivity [6]. Few of the notable ZnO systems that accounts for photocatalytic water splitting are N-doped ZnO nanowires ($\eta = 4\%$) [7], CdTe sensitized ZnO nanorods (1.98%) [8], CdSe sensitized ZnO nanotubes [4], GaN-ZnO (5.2%) [9], ZnS–ZnO core–shell (STH = 0.38%) [10], TiO_2 shell ZnO core NPs ($\eta = 0.17\%$) [11], ZnO/ZnO:Cr [12], Si/ZnO core shell nanowires (0.035%) [13], ZnO and Fe_2O_3 modified TiO_2 fibres (0.12 ml/min mg) [14], etc. Furthermore, doping of transition metals to the semiconductors, used to improve the optical output of these photocatalytic materials. The effect of different transition metals (Fe, Co, Ni, Cu, Zn, In, etc) on the photocatalytic activity of oxide semiconductor was studied for splitting of water into hydrogen and oxygen under UV irradiation [15,16]. In nonoxide semiconductors category, nanocomposite Ni-doped InN/GaZnON and Ni-doped CdS nanoparticles are a good example of semiconductor that release 2.23 μmol h^{-1} and 25.848 mmol/(h g) of H_2, respectively, under visible light irradiation [17,18].

Hence, cobalt doping was employed to modify the surface quality of ZnO. Therefore, it was decided to synthesize nanostructures of ZnO and Co doped ZnO systems for water splitting and hydrogen generation. Consequently, the hydrothermal method [5] was adopted to develop one dimensional (1D) nanorods (NRs) of Co–ZnO by controlling the surfactant (CTAB; cetyltrimethylammonium bromide) concentration in water. Unluckily, neither the ZnO NRs nor Co–ZnO NRs, can exploit sunlight fully due to their wide band gap (WBG) i.e. $E_g = 3.2$ eV. More often the hetero-assemblies (by incorporation of visible light harvesting moiety to oxides) are made by introducing better light harvesting material (chalcogenide quantum dots/dyes) to nanooxide systems that to enhance their light harvesting capacity. A small amount of the state of art hetero-assemblies are mentioned here as $H_4Nb_6O_{17}$/CdS, Pt/TiO_2/Zn-porphyrin, ZnO/Erythrosine, Pt/$SrTiO_3$:Rh/$BiVO_4$, Fe_2O_3/WO_3, ZnO/CdSe, TiO_2/CdS, etc, which was also used for water splitting [19–28]. These heterostructures exhibit excellent stability, capability to utilise the wide portion of visible light, and suppress the recombination of the light generated photo-electrons and photoholes. For this reason, a chalcogenide CdS ($E_g = 2.4$ eV) was introduced as a sensitizer to ZnO or Co–ZnO NRs. Additionally,1.5% Pt was loaded as co-catalyst to generate reduction site to consume the photoelectrons at the surface of CdS/Co–ZnO NRs. Then this nanomolecular machines i.e. 1.5% Pt/CdS/Co–ZnO NRs, were utilised for photocatalytic water cleavage, in aqueous electrolyte (0.35 M $Na_2S + 0.25$ M K_2SO_3, pH = 13.3) under visible light irradiation [29].

Experimental

Synthesis of ZnO and Co–ZnO NRs

Typical synthesis of ZnO or Co–ZnO nanostructures includes two major steps: (i) seed formation and (ii) growth of NRs. First step involves precipitation of Co–ZnO seeds by oxidation of aqueous nitrates for zinc and cobalt in 10:1 ratio, using liquid ammonia. Afterwards, Co–ZnO seeds (2 g; green powder) were utilised to harvest NRs, by varying surfactant (CTAB) concentration (17.5, 20, 25, 30, 35 and 40%) in reverse micelle hydrothermal method at 200 °C for 10 h, reported earlier [25]. Here, CTAB-micelles served as the templates in nanocrystals growth. For the synthesis of ZnO NRs, the same synthesis process was adopted without taking cobalt salt.

Loading of CdS on to the surface of ZnO and Co–ZnO NRs

Direct sulfurization method was employed to add CdS sensitizer to ZnO and Co–ZnO NRs, described somewhere else [30]. Respective pinkish white and yellowish green powder of CdS/ZnO NRs and CdS/Co–ZnO NRs were obtained, which was washed thoroughly with hot water and dried in the oven at 60 °C for 24 h.

Co-catalyst addition to CdS/Co–ZnO NRs surface

CdS-loaded ZnO and Co–ZnO NRs, were decorated with co-catalyst (1.5% Pt) to facilitate the reduction sites on the photocatalytic surface, by impregnation method [24]. Finally, the sample was dried at 60 °C for 12 h in oven and used as such for photocatalytic cleavage of water.

Results and discussion

Study of surface morphology

As fabricated nanomolecular device (1.5% Pt/CdS/Co–ZnO NRs) was rigorously characterised at every step of fabrication process, using variety of analytic tools. Morphological images of ZnO NRs, was recorded using a field emission-scanning electron microscope (FESEM; Hitachi S-4000) after every step of advancement. High resolution transmission electron microscope (HRTEM; JEM-2100F, at 200 kV) and corresponding energy-dispersive X-ray (EDX) spectroscopy, were used to know the lattice fringes and growth directions from selected area electron diffraction (SAED) pattern and elemental ratio. Products of hydrothermal process at varying concentration of aqueous CTAB and seeds, were examined by using FESEM (Fig. S1). All concentrations of CTAB (17.5, 20, 25, 30, 35 and 40%) was kept greater than its critical micelle concentration (CMC; 0.95 mM) to promote one dimensional (1D) augmentation of Co–ZnO seeds [31]. According to the principle of dynamic solvation, there is a selective adsorption (electrostatic) of the cationic surfactant on the hexagonal facets i.e. (100) and (111) planes, which was also evident from HRTEM images of Co–ZnO seeds [32]. Dissimilar rate of attachment/detachment of surfactant on above planes, effectively reduce the energy

Please cite this article in press as: Chouhan N, et al., Visible light harvesting Pt/CdS/Co-doped ZnO nanorods molecular device for hydrogen generation, International Journal of Hydrogen Energy (2015), http://dx.doi.org/10.1016/j.ijhydene.2015.11.019

and growth rate along these planes that allows NRs to grow along (011) plane [33,34]. Sterically bulky cationic surfactant, CTAB plays two major roles in production of one dimensional Co–ZnO structures: (i) As micellizer, it induces 1D molecular aggregation of micelles in aqueous medium and (ii) As stabilizer, it stabilises the micelle-captivated Co–ZnO nanoclusters by preventing their uncontrollable growth. Results of both of these actions collectively promote cylindrical aggregation (wormlike micelle) of ZnO or Co–ZnO seeds (scaffold by CTAB) in opposite directions with time that creates a junction in the middle of the rods (revealed from FESEM images) [35,36]. The growth process of NRs will continuous till the critical mass of the nanorods of ZnO or Co–ZnO, was attained. Afterwards, NRs split into two parts, as illustrated in Fig. 1. Final size of the NRs strictly depend on the size of the reaction volume i.e. driven by the radius of the cavity in water droplets with surfactant R_w, which is expressed by the following Equation (1) [37].

$$\text{Radius of the cavity in water droplets with surfactant} \quad R_w = 3\,V_{aq}[H_2O]/\sigma[s] \tag{1}$$

where, $\sigma[s]$ = polar group area of surfactants' head and $V_{aq}[H_2O]$ = volume of water. It means the size of the nanorod can be regulated by changing the volume of water and the polar head area of micelles (controlled by CTAB concentration). Increase in volume of water droplet directed to increase the volume of the surfactant in surfactant-incorporated water droplets. Increase in CTAB concentration tends to increase in head area of polar group. Both of these effects, contribute equally in keeping the size of the Co–ZnO NRs (~400 nm broad and 2 μm long) same even at higher CTAB concentration reactions.

FESEM images (Fig. S1a and b) of the Co–ZnO nanoarchitects fabricated at different concentrations of the CTAB and the supporting literature [38], give some significant hints about their physical growth mechanism. Gradual morphological transformations were observed in finishing-end shape of the Co–ZnO NRs with augmentation in CTAB amount/concentrations. At 17.5, 20, 25, 30, 35 and 40% CTAB concentration, corresponding shuttle-end, flat end, cocoon-end (without hole), cocoon-end (with hole), cocoon-end (with big hole) and cocoon-end (with hole) hexagonal rods were obtained, respectively. Due to the apt salt/surfactant ratio (Co–ZnO/CTAB = 1:0.20) in 20% CTAB [39], the flat-end Co–ZnO NRs were produced. Beyond 20% CTAB concentration, the enhancement in CTAB concentration, promotes the formation of excess of bromide ions by cleavage of CTAB. These bromide ions induced chemical inching in nanooxides, which was initiated from the centre of the (011) plane of the hexagonal Co–ZnO NRs and created a hole at centre. The size of this hole increases with CTAB concentration from 50 nm (30% CTAB) to 76 nm (35% CTAB) to 98 nm (40% CTAB). Further, whatever may be the concentration of CTAB was used for synthesis, almost same sized (400 nm wide and 2 μm long) hexagonal-nanorods were obtained.

SAED pattern (Fig. 2a) of flat-end Co–ZnO NRs was obtained corresponding to the HRTEM image, which evident the hexagonal orientation of the Lau's spot around central spot, proves the presence of the crystalline single hexagonal phase of the Co–ZnO NRs, consistent with X-ray powder diffraction (XRD) results. Lattice fringes, depicted in the HRTEM image (Fig. 2b), are separated by 2.42 nm distance, illustrate the high crystalline nature of NRs that grow along the (011) plane. EDX profile of the Co–ZnO NRs, possess the Co and Zn peaks that confirms the Co-doping onto ZnO lattice (Fig. 2c). Fig. 2d exhibits the HRTEM image of CdS loaded Co doped ZnO that revealed the presence of the heterojunction between CdS and Co-doped ZnO.

XRD analysis

X-ray diffraction patterns of the synthesised samples were recorded on Philips X'Pert MPD-3 diffractometer (monochromatized radiation of Cu K_α (λ = 0.15418 nm), scan rate = 0.05° $2\theta\ s^{-1}$, at applied voltage 45 kV and current 40 mA). XRD patterns, shown in Fig. 3a–c, verify crystallisation of ZnO and Co–ZnO NRs in a single wurtzite phase. Positions of diffraction peaks of the ZnO and Co–ZnO NRs, are in good agreement with the standard JCPDS (Joint Committee on Powder Diffraction Standards) card No. 36–1451, which

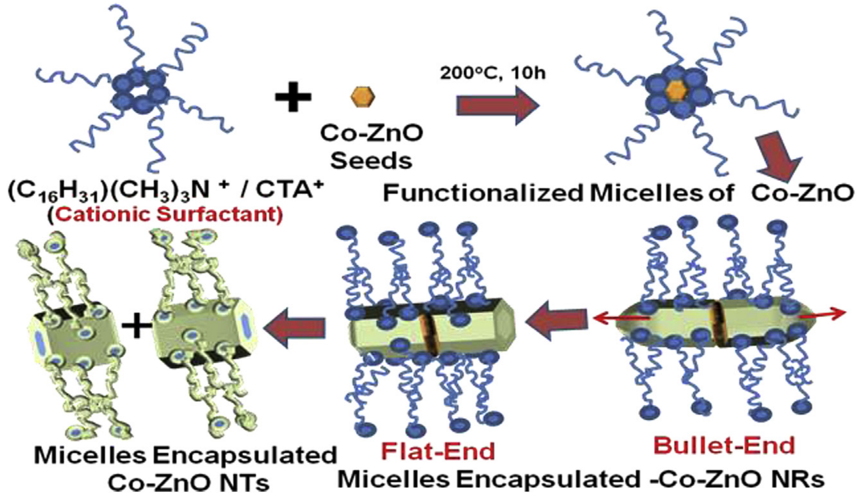

Fig. 1 – A schematic gradual physical growth mechanism for hexagonal faceted Co–ZnO nanorods.

Please cite this article in press as: Chouhan N, et al., Visible light harvesting Pt/CdS/Co-doped ZnO nanorods molecular device for hydrogen generation, International Journal of Hydrogen Energy (2015), http://dx.doi.org/10.1016/j.ijhydene.2015.11.019

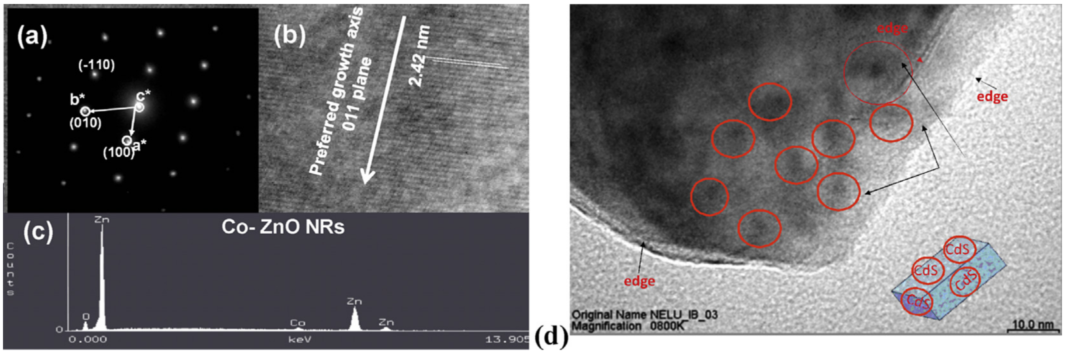

Fig. 2 – **HRTEM micrographs of Co–ZnO NRs including the (a) SAED pattern, (b) lattice fringes, (c) EDX analysis. This shows well ordered crystalline planes along with hexagonal packing of atoms and a lattice spacing of 2.42 nm, corresponding to the growth 011-plane of Co doped-ZnO lattice and (d) HRTEM image of CdS nanoparticles loaded Co-doped ZnO that revealed the presence of the heterojunction between CdS and Co-doped ZnO.**

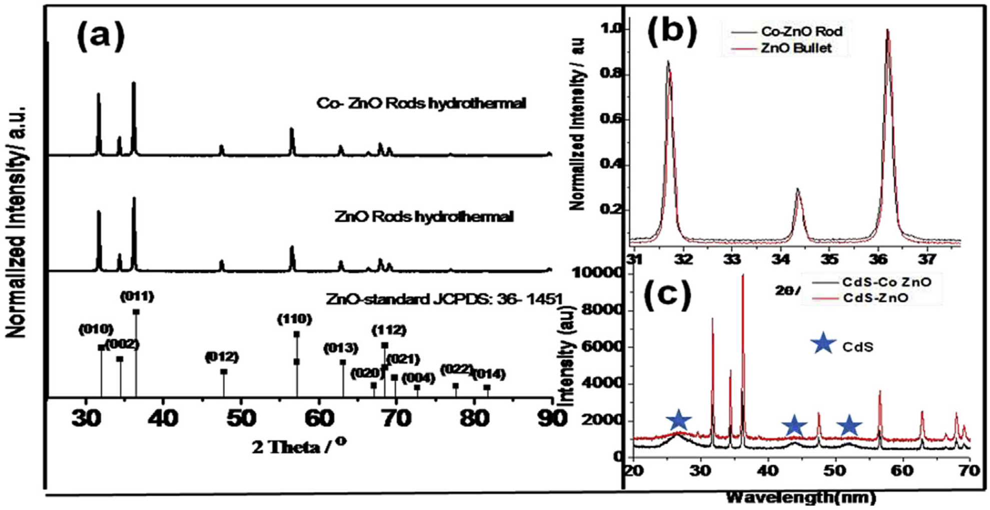

Fig. 3 – **Powder XRD patterns of the (a) pristine ZnO and Co–ZnO NRs with respect to standard ZnO (JCPDS card No. 036-1451) with (b) (100), (002) and (101) reflections highlighted between the angles 31.0–37.5° to demonstrate the insertion of Co in ZnO lattice and (c) loading of CdS on ZnO and Co–ZnO surface and star sign assigned to the hexagonal CdS peaks (JCPDS No. 80-0006). First star at lowest angle represents the combined intensities of (100), (002), and (101) peaks, second and third star belongs to (110), and (112) peaks of CdS, respectively.**

accounts for the hexagonal crystal growth in both samples along the 011 plane. Diffraction patterns of the pristine ZnO and Co–ZnO NRs, shown by Fig. 3a, confirm that both belongs to the $P6_3mC$ space group and their corresponding lattice parameters are $a = b = 3.1919$ Å, $c = 5.1908$ Å, $\alpha = \beta = 90°$, $\gamma = 120°$, at $z = 4$, $V = 52.8800$ Å^3 and $a = b = 3.1942$ Å, $c = 5.1968$ Å, $\alpha = \beta = 90°$, $\gamma = 120°$, at $z = 4$, $V = 52.9600$ Å^3, respectively. Minor shifting in XRD-peaks of Co–ZnO was found towards lower angles in comparison to the pristine ZnO NRs (Fig. 3b) that strongly recommends the incorporation of the slightly bigger ions i.e. Co^{2+} (IR = 0.075 nm > Zn^{2+}; IR = 0.074 nm) into ZnO lattice. Value of c/a ratio was estimated as 1.626 (1.633 for ideal tetrahedra) for the Co–ZnO system that reflected the hexagonal packing of the atoms by geometric occupation of ions at dissimilar sites of slightly distorted tetrahedra. The tetrahedral positions are occupied by anions at four apices and by cations at centre [40].

Another crystal parameter b/c (u) = 0.615 (0.375 for an ideal crystal), shows the existence of the anion–cation bond, parallel to the c-axis. c/a parameter follows an inversely proportional relationship with u. Therefore, on decreasing c/a value with respect to ideal tetrahedra, u adjusts itself in such a way that the four tetrahedral distances get balanced through the distortion in tetrahedral angles and distances. Prominent and sharp peak (011) around $2\theta = 36.26°$, reconfirms the crystal growth along (011) plane. Crystalline domain of the flat end Co–ZnO NRs, was calculated using Debye-Sherrer equation i.e. 385 nm, which is quite near to the average size (~400 nm) of the NRs that measured by FESEM images. Fig. 3c expressed the significantly broad XRD peaks of CdS accompanied with regular wurtzite Co–ZnO peaks, in CdS/Co–ZnO NR's sample. In the same sample presence of the first broad peak centred at $2\theta = 27°$ is an aggregation of (100), (002), and (101) peaks of CdS, (110) peak at $2\theta = 44°$, and (112) peak at $2\theta = 52.5°$, are also in

Please cite this article in press as: Chouhan N, et al., Visible light harvesting Pt/CdS/Co-doped ZnO nanorods molecular device for hydrogen generation, International Journal of Hydrogen Energy (2015), http://dx.doi.org/10.1016/j.ijhydene.2015.11.019

good agreement with the standard CdS (JCPDS card No. 80-0006). It proves the successful loading of the hexagonal CdS nanoparticles onto the ZnO NR's and Co–ZnO NR's surface as shown in Fig. 3c. XRD patterns of the all studied samples are shown in Fig. 3a–c and following Equation (2) [41], is used to measure the crystallinity of the samples.

$$C_{rt}(\%) = \{(I_{011} - I_{am})/I_{011}\} \times 100 \qquad (2)$$

where, C_{rt} = the relative crystallinity (in percentage); I_{011} = the highest intensity of the (011) diffraction angle of the crystal lattice (arbitrary unit; au); and I_{am} = the scattering strength diffracted by the non-crystalline environment (if 2θ is close to angle 21°, the unit is similar to I_{011}). The observed crystallinity (ZnO NRs (95.00%), Co–ZnO NRs (94.00%), CdS/ZnO (90.00%) and CdS/Co–ZnO (78.95%)) of the all studied samples is decreases with gradual modification in the basic ZnO NRs sample.

UV–Vis DRS study

Diffuse reflectance UV–visible absorption spectrum was recorded for the dry and pressed disk samples of powdered ZnO NRs to confirm the doping of Co and deposition of CdS on ZnO NRs, by using UV–visible spectrophotometer (UV-1700, Shimazdu, Japan with UV Probe device). Moisture free $BaSO_4$ was used as a reflectance standard in a UV–Vis diffuse reflectance experiment. Instrumental error was noticed around the wavelength 350 nm due to the shifting of the light source from UV to Visible region, which was found responsible for the noise. Characteristic diffuse reflectance spectra (Fig. 4a and b) of the samples illustrate the red shifts in their edges with broadening in the main peak (300–525 nm) on successive advancement (addition of Co or CdS) in the ZnO NRs for making of the hetero-assembly CdS/Co–ZnO NRs. First excitation peak centred at 450 nm, represents the presence of the CdS. Co^{2+}-incorporated samples (Co–ZnO NRs and CdS/Co–ZnO NRs) exhibit a secondary peak around 525–700 nm that is attributed to the multiple d–d transitions of Co(II) [42]. Band gap (E_g) of the studied system has been estimated at different stages of the advancement of ZnO NRs using the Kubelka–Munk function F(R) *vs* wavelength plot (Fig. 4a and b). Successive surface modification of ZnO nanostructures reduces their band gaps, as follows 3.18 eV (ZnO NRs), 3.00 eV (Co–ZnO NRs), 2.48 eV (CdS/ZnO NRs) and 2.25 eV (CdS/Co–ZnO NRs). Band gap of the CdS/Co–ZnO NRs, ensures us about the good possibility of using it for photocatalytic hydrogen generation.

First excitonic peak of DRS spectrum was utilized to determine the particle size of the sensitizer CdS (ca 5.24 nm) in CdS/Co–ZnO NRs by using following power Equation (3) [43],

$$D = (-6.6521 \times 10^{-8})\lambda^3 + (1.9557 \times 10^{-4})\lambda^2 - (9.2352 \times 10^{-2})\lambda + (13.29) \qquad (3)$$

where, *D* (nm) is the size of the CdS nanosensitizer in heterostructure, and *λ* (nm) is the first excitonic absorption wavelength i.e. 450 nm for the corresponding sample. It represented that the incorporation of 5.24 nm CdS nanoparticles on Co–ZnO NRs (~400 nm broad and 2 μm long).

XAS study

X-Ray absorption spectroscopy (XAS), was used to examine the local electronic environment around the centre atom. XAS (XANES/EXAFS) was recorded at BL-8 dispersive EXAFS beamline at INDUS-2 synchrotron radiation source at RRCAT, Indore. Measurements were made at the Zn K-edge (9659 eV) in fluorescence mode at room temperature with a seven-element HPGe detector and double crystal Si (111) monochromator. Measurements were performed along the c axis perpendicular to electric field vector and along the c axis in the plane of the electric field vector. The raw X-ray absorption data were analysed using a standard procedure (software program ATHENA) that includes the subtraction of the pre- and post-edge background, edge calibration with a reference Zn foil, and normalization of edge jump. The Fourier transform of the normalized k^3-weighted EXAFS spectra was taken using the program ARTEMIS for k from 2 to 11.5 $Å^{-1}$ and Hanning window function followed by a nonlinear least-squares fit between 1.0 and 3.6 Å. Theoretical phase and amplitude functions were calculated using the FEFF (V. 8.4) code.

This technique identifies the lattice disorders and short-range local atomic arrangement around the central atoms, which XRD can't observe [44]. XAS profiles of the ZnO, Co–ZnO

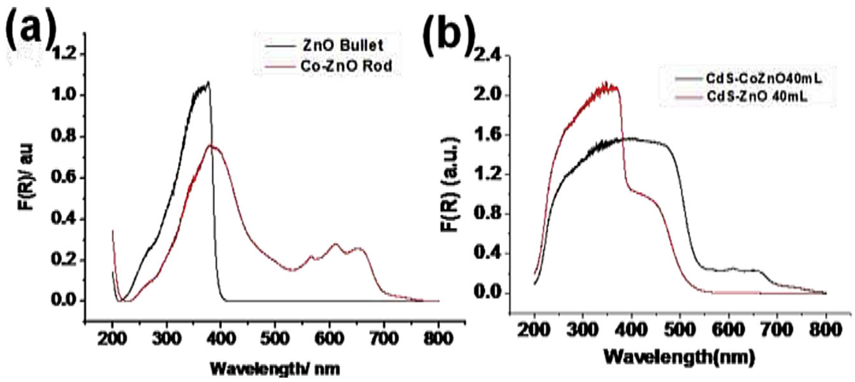

Fig. 4 – Diffuse reflectance spectroscopic Kubelka-Munk plots (F(R) *vs* wavelength) of pristine ZnO NRs and Co–ZnO NRs (a) before and (b) after CdS loading.

Please cite this article in press as: Chouhan N, et al., Visible light harvesting Pt/CdS/Co-doped ZnO nanorods molecular device for hydrogen generation, International Journal of Hydrogen Energy (2015), http://dx.doi.org/10.1016/j.ijhydene.2015.11.019

and CdS/Co–ZnO NRs, were recorded at Zn K edge. Typical normalized XAS plot between X-ray absorption cross-section and photonic energy (PE) are displayed in Fig. 5a–c. XAS profile was divided into four prominent zones with respect to the photonic energy of incoming photons i.e. pre-edge, edge, near-edge (XANES; X-rays absorption near edge spectroscopy) and fine structures (EXAFS; extended X-rays absorption fine structures and NEXAFS; near edge X-ray absorption fine structure) regions. Absence of pre-edge features (ls → 3d; dipole forbidden transition, PE < 9659 eV) in all samples are credited to the fully occupied 3 d^{10} configuration of Zn^{2+} ions [39] and negligible p-band defects. Edge features (ls → 4p) of Co–ZnO shifted towards the higher PE = 9660.23 eV with respect to the pure ZnO and CdS/Co–ZnO NRs (PE = 9659 eV) are attributed to the replacement of the high polarity Zn–O bonds by the low polarity Co–O and Co–Zn bonds in Co–ZnO.

Eventually, the presence of the highly polar bonds of CdS/Co–ZnO NRs i.e. Cd–O, Cd–S and Zn–S, nullified the shifting in edge. It also confirms the existence of the highly oxidised Zn atoms (>2 + oxidation state) in Co–ZnO NRs, attributed to the adsorption process [45]. Almost same edge position of the pristine ZnO and CdS/Co–ZnO NRs, signify the retention of similar oxidation state of Zn (2+) in both. Intense, symmetrical and superimposed white line (WL) peak features of ZnO and Co–ZnO NRs, centred at 9668.50 eV (10.01 eV/step), are originated due to ls-4p hybridization, reflected the similar electronic surroundings in both the species. Short heighted WL peak of CdS/Co–ZnO NRs, predicts the low degree of anisotropy, and highly disordered arrangement of elements around Zn atom [6]. Electronic transition 1s → 4d in Zn is attributed to the EXAFS features at P E ~ 9668.50 + 50 eV. Shoulder peak was observed at 9678.52 eV, followed by the symmetrical third and fourth peaks at PE 9695.96 and 9714.00 eV, respectively for both sample. These fine features reflected that the anions envelop the central Zn atoms in a regular tetrahedral fashion in above two samples. Absence of the 9695.96 eV peak in Co–ZnO, reveals the existence of the cobalt (II) oxide with few Co atoms that substitute zinc in the ZnO system [46]. It stimulates the distorted tetrahedral surrounding around Zn and deviation in the lattice parameters [45]. NEXAFS features for ZnO and CdS/Co–ZnO NRs, coincide within 1 eV PE range, suggesting that both have similar regular tetrahedral environment of anions for Zn atoms. The results also suggested about the distorted tetrahedral arrangement in the Co–ZnO system, where the metallic species Co (II) and Zn are at the centre of the tetrahedra and anions (O^{2-}) are situated at the four apexes of the tetrahedra. NEXAFS features of the all examined systems were refined by keeping typical k^3-weightage in the range of 3.5–12 $Å^{-1}$ and using software FEFF (V-7) (Fig. S2a and b) [47]. Respective refined parameters (least-squares refined R-factor, mean first-shell metal–oxygen bond length, coordination number, and Debye-Waller factor) are extracted for ZnO (3.8wt%, 1.99(8)Å, 5.10 and 0.96 × 10^{-2} $Å^2$), Co–ZnO (4.10wt%, 2.01(4)Å, 5.40 and 0.82 × 10^{-2} $Å^2$) and CdS/Co–ZnO (4.20wt%, 1.95(7)Å, 5.80 and 0.86 × 10^{-2} $Å^2$).

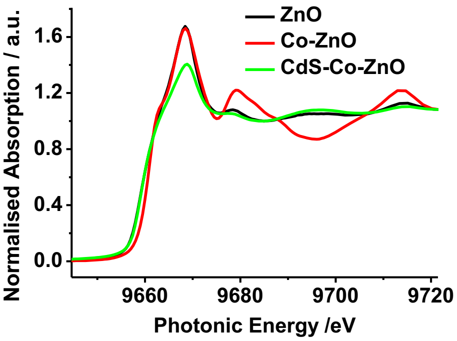

Fig. 5 – Normalized synchrotron-radiation based absorption cross section as a function of photonic energy with the geometry of the c-axis aligned parallel to the electric field vector of the x rays at the Zn K-edge (E = 9659 eV) spectra of (a) pristine ZnO NRs, (b) Co–ZnO NRs and (c) CdS/Co–ZnO NRs, recorded in a florescent mode.

Photocatalytic hydrogen production

The catalyst (0.3 g) was suspended in 140 mL of aqueous electrolyte of 0.35 M Na_2S and 0.25 M K_2SO_3 in a double walled-Pyrex glass reaction cell (volume ~220 mL, with water jacket) that was sealed with a rubber septum. To expel the air-content from the solution, the sample was purged with Ar for 1 h prior to start the photochemical reaction. Ar gas flows continuously in inner jacket, to maintain 1 atm pressure of the solution. Temperature of the outer jacket was set at 25 °C. The suspension was irradiated with a 300 W Xe lamp (>420 nm, light intensity 1 × 10^{22} photons per hour Xe lamp-HX1, Model PE300UV, Perkin Elmer). All the experiments are carried out under ambient conditions. Photocatalytic responses were hourly monitored in terms of the amount of hydrogen generated at 1–7 h time intervals, using gas chromatograph (Shimazdu, Japan, thermal conductivity detector and molecular sieve with 5 A columns) throughout the course of the reaction. Photocatalytic cleavage of water was carried out in presence of the hole-scavenger electrolyte (0.25 M K_2SO_3 + 0.35 M Na_2S) solution of 13 pH, under the irradiation of 1 Sun (100 mW/cm^2, AM1.5 G) visible light. Rough and hexagonal crystalline surface of the CdS/Co–ZnO, loaded with co-catalyst (Pt) to facilitate the active sites for the oxidation (photohole rich) and reduction (photoelectron rich) of water. These active sites suppress the recombination of the photoelectric current carriers i.e. photoelectrons and photoholes. Hole-scavenger electrolyte was used to avoid the photooxidation of CdS nanoparticles present in the nanomolecular device by irreversible consumption of photogenerated holes that prohibited the oxidation of water [48]. Corresponding amount of H_2 evolved without any noticeable degradation of the photocatalytic devices, such as 1.5% Pt/ZnO, 1.5% Pt/Co–ZnO, 1.5% Pt/CdS/ZnO and 1.5% Pt/CdS/Co–ZnO, was recorded as 10.2, 22.56, 50.57 and 67.20 mmol/H_2 g, respectively (Fig. 6a). Quantitative rise in the rate of H_2 evolved, was noticed after each step of the advancement on ZnO NRs, which follows a quadratic relation $y = 1.022(03) x^2 + 14.734(15) x - 6.900(16)$ and satisfy 3/2 order kinetics for advancement paradigm of nanomolecular device (Fig. 6b). Apparent quantum yield (AQY) was estimated for the tested device using Equation (4) with the assumption that all of the incident photons are absorbed during the photochemical reactions [49].

Please cite this article in press as: Chouhan N, et al., Visible light harvesting Pt/CdS/Co-doped ZnO nanorods molecular device for hydrogen generation, International Journal of Hydrogen Energy (2015), http://dx.doi.org/10.1016/j.ijhydene.2015.11.019

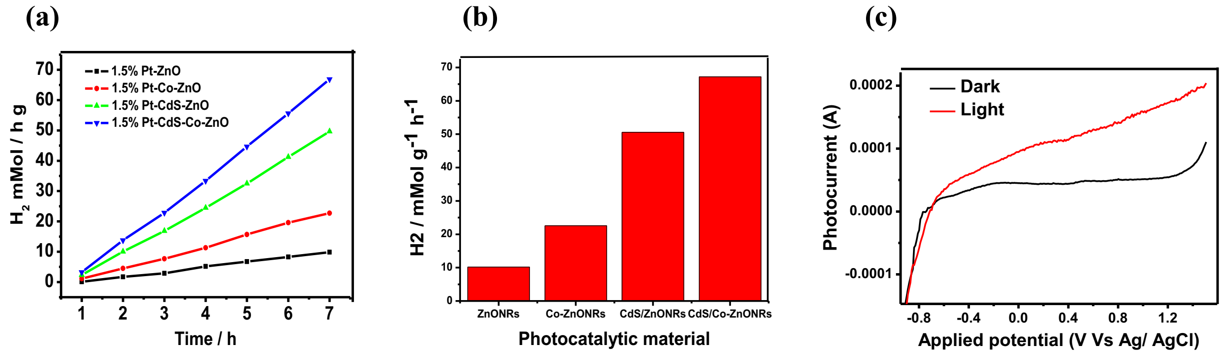

Fig. 6 – **(a) Comparative rate of H_2 evolution by photocatalytic cleavage of water using molecular devices of 1.5% Pt/ZnO NRs, 1.5% Pt/Co–ZnO NRs, 1.5% Pt/CdS/ZnO NRs, and 1.5% Pt/CdS/Co–ZnO NRs; (b) Bar plot of gradual increase in the rate of H_2 evolved after 7 h for each advancement. (c) I–V plot for CdS/Co–ZnO NRs in electrolyte solution (pH = 13.5) under AM1.5 G illumination, recorded at zero bias voltage at 25 °C temperature in the applied potential range −1.0 to +1.5 V (*vs* Ag/AgCl electrode). Exposure area of the sample ~1 cm^2.**

$$\text{AQY }(\%) = \left([\text{Number of } H_2 \text{ molecules evolved} \times 2] \times 100\right) / [\text{Number of incident photons}] \tag{4}$$

where, the number of incident photons was 4.48 × 10^{24} photon h^{-1}, measured using a Si photodiode, at 420 nm wavelength. Corresponding water splitting ability of the device was estimated in terms of AQY at 420 nm. These were found to be 0.30, 0.66, 1.49 and 1.98%, respectively for above mentioned systems (1.5% Pt/ZnO, 1.5% Pt/Co–ZnO, 1.5% Pt/CdS/ZnO and 1.5% Pt/CdS/Co–ZnO). Reproducibility of these systems against their photocatalytic water splitting ability was checked thrice by using the same photocatalytic material (suspended particles in aqueous electrolyte) after their five times washing with the pure de-ionized water and drying at 100 °C for 1 h.

Electrochemical analyzer (Auto lab potentiostat model PGSTAT30) in the midst of software GPES (general purpose electrochemical study) manager, was used to monitor the photovoltaic responses of the test samples. Power density of the light source was controlled at 100 $mWcm^{-2}$ (AM1.5 G), using thermopile (Gentec (ε) Solo-2, Model-UP12E105-H5) at the beginning and checked at end of the each PEC run. Pyrex glass photoelectrochemical (PEC) cell with water jacket was well equipped with a small quartz window and conventional three electrode-system, comprising of a saturated calomel electrode (SCE) as reference electrode, a Pt flag as counter electrode and uniform film of the sample loaded on fluorine-doped tin oxide (FTO) substrate (using doctor blade method) as the working electrode (WE). A wide potential window with a width of 1.5 V (−0.9 to + 0.6 V) recorded during photovoltaic study of 1.5% Pt/CdS/Co–ZnO NRs device, was attributed to good electron exchange quality of the system (Fig. 6c) [50]. Significantly, no saturation in photocurrent was observed at applied positive potentials, which indicates efficient charge separation upon light illumination that is responsible for higher hydrogen evolution amount [51].

On the basis of this study and other supportive analytical evidences [7,52], the most plausible overall photocatalytic water splitting mechanism for the nanodevice (1.5% Pt/CdS/Co–ZnO NRs) in presence of hole sacrificial electrolyte under visible light exposure, is suggested and illustrated by Fig. 7.

During electron transfer, when the surface of the device was illuminated with light, an electron was excited from VB to CB, which generates a pair of photohole and photoelectron in corresponding VB and CB of Co–ZnO. Nascent photoelectrons of CB (Co–ZnO) are transported to the CB of quantum confined nano-sized sensitizer (CdS). This electron arrived at the junction of Pt/electrolyte interface by passing through the electron-pool of the metallic Pt. At the interface, photoelectrons interacts with H^+ ions [53] of the solution and liberates nascent H that combined with another nascent H atom to generate H_2 gas. Hole accumulated at VB of Co–ZnO and CdS, were consumed by hole-scavenger electrolyte. Major chemical reactions [54], responsible for hydrogen evolution by photocatalytic cleavage of the water, are given by the Equations (5–8).

$$\text{On photo} - \text{exposure}: \; CdS/Co - ZnO + h\upsilon \rightarrow e^{-}(CdS/Co - ZnO) + h^{+}(CdS/Co - ZnO) \tag{5}$$

$$\text{Cathode}: \; 2HO + 2e^{-} \rightarrow 2OH^{-} + H_2 \tag{6}$$

$$\text{Anode}: \; SO_3^{2-} + S^{2-} + 2OH^{-} + 1.5H_2O + 6h^{+} \rightarrow 1.5S_2O_3^{2-} + SO_4^{2-} + 4H^{+} \tag{7}$$

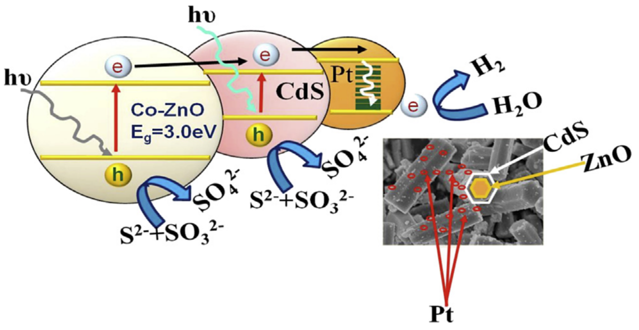

Fig. 7 – **Electron transfer mechanism for the photocatalytic water splitting using the nanomolecular device i.e. 1.5% Pt/CdS/Co–ZnO NRs.**

Please cite this article in press as: Chouhan N, et al., Visible light harvesting Pt/CdS/Co-doped ZnO nanorods molecular device for hydrogen generation, International Journal of Hydrogen Energy (2015), http://dx.doi.org/10.1016/j.ijhydene.2015.11.019

$$\text{Overall Redox Reaction}: \; S^{2-} + SO_3^{2-} + 5H_2O \xrightarrow{h\nu} 5H_2 + 2SO_4^{2-} \quad (8)$$

Conclusion

In short, this study gives us an inside view of the surfactant (CTAB)-controlled low cost fabrication of the ZnO NRs via reverse-micelles synthesis. Current work is focused on the performance of the nanomolecular photoelectrode of ZnO NRs by gradual surface modification for hydrogen production efficiency. A good correlation between atomic arrangement around Zn atom and light harvesting capacity of the modified ZnO NRs has been established. Defects developed on Co–ZnO NR's surface, may act as recombination centres for the photocarriers. These defects were suppressed by the decoration of flat-end Co–ZnO NRs with visible light sensitizer CdS. Heterocouple CdS/Co–ZnO NRs, show a good compatibility of nanoparticles of CdS with Co–ZnO NRs. Whole molecular assembly was utilised as a photoelectrode after Pt-loading for hydrogen generation via water splitting. Gradual increase in the photocatalytic activity of the device was recorded with modification, such as 1.5% Pt/ZnO (10.20 mmol/hg, AQY = 0.30%), 1.5% Pt/Co–ZnO (22.56 mmol/hg, AQY = 0.66%), 1.5% Pt/CdS/ZnO (50.57 mmol/hg, AQY = 1.49%) and 1.5% Pt/CdS/Co–ZnO NRs (67.20 mmol/hg, AQY = 1.98%), which can execute a job of water splitting better than pristine samples. Time dependent hydrothermal synthesis CdS/Co–ZnO NRs is in progress to explore the relationship between their photocatalytic hydrogen generation efficiency and atomic arrangement.

Acknowledgement

One of the authors (NC) gratefully acknowledge the financial support of the Science and Engineering Research Board (SERB) of Department of Science and Technology (DST SR/S1/PC-31/2012), India, for this work. Authors thank Dr. Gupta, of INDUS-2 BeamLine-8 of Raja Ramannna Institute of Advanced Technology, Indore, India, for his assistance in XAS measurements and Prof R. S.Liu, NTU, Taipei, Taiwan for his valuable discussion and assistance in FESEM and HRTEM studies.

Appendix A. Supplementary data

Supplementary data related to this article can be found at http://dx.doi.org/10.1016/j.ijhydene.2015.11.019.

REFERENCES

[1] Balat M. Potential importance of hydrogen as a future solution to environmental and transportation problems. Int J Hydrogen Energy 2008;33:4013–29.

[2] Chouhan N, Liu RS. Electrochemical technologies for energy storage and conversion. In: Liu RS, Zhang L, Sun X, Liu H, Zhang J, editors. Electrochemical technologies for energy storage and conversion, 1. Weinheim, Germany: Wiley-VCH; 2012. p. 23–33. Chap. 1.

[3] Ogden JM. Prospectus of building a hydrogen energy Infrastructure. Annu Rev Energy Environ 1999;24:227–79.

[4] Chouhan N, Yeh L, Hu SF, Liu RS, Chang WS, Chen KH. CdSe(QDs)@ ZnO nanotubes as an effective photoanode. Chem Commun 2011;47:3493–5.

[5] Wang XH, Zhang YC, He WL, Zhu MK, Wang B, Yan H. Hydrothermal synthesis of zinc oxide powders with controllable morphology. Ceram Int 2004;30:93–7.

[6] Wolcott A, Smith WA, Kuykendall TR, Zhao YP, Zhang JZ. Photoelectrochemical generation of hydrogen from water splitting based on dense and aligned TiO_2 nanorod arrays. Small 2008;5(1):104–11.

[7] Yang X, Wolcott A, Wang G, Sobo A, Fitzmorris RC, Qian F, et al. Nitrogen-doped ZnO nanowire arrays for photoelectrochemical water splitting. Nano Lett 2009;9(6):2331–6.

[8] Chen HM, Chen CK, Chang Y-C, Tsai C-W, Liu R-S, Hu S-F, et al. Quantum dot monolayer sensitized ZnO nanowire-array photoelectrodes: true efficiency for water splitting. Angew Chem 2010;122(34):6102–5.

[9] Maeda K, Teramura K, Lu D, Takata T, Saito N, Inoue Y, et al. Photocatalyst releasing hydrogen from water. Nature 2006;440:295.

[10] Kushwaha A, Aslam M. ZnS shielded ZnO nanowire photoanodes for efficient water splitting. Electrochim Acta 2014;130:222–31.

[11] Liu M, Nam C-Y, Black CT, Kamcev J, Zhang L. Enhancing water splitting activity and chemical stability of zinc oxide nanowire photoanodes with ultrathin titania shells. J Phys Chem C 2013;117:13396–402.

[12] Shen S, Kronawitter CX, Jiang J, Guo P, Guo L, Mao SS. A ZnO/ZnO: Cr isostructural nanojunction electrode for photoelectrochemical water splitting. Nano Energy 2013;2:958–65.

[13] Ji J, Zhang W, Zhang H, Qiu Y, Wang Y, Luo Y, et al. High density Si/ZnO core/shell nanowire arrays for photoelectrochemical water splitting. J Mater Sci Mater Electron 2013;24(9):3474–80.

[14] Barakat NAM, Taha A, Motlak M, Nassar MM, Mahmoud MS, Al-Deyab SS, et al. ZnO & Fe_2O_3-incoportaed TiO_2 nanofibers as super effective photocatalyst for water splitting under visible light radiation. Appl Catal A General 2014;481:19–26.

[15] Hameed A, Gondal MA, Yamani ZH. Effect of transition metal doping on photocatalytic activity of WO_3 for water splitting under laser illumination: role of 3d-orbitals. Catal Commun 2004;5(11):715–9.

[16] Sasikala R, Shirole AR, Sudarsan V, Jagannath, Sudakar C, Naik R, et al. Enhanced photocatalytic activity of indium and nitrogen co-doped TiO_2–Pd nanocomposites for hydrogen generation. Appl Catal A General 2010;377(1–2):47–54.

[17] Hou X, Jiang S, Li Y, Xiao J, Li Y. Ni-doped InN/GaZnON composite, catalyst for overall water splitting under visible light irradiation. Int J Hydrogen Energy 2015;40(45):15448–53.

[18] Wang H, Chen W, Zhang J, Huang C, Mao L. Nickel nanoparticles modified CdS–A potential photocatalyst for hydrogen production through water splitting under visible light irradiation. Int J Hydrogen Energy 2015;40(1):340–5.

[19] Hashimoto K, Kawai T, Sakata T. Hydrogen production with visible light by using dye sensitized TiO_2 powder. Nouv J Chim 1983;7:249–53.

Please cite this article in press as: Chouhan N, et al., Visible light harvesting Pt/CdS/Co-doped ZnO nanorods molecular device for hydrogen generation, International Journal of Hydrogen Energy (2015), http://dx.doi.org/10.1016/j.ijhydene.2015.11.019

[20] Tawkaew S, Fujishiro Y, Yin S, Sato T. Synthesis of cadmium sulfide pillared layered compounds and photocatalytic reduction of nitrate under visible light irradiation. Colloids Surf A 2001;179:139–44.
[21] Malinka EA, Kamalov GL, Vodzinskii SV, Melnik VI, Zhilina ZI. Hydrogen production from water by visible light using zinc porphyrin-sensitized platinized titanium dioxide. J Photochem Photobiol A 1995;90:153–8.
[22] Shimidzu T, Iyoda T, Koide Y. An advance visible light induced water reduction with dye sensitised semiconductor powder catalyst. J Am Chem Soc 1985;107:35–41.
[23] Kato H, Hori M, Konta R, Shimodaira Y, Kudo A. Construction of Z scheme type heterogeneous photocatalysis systems for water splitting into H_2 and O_2 under visible light irradiation. Chem Lett 2004;33(10):1348–9.
[24] Wang X, Liu G, Lu GQ, Cheng HM. Stable photocatalytic hydrogen evolution from water over ZnO–CdS core–shell nanorods. Int J Hydrogen Energy 2010;35:8199–205.
[25] Chu D, Zeng YP, Jiang DL. Hydrothermal synthesis and optical properties of Pb^{2+} doped ZnO nanorods. Mater Lett 2006;60:2783–5.
[26] Cheng BC, Xiao YH, Wu GS, Zhang LD. Controlled growth and properties of one-dimensional ZnO nanostructures with Ce as activator/dopant. Adv Funct Mater 2004;14(9):913–9.
[27] Zhou SM, Zhang XH, Meng XM, Wu SSK, Lee T. Enhancement of UV luminescence in sol-gel prepared ZnO thin films by incorporation of Mg. Phys Status Solidi A 2005;202(3):405–10.
[28] Xu CX, Sun XW, Dong ZL, Yu MB, Xiong YZ, Chen JS. Magnetic nanobelts of iron-doped zinc oxide. Appl Phys Lett 2005;86:173110. 3 pages.
[29] Reber JF, Meier K. Photochemical hydrogen production with platinized suspensions of cadmium sulfide and cadmium zinc sulfide modified by silver sulphide. J Phys Chem 1986;90(5):824–34.
[30] Larramona G, Chone C, Jacob A, Sakakura D, Delatouche B, Péré D, et al. Nanostructured photovoltaic cell of the type titanium dioxide, cadmium sulfide thin coating, and copper thiocyanate showing high quantum efficiency. Chem Mater 2006;18(6):1688–96.
[31] Gao HC, Zhu RX, Yang XY, Mao SZ, Zhao S, Yu JY, et al. Properties of polyethylene glycol (23) lauryl ether with cetyltrimethylammonium bromide in mixed aqueous solutions studied by self-diffusion coefficient NMR. Colloid Interface Sci 2004;273(2):626–31.
[32] Yin YD, Alivisatos AP. Colloidal nanocrystal synthesis and the organic–inorganic interface. Nature 2005;437:664–70.
[33] Faeibold E, Michels B, Waton G. Micellar growth study by micocalorimetry in CTAB solutions. J Phys Chem 1996;100:20063–7.
[34] Missel PJ, Mazer NA, Carey MC, Benedek GB. Influence of alkali-metal counterion identity on the sphere-to-rod transition in alkyl sulfate micelles. J Phys Chem 1989;93:8354–66.
[35] Rehage H, Hoffmann H. Rheological properties of viscoelastic surfactant systems. J Phys Chem 1988;92:4712–9.
[36] Porte G, Appell J, Poggi J. Experimental investigations on the flexibility of elongated cetylpyridinium bromide micelles. J Phys Chem 1980;84(23):3105–10.
[37] Appell J, Porte G, Khatory A, Kern A, Candau SJ. Static and dynamic properties of a network of wormlike surfactant micelles (Cetylpyridinium chlorate in sodium chlorate brine). J Phys II 1992;2(5):1045–52.
[38] Pileni M. Reverse micelles as microreactors. J Phys Chem 1993;97(27):6961–74.
[39] Kim WJ, Yang SM. Preparation of mesoporous materials from the flow-induced microstructure in aqueous surfactant solutions. Chem Mater 2000;12:3227–35.
[40] Karzel H, Potzal W, Kofferlein M, Schiessl W, Steiner M, Hiller U, et al. Lattice dynamics and hyperfine Interactions in ZnO and ZnSe at high external pressures. Phys Rev, B Condens Matter 1996;53:11425–39.
[41] Chouhan N, Lin CC, Hu S-F, Liu R-S. Earth-free GaZnON phosphor prepared by combustion for white light-emitting diodes. J Mater Chem C 2015;3:1473–9.
[42] (a)Qiu X, Miyauchi M, Yu H, Irie H, Hashimoto K. Visible-light-driven Cu(II)–$(Sr_{1-y}Na_y)(Ti_{1-x}Mo_x)O_3$ photocatalysts based on conduction band control and surface ion modification. J Am Chem Soc 2010;132:15259–67.
(b)Yu H, Irie H, Hashimoto K. Conduction band energy level control of titanium dioxide: toward an efficient visible-light-sensitive photocatalyst. J Am Chem Soc 2010;132:6898–9.
(c)Irie H, Kamiya K, Shibanuma T, Miura S, Tryk DA, Yokoyama T, et al. Visible light-sensitive Cu(II)-grafted TiO_2 photocatalysts: activities and x-ray absorption Fine structure analyses. J Chem Phys C 2009;113:10761–6.
[43] Yu WW, Qu L, Guo W, Peng X. Experimental determination of the extinction coefficient of CdTe, CdSe, and CdS nanocrystals. Chem Mater 2003;15:2854–60.
[44] Rehr JJ, Albers RC. Theoretical approaches to x-ray absorption fine structure. Rev Mod Phys 2000;72(3):621–54.
[45] Yamamoto T. Assignment of pre-edge peaks in k-edge x-ray absorption spectra of 3d transition metal compounds: electric dipole or quadurpole? X-Ray Spectrom 2008;37:572–84.
[46] Krishnamurthy S, McGuinness C, Dorneles LS, Venkatesan M, Coey JMD, Lunney JG, et al. Soft x-ray spectroscopic investigation of ferromagnetic co-doped ZnO. J Appl Phys 2006;99:08M111. 3-pages.
[47] Stern EA. Theory of EXAFS. In: Koningsberger DC, Prins R, editors. X-ray absorption: principles, applications, techniques of EXAFS, SEXAFS and XANES. New York: Wiley-Interscience; 1988. p. 618–708. Ch. 8.
[48] Neamtu J, Georgescu G, Malaeru T, Gheorghe NG, Costescu RM, Jitaru I, et al. Atomic structure and magnetic properties of cobalt doped ZnO thin films prepared by the sol-gel method. Dig J Nanomater Biostr 2010;5:873–85.
[49] Ankudinov AL, Ravel B, Rehr JJ, Conradson SD. Real-space multiple-scattering calculation and interpretation of x-ray-absorption near-edge structure. Phys. Rev B 1998;58:7565–76.
[50] Sathish M, Viswanathan B, Viswanath RP. Alternate synthetic strategy for the preparation of CdS nanoparticles and its exploitation for water splitting. Int J Hydrogen Energy 2006;31:891–8.
[51] Konta R, Ishii T, Kato H, Kudo A. Photocatalytic activities of Noble metal ion doped $SrTiO_3$ under visible light irradiation. J Phys Chem B 2004;108(26):8992–5.
[52] Poh WC, Loh KP, Zhang WD, Tripathy S, Ye JS, Sheu FS. Biosensing properties of diamond and carbon nanotubes. Langmuir 2004;20:5484–92.
[53] Lindbergh G, Simonsson D. Inhibition of cathode reactions in sodium hydroxide solution containing chromate. J Electrochem Soc 1991;36:1985–94.
[54] Reber JF, Meier K. Photochemical production of hydrogen with zinc sulfide suspensions. J Phys Chem 1984;88(24):5903–13.

International Journal of Advance Research in Science and Engineering
Vol. No.6, Issue No. 01 , January 2017
www.ijarse.com

IJARSE
ISSN (O) 2319 - 8354
ISSN (P) 2319 - 8346

SYNTHESIS OF ZnO NANOPARTICLES FOR ORGANIC POLLUTANT DEGRADATION

Rajesh Kumar Meena[1*], Niranjan Kumar Mandawat[2],
Neeta Gurbani[3], Neelu Chouhan[4*]

[1,2,3,4]*Department of Pure & Applied Chemistry, University of Kota, Kota, Rajasthan, (India)*

ABSTRACT

In this research work, we have synthesized an effective water filtration system based on the photocatalytic performance of semiconducting dense nanoparticles under natural sunlight. The present study, focus on the photocatalytic activity of nanostructures semiconductor like zinc oxide (ZnO) was prepared by sol-gel methods on the degradation of organic dye such as methylene blue that was investigated. Synthesized ZnO nanoparticles are characterized and study of morphology structure and stability of the synthesized ZnO nanoparticles were studied using scanning electron microscope (FESEM), UV-spectro photometer and Fourier Transform Infrared (FTIR) spectroscopy. The results depicted that the synthesized nanoparticles are moderately stable, roughly spherical with maximum particles in size range within 40-50 nm in diameter.

Key Words: Organic pollutant FTIR, XRD, FESEM etc.

I INTRODUCTION

Environmental contaminants similar to dyes, pesticides and heavy metals in water require remediation and probable removal to make the water it for human consumption. A lot of research is established to purify water from its contaminants, a most important portion of which are organic in nature. Further, the photocatalytic degradation of organic pollutants from water using semiconducting materials has attracted a lot of attention. Such semiconductors are increasingly used for oxidation or degradation of organic dyes and other contaminants particularly in industrial wastewater. The basic mechanism for this remediation is primarily based on the oxygen defects on the surface of the semiconducting materials which when activated by photon irradiation are used to destroy the organic contaminants. The various advantages that the process has are (a) the photocatalytic reaction is not specific to compounds and, therefore, is capable of destroying a spectrum of organic chemicals like hydrocarbon fuels, halogenated solvents, surfactants, pesticides and many hazardous organic chemicals,[1,2] (b) this process is very effective mostly owing to the process of its removal, oven achieving a complete degradation, (c) the process is very resistant to toxicity etc., (d) the process can be applied equally well to liquid (e.g. wastewater and contaminated groundwater) and gaseous streams (e.g. VOC emission), and finally (e) there is a potential to utilize solar energy as reported in this particular work.[3–5] Most photo degradation is still accomplished by exposure to UV radiation although UV sources consume considerable amount of energy.

In the past two decades, zinc oxide has paying much attention with respect to the degradation of different pollutants due to its high stability, photosensitivity and wide band gap. Most researchers have earlier used ZnO in a nano-powder form dispersed in industrial water for the photo-degradation of organic pollutants. Further, it has been reported that ZnO has a higher photocatalytic efficiency compared to TiO2 in the degradation of several organic contaminants in both acidic and basic media, which has attracted researchers to explore the properties of zinc oxide in many photocatalytic reactions.[6-8] Zinc oxide is consideration to be as a low cost alternative photocatalyst to TiO_2 for degradation of organics in aqueous solutions. The dispersion and surface area of zinc oxide, which depend on the synthesis method, are significant factors for determining its photocatalytic activity for pollutant degradation. Zinc oxide NPs can be synthesis by various type of methods, such as, alkali precipitation, hydrothermal synthesis, thermal decomposition, spray pyrolysis and microwave irradiation, organo-zinc hydrolysis, plasma heat-decomposing, etc. Composites of zinc oxide and silica nanoparticle could be created through coprecipitation route; in this case, the zinc oxide could be covered on the silica nanoparticle surface[9].Photocatalyst is besides called photochemical catalyst and the function is parallel to the chlorophyll in the photosynthesis. In a photocatalytic scheme, photo-induced molecular transformation or reaction takes place at the surface of catalyst. A basic photocatalytic reaction on the generation of electron–hole pair and its destination is as follows: when a photocatalyst is illuminated by the light stronger than its band gap energy, electron–hole pairs diffuse out to the surface of photocatalyst and participates in the chemical reaction with electron donor and acceptor. Those free electrons and holes transform the neighboring oxygen or water molecules into OH free radicals with super strong oxidization. It can oxygenolyse various kinds of organic compounds and some parts of minerals. It may also deoxidize harmful substances like formaldehyde, benzene and ammonia into CO_2 and water free of toxic, harm, and odor. Therefore, photocatalyst may kill viruses, germs, pollen, epiphytes and the like and may decompose formaldehyde, benzenes, ammonia, and other harmful gases, and it will not bring secondary environmental pollution [10]. The degradation of the pollutants catalyzed by ZnO has been studied broadly. ZnO is known of the important photocatalysts because of its unique advantages, high photocatalytic activity, such as its low price and nontoxicity etc.[11, 12]

II MATERIALS AND METHODS

2.1 Materials

Zinc nitrate and citric acid were purchased from Sigma- Aldrich and were all used without further purification and Double distilled water was used as the solvent during this process.

2.2 Synthesis of Zinc Oxide Nanoparticles

ZnO NPs were prepared by the sol-gel method. Firstly from Sigma- Aldrich of zinc nitrate and citric acid were selected as original materials without any purification. 0.5837 g citric acid and 0.826 g zinc nitrate were dissolved into DIW water. In which citric acid acted as both stabilizer and mineralizer. After stirring for 1h, the mixture solution aged in the next 14 h at near room temperature. Then the mixture solution was evaporated and concentrated until changing to wet-gel at 90℃ water-bath. Then the wet-gel was put into drying oven at 120℃

for 6h, and then the formed mixture was calcined at 500℃ for 3h, and the ZnO nanospheres material was achieved for further characterization.

2.3 Optical Properties

UV-Visible spectroscopy (UV-Vis) refers to absorption spectroscopy in the UV-Visible spectral region. That means it uses beam in the visible and adjacent (near-UV and near-infrared (NIR)) ranges. . In this time uv-vis absorption spectra was takened using a (LABINDIA Uv- Visible 3000_{+}) spectrophotometer where the cuvette path length was set to 1.0 cm. The particles were dissolved in DIW water, and solution was placed in a quarts cuvettes. The absorption in the visible range openly affects the perceived colour of the chemicals involved. In this region of the electromagnetic spectrum generate by the electronic transitions.

2.4. Powder X-Ray Diffraction

XRD patterns of the powdered samples were obtained on a Phillips X'Pert materials research diffractometer using secondary monochromated Cu Kα radiation (λ = 1.54060 A°) at 40 Kv/50mA. Samples were supported on a glass slide. Measurements were taken using a glancing angle of incidence detector at an angle of 2 for 2θ values over 10–70 in steps of 0.05 with a scan speed of 0.012.

2.5. FESEM analysis

The FESEM image was taken with very high resolution and MATLAB analysis gives the pixel depth of the image equal to 24bits and the image format as JPEG. The FESEM Images have been taken from MNIT Jaipur, Rajasthan, India.

2.6. Fourier Transform Infrared (FTIR) Spectroscopy

FTIR analysis range 4000 to 400 cm_{-1} using Bruker -Tensor Spectrum in the diffuse reflectance mode at a resolution of $4cm^{-1}$ in KBr pellets. The powder sample was placed on a sample holder and the spectrum was recorded.

III RESULTS AND DISCUSSION

3.1 UV-Visible Analysis

UV-Visible absorption spectroscopy is widely used technique to examine the optical properties of nano sized particles. The prepared zinc oxide white crystalline powder was not soluble in water and almost in all organic solvents. ZnO nano particles UV-Visible spectra recorded by dispersed in methanol solution and sonicated for 5 to 10 min. Fig. 4 shows the absorption spectroscopy of the ZnO nanoparticles in the UV-spectral region. ZnO exhibits a sharp band at 354 nm, which corresponds to the formation of ZnO nanoparticles.

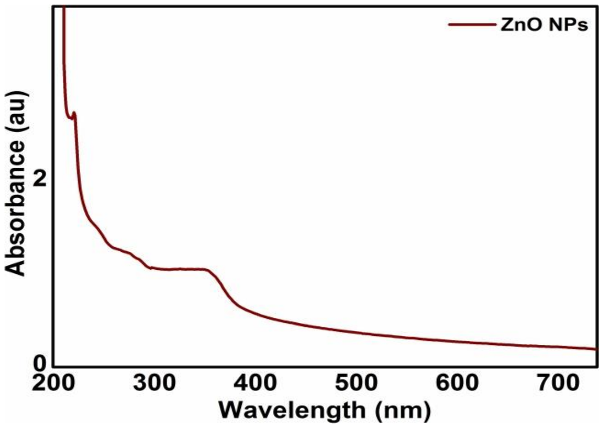

Fig.1. UV-Vis. spectra of ZnO NPs synthesized by sol-gel method

3.2 XRD Analysis

The crystal structures of the synthesized samples were determined by powder X-ray diffraction (XRD) using a copper Kα radiation source at 40 kV and 200 mA in steps of 0.02. Data were recorded ranging from 10° to 70°. Fig. 2 showed the XRD patterns of as-synthesized samples obtained by sol-gel method whose reflection peaks can be readily indexed with the wurtzite ZnO (JCPDS No. 79-2205). Prepared ZnO nanospheres were obtained by the sol-gel method, the crystal structure of ZnO was shown in Fig. 3, which belonged to the wurtzite structure. It can be seen that lattice parameters were a=0.3249 nm and c=0.5206 nm.

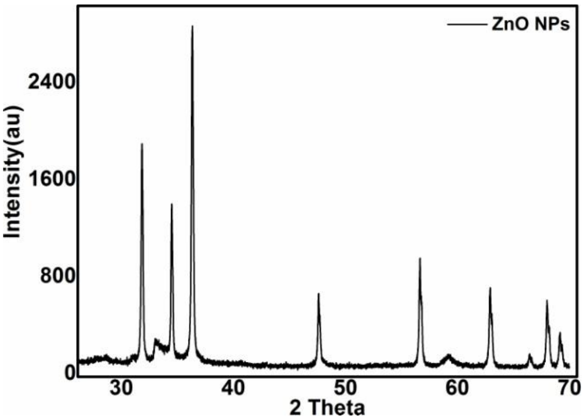

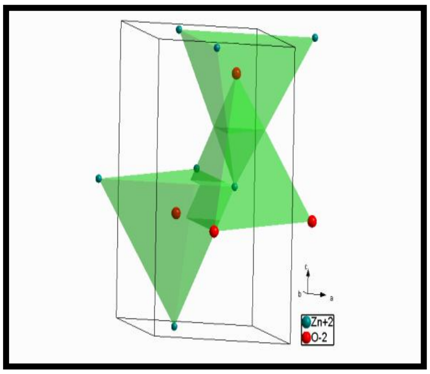

Fig.2. XRD spectra of ZnO synthesized by: sol-gel method **Fig.3. Crystal structure of ZnO**

3.3 Morphology Analysis:

SEM images of the products were shown in Fig. 4. ZnO NPs was prepared by sol-gel method calcined at 500℃ for 3 hours and pH was 8. SEM image showed relatively more uniform ZnO NPs prepared by sol-gel method look like nanospheres, with diameter range 10-50nm.

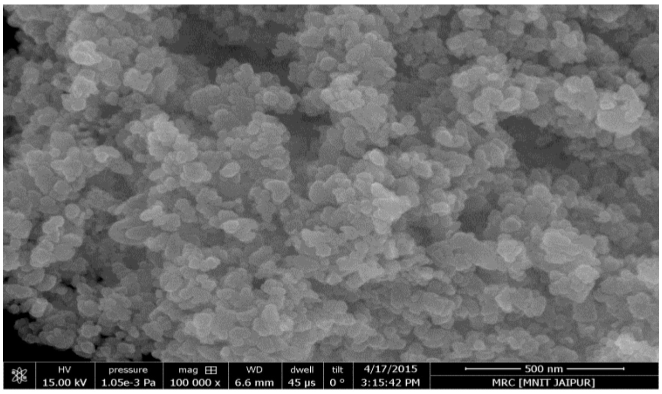

Fig.4. SEM image of ZnO NPs produced by the Sol-gel method

3.4 FTIR Analysis

FT-IR spectrum of ZnO nanoparticles (Fig. 5) showed significant absorption peaks at 573 and 1577, 3372cm^{-1}. The absorption band at 573 cm^{-1} due to Zn-O stretching vibration mode. The weak band near 1577 cm^{-1} is assigned to H-O-H bending vibration mode were presented due to the adsorption of moisture, when FTIR sample disks were ready in an open air atmosphere. These explanations provided the evidence for the presence of hydration in the structure and intense broad band near 3372 cm^{-1} represents the hydrogen bonded O-H stretching vibration mode.

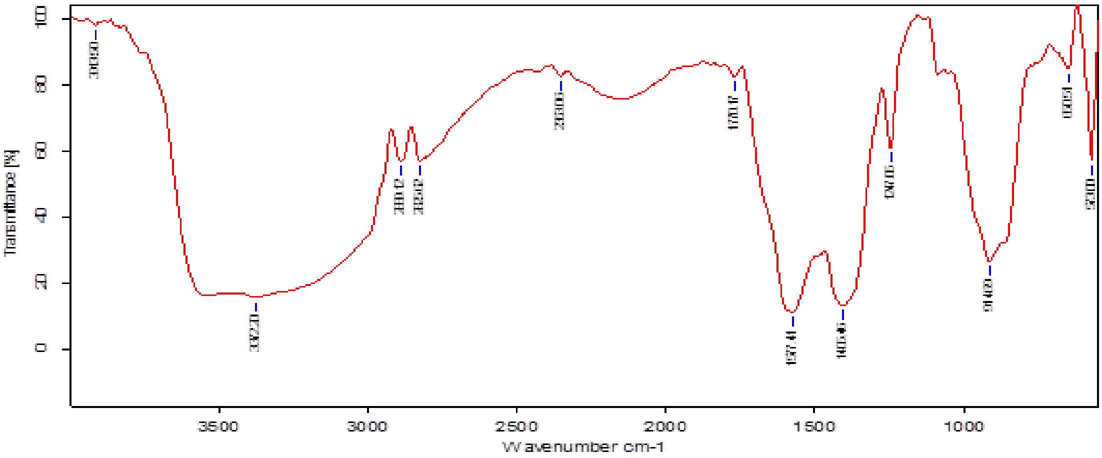

Fig.5 FTIR spectra of synthesized ZnO NPs

3.6 Photocatalytic activity of ZnO NPs

Photocatalytic activity of ZnONPs was investigated by measuring the photocatalytic degradation of methylene blue in water under the illumination of UV light. The ZnO nanoparticles of 50 nm in common particle size were chosen for the evaluation of photocatalytic activity. As shown in Fig. 6, it was found that the ZnO nanoparticles were effective on the degradation of the methylene blue. Higher photocatalytic activity of the ZnO nanoparticles is considered due to the higher surface area of the ZnO nanoparticles. At higher surface area, larger contact area between photocatalyst and target material can be obtained. It also meant that higher degree of UV light absorption could occur at the smaller particle size in the test solution.

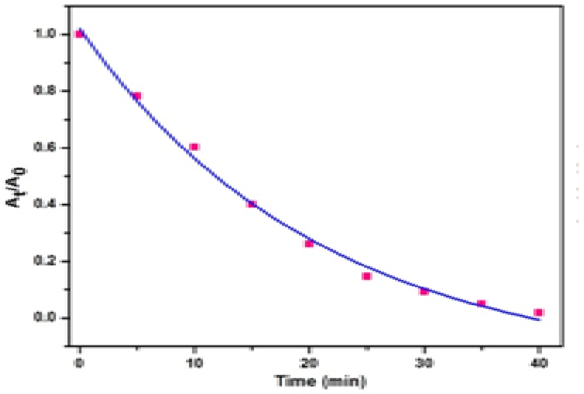

Fig.6. Effect of catalyst loading on the photodegradation of methylene blue using ZnO nanoparticles.

lV. CONCLUSION

In this present study, ZnO NPs have been successfully synthesized using Zinc nitrate and citric acid solution as precursors via sol-gel approach. By carefully controlling the process window, various morphologies of ZnO particles such as disk like and spherical NPs could be produced. The crystallite size calculated from the XRD is 50 nm. FT-IR results confirm that the presence of Zn-O at $573 cm^{-1}$ as well as UV-visible Spectroscopy the absorption spectrum was 374 nm absorbed. The photo degradation of methylene blue using ZnO spherical nanoparticles process was investigated. In which catalysts may further enhance the photocatalytic activity due to its high surface to volume ration which will facilitate the better adsorption of dyes.

V. ACKNOWLEDGMENT

The authors are sincerely thankful to the Department of Science and Technology and their sub wing Science and Engineering Research Board of the, India (SB/S1/PC- 31/2012) for their financial support.NCL, Pune and IIT Rorkee, India, are also thanked by the authors for providing XRD and FESEM facilities, respectively.

REFERENCES

[1] R. Venkatadri and R. W. Peters, Chemical oxidation technologies: ultraviolet light/hydrogen peroxide, Fenton's reagent, and titanium dioxide-assisted photocatalysis, Hazard. *Waste Hazard. Mater.*, 10(2), 1993, 107–149.

[2] M. R. Hoffmann, S. T. Martin, W. Choi and D. W. Bahnemann, Environmental applications of semiconductor photocatalysis, *Chem. Rev.*, 95(1), 1995, 69– 96.

[3] A. L. Pruden and D. F. Ollis, Photoassisted heterogeneous catalysis: the degradation of trichloroethylene in water, *J. Catal.*, 82(2), 1983, 404–417.

[4] C. Kormann, D. W. Bahnemann and M. R. Hoffmann, Photolysis of chloroform and other organic molecules in aqueous titanium dioxide suspensions, *Environ. Sci. Technol.*, 25(3), 1991, 494–500.

[5] J. C. Crittenden, J. Liu, D. W. Hand and D. L. Perram, Photocatalytic oxidation of chlorinated hydrocarbons in water, *Water Research,* 31(3), 1997, 429–438.

[6] M. Muruganandham and J. J. Wu, Synthesis, characterization and catalytic activity of easily recyclable zinc oxide nanobundles, *Appl. Catal., B,* 80(1), 2008, 32–41.

[7] J. C. Lee, S. Park, H.-J. Park, J.-H. Lee, H.-S. Kim and Y.-J. Chung, Photocatalytic degradation of TOC from aqueous phenol solution using solution combusted ZnO nanopowders, *J. Electroceram.*, 22(1–3), 2009, 110–113.

[8] A. A. Khassin, T. M. Yurieva, V. V. Kaichev, V. I. Bukhtiyarov, A. A. Budneva, E. A. Paukshtis and V. N. Parmon, Metal– support interactions in cobalt-aluminum co-precipitated catalysts: XPS and CO adsorption studies, *J. Mol. Catal. A: Chem.*, 175(1), 2001, 189–204.

[9] Wenzhong Sh., Zhijie L ., Hui W., Yihong L., Qingjie G., Yuanli Z., Photocatalytic degradation for methylene blue using zinc oxide prepared by codeposition and sol–gel methods. *Journal of Hazardous Materials.* 152: 2008, 172–175.

[10] Comparelli R., Fanizza E., Curri M L., Cozzi P D., Mascolo G., Agostiano A., Photodegradation of methylene blue using Ta-doped ZnO nanoparticle. *Appl. Catal. B: Environ*. 60: 2005, 1–11.

[11] Akyol A., Yatmaz H C., Bayramoglu M., Photocatalytic degradation of reactive brilliant blue X-BR in aqueous solution using quantum-sized ZnO. *Appl. Catal. B: Environ*. 54: 2004, 19–24.

[12] Liu H Q., Yang J X., Liang J H., Huang Y X., Tangz C Y., Photo-degradation of methylene blue using Ta-doped ZnO nanoparticle. *J. Am. Chem. Soc.* 91: 2008, 1287–1291.

Nanocomposite Ag@AgCl/ZnO for efficient hydrogen generation through water splitting

Niranjan Kumar Mandawat[1] · Hari Shanker Sharma[2] · Neelu Chouhan[1]

© Springer Nature Switzerland AG 2019

Abstract

We had successfully prepared the microwave assisted lotus shaped Ag@AgCl/ZnO nanocomposite (NC) of size 57.72 nm, in aqueous media at 90 °C for 7 min heating. The conventional single pot refluxing method was also used to prepare NCs with spherical shaped nanoparticles of size 59.12 nm at 90 °C heating for 3 h. X-ray diffraction data of the Ag@AgCl/ZnO NCs synthesized by the both methods, confirmed that the nanocomposite crystallized in three phases i.e. face-centered cubic (AgCl), cubic (nanosilver) and wurtzite hexagonal phase (ZnO). Energy dispersive X-rays corresponding to the electron microscopy analysis with their elemental mapping, envisioned the surface morphology and elemental composition i.e., 19% ZnO, 13.79% AgCl, 8.08% Zn and 26.19% Ag in the NC. The Ag@AgCl/ZnO NCs exhibited the visible light harvesting ability with band gap i.e. 3.02 and 2.96 eV with SURS selfsensitization of AgCl. Conventionally made sample and microwave assisted sample emits green and yellow-photoluminescence emissions, respectively. FTIR spectra at different stages of the formation of the nanocomposites, visualized the gradual changes in bonding positions of NCs. We utilized this molecular system as an efficient visible-light harvesting optical devices for water splitting. Conventionally and microwave assisted Ag@AgCl/ZnO samples, librated 6082.9 and 6782.32 μmol H_2 h^{-1} g^{-1}, optimum hydrogen in 8 h, respectively, through photocatalytic water splitting under AM 1.5G irradiation.

Graphical abstract

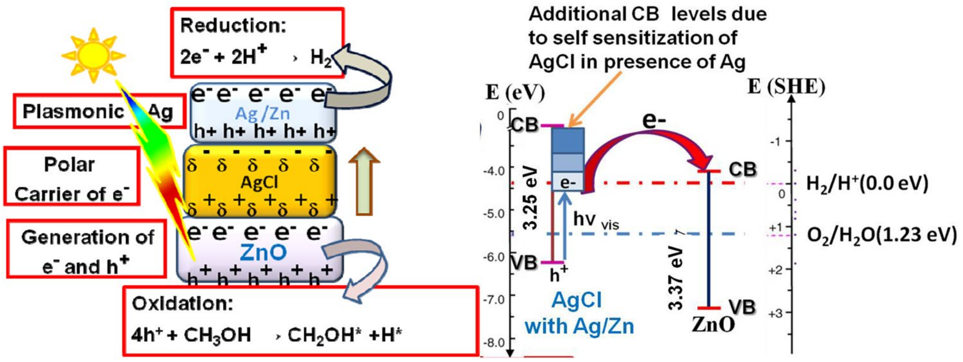

Electronic supplementary material The online version of this article (https://doi.org/10.1007/s42452-019-0578-1) contains supplementary material, which is available to authorized users.

✉ Neelu Chouhan, niloochauhan@hotmail.com | [1]Department of Pure and Applied Chemistry, University of Kota, MBS Road Near Kabir Circle, Kota, Rajasthan 324005, India. [2]Department of Chemistry, Government College, Kota, Rajasthan 324005, India.

Received: 21 October 2018 / Accepted: 8 May 2019

Published online: 16 May 2019

Keywords Nanocomposite · Ag@AgCl/ZnO · One-pot synthesis · Microwave-assisted synthesis · Plasmonic silver nanoparticles · Water splitting · Hydrogen generation

1 Introduction

World had eventually witnessed the ecosystem degradation and political hostility on energy lines, which is a matter of prime global concern. Therefore, we all are looking forward to the clean energy sources that can be replaced with the present conventional energy sources (as a fuel or energy carrier) and save environment. Hydrogen rated as the best option on its fuel merits i.e. high energy density (142 kJ/kg), high heating value (52,000 Btu/lb), high auto ignition temperature (585 °C), high fuel efficiency (75%) and widest range of flammability (4–75%), etc. In contrast to the current hydrogen generation practices (steam reforming of methane), the use of solar energy and carbon-less fuel i.e. water along with a suitable photocatalyst, is an eco-benign way of hydrogen production. A wide variety of photocatalytic materials (oxides, sulfides, nitrides, nanocomposites, etc.) are tested for hydrogen generation via water spitting. Unfortunately, most of them failed on the criteria of stability (in water and light), cost and efficiency (> 10%), simultaneously. Out of these classes nanocomposite is the least studied class. Therefore, we had choosen to work on nanocomposites. Few of the prominently studied nanocomposite systems are: modified graphenes [1–5], CdS/Au/g-C_3N_4 [6], CuS/TiO_2 [7], NiO_x (Ni/NiO)@ calcium tantalite [8], Ag/AgCl@ZnO [9–13], etc. Recently, silver halides based plasmonic nanoparticles (NPs) have been attracted the attention as a superb class of nanocomposites (NCs) that used for visible-light-harvesting device [9–13]. Although, due to instability under sunlight [14], silver halides AgX were seldom used as photocatalysts. However, Kakuta et al. [15] studied the Ag^0 supported AgBr dispersed on a silica that used for continuous H_2 production (1.00 mmol h^{-1} g^{-1} after 2 h) in 20% aqueous CH_3OH (as hole scavenger). They had observed that Ag NPs deposited on AgBr, supported by silica are not destroyed under successive UV/Vis illumination till 200 h, thus assembly Ag/AgBr on silica, was able to act as a stable photocatalyst under visible light, and inspired to synthesized the first visible-light plasmonic photocatalyst Ag@AgCl. Moreover, Schürch et al. [16] proved that the AgCl deposited on a conducting support (Au coated FTO) was used to photocatalyse the water for O_2 production (160 nmol h^{-1}) in the presence of silver ions (as electron scavenger), under UV/Vis light exposure. Similarly, 3D-hierarchical superstructures, concave cubes, and cubes of AgCl, were used as photocatalyst for O_2 generation via water splitting with their activity are 254 mmol g^{-1} for hierarchical superstructures, 187 mmol g^{-1} of concave cubic AgCl and 136 mmol g^{-1} of cubic AgCl in 5 h [17]. The photoactivity of AgCl in presence of Ag^+ ions, extended from the UV to the visible light region under the process known as self-sensitization, [18, 19] which is due to the formation of silver species during the photoreaction, as follows (Eqs. 1–7):

$$\left[nAg^+, mAgCl\right] + \frac{r}{2}H_2O \longrightarrow \text{light}\left[(n-r)Ag^+, mAgCl, rAg^0\right] + rH^+ + \frac{r}{4}O_2 \tag{1}$$

$$\text{light}\left[(n-r)Ag^+, mAgCl, rAg^0\right] \longrightarrow \text{light}\left[nAg^+, mAgCl\right] + re^- \tag{2}$$

$$\left[mAgCl\right]\{Ag^+\}_s \longrightarrow \text{light}\left[(m-1)AgCl\right]\{Ag^+Ag^0\}_{s,i} + \left[Cl^{\cdot}_s\right] \tag{3}$$

$$2Cl^{\cdot}_s \rightarrow Cl_2 \tag{4}$$

$$Cl_2 + H_2O \rightarrow HOCl + H^+ + Cl^- \tag{5}$$

$$2HOCl + Ag^+(\text{catalyst}) \rightarrow O_2 + 2H^+ + 2Cl^- \tag{6}$$

$$(m-1)AgCl + Ag^+ + Cl^- \rightarrow \left[mAgCl\right] \tag{7}$$

Equations (1) to (7), had been experimentally and theoretically analyzed [18, 19]. The comparison of experimental and calculated values for the ionization energy for different sized Ag clusters shows that Ag levels are located below the conduction band edge of AgCl. Additional AgCl surface states (SURS), as well as metal induced gap states (MIGS) from Ag/AgCl cluster composites are also present in the band gap region of silver chloride that induced the self-sensitization in AgCl [20–23]. Therefore, Ag/AgX on variety of support can be used as good photocatalytic system (Table 1).

Some of the notable nanocomposite plasmonic materials are Ag@AgBr [24], Au/TiO_2 [25], gold/layered double hydroxides [26], Ag/AgCl/ZnO [27], Ag embedded TiO_2 [28], Au/ZnO NRs [29], graphene oxide (GO) enwrapped Ag/AgX (X = Cl, Br) [30], Ag/AgBr@TiO_2 [31], Ag/AgCl@$H_2WO_4 \cdot 3H_2O$ [32], AgBr/WO_3 [33], and Ag/ZnO nanorods (NRs) [34], which can act as a good plasmonic nanocomposites, as shown in Table 1. Most of the above molecular devices had been used to degraded dye/organic pollutants (methylene blue, methyl orange, VOCs, ethanol/methanol) and only few of the composite plasmonics, were used to produce hydrogen such as gold/layered double hydroxides (127 μmol h^{-1} for Au/ZnAlCeLDH and 94 μmol h^{-1} of

Table 1 Some state-of-art plasmonic catalyst supported systems for hydrogen generation

Sl. no.	Plasmonic material supported photo-catalyst	Light source	Conditions for H_2 generation	Amount of H_2 generation μ mol H_2 h^{-1} g^{-1}	Amount of O_2 generation μ mol O_2 h^{-1} g^{-1}	Year	Research group [Reference No.]
1	Ag^0 supported-AgBr dispersed on silica-dioxide support	100 W high-pressure Hg lamp-with IR filter	20% CH_3OH (hole scavenger) in H_2O	1000 after 2 h	–	1999	Kakuta et al. [15]
2	Ag@AgCl deposited on Au coated FTO	UV–Vis light exposure	In presence of Ag^+ ions	–	0.160 mol h^{-1}	2002	SchKrch et al. [16]
3.	3D hierarchical super-structures, concave cubes, and cubes of AgCl	300 W Xe arc lamp	In presence of Ag^+ ions	–	254,000, 187,000 and 136,000 in 5 h	2012	Lou et al. [17]
4.	Au/ZnAlCeLDH and Au/ZnAlLDH	Solar light exposure	20% methanol	127 and 94	–	2013	Carja et al. [26]
5.	Ag/ZnONRs and ZnONRs	Xe light source	20% methanol	8.7 and 4.3	–	2013	Chen et al. [34]
6	Ag/AgCl/ZnO	Xe light source	20% methanol	6082.9 (one pot) and 6782.32 (microwave)	–	2019	Present work

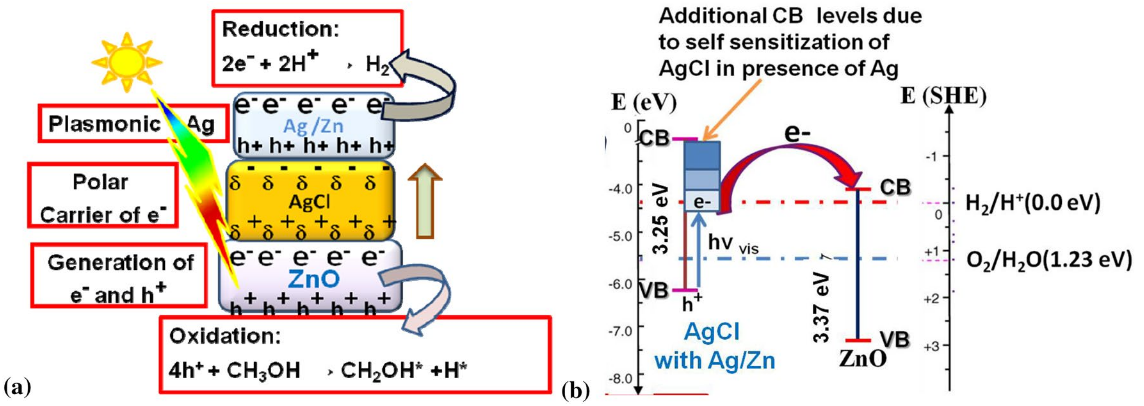

Scheme 1 **a** Schematic representation of the overall water splitting phenomenon using Ag NPs embedded AgCl-ZnO NCs and **b** comparative energy level diagram of nanocomposite device Ag@AgCl/ZnO with their respective band positions [20–22]

H_2 for Au/ZnAlLDH) [26], Ag/ZnONRs (8.7 μmol h^{-1} of H_2 by Ag/ZnO and 4.3 μmol h^{-1} of H_2 by ZnO) [34]. In this direction, several advance synthesis methods such as: ultrasonic assisted deposition–precipitation method [35], ployol process [36, 37], reconstruction process [38], single pot refluxing [27], ionic liquids-assisted hydrothermal method [39], etc., had been used to prepare NCs. Microwave (MW) assisted synthesis is one of the eco-friendly method for molecular assemblies fabrication, where MW-heating provided faster and uniform heating profile than the conventional thermal heating. Therefore, MW assisted-synthesis leads not only homogenous nucleation but also accelerate the reaction rate, improve yield, shorten the reaction time, produce small sized particle of high purity with narrow particle size distribution, and improve physicochemical properties [40]. Some notable materials such as SnO_2 [41], ZnO [42], Ag [43], Pt [44], CuS [45], etc., were fabricated using MW assisted synthesis. But the record was not found for MW assisted synthesis of the Ag@AgCl/ZnO NC. Therefore, we employed the MW assisted synthesis first time for NCs preparation that consist of plasmonic silver NPs embedded in ZnO and AgCl matrix, which was used for water splitting to generate hydrogen. Conventional one pot refluxing method was also used to synthesize the Ag@AgCl/ZnO NC [27] in aqueous medium. Under the sunlight exposure, ZnO and AgCl generates photo-electrons and -holes and AgCl (with expanded CB energy levels) plays an important role of polar carrier for electron-transport from plasmonic material (Ag NPs) to ZnO and whole assembly become capable to harvest visible light, as it schematically illustrated by the Scheme 1a and Energy diagram 1b. Therefore, we can say the nanocomposite Ag@ZnO/AgCl, has the better compatibility for visible light harvesting and supression in the recombination rate of photo carriers. That will be ultimately enhanced the hydrogen generation efficiency of the device. In addition to above, to understand the nature of nanocomposite the advanced technical approaches were used to address the characterization of the device.

2 Experimental design, materials, and methods

2.1 Materials

All chemicals were used as-purchased (of make Sigma Aldrich) in synthesis and water splitting application without further purification. These chemicals are: hexahydrated-zinc nitrate, sodium chloride, sodium hydroxide, and silver nitrate, terepthalic acid, etc.

2.2 Synthesis

2.2.1 Conventional method

Ag nanoparticles-supported ZnO/AgCl NCs were fabricated by using one-pot refluxing method as described somewhere else [27]. In which, 5.22 g hexahydrated zinc nitrate and 2.11 g silver nitrate were mixed in 50 mL of deionised water (DIW) and stirred at room temperature and followed by the addition of aqueous NaOH (5 M) to adjust the pH of the solution 10. Here, NaOH with pH 10 is act as a reducing agent because the hydroxyl ions of NaOH are capable of donating electrons to $AgNO_3$ and $ZnNO_3.6H_2O$, results in their reduction in Ag and Zn. During the above reaction, NaCl act as a dielectric material in production of AgCl and ZnO. Therefore, above mixture was treated with 1.450 g NaCl in 20 mL of water. Then, the suspension was refluxed at 90 °C for 3 h. Resulting product was centrifuged and washed several times with DIW and ethanol and dried in an oven at 60 °C for 24 h.

2.2.2 Microwave method

Microwave synthesizer (CEM, model-Discover) was opted to prepare the AgNPs embedded ZnO/AgCl NCs with 0.383 mol fraction of silver chloride with respect to ZnO. A sundry of 5.220 g $Zn(NO_3)_2.4H_2O$ and 2.110 g $AgNO_3$, were made in 50 mL of deionised water (DIW) and stirred at room temperature. Thereafter the aqueous NaOH (5 M) was added in the solution to adjust the pH of the solution 10. Above solution was treated with 1.450 g NaCl in 20 mL of water. Then, the suspension was heated in microwave at 90 °C for 7 min. Resulted product was centrifuged and washed several times with DIW and ethanol and dried in an oven at 60 °C for 24 h.

2.3 Characterization

Several techniques were used to characterize the nanocomposite Ag@AgCl/ZnO using technical tools such as: UV–Vis absorption spectroscopy, FE-SEM, energy dispersive X-rays (EDX), spectroflurometery, X-ray diffraction (XRD), and FT-IR, etc. The crystalline nature of nanocomposite was characterized by XRD, using diffractometer (PANalytical; Model: Xpert-Pro) of MNIT, Jaipur, well equipped with Ni-K_β filter for Cu$K_{\alpha 1}$ radiation at 40 kV voltage and 30 mA current. Morphology of the sample was evaluated by using FESEM (JEOL; Model: JSM-6700F). The UV–Vis spectra were recorded with multimode microplate reader (Lab India; Model: 3000^+ with Diffuse Reflectance Spectroscopy) in the wavelength range between 200 and 800 nm. An FT-IR spectrum was recorded using spectrophotometer (Bruker; Model: Tensor 27) available in our institute. Furthermore, photoluminescence emission (PLE) spectrum of the Ag@AgCl/ZnO nanocomposite material was recorded by using spectrofluorimeter (Simandzu; Model: RF-5301) of our department.

2.4 Analysis of hydroxyl radical (·OH) in photocatalytic solution

The hydroxyl radicals (*OH) formed during the photo-illumination of the samples/water interface, can be traced by the use of basic terephthalic acid (as a probe molecule) solution in the photoluminescence (PL) method using double beam spectrofluorimeter [23]. In this method, the hydroxylation of the terephthalic acid was taken place when it reacted with *OH radical that resulted in the product 2-hydroxyterephtalic acid (HTA) formation at the water/catalyst interface, which was exhibited by the PLE signal around 428 nm at the excitation wavelength of 315 nm. The intensity of the PLE peak of 2-hydroxyterephtalic acid is directly proportional to the amount of *OH radicals produced in the water. Under the experimental procedure 0.3 g of the sample was added to 110 mL of 5×10^{-4} M terephthalic acid (pH = 10) that was prepared in aqueous 2×10^{-3} M NaOH [23]. Afterwards the solution was exposed to the 300 W Xe light source, by keeping the other experimental conditions same as used in measurement of photocatalytic water splitting activity. Spectrofluorimeter

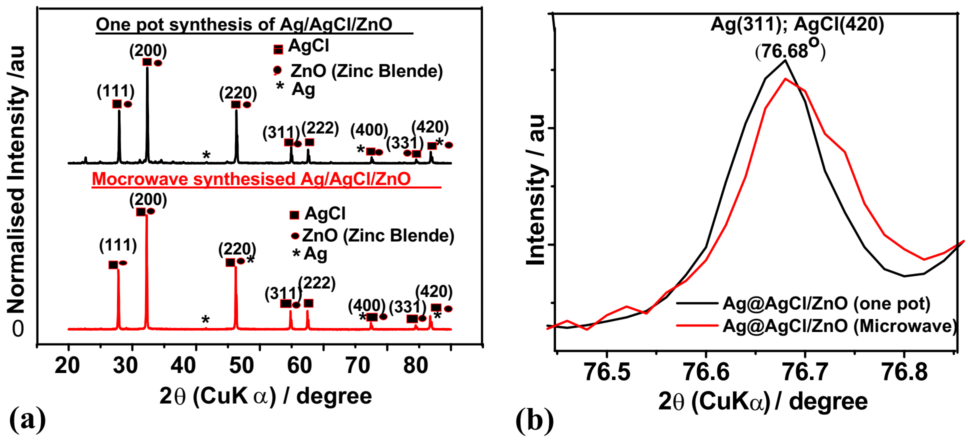

Fig. 1 Diffraction patterns of the nanocomposite Ag@AgCl/ZnO, synthesized by one pot and microwave method. **a** The XRD peaks are exactly matched to those of the bulk FCC chlorargyrite phase (JCPDS Card No. 31-1238) of the AgCl, cubic phase of Ag (JCPDS Card No. 04-0783 of pure silver and FCC zinc blende crystalline phase (JCPDS Card No. 80-0020; ZnS) of ZnO. **b** Enlarge peaks of AgCl (420) and Ag (311) was observed at 76.68°

(Simandzu; Model: RF-5301) of our institute was used to measure the PLE spectrum of the above mentioned solution at room temperature at different time interval.

2.5 Water splitting analysis

Photocatalytic H_2 evolution power testing of the as synthesised nanocomposite was carried out in a 20% methanolic (hole-scavenger) solution of Ag@AgCl/ZnO samples at RT. Where, 0.30 g of the Ag@AgCl/ZnO in an aqueous methanolic solution (160 mL H_2O and 40 mL CH_3OH) was suspended in a double walled reaction cell of Pyrex glass, equipped with a quartz window. Reaction cell was connected to a closed gas circulation (Argon) of 1 atmosphere pressure to evacuate the solution several times up to the complete removal of the air from the reaction vessel and then system was irradiated by a light source (300 W Xe lamp) for the photocatalytic observations. The amount of H_2 evolved during the photocatalytic experiment, was monitored using gas chromatography that was equipped with a thermal conductivity detector (TCD, GC-8A, China gas chromatograph; and Ar as carrier gas).

3 Result

The phase purity of the Ag@AgCl/ZnO NC was tested using XRD profile, depicted in Fig. 1a, b. Diffraction patterns of the studied samples are found at 27.942° (111), 32.34° (200), 46.34° (220), 54.94° (311), 57.58° (222), 67.54° (400), 74.76° (331) and 76.82° (420) attributed to the highly crystalline two prominent phases that corresponds to the face-centered cubic (chlorargyrite) phase (reference JCPDS Card No. 31-1238) of the AgCl with their cell parameters [46]: a = b = c = 5.545 Å α = β = γ = 90° at z = 4, and space group Fm3m (225) and the FCC (zinc blende) crystalline phase (reference JCPDS Card No. 80-0020; ZnS) of ZnO [47, 48] with their cell parameters: a = b = c = 5.345 Å, α = β = γ = 90° at z = 4 and space group F4-3m (216). The careful examination of diffraction peaks exhibits tiny peaks at 38.56° (111), 46.34° (200), 67.54° (220), 76.82° (311) position that belongs to the standard JCPDS Card No. 04-0783 of pure silver (cell constants a = b = c = 4.0857 Å, α = β = γ = 90° at z = 4 and space group Fm3m (225) [46] that also confirmed the presence of the small particles of silver and their size was calculated by using the Scherrer formula. Figure 1b represented the blue shift of enlarged peak of AgCl(420) and Ag(311) at 76.68° for the nanocomposite Ag@AgCl/ZnO synthesized by one pot and microwave methods from their standard positions i.e. 77.50° and 77.66°, respectively.

The elemental composition of the nanocomposite was confirmed by respective EDX profile and FESEM elemental mapping, which is represented by Fig. 2a, d, e. No characteristic peaks for the elements other than Zn (27.08%; at $K_\alpha = 8.63$ keV; $L_\alpha = 1.012$ keV) Ag (39.98%; at $L_\alpha = 2.984$ keV), Cl (13.79%; at $K_\alpha = 2.621$ keV) and O (19% at $K_\alpha = 0.525$ keV) were found in the EDX profile of the Ag@AgCl/ZnO, as illustrated by the Fig. 2a. The actual concentration of oxygen can't be determined precisely due to the presence of the oxygen in air. As per XRD analysis nanocomposite crsytalised in three phases i.e. ZnO, AgCl and Ag/Zn. Therefore, EDX suggested that nanocomposite consist of 19.15% ZnO, 13.79% AgCl, Ag (26.19%) and Zn (7.39%). Surface morphology and particle size of the nanocomposite was investigated by the FESEM images (Fig. 2b, c), as nanolotus shaped particle of size 45.08–60.77 nm (aggregation of particles) for the microwave synthesized sample and 50.87–79.19 nm sized spherical particles for the one plot synthesized sample of the nanocomposite Ag@AgCl/ZnO.

Figure 3a demonstrated the UV–Vis diffuse reflectance spectra [Kubelka–Munk function F(R) *Vs* wavelength] with peaks at 300.4 nm, 352.0 nm and a very weak and broad peak found between 407.9 and 700 nm. Splitting in first absorption peak is found due to the presence

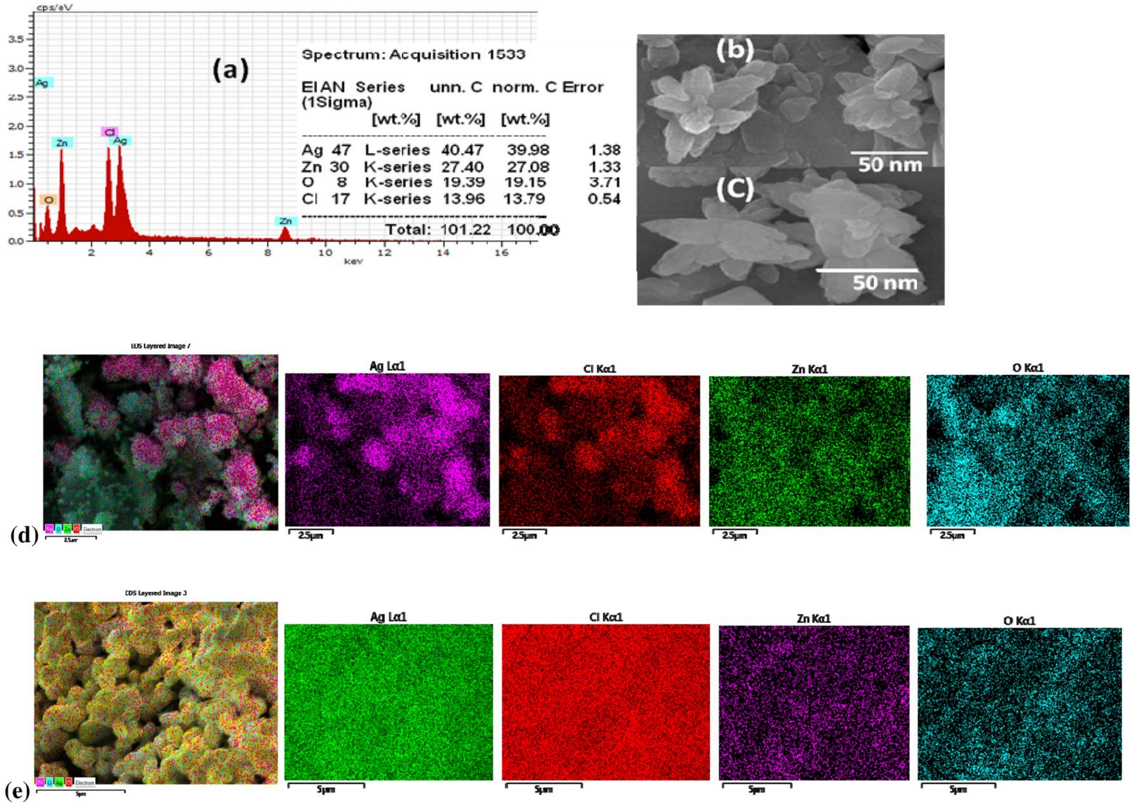

Spectrum: Acquisition 1533

El	AN	Series	unn. C [wt.%]	norm. C [wt.%]	Error (1Sigma) [wt.%]
Ag	47	L-series	40.47	39.98	1.38
Zn	30	K-series	27.40	27.08	1.33
O	8	K-series	19.39	19.15	3.71
Cl	17	K-series	13.96	13.79	0.54
		Total:	101.22	100.00	

Fig. 2 Nanocomposite Ag@AgCl/ZnO with their corresponding **a** FESEM supported EDX showing elemental presence of Ag, Zn, O and Cl. **b** and **c** are FESEM images of nanocomposite, prepared by microwave route. FESEM elemental mapping of Ag, Cl, Zn and O elements in Ag@AgCl/ZnO for corresponding, **d** one pot (conventional) and **e** microwave-assist synthesized nanocomposite

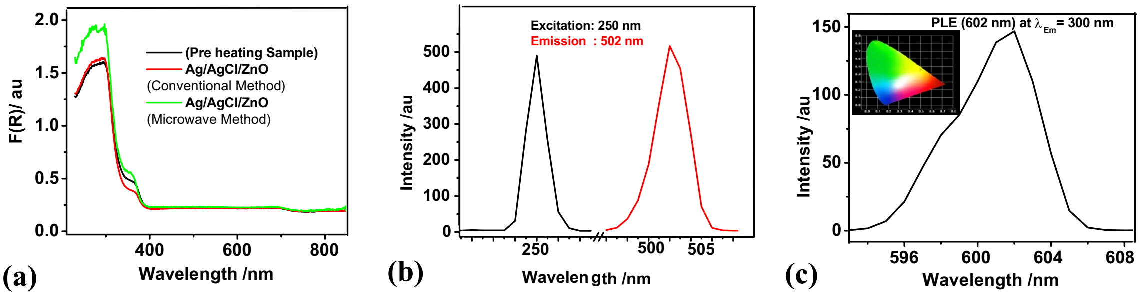

Fig. 3 **a** UV–Vis diffuse reflectance spectra of the pre heated sample along with conventional- and microwave-prepared Ag@AgCl/ZnO nanocomposites with first excitonic peak around 300.4 nm. **b** PLE spectra with maxima at $\lambda_{\max}^{em}$ = 502 nm under the excitation wavelength $\lambda_{\max}^{ex}$ = 250 nm of the sample prepared by one pot reflux method and **c** PLE spectra with maxima at $\lambda_{\max}^{em}$ = 602 nm under the excitation wavelength $\lambda_{\max}^{ex}$ = 300 nm, for the sample prepare using microwave method (CIE plot represented in inset that exhibit the yellow emission)

of the two phases i.e. AgCl and ZnO. These three peaks in UV–Vis absorption spectrum was used to investigate band gap of the nanocomposite Ag@AgCl/ZnO at 300.40 nm ($E_g^m = 3.56$ eV and $E_g^c = 3.62$ eV), at 352.00 nm ($E_g^c = 3.02$ eV and $E_g^m = 2.96$ eV due to additional SURS of AgCl) and at 708.86 nm ($E_g^m = 1.35$ eV and $E_g^c = 1.35$ eV). Where, E_g^m and E_g^c, are band gap for microwave and convention-method, respectively.

Photoluminescence emission (PLE) spectra of Ag@AgCl/ZnO are revealed by Fig. 3b, c, which were taken for the samples prepared by one pot reflux- and microwave assisted-methods, respectively. Figure 3b exhibited

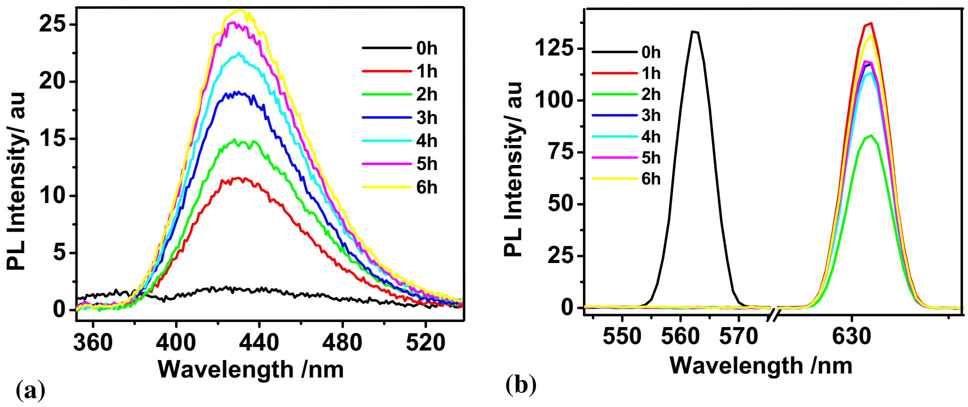

Fig. 4 **a** PLE spectra changes (Soret-band) at 428.0 nm wavelength with visible-light irradiation time for the Ag@AgCl/ZnO (microwave) nanocomposite powder dispersed in alkaline terphallic acid solution and **b** Q-bands of PLE spectrum at 562.8 nm and 6320.9 nm wavelength

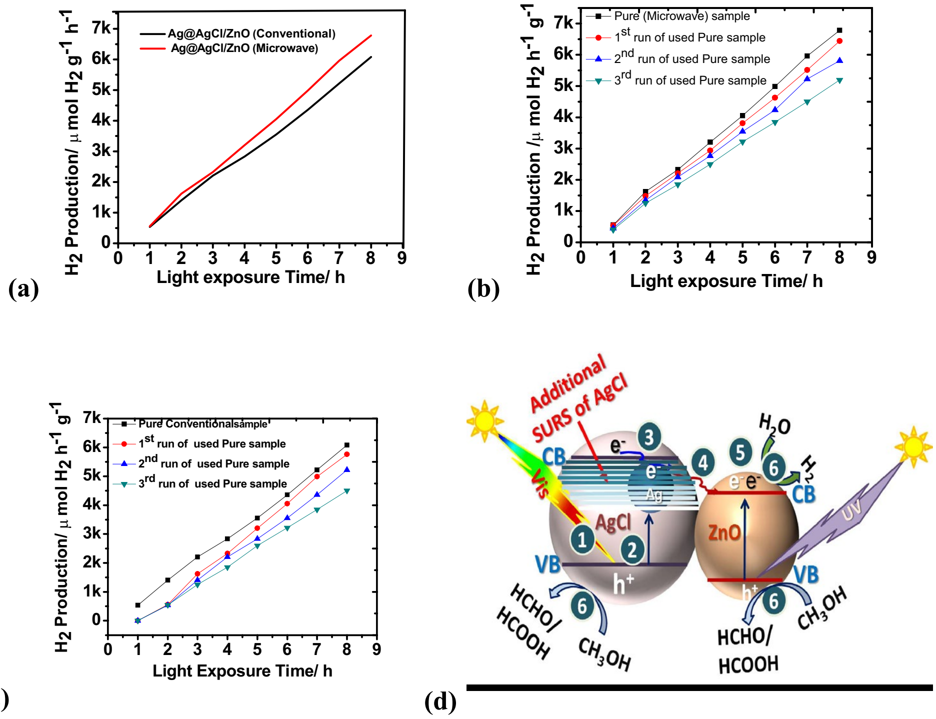

Fig. 5 Photocatalytic hydrogen production by **a** pristine NC (Ag@AgCl/ZnO) prepared by the conventionally (red)- and microwave (green)-method, **b** reproducibility check for the first time-, second time- and third time-used microwave synthesized samples, **c** reproducibility check for the first time-, second time- and third time-used conventionally synthesized sample, with respect to the time (1 to 8 h) under 300 W Xe light exposure. **d** The electron transfer mechanism for water splitting of nanocomposites

the excitation peak at the wavelength of 250 nm under the exposure of emission light of the wavelength $\lambda^{em}_{max} = 502$ nm and green light emission spectra was found at 502 nm under the excitation energy of wavelength $\lambda^{ex}_{max} = 250$ nm for one pot refluxed sample. Similarly, the strong PLE peak was observed for microwave assisted sample at 602 nm under the excitation energy of wavelength 300 nm, as shown by the Fig. 3c.

Figure 4a illustrated the PLE spectra of the conventionally prepared sample to check the presence of *OH radical as a PLE signal of Soret-band at 428 nm and Q-bands at 562.8 nm and 632.9 nm at the 315 nm excitation energy, under visible light irradiation [23].The PLE signal at 428 nm are the result of the reaction between *OH radical and terephthalic acid that produces HTA at the water/catalyst interface. The concentration of HTA increases with reaction time (0 h, 1 h, 2 h, 3 h, 4 h, 5 h and 6 h) that reflected the increase in production of *OH radicals during the reaction (Fig. 4a).

Molecular devices of Ag@AgCl/ZnO NC (prepared via one pot conventional and microwave method), produced hydrogen in 20% methanolic DIW, under visible light exposure of 300 W Xe light. Amount of the released hydrogen, was significantly enhanced with increasing exposure time (i.e. 1, 2, 3, 4, 5, 6, 7 and 8 h) viz. 536.71 and 556.8, 1404.41 and 1621.21, 2207.86 and 2325.37, 2835.26 and 3203.09, 3554.11and 4053.44, 4359.24 and 4987.66, 5221.07 and 5761.86, 6082.9 and 6782.32 µmol H_2 h^{-1} g^{-1}, corresponding to the conventional and microwave prepared nanocomposite samples under 300 W Xe light irradiation

(Fig. 5a–c) at room temperature. Above used samples further used for three time to check the reproducibility of the samples, that was found good for all studied samples with low decrease in photocatalytic activity (Fig. 5b, c).

4 Discussion

The XRD study confirms that the nanocomposite Ag@ AgCl/ZnO crystallized in their three major phases i.e. AgCl, Ag and ZnO. The particle size of these nanocomposites, prepared by one pot conventional and microwave synthesis was determined using Scherrer formula viz. 57.72 nm, and 59.12 nm, respectively with their corresponding lattice strain 0.0022 and 0.0023. Lattice strain associated with the dislocations in crystal structure could either be caused a crystallographic defects or irregularity in lattice arrangement due the presence of three different phases [49]. These topological defects can be highly influenced by the material's native properties. The X-ray diffraction profiles can also be used in determination of the dislocation density (δ) for the samples using following expression given in Eq. (8) [48]:

$$\delta = \frac{15\beta Cos\theta}{4aD} \tag{8}$$

where dislocation density $[\delta = 3.8019 \times 10^{13}\ \mathrm{m}^{-2}$(one pot) and $3.9100 \times 10^{13}\ \mathrm{m}^{-2}$(microwave)] is calculated from broadening of diffraction peak i.e. Full width at its half of maximum intensity β (in radian), Bragg's diffraction angle θ (in degree), lattice constant a (in nm) and particle size D (in nm). Higher strain and delocalization density of the microwave synthesized sample than conventionally prepared sample is associated with higher number of active sites on the large molecular surface area due to lotus shape of the particle. The presence of Zn in Ag lattice is also confirmed from blue shift that observed for Ag XRD peaks due to addition of low weighted element Zn, as shown in Fig. 1b.

EDX profile corresponds to the Fig. 2a used to confirm the presence of 20.65/19.00% ZnO, 12.98/13.79% AgCl, 4.73/8.08% Zn and 28.01/26.19% Ag in the NCs (one pot reflux-/microwave-method %). FESEM elemental mapping are shown in Fig. 2d, e, predicted that the nanoparticles Ag/Zn (nanoparticles of size 30–40 nm)-loaded AgCl were well dispersed on ZnO surface. Above results also revealed that in compare to the six petal-lotus like artifacts of the microwaved sample, the conventionally prepared samples had more homogeneously dispersed elements as illustrated by the Fig. 2d, e.

Intense UV–Vis absorption peak around 300.40 nm (Fig. 3a) appeared due to the ligand metal charge transfer (LMCT) $\pi \rightarrow \sigma^*$ electron transition (the charge transfer of excitons from the VB to CB) in the host material. The broad and small peak at 352.00 nm comes into view due to the *d*–*d* transition of Ag NPs, which were deposited on AgCl/ZnO surface [50]. Vigilant inspection of the spectra speculated a broad and weak plateau between 407.9 and 700 nm, also attributed to the *d*–*d* orbital interactions of Ag/Zn nanoparticles. The ability of visible light absorption for final nanocomposites was drastically enhanced due to the surface plasmonic resonance (SPR) effect of Ag/Zn NPs that associated with the AgCl surface. This combination (Ag@AgCl) prompts the self-sensitization of AgCl that result in additional CB levels [21]. Ag levels are located just below the conduction band edge of AgCl, can develop additional AgCl surface states (SURS), as well as metal induced gap states (MIGS) from Ag@ AgCl composites that present in the band gap region of silver chloride and their presence induce the self-sensitization phenomenon in AgCl (Scheme 1b) [20].

The Fermi levels of ZnO/AgCl and Ag NPs are the same in absence of the visible light exposure. But under the visible light irradiation, ZnO and AgCl cannot be excited in nanocomposite Ag@ AgCl/ZnO due to its wide band gap therefore their Fermi level remains unchanged. In contrast, plasmonic Ag NPs absorbs visible light because of its SPR absorption, results in the up shift of Fermi level of Ag NPs and produces additional SURS at band gap of AgCl that facilitate the photoexcited electrons of the AgCl to be easily injected into the conduction band of ZnO [51]. These injected electrons can reacted with the adsorbed O_2 on surface to produce the superoxide radical anions ($O^{-2}*$) [52], which is converted into HOO* radicals and finally, result in H_2O_2 on protonation. In alkaline medium under light irradiation, H_2O_2 converted into *OH radicals, which can participation in the water splitting. Excitation and emission (PLE) spectra of sample produced by one pot reflux- and microwave methods, corresponded to the Fig. 3b, c, respectively. Inset of Fig. 3c, exhibit the Commission Internationale de l'Eclairage (CIE) plot of the Ag@ AgCl/ZnO (microwave) that confirms the material emits yellow light. The change in preparation method result in shifting of PLE peak from 502 to 602 nm, attributed to the high concentration of the delocalized defects in microwave-prepared sample ($\delta = 3.9100 \times 10^{13}\ \mathrm{m}^{-2}$) than the conventionally (one pot)—prepared sample ($\delta = 3.8019 \times 10^{13}\ \mathrm{m}^{-2}$). Moreover, the photoluminescence phenomena associated with the degree of deviation from the two competing effects i.e. lattice and local coordination effects. The large deviation found for the microwave synthesized sample. Therefore, microwave synthesized samples are more prone to possess more delocalized defects. Green emission (Fig. 3b) of conventionally prepared samples are associated with oxygen deficiency due to a transition between neutral and singly ionized oxygen vacancy [53]. Microwave assisted samples exhibits strong and broad yellow defect emission peak (Fig. 3c) due to the surface defects [54], and contributed the yellow emission.

The concentration of *OH radicals on the surface of the catalyst measured under visible-light exposure in alkaline terephthalic acid solution (initial pH = 10.5) by photoluminescence method [23, 55, 56]. In basic terephalate solution, the Q-bands further split into two bands owing to vibrational excitations due to transition from ground state to two vibrational states of the excited state [Q(0,0) and Q(1,0)] [32]. These transitions can be visualized in the form of Soret band and Q-bands in fluorescence spectra, which was the result of the chemical reactions between basic terephthalic acid and *OH formed during photocatalytic reactions [57]. Figure 4a exhibited the gradual increase in PLE intensity at 428 nm wavelength with increasing irradiation exposure time, associated with the Soret-band (S_0 to S_2 transition) due conversion of terephthalic acid into HTA (Eq. 9). The molar absorption coefficient for the Soret-band is 155–500 M^{-1} cm^{-1} [55].

Other PLE peaks found at 562.8 nm and 632.9 nm, belongs to the Q-bands (S_0 to S_1 transition) [55, 56]. Furthermore, experiments show that no PL signals for the Ag@AgCl/ZnO NC impregnated basic terephthallic acid solution in dark (0 h-PLE curve of Fig. 4a) that result in no production of –OH* radicals because pure molecular device is activated by visible light (as discussed above). The production of –OH* radical not only indicated by the decreases in pH of solution from 10.5 to 8.14 with reaction time but also from the raise in a absorption maximum for PLE peak at 428 nm (Soret-band) with increasing time.

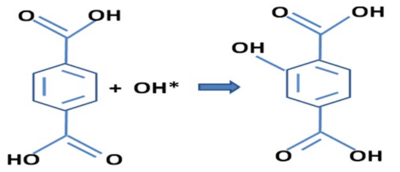

$$\text{Terephthalic acid} + \text{hydroxyl radical} \rightarrow \text{2 - hydroxy Terephthalic acid} \tag{9}$$

The pure water has inefficient energy to decompose all alone but presence of photocatalyst promote this decomposition. Therefore, the study focused on hydrogen production by photocatalytic water splitting using semiconductor NC i.e. Ag/Zn@AgCl/ZnO under light exposure. Minimum four electrons required to stimulate the multistep-water reduction and oxidation reactions of overall water splitting process for H_2 and O_2 production, respectively. The sacrificial molecules (20% methanol in this case) act as an electron donor/hole-acceptor to enhance the efficiency of the H_2 production by consuming the holes and suppress the oxygen production. Various organic compounds such as alcohols, carboxylic acids, and hydrocarbons, etc., can act as an efficient hole-scavengers (or electron donors) for the photocatalytic H_2 generation. Here, we used methanol as sacrificial electron donor that significantly suppress the charge carrier-recombination process, and enhance the hydrogen gas production by avoiding a subsequent gaseous product (H_2 and O_2) separation stage. Accumulative all process, leads to increase the overall H_2 yield. It irreversibly encountered the photo-generated holes to enhance the photocatalytic electron/hole-separation efficiency and give rise to high quantum yields for hydrogen generation [58].

Therefore, photocatalytic water splitting experiments was performed for the hydrogen generation from the molecular nanocomposite Ag@AgCl/ZnO that well dispersed in 20% aqueous methanol scavenger at pH = 7, under 1.5 AM G light irradiation as demonstrated by Fig. 5a–c. The hydrogen generation from water in presence of nanocomposite Ag@AgCl/ZnO might follow the below mentioned reaction mechanism, expressed by Eqs. (10) to (18) [57, 58]:

Generation of hydrogen

$$\text{Ag@AgCl} \xrightarrow{\textit{Visible light}} (CV)e^- + (VB)h^+ \quad \left(\text{photocarriers } \left(e^-/h^+\right) \text{ generation}\right) \tag{10}$$

$$\text{Ag@AgCl}(CV)e^- \rightarrow \text{ZnO}(CV)e^- \quad (\text{transfer of photoelectron}) \tag{11}$$

$$\text{ZnO}(CV)e^- + H_2O \rightarrow H^* + OH^- \quad \left(\text{generation of free radical } H^*\right) [59] \tag{12}$$

$$h^+ + OH^- \rightarrow OH^* \quad (\text{generation of free radical } OH^*) \tag{13}$$

$$H^* + H^* \rightarrow H_2(0.00\ \text{eV}) \quad \left(\text{generation of } H_2\right) \tag{14}$$

Consumption of h^+ using CH_3OH

$$\text{ZnO or AgCl}(VB)h^+ + CH_3OH \rightarrow CH_2OH^* + H^+(-0.1264\ \text{eV})[60] \tag{15}$$

$$CH_2OH^* + OH^* \rightarrow HOCH_2OH^* \rightarrow HCHO + H_2O(-3.848\ \text{eV}) \tag{16}$$

$$CH_2OH^* + O \rightarrow OCH_2OH^* \rightarrow HCHO + OH^*(-3.18\ \text{eV}) \tag{17}$$

$$CH_2OH^* + O \rightarrow OCH_2OH^* \rightarrow HCOOH + H^*(-4.125\ \text{eV}) \tag{18}$$

The first two reactions (Eqs. 10 and 11) devoted to increase the concentration of photoelectrons on surface of molecular device, for favoring the reduction of water in presence of the sunlight and catalyst. The reactions (Eqs. 12, 14, 16–18), involve in generation of free radicals H*/*OH and the formation of the H_2 gas/

HCHO, respectively. These conversion reactions had a large negative Gibbs energy, thus it intrinsically provides a barrier for the undesired reverse consumption of the H_2. Furthermore, two possible mechanisms are proposed for photocatalytic oxidation of methanol: (1) the direct oxidation by photogenerated holes and (2) the indirect oxidation via interfacial *OH radicals [59]. To distinguish the two mechanisms in practice is still a challenge due to the lack of suitable probe techniques. In present case, it follows the indirect oxidation via interfacial *OH radicals mechanism that studied by spectroflurimetry. Therefore, the experiments hydroxyl ions converted into hydroxyl radicals under the light exposure, which degrade the methanol and result in production of HCHO or HCOOH, as shown by Eqs. (15)–(18). Finally, the hydrogen produce through photocatalytic hassle-free reduction of the water. It was found that no detectable amount of hydrogen production was observed even after the 72 h exposure of water with or without catalyst in dark. The H_2 generation capacity of catalyst was continuously estimated for 20% methanol solution in an argon atmosphere via gas chromatograph [Agilent, TCD (8A column); model: 2780]. Close examination of the spectra told us microwave synthesized samples are more active than conventionally prepared sample.

Gradual increase in hydrogen evolution with time was observed as: from 536.71 to 6082.9 µmol H_2 h^{-1} g^{-1} (conventional) and from 556.8 to 6782.32 µmol H_2 h^{-1} g^{-1} (Microwave) under irradiation of 300 W Xe light source. These experimentally observed rate of hydrogen evolution are in good agreement with state of art nanocomposite Ag/AgBr/TiO_2 that releases 1.00 µmol H_2 h^{-1} g^{-1} after 2 h, under the irradiation of 100 W high-pressure Hg lamp-with IR filter [61]. Catalytic activity of the nanocomposite Ag@AgCl/ZnO was rejuvenated during the photocatalysis process, as it expressed by Eqs. (1) to (7) [18, 19]. After photocatalytic activity of H_2 production-measured, the catalyst (pinkish grey) was thoroughly washed with distilled water and reused after drying at 80 °C for 12 h. It was found that there is no significant lost in catalytic activity even after three time use as shown in Fig. 5b, c. Above UV–Vis absorption spectra, spectroflurometric and photocatalytic study gives us sufficient evidence to the electron transfer mechanism of the photocatalytic water splitting for the H_2 production process, which is well illustrated by the Fig. 5d. When the light falls upon the surface of the NC Ag@AgCl/ZnO then electron of VB jumped over to the CB. Additional CB layers (SURS) of AgCl required less energy for electron transfer from VB to CB than pristine AgCl. Moreover, this electronic transformation was induced by visible light whether the individual transition in AgCl or ZnO, was exposed to light. Finally, the electrons transferred to CB of ZnO though SURS of Ag@AgCl. Where, this photoelectron reduces the water to liberate H_2 and holes consumed to generate HCHO or HCOOH by oxidation of CH_3OH.

5 Conclusion

We explored nanocomposite Ag@AgCl/ZnO NC as a smart material (fabricated by two ways i.e. Microwave and conventional) that can be utilized as a photocatalyst for hydrogen generation through water splitting under visible light exposure. The molecular device exhibits good activity towards photocatalytic hydrogen generation among the state of art photocatalyst of the same class. Moreover, it was established for the molecular device that the photoelectrons generated during the light irradiation was used to reduce water for better hydrogen production and photo-holes reacted with OH^- to form *OH radicals, which used as a scavenger to degrade the methanol into HCHO or HCOOH. Furthermore, the advancement in the molecular device is in progress by replacing halides with other anions and other plasmonic materials in nanocomposite Ag@AgX/ZnO (X = halide).

Acknowledgements NC thanks to the Science and Engineering Research Board, Department of Science and Technology, India (SB/S1/PC-31/2012) and UGC-DAE, CSR-Indore (CSR-IC-MSRSR-25/CRS-233/2017-18/1314) for their financial support and Dr. Gururao of IIT, Kanpur (India) for providing SEM supported Elemental mapping facility to us.

Compliance with ethical standards

Conflict of interest The authors declare that they have no conflict of interest.

References

1. Li Q, Guo B, Yu J, Ran J, Zhang B, Yan H, Gong JR (2011) Highly efficient visible-light-driven photocatalytic hydrogen production of CdS-cluster-decorated graphene nanosheets. J Am Chem Soc 133:10878–10884
2. Zhang J, Yu J, Jaroniec M, Gong JR (2012) Noble metal-free reduced graphene oxide-$Zn_xCd_{1-x}S$ nanocomposite with enhanced solar photocatalytic H_2-production performance. Nano Lett 12(9):4584–4589
3. Xie G, Zhang K, Guo B, Liu Q, Fang L, Gong JR (2013) Graphene-based materials for hydrogen generation from light-driven water splitting. Adv Mater 25:3820–3839
4. Xie G, Zhang K, Fang H, Guo B, Wang R, Yan H, Fang L, Gong JR (2013) A photoelectrochemical investigation on the synergetic effect between CdS and reduced graphene oxide for solar-energy conversion. Chem Asian J 8:2395–2400
5. Bartali R, Speranza G, Aguey-Zinsou KF, Testi M, Micheli V, Canteri R, Fedrizzi M, Gottardi G, Coser G, Crema L, Pucker G, Setijadi E,

Laidani N (2018) Efficient hydrogen generation from water using nanocomposite flakes based on graphene and magnesium. Sustainable Energy Fuels 2:2516–2525

6. Ding X, Li Y, Zhao J, Zhu Y, Li Y, Deng W, Wang C (2015) Enhanced photocatalytic H_2 evolution over CdS/Au/g-C_3N_4 composite photocatalyst under visible-light irradiation. APL Materials 3:104410
7. Chandra M, Bhunia K, Pradhan D (2018) Controlled synthesis of CuS/TiO_2 heterostructured nanocomposites for enhanced photocatalytic hydrogen generation through water splitting. Inorg Chem 57(8):4524–4533
8. Wang P, Weide P, Muhler M, Marschall R, Wark M (2015) New insight into calcium tantalate nanocomposite photocatalysts for overall water splitting and reforming of alcohols and biomass derivatives. APL Materials 3:104412
9. Xu Y, Xu H, Li H, Xia J, Liu C, Liu L (2011) Enhanced photocatalytic activity of new photocatalyst Ag/AgCl/ZnO. J Alloys Compound 509:3286–3292
10. Wang D, Duan Y, Luo Q, Li X, Bao L (2011) Visible light photocatalytic activities of plasmonic Ag/AgBr particles synthesized by a double jet method. Desalination 270:174–180
11. Li W, Hua F, Yue J, Li J (2013) Ag@AgCl plasmon-induced sensitized ZnO particle for high-efficiency photocatalytic property under visible light. Appl Surf Sci 285:490–497
12. Adhikari R, Gyawali G, Sekino T, Lee SW (2013) Microwave assisted hydrothermal synthesis of Ag/AgCl/WO_3 photocatalyst and its photocatalytic activity under simulated solar light. J Solid State Chem 197:560–565
13. Guo R, Zhang G, Liu J (2013) Preparation of Ag/AgCl/BiMg_2VO_6 composite and its visible-light photocatalytic activity. Mater Res Bull 48:1857–1863
14. Hamilton JF (1974) Physical-properties of silver-halide microcrystals. Photogr Sci Eng 18:493–500
15. Kakuta N, Goto N, Ohkita H, Mizushima T (1999) Silver bromide as a photocatalyst for hydrogen generation from CH_3OH/H_2O solution. J Phys Chem B 103:5917–5919
16. Schürch D, Currao A, Sarkar S, Hodes G, Calzaferri G (2002) The silver chloride photoanode in photoelectrochemical water splitting. J Phys Chem B 106:12764–12775
17. Lou Z, Huang B, Ma X, Zhang X, Qin X, Wang Z, Dai Y, Liu Y (2012) A 3D AgCl hierarchical superstructure synthesized by a wet chemical oxidation method. Chem Eur J 18:16090–16096
18. Pfanner K, Gfeller N, Calzaferri G (1996) Photochemical oxidation of water with thin AgCl layers. J Photoch Photobio A 95:175–180
19. Glaus S, Calzaferri G (1999) Silver chloride clusters and surface states. J Phys Chem B 103:5622–5630
20. Calzaferri G, Brühwiler D, Glaus S, Schürch D, Currao A, Leiggener C (2001) Quantum-sized silver, silver chloride and silver sulfide clusters. J Imaging Sci Technol 45:331–339
21. Glaus S, Calzaferri G, Hoffmann R (2002) Electronic properties of the silver–silver chloride cluster interface. Chem Eur J 8:1785–1794
22. Sumi S, Watanabe T, Fujishima A, Honda K (1980) Effect of Cl^- and Br^- ions and pH on the flatband potentials of silver halide sheet crystal electrodes. Bull Chem Soc Jpn 53:2742–2747
23. Zhou J, Cheng Y, Yu J (2011) Preparation and characterization of visible-light-driven plasmonic photocatalyst Ag/AgCl/TiO_2 nanocomposite thin films. J Photoch Photobio A 223:82–87
24. Longhui N, Zhengqing H, Hongtao X, Wangxi Z, Borui Y, Lei F, Shuaihua L (2012) Synthesis of Ag@AgBr photocatalyst and its performance for degradation of methylene blue under visible-light irridiation. Chin J Catal 33:1209–1216
25. Tian Y, Tatsuma T (2005) Mechanisms and applications of plasmon-induced charge separation at TiO_2 films loaded with gold nanoparticles. J Am Chem Soc 127:7632–7637
26. Carja G, Birsanu M, Okadac K, Garcia H (2013) Composite plasmonic gold/layered double hydroxides and derived mixed oxides as novel photocatalysts for hydrogen generation under solar irradiation. J Mater Chem A 1:9092–9098
27. Pirhashemi M, Habibi-Yangjeh A (2014) Preparation of AgCl–ZnO nanocomposites as highly efficient visible-light photocatalysts in water by one-pot refluxing method. J Alloys Compound 601:1–8
28. Awazu K, Fujimaki M, Rockstuhl C, Tominaga J, Murakami H, Ohki Y, Yoshida N, Watanabe T (2008) A plasmonic photocatalyst consisting of silver nanoparticles embedded in titanium dioxide. J Am Chem Soc 130:1676–1680
29. Chen HM, Chen CK, Chen CJ, Cheng LC, Wu PC, Cheng BH, Ho YZ, Tseng ML, Hsu YY, Chan TS, Lee JF, Liu RS, Tsai DP (2012) Plasmon inducing effects for enhanced photoelectrochemical water splitting: X-ray absorption approach to electronic structures. ACS Nano 6(8):7362–7372
30. Zhu MS, Chen PL, Liu MH (2011) Graphene oxide enwrapped Ag/AgX (X = Br, Cl) nanocomposite as a highly efficient visible-light plasmonic photocatalyst. ACS Nano 5:4529–4536
31. Zhang YH, Tang ZR, Fu XZ, Xu Y (2011) Nanocomposite of Ag–AgBr–TiO_2 as a photoactive and durable catalyst for degradation of volatile organic compounds in the gas phase. J Appl Catal B 106(3–4):445–452
32. Wang XF, Li SF, Ma YQ, Yu HG, Yu JG (2011) $H_2WO_4 \cdot H_2O$/Ag/AgCl composite nanoplates: a plasmonic Z-scheme visible-light photocatalyst. J Phys Chem C 115:14648–14655
33. Cao J, Luo BD, Lin HL, Chen SF (2011) Photocatalytic activity of novel AgBr/WO_3 composite photocatalyst under visible light irradiation for methyl orange degradation. J Hazard Mater 190:700–706
34. Chen HM, Chen CK, Tseng ML, Wu PC, Chang CM, Cheng LC, Huang HW, Chan TS, Huang DW, Liu RS, Tsai DP (2013) Plasmonic ZnO/Ag embedded structures as collecting layers for photogenerating electrons in solar hydrogen generation photoelectrodes. Small 9(17):2926–2936
35. Shi H, Chen J, Li G, Nie X, Zhao H, Wong PK, An T (2013) Synthesis and characterization of novel plasmonic Ag/AgX-CNTs (X = Cl, Br, I) nanocomposite photocatalysts and dynergetic degradation of organic pollutant under visible light. ACS Appl Mater Interfaces 5(15):6959–6967
36. Christopher P, Xin H, Linic S (2011) Visible-light-enhanced catalytic oxidation reactions on plasmonic silver nanostructures. Nat Chem 3:467
37. Im SH, Lee YT, Wiley B, Xia Y (2005) Large-scale synthesis of silver nanocubes: the role of HCl in promoting cube perfection and monodispersity. Angew Chem Int Ed 44:2154
38. Carja G, Nakajima A, Dranca S, Dranca C, Okada K (2010) Nanoparticles of nickel oxide: growth and organization on zinc substituted anionic clay matrix by one-pot route at room temperature. J Phys Chem C 114:14722–14728
39. Lou ZZ, Huang BB, Qin XY, Zhang XY, Wang ZY, Zheng ZK, Cheng HF, Wang P, Dai Y (2011) One-step synthesis of AgBr microcrystals with different morphologies by ILs-assisted hydrothermal method. Cryst Eng Comm 6:1789–1793
40. Perreux L, Loupy A (2001) A tentative rationalization of microwave effects in organic synthesis according to the reaction medium, and mechanistic considerations. Tetrahedron 7:9199–9223
41. Singh AK, Nakate UT (2013) Microwave synthesis, characterization and photocatalytic properties of SnO_2 nanoparticles. Advances in Nanoparticles 2:66–70
42. Barreto GP, Morales G, Quintanilla ML (2013) Microwave assisted synthesis of ZnO nanoparticles: effect of precursor reagents, temperature, irradiation time, and additives on nano-ZnO morphology development. Journal of Materials 2013, 478681

43. Yamamoto T, Wada Y, Sakata T, Mori H, Goto M, Hibino S, Yanagida S (2004) Microwave-assisted preparation of silver nanoparticles. Chem Lett 33:158
44. Komarneni S, Li DS, Newalkar B, Katsuki H, Bhalla AS (2002) Microwave-polyol process for Pt and Ag nanoparticles. Langmuir 18:5959–5962
45. Tadjarodi A, Khaledi D (2010) Preparation of CuS nanoparticles by microwave irradiation. In: 14th International electronic conference on synthetic organic chemistry, 1–30 Nov 2010 (C010)
46. Ai L, Zhang C, Jiang J (2013) Hierarchical porous AgCl@Ag hollow architectures: self-templating synthesis and highly enhanced visible light photocatalytic activity. Appl Catal B 142–143:744–751
47. Fang Y, Li Z, Xu S, Han D, Lu D (2013) Optical properties and photocatalytic activities of spherical ZnO and flower-like ZnO structures synthesized by facile hydrothermal method. J. Alloys Comp. 575:359–363
48. Venkata Subbaiah YP, Prathap P, Ramakrishna Reddy KT (2006) Structural, electrical and optical properties of ZnS films deposited by close-spaced evaporation. Appl Surf Sci 253:2409–2415
49. Callister WD (2004) Materials science and engineering—an introduction, 6th edn. Wiley, New York
50. Suhai S (1986) On the excitonic nature of the first UV absorption peak in polyene. Int J Quantum Chem 29(3):469–476
51. Yu J, Dai G, Huang B (2009) Fabrication and characterization of visible-light-driven plasmonic photocatalyst Ag/AgCl/TiO_2 nanotube arrays. J Phys Chem C 113(37):16394–16401
52. Draper RB, Fox MA (1990) Titanium dioxide photosensitized reactions studied by diffuse reflectance flash photolysis in aqueous suspensions of TiO_2 powder. Langmuir 6(8):1396–1402
53. Hichou AE, Addou M, Ebothé J, Troyon M (2005) Influence of deposition temperature (T_s), air flow rate (f) and precursors on cathodoluminescence properties of ZnO thin films prepared by spray pyrolysis. J Lumin 113:183–190
54. Li D, Leung YH, Djurišić AB, Liu ZT, Xie MH, Shi SL, Xu SJ, Chan WK (2004) Different origins of visible luminescence in ZnO nanostructures fabricated by the chemical and evaporation methods. Appl Phys Lett 85:1601
55. Xiang QJ, Yu JG, Cheng B, Ong HC (2010) Microwave-hydrothermal preparation and visible-light photoactivity of plasmonic photocatalyst Ag–TiO_2 nanocomposite hollow spheres. Chem Asian J 5(6):1466–1474
56. Xiang Q, Yu J, Wong PK (2011) Quantitative characterization of hydroxyl radicals produced by various photocatalysts. J Colloid Interface Sci 357:163–167
57. Spellane PJ, Gouterman M, Antipas A, Kim S, Liu YC (1980) Porphyrins. 40. Electronic spectra and four-orbital energies of free-base, zinc, copper, and palladium tetrakis (perfluorophenyl) porphyrins. Inorg Chem 19(2):386–391
58. Schneider J, Bahnemann DW (2013) Undesired role of sacrificial reagents in photocatalysis. J Phys Chem Lett 4:3479–3483
59. Schwarz HA (1992) Reaction of the hydrated electron with water. J Phys Chem 96(22):8937–8941
60. Seetula JA, Kalinovski IJ, Slagle IR, Gutman D (1994) Kinetics of the reaction of CH_2OH radical with oxygen atoms. Chem Phys Lett 224(5–6):533–538
61. Yu G, Dai GP, Huang BB (2009) Fabrication and characterization of visible-light-driven plasmonic photocatalyst Ag/AgCl/TiO_2 nanotube arrays. J Phys Chem C 113:16394–16401

Publisher's Note Springer Nature remains neutral with regard to jurisdictional claims in published maps and institutional affiliations.

LIST OF SEMINAR/ SYMPOSIUMS/CONFERENCES

1. **“Indo Swedish Symposium on Strategic Knowledge on Climate Change”** (Designing Climate Smart Water Adaption Strategies for Sustainable Development) organized by Department of Pure & Applied Chemistry, University of Kota, Kota, Rajasthan 09thOctober 2012.
2. **19th ISCB International Conference (ISCBC-2013)** entitled as “Recent Advances and Current Trends in Chemical and Biological Science” jointly Organized by Indian Society of Chemistry & Biologists, Lucknow (UP) India and Department of Chemistry, Mohan Lal Sukhadia University, Udaipur (Rajasthan) India.2th -5thMarch 2013. (Poster Presentation)
3. **5th National Academic Workshop** on “Organic Reaction Mechanisms & Analytical Techniques Used in Chemical Science” organized by Department of Pure & Applied Chemistry, University of Kota, Kota, Rajasthan on 21th -25th October 2013.
4. **Symposium on** “E-resources” organized by Department of Library and Information Science, University of Kota, Kota, Rajasthan during 16th – 17th Dec. 2013.
5. **National Seminar** on “Environmental Issues and Social Concerns” organized by Department of Social Science, University of Kota, Kota, Rajasthan 21th-22thMarch 2014.
6. **“Recent Advancements in Protection of Environment and its Management Issues”** organized by Maharishi Arvind College of Engineering & Technology, Ranpur, Kota during 27th -28thFebruary 2015. (poster Presentation)
7. **National conference** on “Frontiers at the Chemistry Allied Sciences Interface” organized by Center of Advanced Study Department of Chemistry, University of Rajasthan, Jaipur during 13th-14th March 2015.
8. **National Conference** on “Frontiers in Chemical Sciences” organized by Department of PG Studies and Department of Chemistry (Udaipur) in association with Indian Chemical Society, Kolkata(India) on 4th October 2016.
9. **“International Conference ICRCS-2017”** organized by Govt. Engineering College, Bikaner, (Rajasthan) during 12th-13th January 2017.

10. **“Global Environmental Challenges Present Scenario**” organized by Department of Botany, University of Rajasthan, Jaipur on 21th January 2017.
11. **International Conference** on “Innovative Research in Science, Technology and Management” organized by Modi institute of Management & Technology Dada Bari, Kota, Rajasthan during 22th-23th January 2017. (Paper Presentation)
12. “**Author Workshop”** jointly organized by Springer Nature and University of Kota, Rajasthan, on 2nd March 2017.
13. **Workshop** on “LaTeX-An Efficient Documentation Tool” organized by Department of Computer Science & Informatics, University of Kota, Kota, Rajasthan on 17th-18thMarch 2017
14. **National Seminar** on “Recent Trends & Advances in Chemical Science and their Impact on Environment” (RTACIE-2018) organized by Amity University Jaipur Rajasthan on 13th April 2018. (Poster Presentation)
15. **International Conference** on “Chemical Science in New Era” organized by Department of PG Studies and Department of Chemistry, Pacific Academy of Higher Education and Research University, Udaipur(Rajasthan) in association Indian Chemical Society, Kolkata (India) during October 5th-6th2018. (Poster Presentation)
16. **National Seminar** on “Aspects of Geographical Indications for Sustainable Development” organized by Intellectual Property Rights Cell, University of Kota, Kota during 28th -29thMarch 2019.